UNIVERSITY OF LJUBLJANA
FACULTY OF MATHEMATICS AND PHYSICS
DEPARTMENT OF PHYSICS

Andrii Tykhonov

Searches for dark matter and lepton-jets with the ATLAS detector

Doctoral thesis

advisor: Prof. Dr. Borut Paul Kerševan

Ljubljana, 2013

UNIVERZA V LJUBLJANI
FAKULTETA ZA MATEMATIKO IN FIZIKO
ODDELEK ZA FIZIKO

Andrii Tykhonov

Iskanje temne snovi in leptonskih pljuskov z detektorjem ATLAS

Doktorska disertacija

mentor: Prof. Dr. Borut Paul Kerševan

Ljubljana, 2013

Abstract

A search is performed for Higgs boson decaying to hidden sector and subsequently into highly collimated jets of electrons, known as electron-jets. The hidden sectors and lepton-jets are predicted in the new theories of dark matter, motivated by the recent proliferation of astrophysical anomalies, observed by cosmic-ray and dark matter direct-detection experiments. The search is performed with 2.04 fb^{-1} of data collected in 2011 with the ATLAS detector at the LHC in proton–proton collisions at $\sqrt{s} = 7$ TeV. To select electron jets, various jet identification parameters are exploited, based on the combined calorimeter and tracking information, providing good discrimination against background sources, and avoiding sensitivity to the detailed topology of the electrons within the electron-jet. Background contamination in the signal region is determined using a completely data-driven technique, and is cross-checked with two alternate methods of background evaluation. Systematic uncertainties for the signal selection efficiency are estimated using data-driven methods, by examining the electrons from $Z \to ee$ decay and photons that have converted in the detector into highly collimated electron-positron pairs. One event satisfying the signal selection criteria is observed after the final selection, which is consistent with the expected background rate. Consequently, 95% confidence level limits are set on the Higgs boson production cross section times the branching ratio into electron-jets, assuming the two benchmark models of a hidden sector and the condition of a dark photon mass below 210 MeV. The prospects are discussed for further lepton-jet searches, using the full data set collected by the ATLAS detector in 2012 at $\sqrt{s} = 8$ TeV. The work presented in the thesis has been published as a scientific article on behalf of the ATLAS collaboration.

PACS: 95.35.+d, 12.60.-i, 12.60.Rc, 12.60.Fr, 14.60.Cd, 14.80.Cp

Keywords: dark matter, ATLAS detector, lepton-jets, Higgs boson, exotics, dark photon

Izvleček

Izvedeno je iskanje razpadov Higgsovega bozona v skriti sektor in posledično v zelo kolimirane snope elektronov, znane kot elektronski pljuski. Skriti sektorji in leptonski pljuski so predvideni v novih teorijah temne snovi, ki jih motivirajo nedavno širjenje astrofizikalnih anomalij, ki so jih opazili v eksperimentih z kozmičnimi žarki in z neposrednim iskanjem temne snovi. Iskanje je izvedeno s 2.04 fb^{-1} podatkov, zbranih v letu 2011 z detektorjem ATLAS na LHC v trkih protonov s težiščno energijo 7 TeV. Za izbor elektronskih pljuskov smo uporabili različne parametre identifikacije pljuskov, ki temelji na kombinaciji informacij kalorimetra in sledi v notranjem detektorju. Ta izbor zagotavlja dobro diskriminacijo signala od ozadja in ni občutljiv na podrobno topologijo elektronov v elektronskem pljusku. Kontaminacijo ozadja v obmocju signala smo določili z uporabo tehnike, ki temelji popolnoma na podatkih, in jo navzkrižno preverili z dvema dodatnima metodama ocene ozadja. Sistematične negotovosti za učinkovitost izbire signala so ocenjene z uporabo metod, ki temeljijo na podatkih, s preučitvijo elektronov iz razpada bozona Z in fotonov, ki se v detektorju pretvorijo v zelo kolimirane pare elektronov in pozitronov. Opazili smo en dogodek, ki izpolnjuje merila za izbor signalov po končnem izboru, kar je v skladu s pričakovanim ozadjem. Zato smo ocenili 95% mejo intervala zaupanja za velikost produkta sipalnega preseka produkcjie Higgsovega bozona in razvejitvenega razmerja za razpad v elektronske pljuske, ob predpostavki za dva referenčna modela skritega sektorja in maso temnega fotona pod 210 MeV. V načrtu je nadaljnje iskanje leptonskih pljuskov z uporabo celotnega nabora podatkov, ki so bili zbrani z detektorjem ATLAS v letu 2012 pri trkih protonov s težiščno energijo 8 TeV. Delo, predstavljeno v disertaciji, je bilo objavljeno v znanstvenem članku v imenu kolaboracije ATLAS.

PACS: 95.35.+d, 12.60.-i, 12.60.Rc, 12.60.Fr, 14.60.Cd, 14.80.Cp

Ključne besede: temna snov, detektor ATLAS, leptonski pljuski, Higgsov bozon, eksotiko, temni foton

Acknowledgements

I am profoundly indebted to my family for their constant support, love and understanding, under frequently difficult circumstances, and for providing me a stable environment at home, for keeping pushing me forward in my scientific efforts. For his help and support, I am very grateful to my supervisor Dr. Borut Kerševen, without whose wise guidance the work would not have been brought up to the valuable achievement. I am also very grateful to my colleagues at Jozef Stefan Institute, for providing me with a cheerful, helpful and friendly ambient during the doctoral study. I would like to thank the head of our department, Dr. Marko Mikuž, for his wise advices, management and support, Jure Zupan for pointing out theoretical subtleties of hidden-sector models, Maksym Deliyergiyev for the useful cross-checks, and Tina Sfiligoj for her prompt help in preparing the Slovene chapter of the thesis.

This work would not have been possible without the significant inputs and support of my ATLAS colleagues, in particular, collaborators from Exotics physics group, as well as without the formidable and amazing endeavour of the ATLAS collaboration and LHC staff, held in the past two decades, which has resulted in the brilliant performance of the ATLAS experiment at the Large Hadron Collider.

“Stuff your eyes with wonder, live as if you’d drop dead in ten seconds. See the world. It’s more fantastic than any dream made or paid for in factories...”

Ray Bradbury

Contents

1

Introduction

The new experiment-driven era in physics has begun as the first stable bunches of protons have started circulating in the Large Hadron Collider (LHC). So far, Standard Model (SM) appears to be very successful theory of Nature at the energy scales up to about 100 GeV, withstanding the tests of unprecedented precision. Recently, ATLAS [1] and CMS [2] experiments at LHC have discovered the Higgs boson – the first fundamental particle with spin different from 1 and 1/2 – the last missing piece of the SM[1].

Despite the doubtless success, there are, however, physics aspects which can not be addressed in the SM. First of all, Standard Model is the combined theory of electroweak and strong interactions. By construction, it doesn't attempt to describe gravity. Gravity is expected to become strongly coupled (hence, observable at the microscopic level) at the energies close to the Planck scale[2], which is considered as the ultimate cutoff for the SM. Furthermore, there are clear evidences that SM should be altered with some new theory, acting at the energies slightly above the electroweak cutoff (1–10 TeV), for which the SM can be considered as an effective approximation at lower energies. Most frequently, this is understood in the context of so-called hierarchy problem, i.e. that some as yet unknown physics is required in order to address the stability of electroweak scale against the Planck scale [4]. Otherwise, if there is no new physics, Standard Model looks like a fine-tuned theory, where different terms (couplings) are tuned by hand to enormously high precision, in order to cancel the divergences that occur in the theory. The more natural explanation of the hierarchy problem may come from a new symmetry, like Supersymmetry (SUSY) [5]. In supersymmetrical models, the hierarchy problem is addressed in

---

[1] According to the latest measurements, the spin-0 hypothesis for the Higgs boson is fully compatible with the data, while spin-2 hypothesis is excluded at 95% confidence level [3].

[2] The Planck energy scale ($\sim 10^{19}$ GeV) is obtained if one assumes a particle, which has a De-Broglie wavelength equal to the Schwarzschild radius, corresponding to the mass of this particle. In other words, the particle is a "black hole" itself. Of course, this energy range is not accessible at any accelerator or cosmic-ray experiment, neither in present, nor in the predictable future.

an elegant way, cancelling the divergent terms in the propagator of the Higgs field. This makes supersymmetry a very appealing paradigm. There is a broad physics programme underway at LHC experiments, searching for evidence of supersymmetric theories. Most naturally, these models appear at the TeV energy scale, in order to ameliorate the hierarchy problem. No evidence of supersymmetry is spotted so far, and a large fraction of parameter space of these models have been excluded during the first LHC run. However, there is still large room for searches, and, if supersymmetry exists in Nature, it would be probably fished out during the second phase of LHC running.

Next, from the observation of motion of distant galaxies and from the results of gravitational lensing it has been inferred that the matter we can see constitutes only about 20% of the mass in the universe [6, 7], while the origin of other 80% remains unknown. This fact is unambiguously confirmed by many other observations and theoretical implications, such as arguments from Big Bang nucleosynthesis [8]. This unknown matter is referred to as dark matter (DM). Dark matter is seen only via gravitational effects it exerts on the motion of galaxies and on the light passing through it. Dark matter is not accounted for in the Standard Model. Observations of many distant galaxies reveal that all of them are immersed into a massive DM halo. Dark matter and normal (observed) matter together constitute up to 30% of energy density in the Universe, while other 70% pertains to dark energy – entity of as yet unknown nature which is responsible for the fact that our Universe is expanding with the positive acceleration [7, 9]. Dark energy doesn't cluster into galaxies or other stellar formations, but is likely distributed "uniformly" across the Universe. Despite the origin of dark matter and dark energy remaining a mystery, their relative content in Nature seem to be unambiguously determined and cross-checked by various astrophysical observations.

The most attractive candidates for dark matter are Weakly Interacting Massive Particles (WIMPs), which most naturally arise in the Supersymmetric models. These particles are assumed to have mass of up to 10 TeV and participate only in weak interactions. The annihilation cross section of weak strength automatically produces the right abundance of dark matter in the present Universe. This fact is known as a WIMP miracle. However, a series of cosmic-ray and dark matter direct-detection experiments in the past decade have brought up new results, which can be hardly addressed in the conventional WIMP models. The most prominent are the measurements of electron (positron) flux and the relative positron-to-electron fraction in cosmic rays [10–14]. These observations exhibit both an enhancement in the electron energy spectrum at energies above ~ 800 GeV, and an anomalously high fraction of positrons at theses energies, indicative of the fact that there exists some unknown source of electrons or muons[3] in Nature. Although the possible interpretations of this anomaly do not necessarily involve dark matter – this is indeed the most discussed scenario, especially taking into account other compelling astrophysical results, in particular, observation of annual modulation in dark matter direct-detection experiments [15–18]. The conventional WIMP models can't address the electron (positron) anomaly for two main reasons: first, in order to raise the required electron (positron) flux the annihilation rate of dark matter should be a few orders of magnitude larger than the

---

[3] Muons are not stable and eventually decay to electron and two neutrinos. By mentioning electrons and muons we also assume their antiparticles.

annihilation rate that produces the correct DM relic abundance; second, the dark matter should annihilate predominantly into leptons and not hadrons.

An appealing solution was introduced by Arkani-Hamed [19] in order to reconcile tensions between recently observed astrophysical anomalies and WIMP models of dark matter. It was suggested that a new sector of particles exists, a hidden-sector. A hidden-sector fields are singlets with respect to SM gauge group, in other words, they do not participate in strong, weak, or electromagnetic interactions. However, hidden-sector particles interact with the SM gauge or Higgs boson through the so-called portals. The most important one is the kinetic mixing portal [20], which connects the SM hypercharge with a gauge boson that corresponds to a hidden-sector abelian gauge symmetry. The latter boson is called a dark photon. The important assumption is that a dark matter is charged under the hidden-sector symmetries. Next, if dark photon is massive[4] and its mass is about 100 MeV $-$ 1 GeV, then: (1) due to hidden-sector interactions, dark matter annihilates or decays predominantly to leptons (electrons and muons); at the same time the decays to protons or heavier hadrons are kinematically forbidden; (2) due to a presence of a massive dark photon, the annihilation cross-section is enhanced via the Sommerfeld mechanism [21]; that produces a high-energy electron (positron) flux, which accounts for the observed astrophysical e^+e^- anomaly.

The important signature of hidden-sector DM models are *lepton jets*. These are collimated jet-like bundles of electrons or muons. The decays of dark matter or SM particles to the hidden-sector are followed by cascade decays in hidden-particles, yielding a high multiplicity of final-state leptons, forming lepton-jets. The possible discovery of lepton-jets could provide a prominent signal of a new physics and indicate the origin of dark matter. Motivated by the proliferation of astrophysical anomalies in electron (positron) cosmic-ray fluxes, observed by the cosmic-ray and dark matter direct-detection experiments in the past two decades [10–14], searches for them is an important ingredient of physics program at colliders. Searches for lepton-jets are also important in view of recent discovery of the production of a Higgs boson with a mass of about 125 GeV by the ATLAS [1] and CMS [2] collaborations. This observation is compatible with the production and decay of the SM Higgs boson [22–24] at this mass. Strengthening or rejecting the SM Higgs boson hypothesis is currently of utmost importance and thus a search for non-SM Higgs boson decays, in particular to electron-jets, is of high interest. Moreover, in addition to a recently discovered state consistent with the SM Higgs boson, there may be other scalar fields that arise in the Higgs boson sector in many extensions of the SM, and electron-jets could be the primary discovery channel for these new states.

In this work, the search for associate WH production with Higgs boson decaying into electron-jets is presented. This is the first search performed for this particular signature. The thesis contains a detailed studies upon which the article [25] is based. The dissertation is structured as follows: in chapter 2 we briefly review the dark matter problem and its connection to lepton-jets. Theoretical model of lepton jets, used for data analysis, is also described in this chapter. The overview of experimental facilities is given in Chapter 3. This includes the description of Large Hadron Collider and ATLAS experiment. The emphasis is put on the sub-detectors of ATLAS relevant to the lepton-jet analysis. In

---

[4] Massiveness of dark photon implies the hidden-sector gauge symmetry is broken.

Chapter 4 we present the details of lepton-jet data analysis with the ATLAS detector. The results of data analysis, conclusions and prospective for further lepton-jet searches are given in the last two chapters.

2

Theoretical motivation

2.1 Introduction to dark matter and dark energy

The formal definition of dark matter is a kind of matter which emits no light and is unobservable directly by telescopes [6]. According to [26], the notion of dark matter was coined for the first time around the middle of 18th century. Already at that time astronomers had begun to realize that the disturbed motion of a planet, or a changed position of a star, was due to the gravitational impact exerted by a celestial body – a body that formed a part of ‘dark matter’. For instance, at the time when Neptune was discovered in 1846, it was considered as a constituent of ‘dark matter’. However, it took about century from that to seriously argue that there was a widely spread non-luminous matter in our galaxy.

For the first time it was suggested by Oort [27] in 1932 that there was a dark matter near the Sun. He used the observed vertical motions of stars for his studies, and derived the value of total density of matter near the sun as $\sim 0.02 \mathrm{M}_{\odot} \mathrm{pc}^{-3}$. This value is twice as large as the present observed density of matter near the sun. Ironically, the question regarding the amount of dark matter near the sun is unsettled to this day –due to the lack of agreement on the assumptions that need to be made before the equations governing the content of dark matter can be solved. Inspite of great advances in dark matter science and huge experimental efforts, the values based on Oort’s work are still regarded as a reliability limits for the dark matter amount in the universe. Alongside with considering the existence of dark matter [28], in the early 1990s scientists also examined the non-existence of dark matter [29]. In fact, the former group [28] concluded that a model with no dark matter is inconsistent with the data.

The combination of modern data based on the astrophysical observational studies carried out in the past decade yields the following relative content of cosmic matter (energy) in the Universe (for the detailed review see Refs. [6, 9]):

- **Ordinary matter (5%)**: also known as baryonic matter – includes protons, neutrons, and electrons, which constitute planets, stars, and other ordinary natural bodies; this type of matter is traditionally called baryons, although electrons are not baryons;
- **Dark energy (70%):** the energy of as yet unknown origin, with positive density and negative pressure. It is responsible for the cosmic repulsion of distant galaxies and acts as a competitor to gravitational force which tends to collapse galaxies together;
- **Dark matter (25%):** the type of matter in the Universe which is deduced from the gravitational effects that can not be explained by the presence of ordinary (observed) matter only, impacting the behavior of astrophysical systems on different cosmological scales, from galaxies to the cosmological horizon.
- **Radiation (∼ 0.01%):** relic photons (and, perhaps, gravitons as well);

The observed matter comprises only 5% of energy density in the Universe, while the nature of other 95% remains unknown. Results of various astrophysical observations confirm that the existence of dark matter and dark energy withstands the reliability test [9]. A detailed discussion of the dark-energy problem is beyond the scope of this thesis. A brief overview of this problem is given in Section 2.1.1.

The ordinary matter is usually dubbed baryonic. However, the dark matter itself can be split into baryonic and non-baryonic (exotic) candidates. The baryonic dark matter candidates comprise faint stars, galactic haloes, intergalactic gas, jupiters, black holes and so forth [26]. With continuous improvements in observational techniques and tools a portion of invisible baryons gradually slip into class of visible, for instance “L dwarfs” are no longer considered as dark matter.

For the non-baryonic matter, different forms has been proposed over the last years. These include weakly interacting massive particles (WIMPs) – the most popular candidate for dark matter, neutrinos – either the Standard Model ones or its more exotic forms, gravitinos and neutralinos – which arise in various implementations of Supersymmetric models, axions and topological clusters in a gauge field, etc. (see Section 2.1.3). It should be emphasised that although the existence of exotic dark matter is speculative, the significant gap between total density of baryonic and non-baryonic dark matter is indicative of the fact that our speculation on the existence of exotic dark metter is correct.

2.1.1 On the dark energy and antigravity

The concept of dark energy is much younger than the dark matter. It is a common belief that dark energy is responsible for the accelerated cosmological expansion [9].

Despite the fact that velocities and distances of scattering galaxies have been undergoing measurements for almost a century, the acceleration of galaxies was first measured only fifteen years ago after long systematic observations, which were carried out by two independent groups of astronomers led by Brian Schmidt [30] and Saul Perlmutter [31]. The observations were carried out with the most sophisticated modern astronomical instruments, the Hubble Space Telescope and the largest ground-based reflectors. Their studies were focused on the supernovae of a certain type (Ia[1]) at the distances of a few billion light years, almost at the edge of the observable Universe. The supernovae of this type are so bright that this allowed discovering and measuring a fine relativistic effect that modifies apparent brightness of a source depending on the red-shift[2]. The effect is due to the acceleration of motion of luminous source and is noticeable only at large distances, when red-shift becomes comparable to unity. In this way it was discovered that the Universe expands with positive acceleration.

In the simplest (and apparently most realistic) interpretation dark energy is usually understood in connection with the so-called Λ-term in the equations of Einstein's general theory of relativity. The Λ-term was introduced in 1917 in order to provide a source of cosmic repulsion in the Universe (antigravity), to balance the gravitational force [32]. A few years later Friedmann constructed a model of expanding Universe [33], which is based on the exact solutions of general relativity equations and incorporates Λ-term as a free parameter. The exact value of Λ doesn't follow from theory and is a subject to measurements in certain cosmological observations. The model possessed uniformity and isotropy in space, however was not static (symmetric in time). Friedmann's theory with the value of the constant Λ following from the latest observational discoveries well describes the inflating universe and is completely consistent with comprehensive set of modern astronomical data. It is the basis of the present-day cosmological 'Standard Model', known as ΛCDM cosmology (CDM stands for Cold Dark Matter).

The main quantitative feature of dark energy is density. Its value of about 70% was estimated in the earliest papers where the discovery of accelerating universe was reported [30, 31]. In short, the density of dark energy roughly corresponds to about three hydrogen atoms in each cubic meter of space [9]. To imagine the antigravitation force exerted by such a medium, let us consider two neutral hydrogen atoms put in space where nothing but dark energy is present. These atoms are subjected to two forces, Newton's force of mutual attraction and Einstein's repulsion force. It turns out that antigravitation is stronger than gravitation if the atoms are separated by more than half a meter.

But even before the observations of supernovae Ia were made, the existence of dark energy was anticipated in the middle of 1990's (see f.ex. Refs. [34–37]). The analysis of galactic catalogues aimed at revealing the distribution of matter in space, the use of

---

[1] Ia – the type of supernovae which result from white dwarfs. They originate from white dwarfs that have picked up the material of companion stars. They all have approximately the same mass of about $1.4M_{\odot}$ and reside in the galaxies much further away than other supernovae. As a result their brightness appears minimal and their detection becomes a challenge. In spite of this, due to impressive uniformity of their masses and of their 'light curves' these supernovae are treated as a standard candles in cosmology.

[2] Red-shift – the shift of spectral lines towards the longer wavelengths and lower frequencies at the red end of the spectrum in a luminous celestial body. This is due to the relativistic Doppler effect and indicates that the light source is moving (with great speed) away from the observer.

various methods to determine the mass of clustered (clumped) matter (which includes both ordinary and dark matter), and measurements of the cosmic micro-wave background and the Hubble parameter revealed that total density of matter in the Universe is about 30% of the critical density:

$$\Omega_M = \frac{\rho_D + \rho_B}{\rho_C} \lesssim 0.3 \tag{2.1}$$

where ρ_D and ρ_B are the densities of baryonic (ordinary) and dark matter respectively; ρ_C denotes the critical density of the Universe. The critical density corresponds to the density of matter required upon the assumption that our Universe is described by the Newtonian model with zero energy, or by relativistic model with zero pressure and zero space curvature (the Einstein-de Sitter model). The value of critical density can be derived in Newtonian mechanics as follows (for details see Ref. [26]). Consider two objects at the moment of time t_0 are at the distance of r_0 from each other, large enough to assume the medium between the objects is uniform. Then, according to Newton's law of gravity, at any given moment t the distance r between these two is governed by the following equation

$$\ddot{r} = -\frac{4\pi\rho_0 r_0^3 G}{3r^2} \tag{2.2}$$

where ρ_0 denotes the density of medium at moment t_0 and G is the Newtonian constant of gravity. Now, integrating this with respect to r gives

$$\dot{r}^2 = \frac{8\pi\rho_0 r_0^3 G}{3r} + k \tag{2.3}$$

where integration constant k represents the sum of object's kinetic and potential energy. Putting $k = 0$ (Newtonian model with zero energy), and considering top equation at moment t_0 results in

$$\dot{r}(t = t_0) = \sqrt{\frac{8\pi\rho_0 G}{3}} r_0 \tag{2.4}$$

This is also true at any given moment of time

$$\dot{r}(t) = \sqrt{\frac{8\pi\rho(t) G}{3}} r(t) \equiv H(t) r(t) \tag{2.5}$$

That is the Hubble's law, which states: the velocities of distant galaxies moving away from Earth are directly proportional to the distance from Earth. From the value of Hubble's constant $H(t)$ we get the value of critical density

$$\rho_C = \frac{3H^2(t)}{8\pi G} = 2h^2 \times 10^{-29} \frac{\mathrm{g}}{\mathrm{cm}^3} \tag{2.6}$$

where h stands for $0.5 \leq h \leq 1$ and represents the uncertainty of determination the Hubble's constant [26].

The result in Eq. 2.1 is regarded as one of the most important results in modern cosmology. For a long time, it has been interpreted as evidence of the Universe having nonzero curvature, however this interpretation faced difficulties both from theoretical and observational point of view. Thus, if the spatial curvature is zero, result Eq. 2.1 suggests that

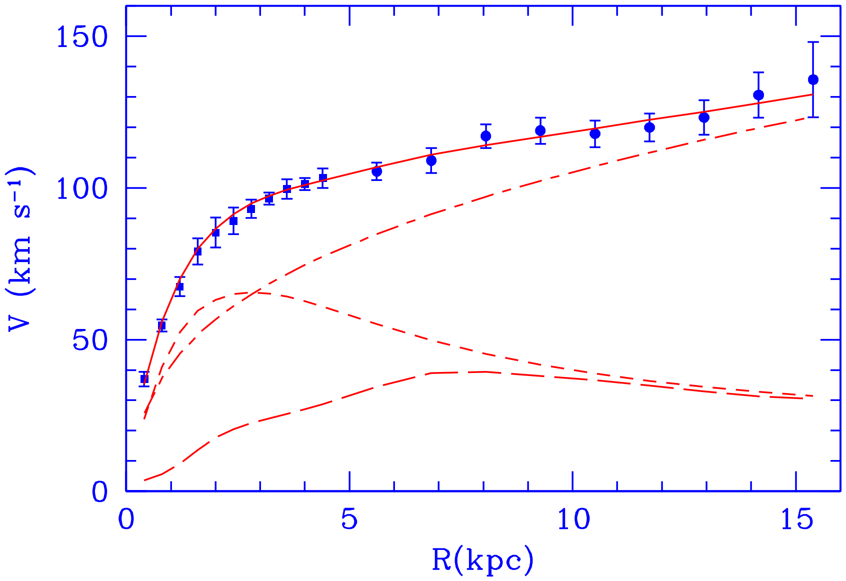

Figure 2.1: The rotation curve of M33 galaxy (blue dots). Solid line represents the best fit model. In M33 galaxy there are four types of observed matter: stellar disk, atomic gas, worm ionized gas and molecular gas. The contributions are shown for the dark matter (dash-dotted line) as well as for the observed ‘stellar disk’ (short dashed line) and gaseous matter (long dashed line). Figure from [38].

at least 70% of the energy density in the modern Universe is due to matter of a type that cannot be perturbed by gravitational fields and remains unclumped (unclustered) in the course of cosmological evolution. This implies that the effective pressure of matter is negative and its absolute value is sufficiently large, i.e., $p \approx -\rho$. Hence, this is dark energy.

2.1.2 Experimental evidences for dark matter

Rotation curves

One of the most direct and convincing evidences for dark matter on the galactic scale comes from the analysis of so-called ‘rotation curves’ – the plots of orbital velocities of stars and gases with respect to the distance from galactic centre[3]. According to simple Newtonian mechanics the orbital velocity of an object at distance r from galactic centre is

$$v^2(r) = \frac{GM(r)}{r} \tag{2.7}$$

which is the Kepler’s law; $M(r)$ – is the distribution of mass of galaxy embedded into a sphere of radius r. Now, let us move away from the observed part of galaxy. At a certain

---

[3] In the outer galactic region containing only cold neutral hydrogen and no stars, the gas rotation rate is measured by observing emission at the wavelength of 21 cm corresponding to ultrathin splitting due to proton–electron spin interactions [38]. The orbiting of a galaxy leads to a Doppler shift of the 21 cm line, which allows estimating the gas rotational velocity in the outer region of the galaxy. The orbital speed of the gas, like that of the stars, remains unaltered far beyond the limits of the visible galaxy.

value of r the observed mass $M(r)$ starts to remain constant with the growth of r, hence a velocity of distant object should behave as

$$v \sim \frac{1}{\sqrt{r}} \tag{2.8}$$

However, observations do not confirm this prediction [39, 40]. Instead, in 1985 Carignan and Freeman unambiguously established that rotation curves exhibit the 'flat' behaviour $v \sim \text{const}$ [41], similar to that depicted in Figure 2.1 (comprehensive survey of rotation curves of spiral galaxies is given f.ex. in Ref. [42]). The fact that the mean rotational velocity $\bar{v}$ is constant with respect to r implies that the mass $M(r)$ is proportional to r:

$$M(r) = \frac{\bar{v}^2 r}{G} \tag{2.9}$$

This means that the large fraction of total mass of any given galaxy is in the form of non-luminous 'dark' component located at large radii. The mass increases linearly with r. Measurements of a few hundred spiral galaxies indicate that all of them are embedded into massive dark halo [38–43].

Gravitational lensing

Another compelling evidence of dark matter is gravitational lensing – distortion and magnification of light emitted by distant galaxies, caused by inhomogeneities in the matter distribution that perturb the paths of photons. The effect is equivalent to viewing the light sources through a piece of glass with a spatially varying index of refraction. Both distortion and magnification can be measured, and can be used to determine the mass distribution in a galaxy cluster [44]. Namely, the mass contained in a cluster acts as a gravitational lens on the light emitted by distant galaxies. The image appears as a giant arc and the radius of arc determines the mass within the cluster. The distant galaxies often appear as a tiny elliptical images, which are called "arclets" [45]. The example of such arclets of the cluster RX J1347–1145 is shown in Figure 2.2. In this section we briefly discuss the idea behind the magnification and distortion, and how it leads to a concepts of weak and strong gravitational lensing.

From the historical point of view, the bending of light by matter is already embedded into Newtonian gravity, in which light attracts to matter just as other objects do. However, the deflection of light predicted by Newtonian gravity is only half as strong as that obtained in General Relativity, where space–time is curved [26]. It was Eddington who first measured the deflection of light during his famous expedition in 1919 at the time of solar eclipse. He confirmed the prediction of General Relativity and made Einstein a world celebrity.

A typical sketch of gravitational lens system is shown in Figure 2.5. A mass concentration is placed on the distance $\mathrm{D_d}$ from the observer. This lens deflects the light coming from the source placed at the distance $\mathrm{D_s}$. The 'true' and observed angular positions of the source are denoted through β and θ respectively; α – is the position shift due to gravitational

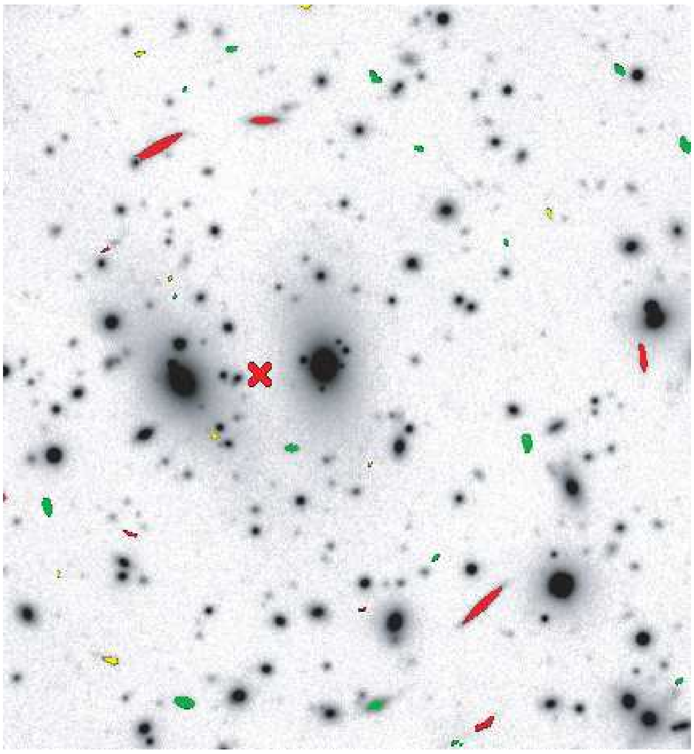

Figure 2.2: Image of the cluster RX J1347-1145 with anisotropic diffusion filtering applied. The colors encode the objects eccentricity: [0.7, 0.8] green, [0.8, 0.9] yellow, [0.9, 1.0] red, i.e. the red objects are most likely arcs. The assumed center of the cluster is marked with a red cross. Figure from [45].

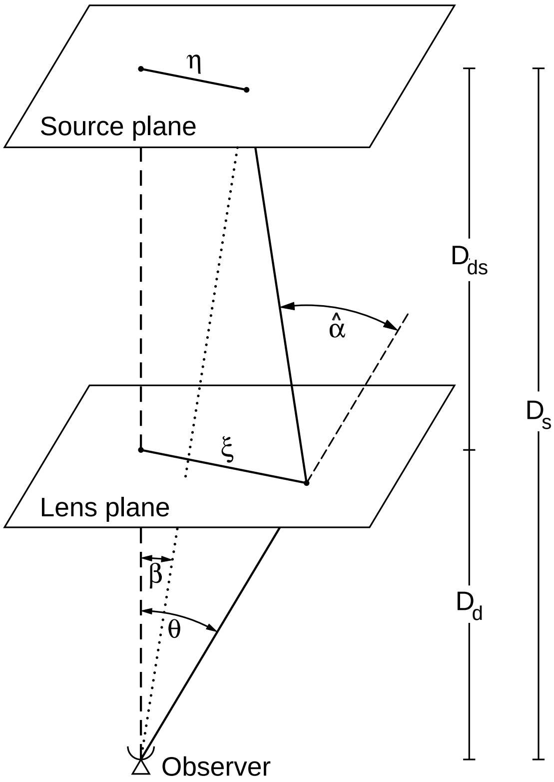

Figure 2.3: Sketch of a typical gravitational lens system. Figure from [46].

lensing. If β, θ and α are small then the simple geometrical relation between theses three takes place and can be written as

$$\theta \mathrm{D_s} = \beta \mathrm{D_s} + \alpha \mathrm{D_{ds}} \tag{2.10}$$

This expression is called *the lens equation* [26, 46]. It should be noted that the above formula is based on the relation

[physical size] = [angular size] × [distance]

which holds in Euclidean space. However, relation 2.10 also holds in the curved space–time. The only modification one has to make in the latter case is to redefine $\mathrm{D_s}$, $\mathrm{D_d}$ and $\mathrm{D_{ds}}$ as angular diameter distances [26].

It is convenient to rewrite lens equation as follows

$$\vec{\beta} = \vec{\theta} - \frac{\mathrm{D_{ds}}}{\mathrm{D_s}} \vec{\alpha}(\vec{\theta}) \tag{2.11}$$

or

$$\vec{\beta} = \vec{\theta} - \vec{\boldsymbol{\alpha}}(\vec{\theta}) \tag{2.12}$$

where the angle is given a direction in the lens plane (or source plane). The important physics arises from the fact that $\boldsymbol{\alpha}(\vec{\theta})$ is the function of θ.

As mentioned above, the most important feature of gravitational lensing is distortion and magnification. The effect is particularly evident when the source has a non-negligible apparent size. The distortion itself can be split into convergence and share transformations (distortion is the sum of these two). The distortion arises because light is deflected differentially. In particular, if the source is much smaller than the angular size on which the physical properties of the lens change, the relation between source and its image positions can be locally linearized. In other words the distortion of images can be expressed via Jacobian matrix

$$A \equiv \frac{\partial \vec{y}}{\partial \vec{x}} = \left(\delta_{ij} - \frac{\partial \alpha_i(\vec{x})}{\partial x_j} \right) = \left(\delta_{ij} - \frac{\partial^2 \Psi(\vec{x})}{\partial x_i \partial x_j} \right) \tag{2.13}$$

where $\vec{x}$ and $\vec{y}$ are true and projected positions of source respectively; $\Psi(\vec{x})$ – is the effective lensing potential [47], obtained by projecting the three-dimensional Newtonian potential on the lens plane. This Jacobian is responsible for the distortion of an object image. For clarity we use the following notation

$$\frac{\partial^2 \Psi(\vec{x})}{\partial x_i \partial x_j} \equiv \Psi_{ij} \tag{2.14}$$

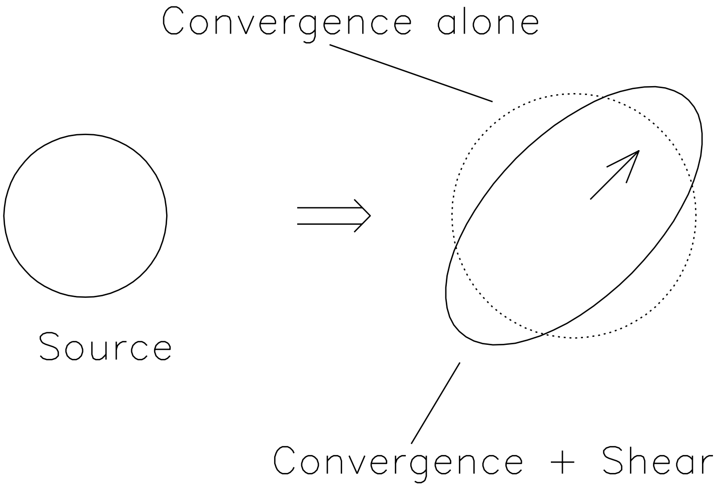

Figure 2.4: Illustration of the effects of convergence and shear on a circular source. Convergence magnifies the image isotropically, and shear deforms it to an ellipse. Figure from [47].

The Jacobian matrix can be split into convergence and shear parts [47]. Let us introduce the following notations

$$\begin{aligned} k &\equiv \frac{1}{2}\left(\Psi_{11}+\Psi_{22}\right) \\ \gamma_1 &\equiv \frac{1}{2}\left(\Psi_{11}-\Psi_{22}\right) \\ \gamma_2 &\equiv \Psi_{12}=\Psi_{21} \\ \gamma &\equiv \sqrt{\gamma_1^2+\gamma_2^2} \end{aligned} \tag{2.15}$$

Now, Jacobian 2.13 can be written in the form

$$\begin{aligned} A &= \begin{pmatrix} 1-k-\gamma_1 & -\gamma_2 \\ -\gamma_2 & 1-k+\gamma_1 \end{pmatrix} \\ &= (1-k)\begin{pmatrix} 1 & 0 \\ 0 & 1 \end{pmatrix} - \gamma \begin{pmatrix} \cos 2\phi & \sin 2\phi \\ \sin 2\phi & -\cos 2\phi \end{pmatrix} \end{aligned} \tag{2.16}$$

From the equation above the meaning of terms convergence and shear becomes clear. First term in formula 2.16 is the convergence matrix. It is a diagonal matrix and is responsible for isotropic distortion of image, i.e. the images are only rescaled by a constant factor in all directions. Second term it the share matrix, which is asymmetric and trace-free. It stretches the shape of the source along one privileged direction. The quantity γ describes the magnitude of the shear and ϕ describes its orientation. In particular, a circular source, which is small enough compared to the scale of the lens is mapped into an ellipse when k and γ are both non-zero. The semi-major and -minor axes are

$$a=\frac{r}{1-k-\gamma}\ ,\ b=\frac{r}{1-k+\gamma} \tag{2.17}$$

where r is the radius of the source. The corresponding illustration is shown in Figure 2.4.

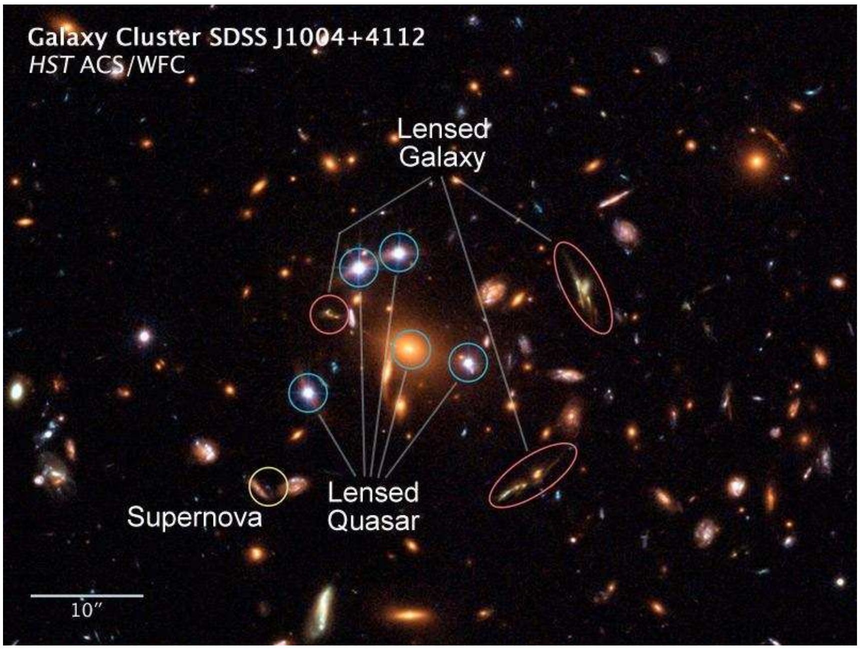

Figure 2.5: The galaxy cluster SDSS J1004+4112 has 5 images of a the same quasar close to its centre. A the same time, several other background galaxies are strongly lensed by this cluster. Figure from [48].

Magnification is a consequence of distortion. The lens equation maps the surface element ∂y into a surface element ∂x. According to Liouville theorem the absence of absorption or emission in gravitational light deflection ensures the conservation of the source surface brightness. In other words the total amount of light coming from source remains unchanged. Since solid angle under which we see the object is altered, the flux of light received from the source is magnified (demagnified). The magnification is

$$\mu = \frac{1}{\det A} = \frac{1}{(1-k)^2 - \gamma^2} \tag{2.18}$$

The eigenvalues of the magnification tensor (or the inverse of the eigenvalues of the Jacobian matrix) measure the amplification in the tangential and in the radial direction and are given by

$$\mu_{\mathrm{t}} = \frac{1}{\lambda_{\mathrm{t}}} = \frac{1}{1-k-\gamma} \tag{2.19}$$

$$\mu_{\mathrm{r}} = \frac{1}{\lambda_{\mathrm{r}}} = \frac{1}{1-k+\gamma} \tag{2.20}$$

The magnification is ideally infinite when $\lambda_{\mathrm{t}} = 0$ or $\lambda_{\mathrm{r}} = 0$. Theses conditions define two critical lines in the lens plane, called the tangential and radial critical lines respectively. Objects close to tangential line are stretched along this line, while objects close to radial line are distorted in the direction perpendicular to this line.

Due to distortion, the circular images of distant galaxies are mapped by a gravitational lens into ellipses. This effect is usually referred to as a *weak lensing* [46, 50]. The surface density of mass in gravitational lens is directly proportional to the convergence factor

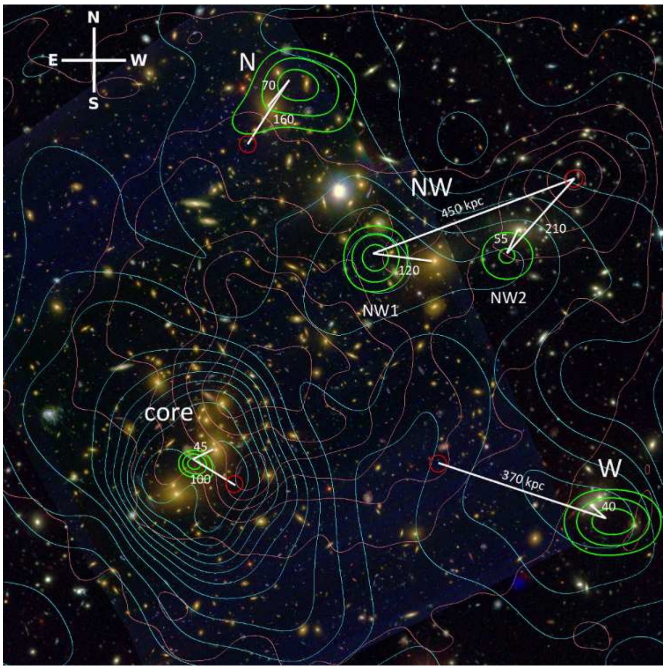

Figure 2.6: Mass reconstruction of Abell 2744 (Pandora's cluster). Cyan contours indicate the mass density reconstructed using gravitational lensing. X-ray surface brightness contours are given in magenta. The peak positions of the core and clumps are indicated by the green likelihood contours. Contours are 86%, 61%, and 37% of the peak likelihood for each clump (assuming a Gaussian probability distribution, these would correspond to 0.3, 1, and 2-sigma confidence contours). Figure from [49].

k [26]. Image in Figure 2.2 is an example of weak lensing. The *strong lens* is usually understood as a gravitational lens which is capable of producing multiple images from the single source [44, 47, 51]. It occurs when the mass density in the lens plane becomes critical, i.e. it produces tangential or radial critical lines. In other words either condition is fulfilled

$$\lambda_{\mathrm{t}} = 1 - k - \gamma = 0 \tag{2.21}$$

$$\lambda_{\mathrm{r}} = 1 - k + \gamma = 0 \tag{2.22}$$

Strong lensing is usually observed in the central regions of galaxies and galaxy clusters [47]. A representative example of strong gravitational lensing is shown in Figure 2.5, where five images of the same quasar are observed due to gravitational lens. Strong lensing provides the most direct way of estimating the mass embedded into lens.

In Figure 2.6 an example is shown of overlaying the lensing mass reconstruction and X-ray emission data for Pandora's cluster [49]. The difference between lensing and X-ray data enables to evaluate the dark matter distribution in the cluster.

Analysis of the results of gravitational lensing made in the last ten years has revealed that the diameter of the dark halo in the galaxies may be more than one order of magnitude greater than the visible diameter of a galaxy itself [6].

2.1.3 Dark matter candidates and WIMPs

The existence of Dark Matter in the Universe is deduced exclusively from its gravitational effect on the behavior of astrophysical systems. While the amount of Dark Matter is fairly well known, its origin still remains a puzzle. The possible nature of dark matter is debated for a long time and spans over a dozen of most-viable dark matter candidates. Despite the baryonic dark matter not completely being ruled out, most of DM discussions are dedicated to exotic dark matter. Among others, this includes neutrinos (SM, sterile, and heavy neutrinos [52–54]), supersymmetric particles [55], Kaluza-Klein particles in models with extra-dimensions [56], magnetic monopoles (see f.ex. [57]), axions [58], crypto-baryonic matter [59], technicolor particles [60], mirror-world particles [61], etc. A comprehensive review of DM candidates can be found in Refs. [6, 62].

The leading candidate for dark matter are *Weakly Interacting Massive Particles* (WIMPs). The terminology refers to the fact that these these particles undergo weak interactions in addition to feeling the effects of gravity, but do not participate in electromagnetic or strong interactions. The expected WIMP mass is usually considered in the range 1 GeV – 10 TeV. These particles, if present in thermal equilibrium in the early universe, annihilate with one another so that a predictable number of them remain today. An annihilation cross section of weak interaction strength automatically gives the right abundance in the present Universe, near the value measured by WMAP experiment [63]. This coincident is known as a WIMP miracle [64].

The most naturally WIMPs arise in supersymmetric models, for instance the lightest neutralino in the Minimal Supersymmetric Standard Model (MSSM)[4] and its extensions [55]. However, other WIMP candidates arise in a variety of theories beyond the Standard Model (see f.ex. Refs. [62, 66] for review).

Despite its obvious allure, the viability of conventional WIMP models have been recently put in doubt in the view of recent observations, performed by dark matter direct-detection and cosmic-ray (CR) experiments, requiring a significant modification of WIMP models. That is discussed in detail in the next section.

---

[4] Minimal is meant in the sense that the particle contents and interactions in the known Standard Model is minimally enlarged by supersymmetry, where SM boson and fermions are complemented with supersymmetric fermionic and bosonic partners respectively (see f.ex. Ref. [65]).

2.2 Lepton-jets, hidden sectors and dark matter

2.2.1 Introduction

So far, Nature at the most microscopic scales, observable to experiments, at the energies up to about 1 TeV and distances as low as 10^{-19} m, appears to be very successfully described by the Standard Model (SM). That is a unified theory that addresses three of four known fundamental interactions, the strong, electromagnetic and weak interactions, keeping Gravity, the fourth known fundamental force, aside. The common point of all interactions in the Standard Model is that, by construction, all of them arise in the theory as a consequence of invariance of any physical system with respect to various symmetry transformations. These symmetry transformations act upon wave functions of fundamental constituents of matter and are unitary by construction. The unitarity means that the scalar square of wave functions (which is the observable quantity) must remain unaltered upon these transformations. Unitary transformations acting on one-dimensional complex space are described by the $U(1)$ Lie algebra, those on two-dimensional and three-dimensional spaces are $SU(2)$ and $SU(3)$, respectively, and so forth. Furthermore, yet another assumption has to be made before the interactions emerge in the theory. That is, the considered above unitary transformations can not take place in the whole volume of physical system simultaneously, and the parameters, governing these transformations, must be considered as a functions of space-time coordinates. Given this assumption, our physical system is invariant no more upon the considered transformations, unless the new fields are introduced in order to “gauge” the system [67]. These are so-called gauge fields, or, equally, the Yang-Mills fields. They are responsible for the interactions in the Standard Model, where $U(1) \times SU(2)$ corresponds to weak and electromagnetic forces, and $SU(3)$ gives raise to the strong interaction. The mediators of forces are gauge bosons with spin 1, while all fundamental matter constituents are fermions, having spin 1/2. Finally, there is yet another entity in the Standard Model, which pertains neither to matter nor to interactions – the Higgs field. The quantum of this field is the Higgs boson – the only fundamental particle with spin zero. The Higgs field gives raise to the masses of fermions and gauge bosons in the Standard Model by means of the spontaneous symmetry breaking mechanism [22–24]. The summary of all SM particles is given in Table 2.1.

The new LHC data-driven era brings physics to a TeV energy regime, anticipating the new physics beyond the reach of the Standard Model. However, along with the possible existence of new physics at the TeV energy scale, there exists another equally possible scenario – the existence of new physics at low energies, i.e. not higher than electroweak gauge boson mass (~ 100 GeV), with the new physics very weakly coupled to the Standard Model. This new physics is usually refereed to as the hidden sector, or, equally, the dark sector, or, yet equally, the secluded sector. Hidden-sector matter may have its own gauge symmetries with the corresponding force mediators. Since it is not charged under the SM $SU(3) \times SU(2) \times U(1)$ group, it interacts with normal (baryonic) matter only through gravity and via the portals, in particular, through kinetic mixing of SM hypercharge with the dark photon [20]. The dark photon is the force mediator associated with the hidden-sector $U(1)$ gauge symmetry.

Particle name		symbol	mass (MeV)	electric charge
Matter (spin=1/2)				
quarks	up	u	$2.3^{+0.7}_{-0.5}$	$+2/3$
	down	d	$4.8^{+0.5}_{-0.3}$	$-1/3$
	charm	c	1275.0 ± 25.0	$+2/3$
	strange	s	95.0 ± 5.0	$-1/3$
	top	t	$173070.0 \pm 520.0 \pm 720.0$	$+2/3$
	bottom	b	4180.0 ± 30.0	$-1/3$
leptons	electron	e	0.511 ± 0.000	1
	electron neutrino	ν_e	<0.002	0
	muon	μ	105.7 ± 0.0	1
	muon neutrino	ν_μ	<0.19	0
	tau	τ	1776.8 ± 0.2	1
	tau neutrino	ν_τ	<18.2	0
Interactions (spin=1)				
electromagnetic	photon	γ	0	0
strong	gluon	g	0	0
weak	W	$W^{\pm}$	80385.0 ± 15.0	±1
	Z	Z^0	91188.0 ± 2.0	0
Higgs field (spin=0)				
	Higgs	H	$125500.0 \pm 200.0\,^{+500.0}_{-600.0}$	0

Table 2.1: List of all fundamental particles in the Standard Model. There are two species of matter in the SM – quarks and leptons. The former participate in all the three interactions in SM, while the latter are involved in weak and electromagnetic interactions only and do not feel the effects of strong interaction. Numbers are taken from [68, 69].

Many models of physics beyond the SM contain a light hidden sector, which is composed of as yet unobserved fields that are singlets under the SM group $SU(3) \times SU(2) \times U(1)$ and that can be probed at the LHC [19, 70–80]. Models of this hidden sector vary from simple modifications of the SM [75, 76] to models motivated by string theory [77] to so-called unparticle models [78]. One could consider these models just speculations and manipulations with the apparatus of quantum field theory. However, in the view of recent proliferation of anomalies observed in cosmic-ray electron and positron flux, the hidden-sector paradigm finds its elegant implementation. Below we describe the astrophysical motivation for hidden sector models and introduce lepton-jets, which are the the prominent signature of hidden sectors in proton–proton collisions at the LHC.

2.2.2 Astrophysical motivation and dark matter

PAMELA electron-positron anomaly

Several cosmic-ray[5] and dark matter direct-detection experiments (PAMELA, AMS, ATIC, FermiLAT, HEAT) [10–14] observe an unexpectedly high flux of electrons and positrons in the energy range from one GeV to about one TeV (Fig. 2.7). Furthermore, they also observe the excess of positron-to-electron fraction with respect to theoretical prediction (Fig. 2.8). At the same time there is no experimental evidence of excess in antiproton flux (Fig. 2.9).

Most cosmic-ray electrons are assumed to originate from the supernova remnants while the cosmic-ray positrons are mainly produced through hadronic processes when cosmic-ray protons collide with intergalactic hydrogen [81]. In such a scenario there should be no prominent feature at the TeV energies in the electron (positron) total spectrum, and the positron-to-electron ratio should drop with energy monotonously. Hence, extra electrons (positrons) are assumed to originate either from the annihilation or decays of dark matter, or from some other non-conventional astrophysical process, like electron-positron pair production in ultra-strong magnetic fields of pulsars, annihilation of high energy photons from γ-ray bursts with background photons (supernovae source) [82], and acceleration of electrons in shocks or in magnetic turbulence of microqusars [81].

Although astrophysical sources are not ruled out, the most extensively discussed interpretation of the electron (positron) excesses is the annihilations or decays of dark matter. Assuming the extra electrons and postrions are produced in the annihilations of dark matter, the conventional WIMP models, however, can hardly accommodate the observed anomaly for two main reasons. First, assuming thermal freeze-out, the standard relic abundance calculation implies an annihilation cross-section that is at least a hundred times too small to explain the lepton excesses observed in astrophysical experiments [19]. Second difficulty is the non-observation of corresponding excesses in anti-protons [89] and gamma rays [90], which puts strong bounds on hadronic channels that are present in many dark matter models. In turn, the anomaly can be addressed in the supersymmetric WIMP models with decaying dark matter [91]. Although this scenario is somewhat non-typical, and implies very heavy gravitinos[6] with the mass of about few TeV and sleptons[7] with masses above $\sim$500 TeV, it is still a relevant explanation. Detailed discussion of this model setup is beyond the scope of this thesis (for review of gravitino as dark matter candidate see Ref. [93]). Another plausible scenario was introduced by Arkani-Hamed [19] suggesting that a WIMP-like dark matter of TeV mass scale is charged under the GeV-scale hidden-sector gauge group. In this scenario the two apparent contradictions, considered above, are reconciled. The WIMP-like dark matter couples to a GeV

---

[5] Cosmic rays comprise mostly protons, almost 90%, about 10% are helium nuclei (alpha particles), and slightly below 1% are heavier elements and electrons [81].

[6] In the supersymmetric theories that include gravity, the quantum of gravity field, spin-2 graviton, has a spin-3/2 fermion superpartner called the gravitino [5]. Usually, gravitinos are assumed to have very tiny mass, of the order of 10^{-4} eV, as discussed for example in Ref. [92].

[7] The sleptons term, according to usual supersymmetric naming convention [5], stands for the supersymmetric bosonic partners of SM leptons.

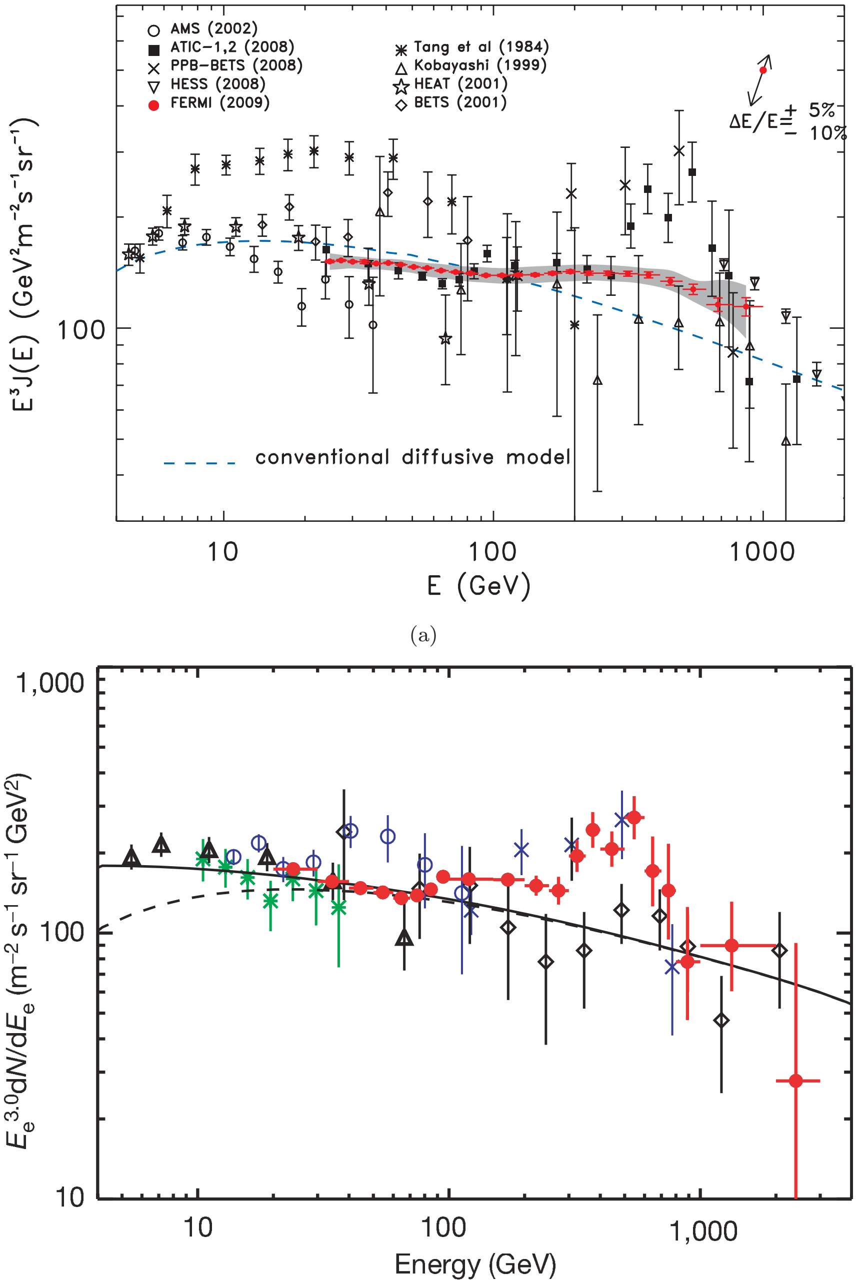

(a)

(b)

Figure 2.7: The electron differential energy spectrum measured (a) by the satellite-born Fermi/LAT telescope (red circles), and (b) by the balloon-born ATIC experiment at the top of the atmosphere (red rectangles). The spectrum is scaled by E^3. An enhancement in the electron (positron) intensity is clearly seen in the energy range close 800 GeV with respect to theory prediction, obtained from a conventional diffusive model (blue dashed line in the top plot, and black solid line in the bottom plot) [83, 84]. The dashed curve in the bottom plot represent the solar modulated electron spectrum and shows that the modulation is unimportant above 20 GeV. The theoretical prediction is based on the supernova shocks and interactions of cosmic ray protons with the interstellar medium [19, 83, 84]. Figures from [12, 14].

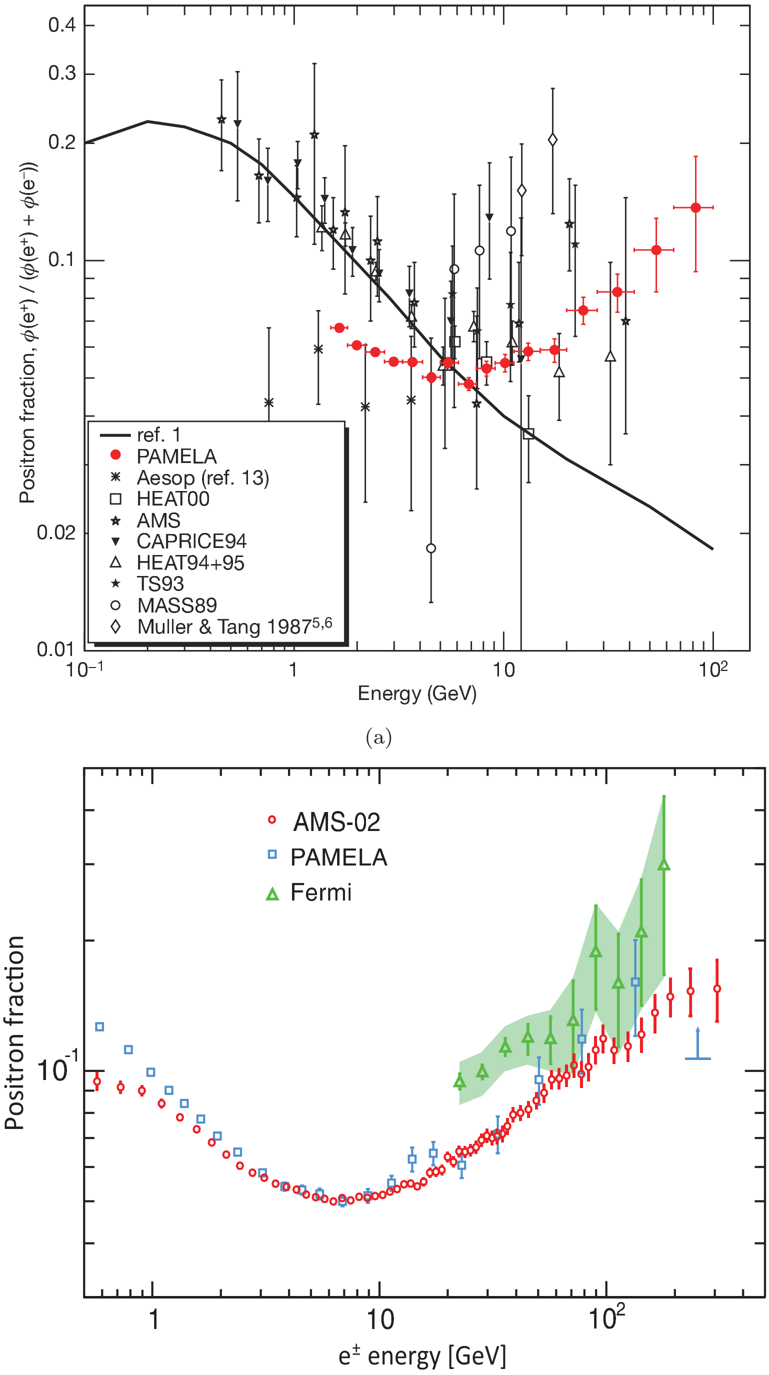

(a)

(b)

Figure 2.8: The positron fraction measured by different experiments. The most precise measurements pertain to PAMELA (a) and AMS-02 (b). The solid line (a) shows a calculation for pure secondary production of positrons during the propagation of cosmic rays in the Galaxy without reacceleration processes [85]. Figures from [10, 13].

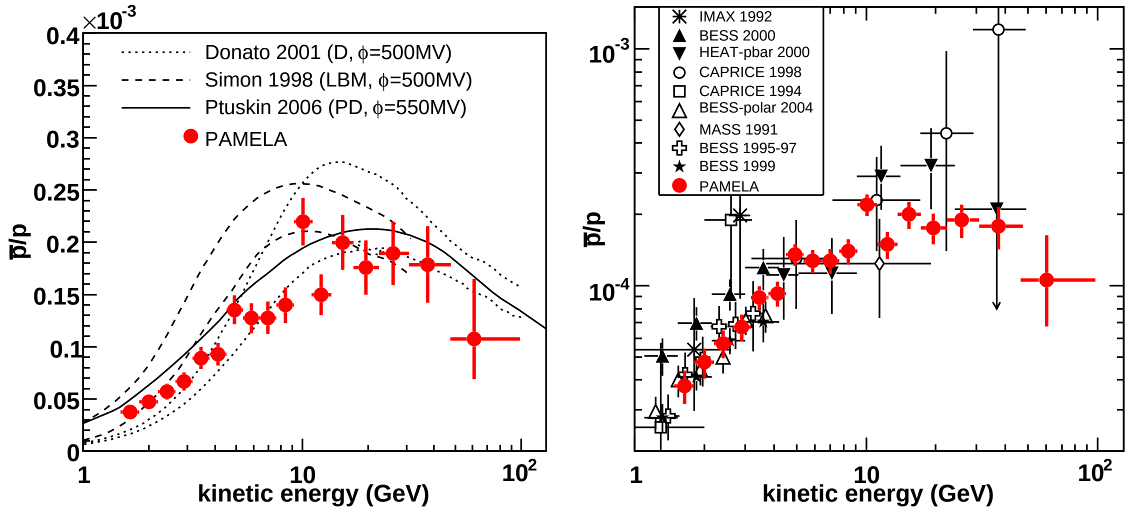

(a) (b)

Figure 2.9: The antiproton-to-proton flux ratio obtained by PAMELA collaboration and compared with theoretical calculations (left) and with the results of other experiments (right). Theoretical curves are shown for a pure secondary production of antiprotons during the propagation of cosmic rays in the galaxy. The dashed lines show the upper and lower limits calculated by Simon et al. [86] for the standard Leaky Box Model, while the dotted lines show the limits from Donato et al. [87] for a Diffusion model with reacceleration. The solid line shows the calculation by Ptuskin et al. [88] for the case of a Plain Diffusion model. The curves were obtained using appropriate solar modulation parameters (indicated as ϕ) for the PAMELA data taking period. Figures from [89].

scale dark gauge boson (hidden photon) that kinetically mixes with the photon of the Standard Model [79, 80]. If the dark photon mass is below $\sim$ 1 GeV, the Dark Matter annihilates primarily into muons and/or electrons, providing a source of additional electrons (positrons) without giving rise to proton excess. Next, one of the important modifications that can arise with a new light boson is an enhancement of the annihilation cross section via a mechanism first described by Sommerfeld [21]. This mechanism yields the DM-annihilation cross section large enough to describe electron-positron anomalies. As shown in Ref. [19] the Sommerfeld enhancement can only arise if the hidden-sector gauge boson mass is $m_{\rm dark} \leq \alpha m_{\rm DM} \ \sim 100$ MeV [94], where α is the strength of dark matter coupling to hidden sector. The similar DM picture is considered also in Ref [95].

DAMA modulation and inelastic dark matter

In addition to the primary motivation described above, the hidden-sector models also naturally describe another compelling astrophysical observation – the annual modulation of signal in the dark matter direct-detection experiments. These experiments are designed to detect the scattering of dark matter on nuclei of detector elements. The count rate in these experiments should experience an annual modulation due to the relative motion of the Earth around the Sun [64], as shown in Fig. 2.10. In addition, the modulation is usually required to fulfil a set of requirements [15], in order to get rid of backgrounds,

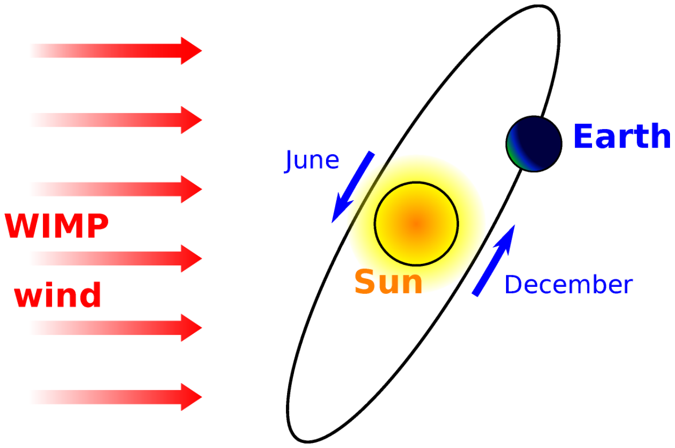

Figure 2.10: An illustration of WIMP wind as seen from Earth and Sun. Due to the rotation of the Galactic Disk (containing the Earth and Sun) through the essentially non-rotating dark matter halo, the solar system experiences an effective “WIMP wind”. From the perspective of the Earth, the wind changes throughout the year due to the Earth’s orbital motion: the wind is at maximum speed around the beginning of June, when the Earth is moving fastest in the direction of the disk rotation, and at a minimum speed around the beginning of December, when the Earth is moving fastest in the direction opposite to the disk rotation. The Earth’s orbit is inclined at about 60° relative to the plane of the Disk. Figure from [64].

and keep only those events which are assumed to originate from interactions with dark matter only. The requirements are

- The rate must contain a component modulated according to a cosine function with one year period and a phase that peaks roughly around 2nd June;
- This modulation must only be found in a well-defined low energy range, where DM particle induced events can be present;
- It must apply only to those events in which just one detector of many actually ‘fires’ (single-hit events), since the DM particle multi-interaction probability is negligible;
- The modulation amplitude is usually constrained from above using the usually-adopted DM halo distributions.

Such a modulation, is not present for most known background sources. The most evident observation of such modulation has been reported by DAMA collaboration [15, 96, 97]. Some other experiments, like CoGent and MINOS, also confirm the existence of modulation in their signal [16–18]. The modulation observed by DAMA is shown in Fig. 2.11. This experiment exploits highly radiopure NaI(Tl) scintillators as target detectors in order to assure a sensitivity to wide ranges of DM candidates, of interaction types and of astrophysical scenarios [15]. The recoil-energy spectrum of nuclei in the detector depends on the specifics of both the particle physics model and the distribution of DM in the Galaxy. DAMA reports the modulation signal at about 9σ confidence level [15], which is consistent with ~ 80 GeV or 10 GeV WIMP scattering predominantly off of iodine or

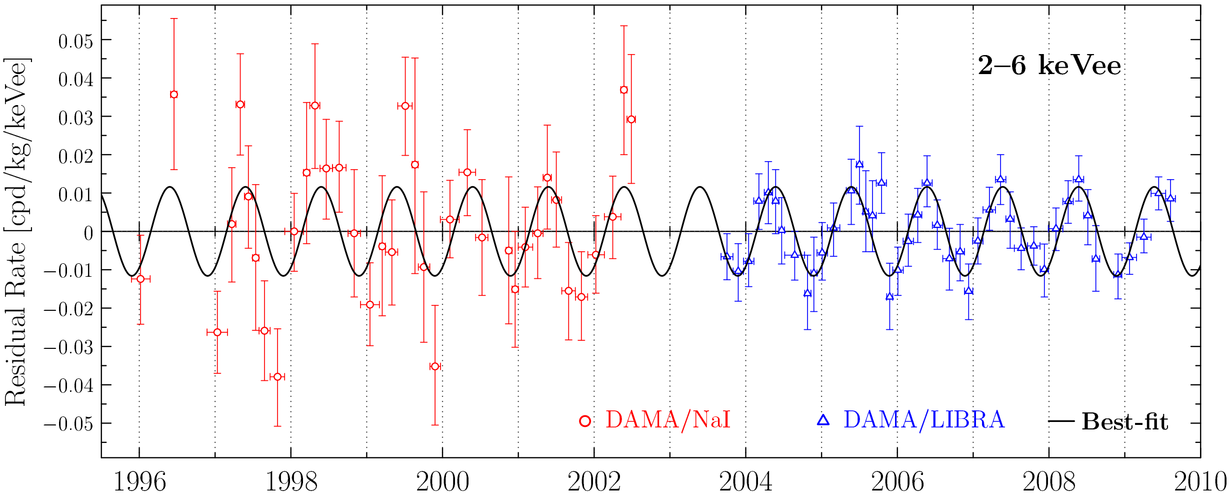

Figure 2.11: Experimental model-independent residual rate of the single-hit scintillation events, measured by DAMA/NaI (red circles, 0.29 ton×year exposure over 1995 – 2002) and DAMA/LIBRA (blue triangles, 0.87 ton×year exposure over 2003 – 2010) in the 2–6 keV nuclear-recoil energy interval, as a function of time. The residual rates are calculated from the measured rate of the single-hit events (already corrected for the overall efficiency and for the acquisition dead time) after subtracting the constant part. The cumulative exposure of two runs (DAMA/LIBRA and DAMA/NaI) is 1.17 ton×year. The experimental points present the errors as vertical bars and the associated time bin width as horizontal bars. The superimposed curve is the cosinusoidal function $A \cos \omega(t - t_0)$ with a period $T = \frac{2\pi}{\omega} = 0.999 \pm 0.002$ year, amplitude $A = 0.0116 \pm 0.0013$ cpd/kg/keV, and phase $t_0 = 0.400 \pm 0.019$ year (May 26±7 days), equal to the central values obtained by best fit over the whole data, where *cpd* denotes counts per day. Figure from [64], where data are taken from [8, 15].

sodium, respectively [64]. However, assuming the conventional WIMP models, this result comes in clear contradiction with null-results of other experiments, which do not confirm the modulation hypothesis [98–103]. This apparent tension is reconciled in the theories where DM can scatter inelastically, in particular in hidden-sector models [19].

The hidden-sector models include the possibility that there are several DM states with small mass splittings on the order of $\alpha m_{\rm dark}$ ∼100 keV, such that DM can scatter inelastically against nuclei into an excited state[8]. This is usually referred to as inelastic dark matter (iDM). As discussed in Refs. [104, 105], iDM provides a mechanism to explain the modulation observed by the DAMA, and at the same time addresses the lack of signal in other experiments.

---

[8] In the initial proposal [19] it has been assumed that dark gauge group $G_{\rm dark}$ is non-abelian and broken at a GeV scale, then loops of the resulting GeV dark gauge bosons will generate 100 keV - 1 MeV mass splittings within the dark matter multiplet of $G_{\rm dark}$. However, it has been shown later that such a mass splittings can be naturally adopted in abelian $G_{\rm dark} = U(1)_{\rm d}$ hidden-sectors [20] as well. These models are remarkably simple and has a small number of free parameters that can be fixed by observations. For instance, the size of the kinetic mixing, ϵ, is constrained by the boost factor (Sommerfeld cross-section enhancement) required to explain the PAMELA positron excess.

INTEGRAL anomaly

Lastly, there is one more astrophysical anomaly which can be hardly addressed in conventional DM models. It is known that the strongest γ-ray line signal from our Galaxy comes from the electron-positron annihilation [106]. The INTEGRAL (International Gamma-Ray Astrophysical Laboratory) γ-ray satellite observatory has measured the 511 keV signal [107, 108] and it turned out that the signal is strongest within a few degrees of the galactic center. This region has the largest concentration of electron-positron annihilation, about 3×10^{42} electron-positron pair annihilations per second (far more than expected from supernovae). Its origin remains unknown despite decades of scrutiny. The spectrum suggests that these positrons (electrons) are injected with relatively low energies, $E \leq$ few MeV. According to Ref. [109], the dark matter candidate with an "excited state" 1–2 MeV above the ground state can naturally explain such low energy positrons (electrons) while still producing the high-energy positrons via annihilation [106]. Dark matter featuring such an excited states is usually referred to as excited dark mater (XDM). It was shown that hidden-sector models with non-abelian dark gauge group G_{dark} nicely accommodate XDM [109]. It should be emphasized that both XDM and iDM are non-standard WIMP scenarios in which a DM ground state can transition to and from new excited states via the emission of some field that couples back to the SM.

2.2.3 Lepton jets

Lepton jets are the prominent potential manifestation of hidden-sector models. These are collimated sets of electrons and muons (and possibly pions), which are produced in the cascade decays in the hidden sector.

As mentioned above, hidden-sector models yield a massive gauge boson associated with $U(1)$ symmetry in the hidden sector, the dark photon. The SM is coupled to the dark sector via a kinetic mixing term between SM hypercharge and a dark sector $U(1)$ gauge field [19]. The Lagrangian of SM $U(1)$ hypercharge and hidden-sector $U(1)_{\text{d}}$ can be written as follows

$$L_{\text{gauge}} = -\frac{1}{4}B_{\mu\nu}B^{\mu\nu} - \frac{1}{4}b_{\mu\nu}b^{\mu\nu} + \frac{\epsilon}{2}B_{\mu\nu}b^{\mu\nu} \tag{2.23}$$

where $B_{\mu\nu}$ is the SM hypercharge and $b_{\mu\nu}$ is the dark sector $U(1)_{\text{d}}$ gauge-field strength, respectively, and ϵ is the kinetic-mixing coupling strength. The kinetic mixing part is

$$L_{\text{mix}} = \frac{\epsilon}{2}B_{\mu\nu}b^{\mu\nu} = \frac{\epsilon}{2}b^{\mu\nu}(\cos\theta_W A_{\mu\nu} - \sin\theta_W Z_{\mu\nu}) \tag{2.24}$$

where A and Z are the SM photon and Z boson gauge fields respectively, and θ_W is the Weinberg angle. As a result, the dark photon couples to all electrically charged particles. Decays of the dark photon to electrically neutral particles that couple to the Z boson, such as neutrinos, are suppressed by $m^2_{\gamma_{\text{d}}}/m^2_Z$, and will not play an important role [70]. Fig. 2.12 illustrates the SM coupling to the hidden sector. Due to kinetic mixing, dark photon decays to electrons, muons, and possibly pions, as shown in Fig. 2.13. Branching fraction of each decay mode depends on the dark photon mass (Fig. 2.14). As long as

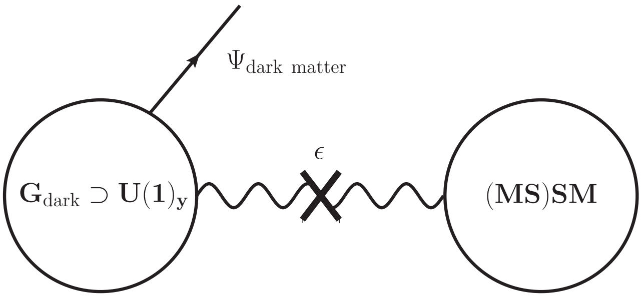

Figure 2.12: Schematic sketch of minimal setup, in which the hidden sector and the SM are connected through kinetic mixing term. The dark matter is charged under the hidden-sector group and may or may not couple directly to the SM. Figure from [74].

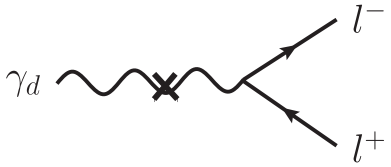

Figure 2.13: A Feynman diagram illustrating hidden photon decay to leptons via the kinetic mixing with SM photon. Figure from [70].

dark-photon mass is lower than 210 MeV, dark photon decays exclusively to electron-positron pairs.

The decays of dark photon originating from dark-matter annihilation produce the electron (positron) flux needed to account for PAMELA-like anomalies. In addition, dark photons may be produced also in the decays of a Higgs and SM gauge bosons [70, 74]. The decays of dark matter or SM particles to the hidden sector are followed by cascade decays in the hidden sector yielding high multiplicity of final-state leptons (and possibly pions) and lightest non-interacting hidden-sector particles (Fig. 2.15). These form jet-like objects composed of leptons which can be probed at colliders and are usually referred to as *lepton jets*. The discovery of an excess of lepton jets would constitute a smoking-gun signature of the existence of a light hidden sector.

The multiplicity of leptons in a lepton jet may vary from two to few tens, depending on the particle content in the hidden sector. Next, depending on the strength of kinetic mixing, ϵ, lepton jets can be prompt ($\epsilon > 10^{-5}$), or, produce displaced vertices in the detector ($\epsilon \lesssim 10^{-5}$) [70]. Bounds on the strength of kinetic mixing depend on the dark photon mass. For the dark photon masses relevant to the explanation of astrophysical anomalies, kinetic mixing is bounded from above $\epsilon \lesssim 10^{-3}$, where limits arise from the numerous e^+e^- and beam-dump experiments by looking for possible impact of virtual dark photon on precision SM observables [111, 112].

The phenomenology of hidden sectors and lepton jets is now being extensively studied (see f.ex. Refs. [19, 20, 70–75, 113–119] and the experimental searches for them are performed by ATLAS and CMS experiments at LHC [120–122] and D0 and CDF experiments at Tevatron collider [123, 124]. Production of lepton jets at colliders can be characterized by two main scenarios, as described below.

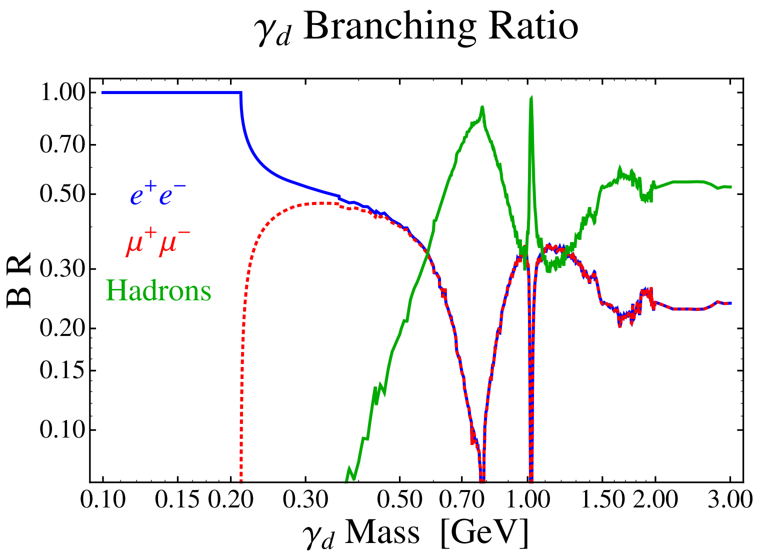

Figure 2.14: Dark photon branching ratios to electrons, muons, and hadrons through the electromagnetic current, as a function of the dark photon mass, m_{γ_d}. The hadronic branching ratio is derived from the measured quantity $R \equiv \mathrm{BR}(e^+e^- \to \mathrm{had})/\mathrm{BR}(e^+e^- \to \mu^+\mu^-)$ [110]. It is seen that for $m_{\gamma_\mathrm{d}} \leq 500$ MeV, the dark photon decays predominantly to leptons, including muons for $m_{\gamma_\mathrm{d}} > 210$ MeV. Figure from [70].

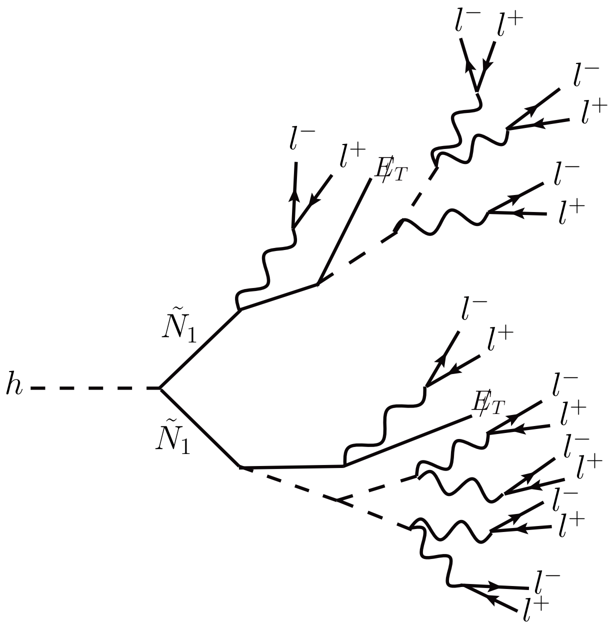

Figure 2.15: An example of a Higgs boson decaying to lepton-jets. A Higgs boson is decaying to a pair of MSSM neutralinos, which subsequently decay into the hidden sector. The hidden-sector cascades result in a lepton jets. This example uses the particle content and vertices of the minimal $U(1)_\mathrm{d}$ hidden-sector model described in Ref. [70]. A larger hidden sector can lead to even larger multiplicities. If the neutralinos are heavy enough to be produced close to rest, their decay products will be well-separated, and the leptons will partition into 4 distinct lepton jets. Alternatively, if the neutralinos are light and boosted, the event will consist of two groups of collimated leptons. Figure from [70].

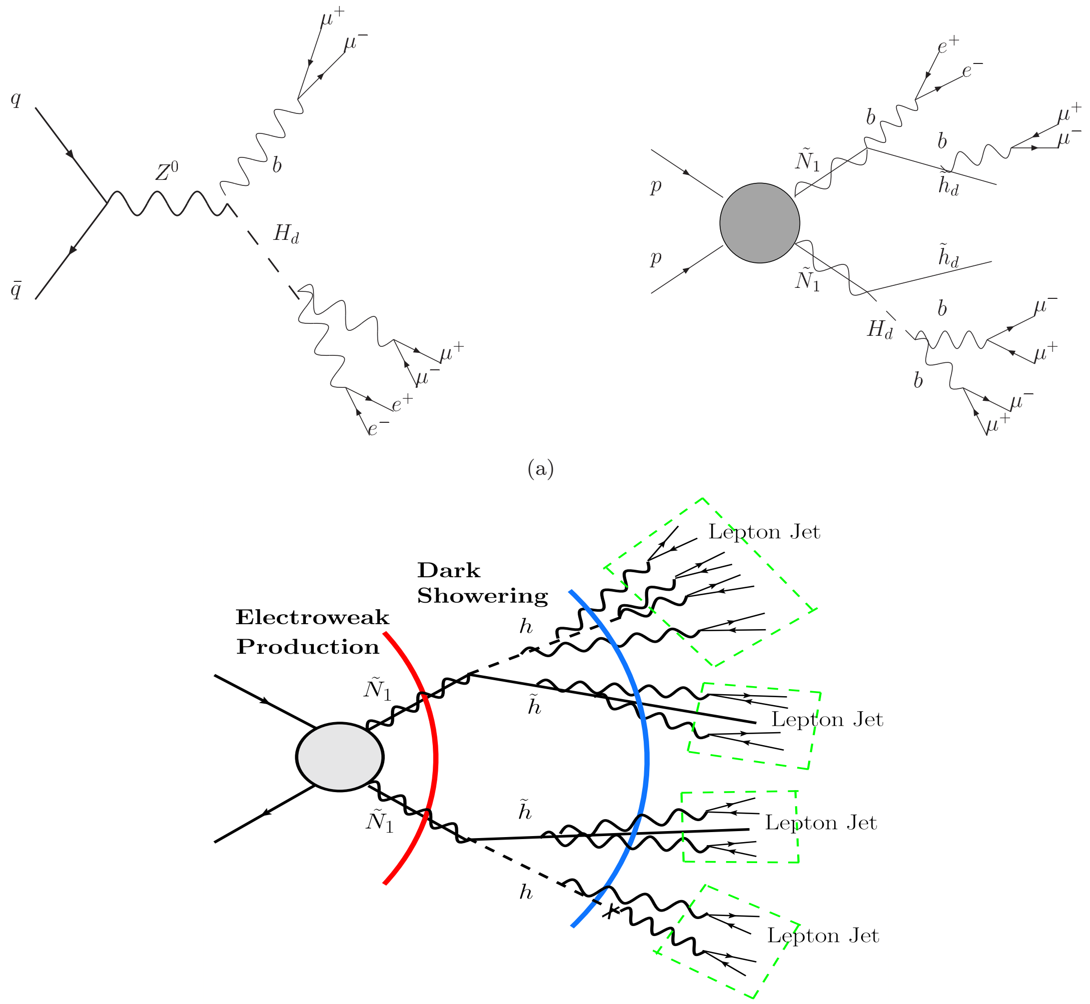

(a)

(b)

Figure 2.16: The production of lepton jets in models where hidden sector is connected to SM only via kinetic mixing (a), and schematic sketch of lepton jet evolution in these models (b). The models feature two possible types of lepton jet production: rare Z decay into hidden states (left), and a neutralino pair production with the neutralino ultimately decaying into the dark sector (right). In the figure H_d denotes the hidden-sector scalar and b denotes the dark photon. The dark fermions are considered stable, aside from possible radiation [114]. The events therefore consist of 2 hard lepton jets, missing energy, and softer leptons coming from radiation of the dark fermions (radiation from the dark bosons would normally be clumped together with the harder leptons coming from the cascade.). The neutralino mass is a free parameter and was set to ~ 100 GeV in Ref. [114]. Figure from [114].

Lepton jets in the supersymmetric production

In the minimal scenario the SM sector and the hidden sector are coupled only via the kinetic mixing [114]. Then, upon supersymmetrizing this setup, hidden-sector fermions and scalars have a small coupling to the SM Z boson and the MSSM bino[9], while the

---

[9] Bino is the superpartner of the SM $U(1)$ gauge boson, B, corresponding to weak hypercharge [5].

hidden-sector gauge boson couples weakly to the SM electromagnetic current. As a result, the typical collision event factorizes into the following stages (see Fig. 2.16b):

- **Lepton jet production:** Z boson or neutralino pair[10] is produced in collision, as shown in Fig. 2.16a; then, these are decaying into the hidden sector;
- **Hidden sector showering:** the electroweak(-ino) states have decayed into the hidden sector; the resulting hidden states are highly boosted and cascade decay down to the bottom of the dark sector spectrum[11];
- **Dark photon decays to leptons:** cascade decays and soft emissions in the hidden sector result in radiated dark photons which decay into lepton pairs, hence, return to the visible sector as collimated lepton jets.

Due to the relatively high mass of neutralinos ($\sim$ 100 GeV) the lepton jets produced in their decays have quite hard momentum spectrum (the magnitude of dark photon momentum is of the same order as neutralino mass). For the rare Z decays, lepton jets are usually softer, since masses of intermediate hidden-sector particles are in general confined to a GeV scale.

Lepton jets in a Higgs boson decays

It has been already pointed out by Patt and Wilczek [75] that the Higgs field mass term, being superrenomalizable, has a unique status within the Standard Model. With one exception, all components of the Standard Model are associated with strictly renormalizable terms. In other words, the interactions and kinetic terms are represented by operators of mass dimension 4. That is, their associated couplings are dimensionless. At the same time the SM Higgs mass term $\Delta L = -\mu^2\phi^\dagger\phi$ with a coupling of mass dimension 2 and an interaction operator of mass dimension 2, is the exception. Such terms are usually referred to as *portals*. Due to this, the Higgs field is uniquely open to renormalizable (or super-renormalizable) coupling to the fields, which are singlets under SM $SU(3)\times SU(2)\times U(1)$ gauge group. These (hidden-sector) fields may enter the μ mass term in the aforementioned Lagrangian. This idea was elaborated further by Batell *et. al.* [125], where the simple example of a Higgs interaction with a hidden-sector was written down as follows

$$L_{\text{int}} = (H^\dagger H)(\Lambda S^2 + AS) = hv(\Lambda S^2 + AS) + ... \tag{2.25}$$

where, after the spontaneous breaking of the electroweak symmetry, $H = \left(0, \frac{v+h}{\sqrt{2}}\right)$. S is taken as a hidden-sector scalar, and Λ and A are treated as free parameters.

Although considering Higgs interactions with hidden sector doesn't necessarily require supersymmetry, it is the most plausible scenario, since the presence of SUSY ameliorates

---

[10] Neutralinos are mass eigenstates of the combination of neutral supersymmetric particles, higgsinos and gauginos [5]

[11] A universal feature of these dark matter scenarios is that there is log enhanced soft emission of hidden gauge bosons, which increases the multiplicity of light hidden sector states and ultimately yields a greater number of dark photons [114].

the little hierarchy problem[12] if Higgs boson mass is about 100 GeV – 150GeV [70, 126]. Falkowski *et.al.* suggested a minimal supersymmetric scenario with MSSM complemented by the hidden sector (either abelian or non-abelian) [70]. In such a setup the lightest 'visible' superpartner (LVSP – the equivalent of the Lightest Supersymmetric Partner in the MSSM) is allowed to cascade into the hidden sector, typically producing visible particles in the process. Authors categorize Higgs decays to hidden sector into three main channels: in the *singlet channel* the Higgs decays to the hidden sector through direct couplings; in the other two scenarios the Higgs first decays to a pair of LVSPs which, having no visible decay channels open, decay into the hidden sector. The MSSM contains two types of electrically neutral and colorless superpartners which leads to the *neutralino channel* and the *sneutrino channel* scenarios.

In all of these models, hidden sector cascades produce a large multiplicity of boosted hidden sector particles. Most of hidden sector particles decay to leptons, while other – lightest hidden particles – escape the detector, giving raise to missing energy. The final state of the Higgs decay is therefore characterized by several groups of collimated leptons – lepton jets, plus missing energy, as shown in Fig. 2.15

---

[12] The hierarchy problem is connected to the difference in the physical energy scales. The first type of hierarchy problem – *little hierarchy problem* refers to a difference between scalar (Higgs) mass and ultraviolet cutoff of the electroweak scale (the difference is about two orders of magnitude for a Higgs boson mass ~ 125 GeV). The problem arises in the radiative corrections to the mass of the Higgs boson. That is, the mass of a scalar (Higgs) field receives large radiative corrections due to quadratic divergences. Thus, the tree-level mass of the Higgs field and the loop contributions of the electroweak cutoff order must cancel to a very high precision. This cancellation may either come from a symmetry as it is the case in supersymmetric models or be an accident in which the various terms "conspire" to cancel against each other. In the latter case the cancellation is usually understood as a dynamical mechanism, operating above the cutoff scale, which we simulate by fixing some terms in the effective (SM) lagrangian.

Another type of the hierarchy problem is caused by logarithmic divergences. It arises when a theory includes multiple physical scales, like grand-unification scale (10^{15} GeV) or Planck scale (10^{19} GeV). Even if the quadratic divergence is disposed off, the lower mass scale generically receives large radiative corrections of the higher mass scales, and a fine-tuning is necessary to keep the separation of the multiple scales (for review see f.ex. Ref. [4]).

2.3 The lepton jet model

In the data analysis, described in this dissertation, two models, discussed in Ref. [71], are considered. These differ in the way the Higgs boson decays, either via a three-step cascade (Fig. 2.17 right) or a two-step cascade (Fig. 2.17 bottom) to hidden-sector particles. In both models the masses of particles in a hidden-sector cascade are taken to be substantially lower than the Higgs boson mass, thus the Higgs boson decay has a two-jet topology. The models feature a dark photon $\gamma_{\rm d}$ that kinetically mixes with the SM photon [79, 80], a neutral weakly interacting stable scalar n_d and two hidden scalars $h_{\rm d,1}$ and $h_{\rm d,2}$. A value of the kinetic mixing parameter ϵ larger than 10^{-5} implies dark photons with very short lifetimes; thus the chosen value of $\epsilon = 10^{-4}$, recommended in Ref. [71], ensures that the decay products are prompt. The dark photon mass must be less than 2 GeV for these models to provide a viable explanation of the results of cosmic-ray and dark matter direct-detection experiments [11–14], which observe an unexpected excess of cosmic electrons and/or positrons, while there is no observed proton excess. For a dark photon mass below 210 MeV, the dark photons decay exclusively to e^+e^- pairs; consequently dark photon masses of 100 MeV and 200 MeV are considered in this analysis.

Parameter	
$m_{h_{\rm d,1}}$	10 GeV
$m_{h_{\rm d,2}}$	4 GeV
m_{n_d}	90 MeV
$m_{\gamma_{\rm d}}$	100, 200 MeV
ϵ	10^{-4}
three-step model	
BR($h_{\rm d,1} \to h_{\rm d,2} h_{\rm d,2}$)	1
BR($h_{\rm d,2} \to \gamma_{\rm d}\gamma_{\rm d}$)	0.8
BR($h_{\rm d,2} \to n_{\rm d} n_{\rm d}$)	0.2
two-step model	
BR($h_{\rm d,2} \to \gamma_{\rm d}\gamma_{\rm d}$)	1
BR($h_{\rm d,2} \to n_{\rm d} n_{\rm d}$)	0

Table 2.2: Parameters of the benchmark hidden-sector models: hidden-sector particle masses, the $\gamma - \gamma_{\rm d}$ kinetic mixing, and decay branching ratios of $h_{\rm d,1}$ and $h_{\rm d,2}$ in the three-step and two-step models.

The signal has a distinct two-jet topology with each electron-jet having a multiplicity of ≥ 4 electrons per jet, where the electrons are highly collimated. The specific hidden-sector parameters are given in Table 2.2, and the chosen masses of the Higgs boson are 100 GeV, 125 GeV and 140 GeV. The results of the analysis are expected to be robust with respect to the specific choice of the $h_{\rm d,1}$, $h_{\rm d,2}$ and $n_{\rm d}$ masses as long as these masses are significantly smaller than the Higgs boson mass, i.e. $m_{h_{\rm d,1|2}} \leq 10$ GeV. In particular, as long as the $h_{\rm d,1}$ and $h_{\rm d,2}$ scalars are much lighter than the Higgs boson, the $h_{\rm d,1}$ and $h_{\rm d,2}$ are boosted, and their decay products are collimated, resulting in two distinct electron-jets. Also in the three-step model, the results are expected to be robust against the explicit choice of the branching ratio of the $h_{\rm d,2}$ particle into weakly interacting neutral particles, $n_{\rm d}$, as

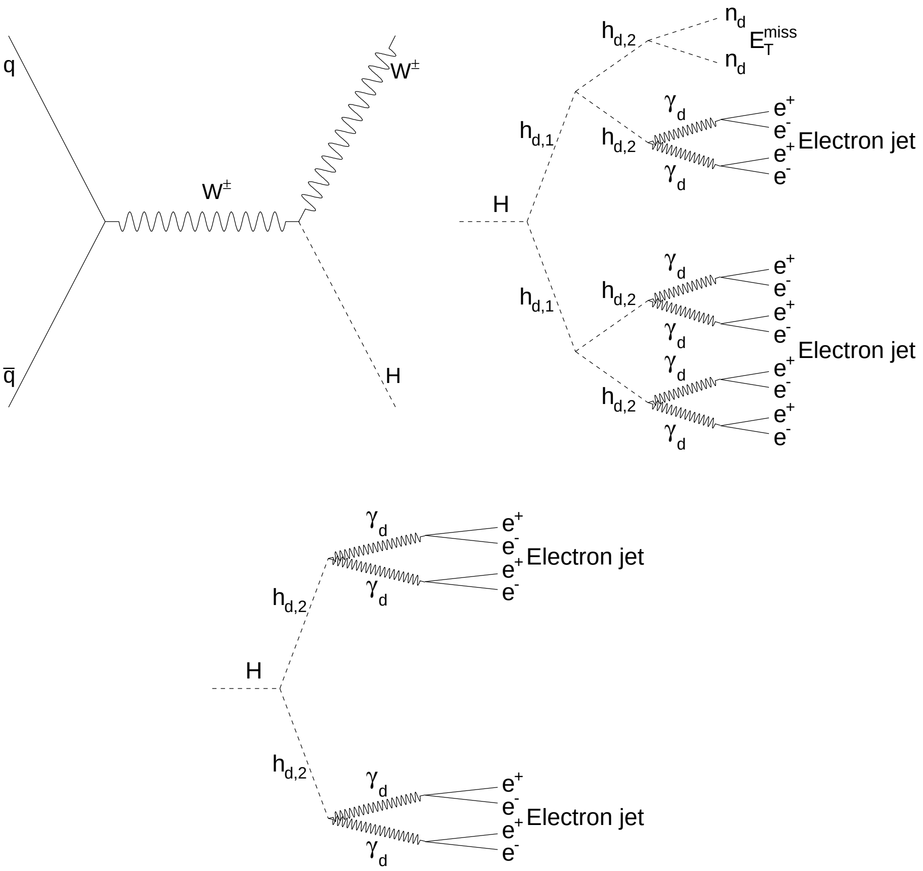

Figure 2.17: Feynman diagrams illustrating the Higgs boson associate production (with W boson) in proton–proton collisions and its decay to hidden-sector particles in the (left) three-step and (right) two-step models. Each $h_{\mathrm{d},2}$ particle can decay to a pair of dark photons γ_d or stable scalars n_d, with the corresponding branching ratios given in Table 2.2.

long as this branching ratio is relatively small, i.e. $\mathrm{BR}(h_{\mathrm{d},2} \to n_{\mathrm{d}}n_{\mathrm{d}}) \leq 0.2$. For this range of branching ratios, both the $h_{\mathrm{d},1}$ particles decay to visible decay products with greater than 90% probability; for larger branching ratios, there will be a considerable fraction of events where only one (or neither) $h_{\mathrm{d},1}$ particle decays to visible decay products.

The search is performed in the Higgs boson mass range between 100 GeV and 140 GeV. The analysis examines the associated Higgs boson production mechanism, $pp \to WH$, assuming SM couplings between the Higgs boson and the W boson (Fig. 2.17 left). In this analysis, the W boson produced in association with the Higgs boson is reconstructed in the $W \to e\nu$ and $W \to \mu\nu$ decay modes in order to achieve a high efficiency for online event selection and a high signal-to-background ratio. The signal topology is consequently an isolated large transverse momentum lepton accompanied by missing transverse momentum and two or more electron-jets.

3

The experimental facility

3.1 The Large Hadron Collider

3.1.1 Overview

The Large Hadron Collider (LHC) is the most powerful state-of-the-art tool for particle physics research [127, 128]. It is a synchrotron that, during its regular operation in 2010-2012, accelerated and collided beams of protons with unprecedented center-of-mass energy of up to 8 TeV at a peak instantaneous luminosity of almost $10^{34}\text{cm}^{-2}\text{s}^{-1}$. Moreover, after the technical upgrade which will take place during 2013-2014, it is planned to increase energy even further[1], up to the design value of 14 TeV, along with increasing the luminosity further. Apart from proton–proton collisions, the LHC machine is also capable of accelerating and colliding beams of heavy ions as well as heavy ions and protons [127, 128].

The main goal of the LHC is the exploration of the Standard Model in the TeV energy range, the search for the Higgs Boson (studying of its properties), and searches for potential new physics signatures that one hope to observe at TeV energy regime [127, 128, 130, 131]. The LHC can be considered a discovery machine, which uses collisions of hadrons.

---

[1] Of course, the LHC's collision-energy is far not the highest observed in nature. For example, the energy of protons in cosmic rays penetrating the Earth's atmosphere reaches 10^{20} eV [129]. These cosmic-ray protons interact with hadrons in atmosphere at a center-of-mass energy of about 200 TeV (about 20 times higher than that of LHC). However, these happen at a rate of less than once per year within the Pierre Auger Observatory [129] making them much less useful for studying processes which are themselves rare. At the same time, the LHC is a precision instrument capable of delivering proton–proton collisions millions of times per second in a volume whose dimensions are similar to that of a human hair.

Placed at the CERN laboratory outside the Geneva, about 100 meters deep underground, LHC is about 27 km in circumference (Fig. 3.1). The proton (heavy-ion) beams are running within two different beam-pipes, and intersect in four interaction points, where the four major experiments that study the collisions they produce are installed, as shown in Fig 3.1. This allows particles of the same charge – proton–proton (heavy ions) to be accelerated in opposite directions, and collided. The experiments are ATLAS [132], CMS [133], ALICE [134], and LHCb [135]. In addition, there are also three minor (more specific) experiments operating at LHC. These are LHCf [136], TOTEM [137] and MoEDAL [138].

3.1.2 The LHC experiments and their physics programme

ATLAS and CMS

Being multipurpose experiments, the ATLAS and CMS are optimized, first of all, to the searches for the SM Higgs boson and searches for the new phenomena that are generally predicted to occur at the TeV energy scale [130]. Apart from the TeV-scale physics, the high luminosity and increased cross-sections at the LHC enable further high precision tests of QCD, electroweak interactions, and flavour physics [131–133, 140]. For example, the top quark is produced at the LHC at a rate of a few tens of Hz, providing the opportunity to test its couplings and spin.

The formidable luminosity and, therefore, the high interaction rate are required for these experiments, since the cross-sections for many processes mentioned above are very small. For example, the cross-section for the SM Higgs boson production is about ten orders of magnitude lower than the total cross-section of p–p scattering (Fig. 3.2). At the same time the nature of hadron interactions implies that proton–proton collision products are dominated by the multi-jet production via the non-perturbative QCD processes. While prevailing over the other processes, multi-jet production usually occurs with low momentum (transverse momentum) transfer between the interacting hadrons. Hence, ATLAS and CMS are designed to explore those collisions which exhibit high transverse momentum transfer.

LHCb and ALICE

The two mid-size experiments are ALICE and LHCb. The former is designed to study QCD, the strong-interaction sector of the Standard Model. It is aimed to address the physics of strongly interacting matter and the quark-gluon plasma at extreme values of energy density and temperature in nucleus-nucleus collisions [134, 140]. The later is dedicated to heavy flavour physics at the LHC. Its primary goal is to look for indirect evidence of new physics in CP violation and rare decays of beauty and charm hadrons [135, 140].

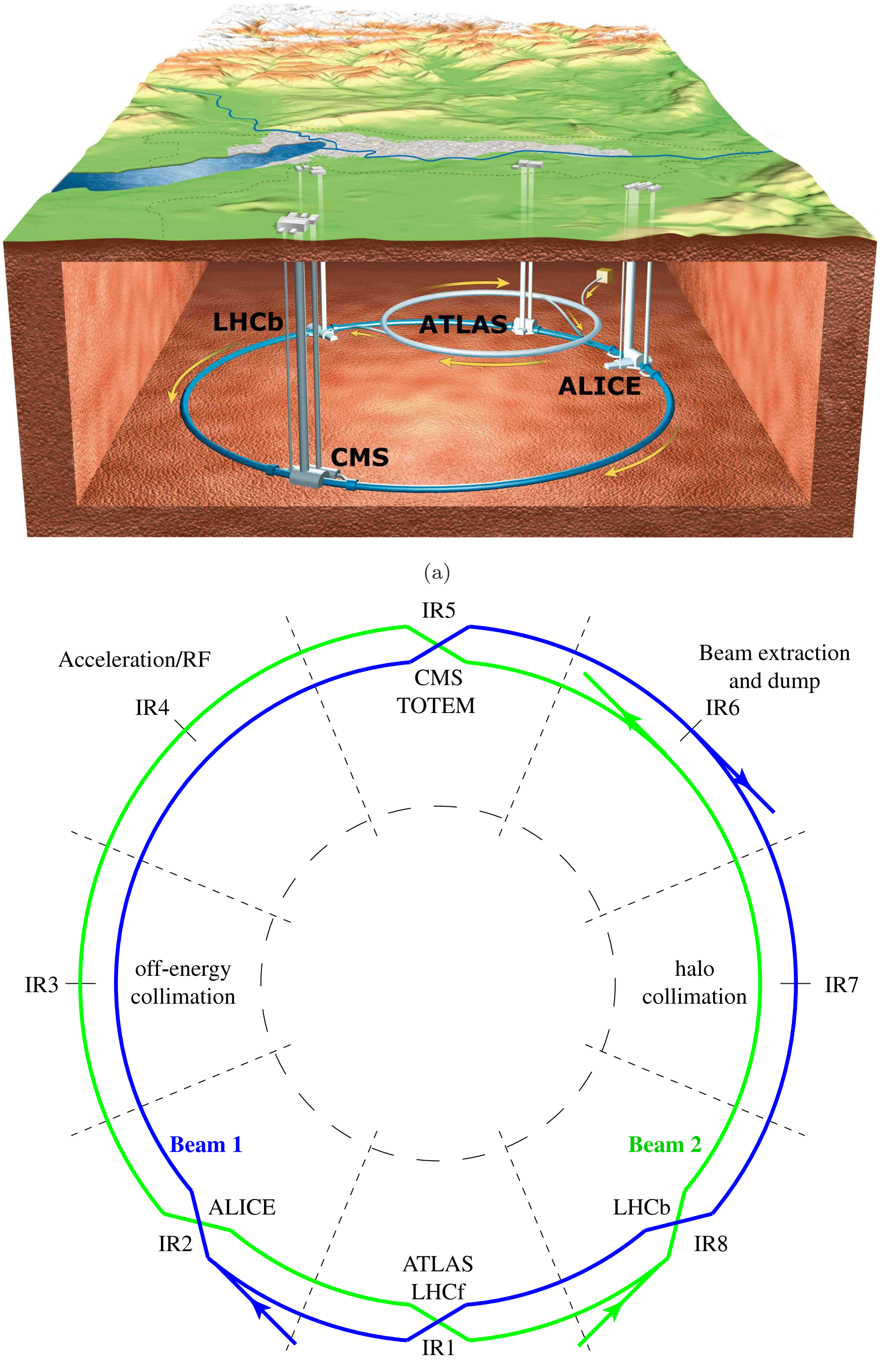

(a)

(b)

Figure 3.1: (a) Geographic location of LHC (dark blue ring), super proton synchrotron (SPS) as an injector (light blue ring), and four interaction points with the experiments installed there. (b) Schematic sketch of LHC with its eight arc sections and eight straight sections. The straight section are labelled as interaction regions IR 1 to IR 8. The beams cross in four of these, IR 1,2,5,8, where the experiments are housed. The dashed lines indicate the centres of arc sections. The paths of two opposite proton beams are shown with green and blue lines respectively (Beam 1 – clockwise, Beam 2 – anticlockwise). Figure from [128].

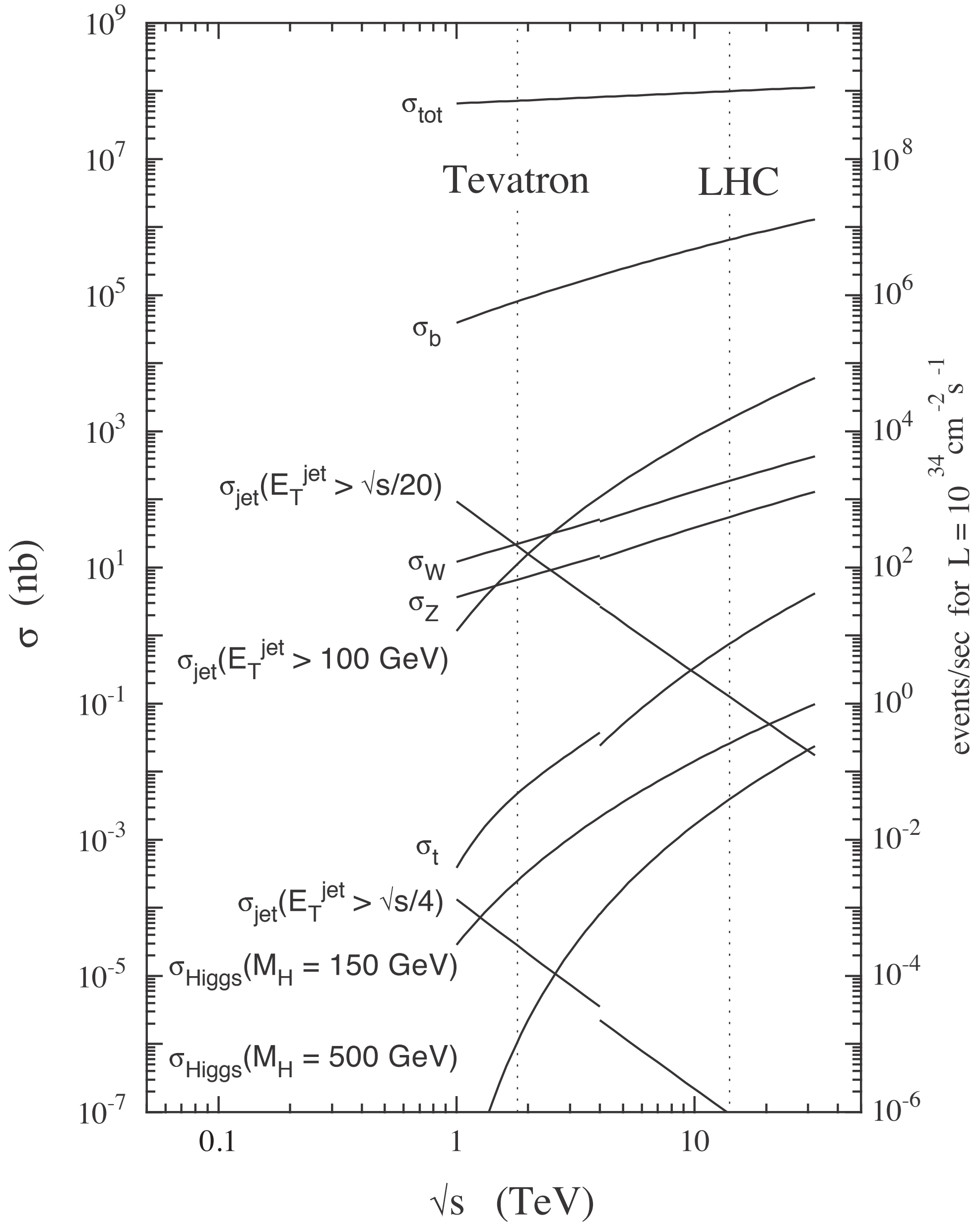

Figure 3.2: Cross sections for important processes in proton–proton collisions as a function of centre-of-mass energy of colliding particles. Figure from [139].

LHCf, TOTEM and MoEDAL

LHCf experiment is designed to calibrate hadron interaction models used in high-energy cosmic ray physics by measuring the properties of forward neutral particles produced in p–p interactions [136, 140, 141]. The MoEDAL experiment is dedicated to the searches for the Dirac's Magnetic Monopoles and other highly-ionizing Stable Massive Particles (SMPs) [138, 140, 142, 143]. The TOTEM detector is dedicated to the measurement of the total proton–proton cross-sections with a luminosity-independent method and to the study of elastic and diffractive scattering at the LHC [137, 140, 144].

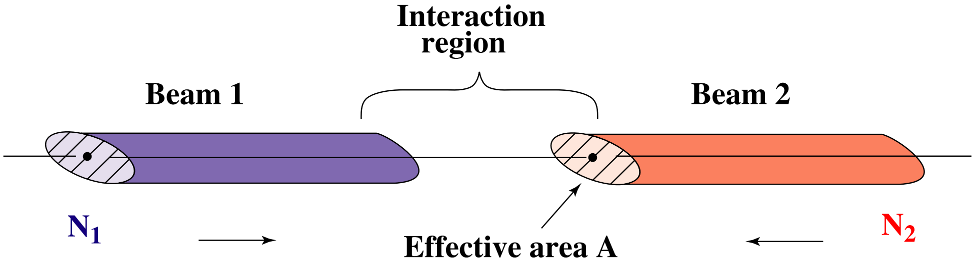

Figure 3.3: The head-on collision of bunches in the interaction point. Figure from [128].

3.1.3 Luminosity and energy of the LHC

The most important design parameters for the particle accelerator are the maximum achievable energy and luminosity. High energy is required to allow the production of new, heavy particles. High enough rate of event production and, hence, a sufficiently high number of collisions and subsequently achievable statistical impact of rare processes is equally important.

Luminosity

The collision rate $\dot{n}$ for a given physics process of cross section σ is the product of the luminosity L and the cross section

$$\dot{n} = L\sigma \tag{3.1}$$

Cross sections are usually given in units of barn (symbol b), where 1 b = 10^{-24}cm^2. The luminosity of a collider is determined by the particle flux and geometry [145]. For head-on collisions, as illustrated in Fig. 3.3, the instantaneous luminosity is

$$L = \frac{N_1 N_2 n_b f_{\text{rev}}}{A} \tag{3.2}$$

where N_1, N_2 are the number of particles per bunch in beam 1 and 2, n_b is the number of bunches, f_{rev} the revolution frequency and A the effective beam overlap cross section at the interaction point. For beams with Gaussian shape of horizontal and vertical r.m.s. beams sizes σ_x, σ_y colliding head on, the effective beam overlap is [128]

$$A = 4\pi\sigma_x\sigma_y \tag{3.3}$$

The main path to high luminosities in the LHC is, first, to use many bunches, nearly 3000, and, second, to reduce the transverse beam size at the interaction points by manipulations of the magnetic focusing system to squeeze beams before the they are brought into collisions.

Since the bunch intensities and beam sizes vary over time, the instantaneous luminosity is implicitly a function of time. In particle physics, it is more convenient to deal with the *integrated luminosity* – the measure for the total number of events generated in the collider over a period of time. It is is defined as

$$\hat{L}(t_{\text{end}} - t_{\text{start}}) = \int_{t_{\text{start}}}^{t_{\text{end}}} L(t)dt \tag{3.4}$$

As mentioned above, the LHC has been designed with four experimental insertions. Two of them are for high luminosity experiments (ATLAS and CMS) using proton–proton collisions with anticipated luminosity of about $L \geq 10^{34}\text{cm}^{-2}\text{s}^{-1}$, one heavy-flavour experiment (LHCb) requiring medium luminosities for proton–proton collisions ($L \geq 10^{32}\text{cm}^{-2}\text{s}^{-1}$) and one dedicated experiment for ion collisions (ALICE) requiring low luminosities ($L \geq 10^{29}\text{cm}^{-2}\text{s}^{-1}$) for the operation with proton beams.

Beam energy

Although the synchrotron radiation from protons at LHC energies becomes noticeable, it is not a limitation on the maximum energy of proton beams. Instead, the limitation is dictated by the maximum bending strength of magnetic field B, needed to guide proton beams in the LHC tunnel [128]. According to this, the maximal proton energy, or, more precisely, the maximal momentum is

$$P = B \cdot r \tag{3.5}$$

where r the bending radius with the value of $r = 2804$ m, given by the LHC tunnel geometry. Numerically, the maximal momentum is

$$P \text{ [GeV/c] } = B \text{ [T] } \frac{r \text{ [m]}}{3.336} \tag{3.6}$$

The LHC is equipped with superconducting NbTi dipole magnets operated at superfluid Helium temperature of 1.9 K. This allows for magnetic field approaching 8.3 T and, therefore, maximal proton momentum of up to 7 TeV/c (this corresponds to 14 TeV centre-of-mass energy of colliding protons). This is almost the maximal magnetic field that can be achieved with existing NbTi superconductors [146]. In other words, the LHC parameters for the magnetic field and beam intensity are designed to get the maximum energy and luminosity achievable with the current technology. The comprehensive list of LHC operation parameters can be found in Ref. [128].

3.1.4 The LHC magnet system

The LHC is unique among superconducting synchrotrons, because its operating temperature is below 2 K to maximise the field strength of the superconducting magnets with NbTi windings [146, 147]. Apart from dedicated magnets in the interaction points, the LHC magnets can be summarized in two types:

- dipole magnets – required to bend particle trajectories in the LHC ring

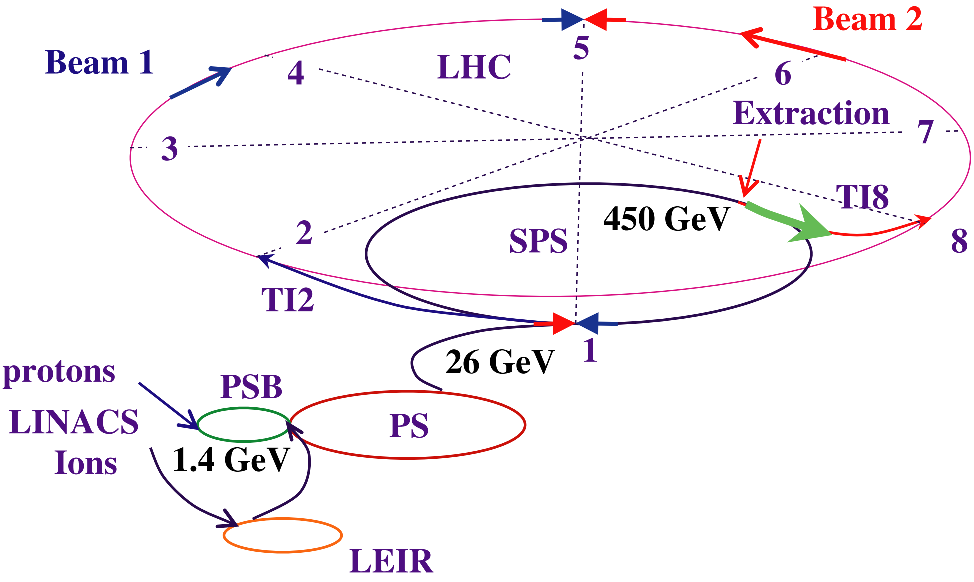

Figure 3.4: Schematic view of LHC with its pre-accelerators (injectors). Figure from [128].

- quadrupole magnets – required for the stabilization of the particle trajectories and the transverse r.m.s. beam size.

Being placed in the tunnel that was previously used to house another powerful CERN machine, LEP e^+e^- collider [148], the LHC has a total circumference of 27.6 km. This includes 5 km split into 8 straight sections and space for dispersion suppression, and 22 km split into 8 arc sections of continuous curvature, as shown in Fig. 3.1(b). The arc sections are equipped with dipole and quadrupole magnets. The distribution of the arc space between dipole and quadrupole magnets is dictated by the tradeoff between the achievable maximum dipole field and quadrupole gradients and the feasible maximum magnet aperture. This led to the design of rather long dipole magnets (15 m), requiring a slightly curved magnet design with a 5 cm Sagitta, covering in total approximately 80% of the arc sections of the old LEP tunnel [147].

3.1.5 The LHC accelerator chain and proton bunch structure

Before entering the main LHC ring protons or ions require a series of pre-accelerators. The energy of proton gradually rises with each step. It starts from 50 MeV in the first stage in the linear accelerator "LINAC", then it enters to the first circular accelerator, the the Proton Synchrotron Booster (PSB), which yields the energy of 1.4 GeV, followed by Proton Synchrotron (PS) which increases energy up to 25 GeV. Finally, the Super Proton Synchrotron (SPS) increases proton energy up to 450 GeV, which is the injection energy of protons in LHC. The pre-acceleration scheme is shown in Fig. 3.4. The more in-depth description of LHC accelerating facilities can be found in Ref. [149].

The particle motion in LHC ring is constrained into longitudinal "buckets" using the so-called radio frequency (RF) systems [150, 151]. The RF-frequency of the LHC is 400

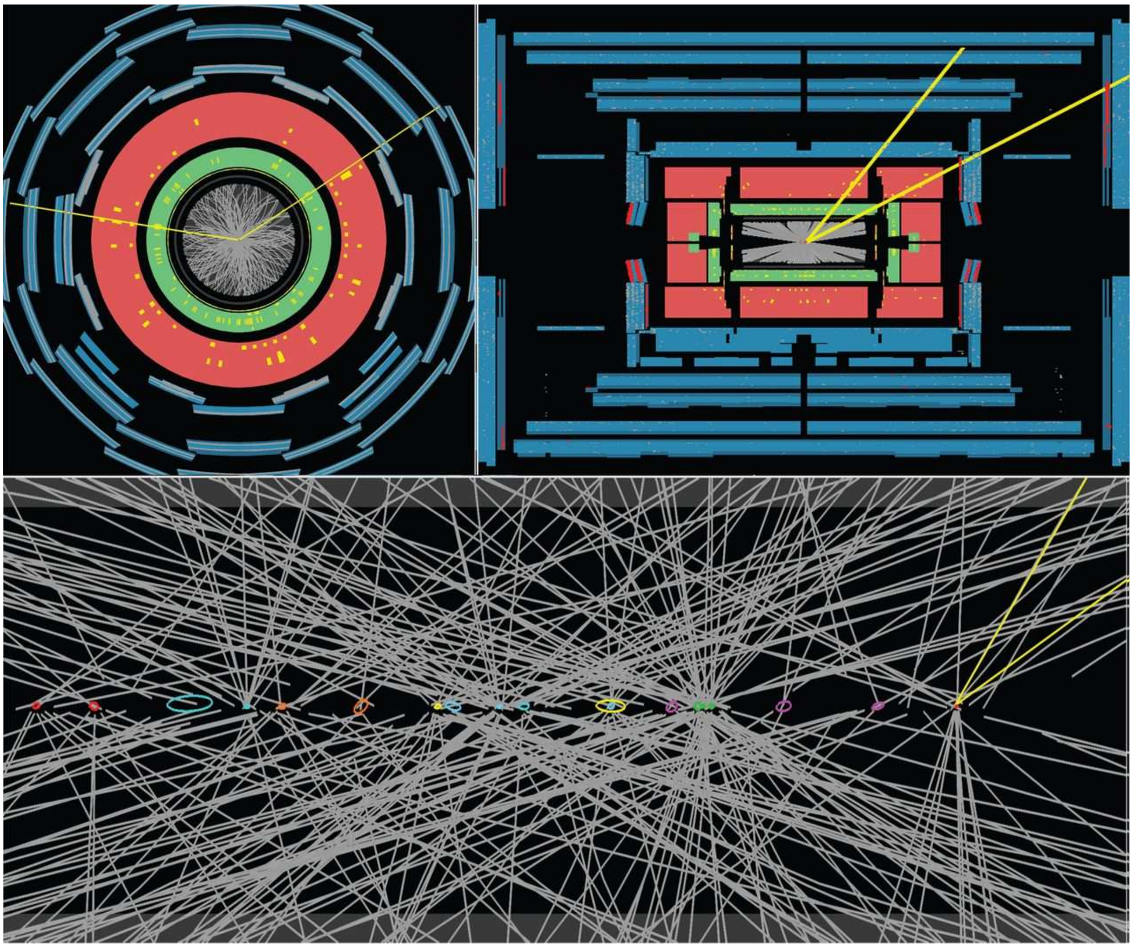

Figure 3.5: A display of real-data collision of proton bunches at the ATLAS experiment. Multiple proton–proton interaction are clearly seen. A candidate $Z \rightarrow \mu\mu$ decay is shown together with 20 reconstructed vertices – the typical pile-up condition in the 8 TeV data (each reconstructed vertex correspond to one proton–proton collision). (Top) The transverse (left) and longitudinal (right) projections in the full ATLAS detector where the two muons (yellow) are clearly identified. (Bottom) The detail of the 20-cm-long region along the beam axis at the interaction point, as reconstructed by ATLAS detector. The two muons can both be seen to emerge from the same vertex. The error ellipses of the reconstructed vertices are shown scaled up by a factor of 10 so that they are visible. Figure from [155].

MHz which corresponds to 75 cm wavelength or buckets of 2.5 ns length. The LHC circumference is 35640 RF-wavelengths which would theoretically allow for the same number of proton bunches. Filling all buckets with particles would produce collisions spaced by only 37.5 cm. However, a more realistic bunch spacing for the LHC is one per 10 RF-buckets or 25 ns. In other words, only one of ten buckets is filled with protons (proton bunch) while other nine are empty. It is constrained by the so-called multipactoring effects [152], like the electron-cloud effect [153, 154], and the strength and number of acceptable parasitic long-range collisions in the common vacuum chamber of the two beams. The total beam current is constrained by hardware limitations and collective effects, like multi-bunch instabilities [128].

Although the designed bunch spacing at LHC is 25 ns, it was so far running with minimum bunch spacing of 50 ns, which corresponds to the potential maximum number of 1400 bunches per beam. This is due to beam and vacuum instabilities produced by the electron cloud effect. This effect has been predicted for the LHC [154] and the beam cleaning procedure was done first with bunch spacings of 75 ns (up to April 2011) and then with bunch spacings of 50 ns. Following the successful beam cleaning runs with 50 ns spacing it was decided to keep physics operation at this value of bunch spacing [128].

Since bunch spacing was eventually lower than the designed value, the high integrated luminosity, envisioned at LHC, was attained by increasing the number of protons per bunch ("fatter" bunches). The high intensity of the proton bunches, however, results in multiple proton–proton collisions occurring during each crossing of proton bunches, an effect known as "pile-up" (Fig. 3.5). Thus, high luminosity was attained at the cost of substantially higher pile-up. The average number of interactions per bunch crossing was $\sim$10 in 2011 and increased to $\sim$ 20 in 2012. Fortunately, the LHC experiments have successfully adopted their analysis techniques to mitigate the effects of the harsher pile-up environment.

3.2 The ATLAS detector

As already stated, the LHC has provided and will provide further the hadron collisions at unprecedented center-of-mass energy and luminosity, and ATLAS[2] is one of two general-purpose detectors, designed to fully exploit the LHC discovery potential. As a general-purpose experiment, it consists of sub-detectors, dedicated to identification and measurement of properties of particles that are produced in the hadron collisions it is exposed to. A brief overview of the ATLAS detector is given in this section with the emphasis on the sub-detectors, relevant to physics studies that are described in the thesis. The detailed survey of ATLAS detector can be found in Ref [132].

The ATLAS experiment is an impressive result of successful cooperative work of more than three thousand physicists and engineers from all over the world. Being the largest scientific collaboration in the history of mankind, it comprises efforts of about two hundred institutions in forty countries. The ATLAS endeavour has started twenty years ago, and, as the first successful data taking has started at LHC in 2009, has brought physics to the new experiment-driven era, which anticipates along with the results obtained so far a series of further fundamental discoveries, putting on test the most profound theoretical ideas discussed in the last half a century.

3.2.1 Overview

The ATLAS detector is shaped like a cylinder with a forward-backward symmetry with respect to the interaction point. It is built concentrically around the LHC beam pipe with a radius of 11 m and length of 44 m, and installed in the interaction region 1 (IR 1 – see Fig. 3.1). Fig. 3.6 gives the overview of the experiment and its different sub-detectors. As any modern general-purpose detector in particle physics, ATLAS consists of the following main sub-detectors (see Fig 3.7):

- **Inner Detector (ID)**. An inner tracking detector immersed in a solenoidal 2 T magnetic field, providing precision measurements of momenta of charged particles that originate at (or near) the interaction point[3] [159].
- **Electromagnetic and Hadronic Calorimeters.** A calorimetry system sensitive to both electromagnetic and hadronic interactions. It provides an accurate measurement of the energy (transverse energy) of particles as well as the reasonable particle identification capabilities [160, 161]. In addition, the cylinder-shaped calorimeters (together with muon system described below) surrounding the interaction axis allow for measuring the missing-transverse momentum – the total momentum in the plane, transverse to beam direction, which is carried by the particles that evade detection (like neutrinos).

---

[2] ATLAS stands for A Toroidal LHC ApparatuS

[3] It is also capable of measuring the ionization energy loss for non-relativistic particles. This plays a key role in the searches for exotic stable massive particles that are predicted, for example, in R-parity violating supersymmetry (SUSY) and universal extra-dimensions models, as described in Refs. [157,158].

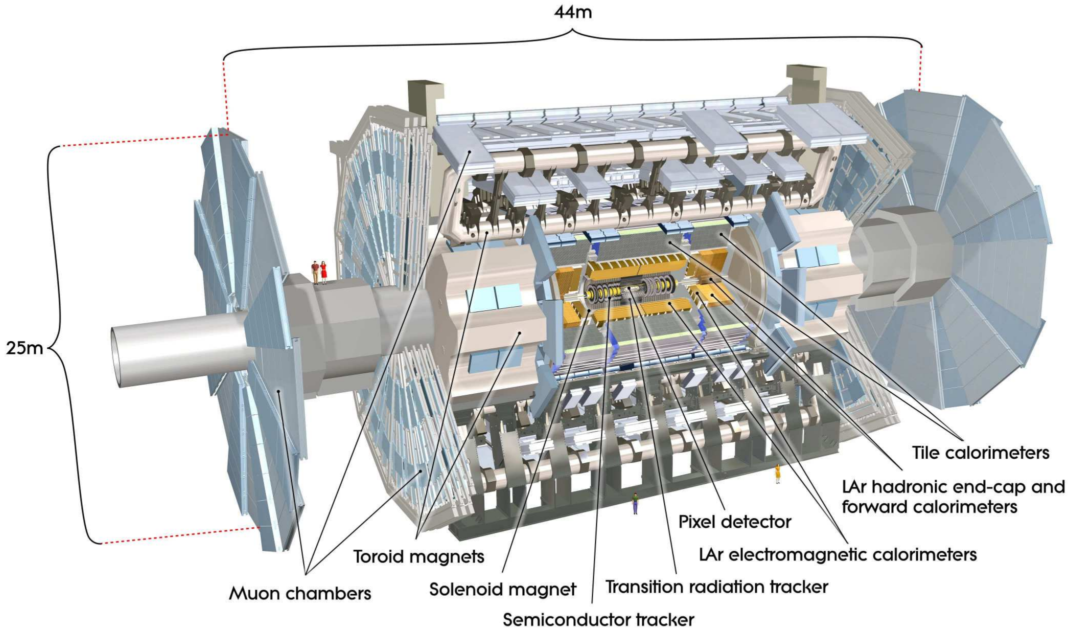

Figure 3.6: Cut-away view of the ATLAS detector. The dimensions of the detector are 25 m in height and 44 m in length. The overall weight of the detector is approximately 7000 tonnes. Figure from [132].

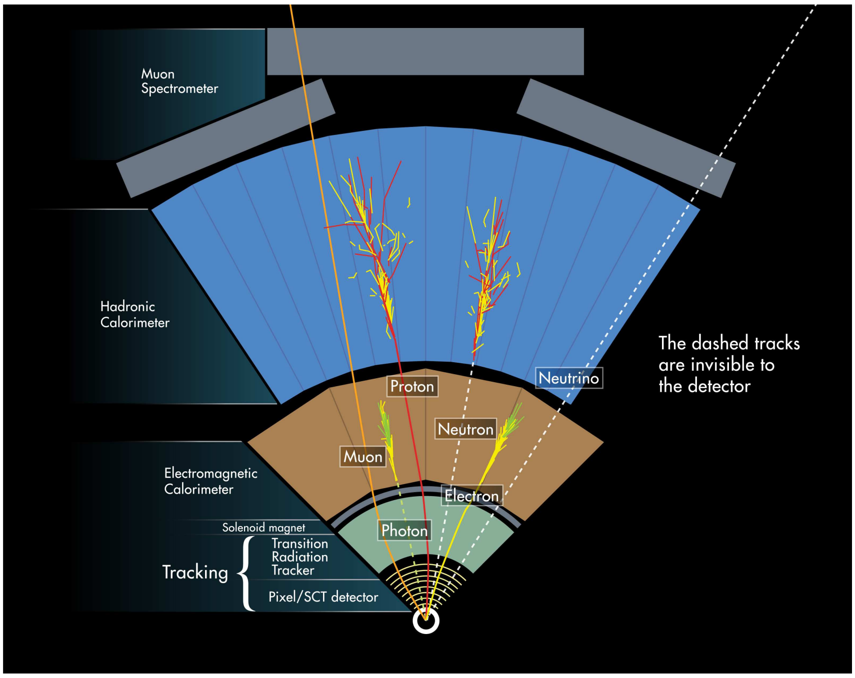

Figure 3.7: Principle of operation of general-purpose detector (ATLAS or CMS) at LHC. The detection of basic elementary particles emanating from hadron collisions is illustrated: charged hadrons and electrons produce tracks in inner detector; electrons and photons are absorbed and their energy is measured in electromagnetic calorimeter; hadrons deposit a small fraction of their energy in electromagnetic calorimeter and are totally absorbed in hadronic calorimeter, where their energy is measured; finally, muons are the only charged particles that escape both calorimeters and produce tracks in the muon spectrometer, as well as in the inner detector. Figure from [156]

- **Muon spectrometer.** The muon detector is immersed in a toroidal magnetic field of approximately 0.5 T (1 T – depending on the region), which provides muon identification and accurate momentum measurements in the wide range of muon momenta [162].

ATLAS detector distinguishes itself from other, similar experiments, in particular from CMS, in two important ways. First, in addition to silicon pixel and silicon strip sensors in the inner detector, ATLAS uses a straw-tube tracker with transition radiation detection capabilities for electron/pion discrimination [163, 164]. This feature is particularly important for the searches of new phenomena in multi-electron final states, as described in this thesis. Second, the magnet system used for the muon spectrometer is composed of superconducting air-core toroids, rather than a second solenoidal field.

An important part of any hadron collider experiment is the *trigger system* [165]. Composed of both hardware-based and software-based decision making elements, it selects only those collisions that are of potential interest for further analysis. This allows to reduce the initial event rate of about 20 MHz (at the bunch spacing of 50 ns) to about 300 Hz, which can be then saved to disk (tape) for further offline processing.

3.2.2 The ATLAS coordinate system and useful definitions

In ATLAS, the polar coordinate system is defined with the origin in the interaction point, while the beam direction defines the z-axis and the x-y plane is transverse to the beam direction. The positive x-axis is defined as pointing from the interaction point to the centre of the LHC ring and the positive y-axis is defined as pointing upwards. The side-A of the detector is defined as that with positive z and side-C is that with negative z. The azimuthal angle ϕ is measured as usual around the beam axis, and the polar angle θ is the angle from the beam axis. At hadron colliders, *pseudorapidity* is usually preferred instead of polar angle. It is defined as

$$\eta \equiv -\ln\tan\frac{\theta}{2} \tag{3.7}$$

In case of massless particles, pseudorapidity is equal to true particle's rapidity (for example, electrons can be safely considered as massless at the momentum range relevant to ATLAS detector). For massless particles, $d\eta$ is invariant under the Lorentz-boost transformation along the beam axis. At the same time, for particles moving perpendicular to z-axis, $d\eta$ is equal to $d\theta$. Next, the cone separation is defined as

$$\Delta R = \sqrt{(\Delta\phi)^2 + (\Delta\eta)^2} \tag{3.8}$$

Finally, the transverse momentum, p_{T}, is defined as a the momentum perpendicular to beam axis

$$p_{\mathrm{T}} = \sqrt{p_x^2 + p_y^2} \tag{3.9}$$

3.2.3 The ATLAS magnet system

The fundamental choice of magnet configuration at ATLAS has driven the design of the rest of the detector. The magnet system comprises two main parts, cooled with liquid helium, with operating temperature of 4.5 K. The constituents are

- **Thin superconducting solenoid (central solenoid)**– *for momentum measurement in inner detector*. Surrounding the inner-detector cavity, it provides momentum measurement of particles in the inner detector by bending their trajectories in the transverse plane in the magnetic field of about 2 T. The solenoid is constructed as a single-layer coil wound with a high-strength Al-stabilised NbTi superconductor. It stretches about 6 m along the z-axis and the inner at the radii of 2.46 m and 2.56 m, respectively.
- **Superconducting toroid**– *for momentum measurement in muon spectrometer*. In ATLAS there are three large superconducting toroids, one barrel and two end-caps, each with eight coils. Arranged with an eight-fold azimuthal symmetry around the calorimeters, they provide the momentum measurement of muons by bending their trajectories in the η–direction. The toroids feature a magnetic field of approximately 0.5 T in the barrel region and 1 T in the end-caps.

  The conductor and coil-winding technology is the same in the barrel and end-cap toroids. It is based on winding a pure Al-stabilised Nb/Ti/Cu conductor into pancake-shaped coils, followed by vacuum impregnation. The inner and outer diameters of the barrel toroid magnet system are 9.4 m and 20.1 m, respectively, and the magnet system spans 25.3 m along the beam direction.

3.2.4 The ATLAS inner detector

The inner detector (ID), or similarly – inner tracker, consists of three subsystems, two of them are silicon-based tracking detectors, and the third one is based on transition radiation, as shown in Fig. 3.8. They are dedicated mostly to measuring the momentum of charged particles (in the transverse-momentum range from 0.1 GeV to several TeV) and determining the location of primary and secondary vertices, via the hits that are produced by charged particles traversing different stations of these sub-detectors (see Fig. 3.9). Each subsystem is composed of a barrel and two endcaps (in the forward and backward regions). The inner detector subsystems are:

- **Pixel Detector (Pixels)**. This subsystem is composed of silicon pixel sensors, placed closest to the interaction point, at the distance of 50.5 mm from the center of the beam pipe. This detector provides the most accurate position measurements in ATLAS. It has three stations with the outermost one at the distance of 122.5 mm from the beam axis. Typically, all tracks in the acceptance of the Pixels get three hits, each with an intrinsic accuracy of $\mathrm{R}\Delta\phi \times \Delta\mathrm{z} = 10 \times 115\ \mu\mathrm{m}$ in the barrel region [132, 166].

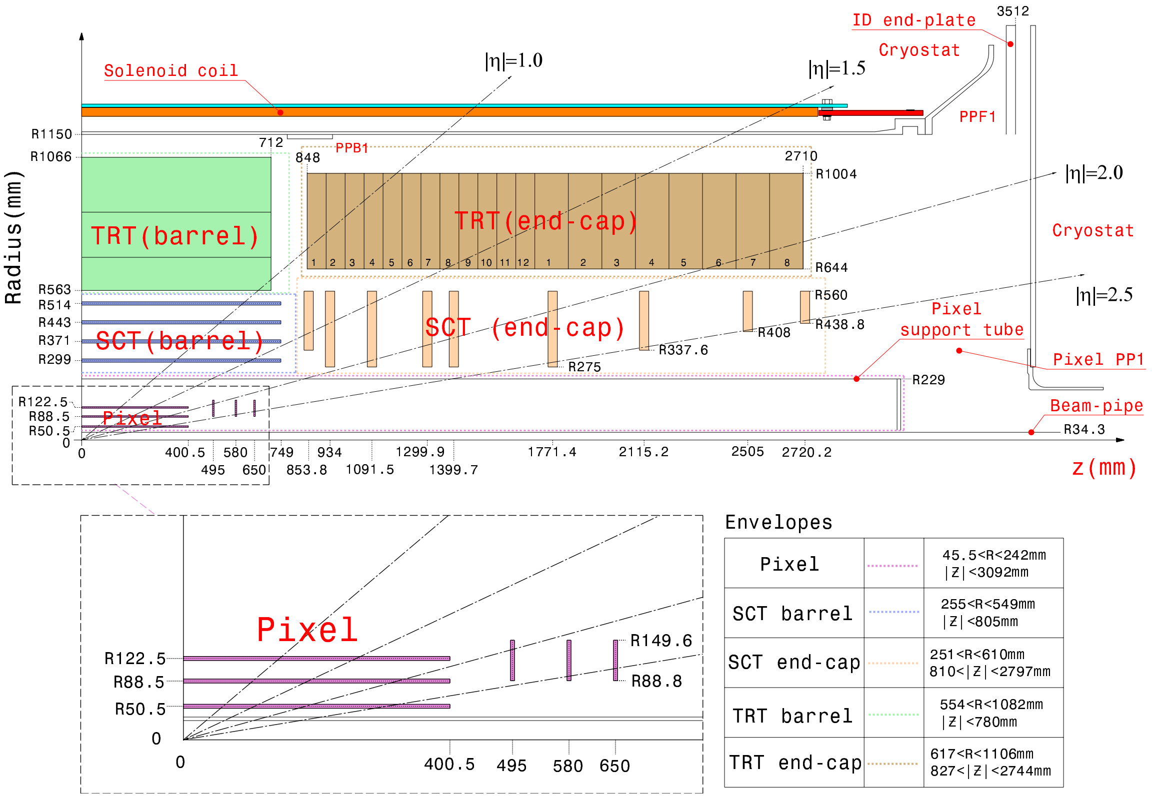

Figure 3.8: Cross-section view of ATLAS inner detector in η (track-bending) plane, showing each of the major detector elements with its active dimensions and envelopes. Figure from [132].

- **Semi-Conductor Tracker (SCT)**. This subsystem placed outside of the pixels is a silicon microstrip detector. The Semiconductor Tracker is also based on silicon technology, but in the form of strips mounted with a 40 mrad stereo angle. It has four stations in the barrel region with innermost and outermost radii of 299 and 514 mm respectively, providing up to eight hits per tracks. This forms four space-point measurements, each with an intrinsic accuracy in the barrel region of $\mathrm{R}\Delta\phi \times \Delta \mathrm{z} = 17 \times 580\ \mu\mathrm{m}$. In the SCT, reconstructed hits are expected whenever a sensor is crossed by a charged particle, regardless of charge, and there is no risk of hits being lost due to saturation [132, 167].

- **Transition Radiation Tracker (TRT)**. Placed at the outermost radii of inner detector, the TRT is composed of many layers of gaseous straw tube elements filled with $\mathrm{Xe} + \mathrm{CO}_2 + \mathrm{O}_2$ gas mixture, interleaved with transition radiation material. Low-energy transition radiation (TR) photons are absorbed in the Xe-based gas mixture, and yield much larger signal amplitudes than minimum-ionising charged particles. With an average of 36 hits per track, it provides continuous tracking to enhance the pattern recognition of tracks. The TRT straws only provide measurements in the bending plane, with an intrinsic accuracy of $\mathrm{R}\Delta\phi = 130\ \mu\mathrm{m}$, and no measurements can be made along the straw direction [132, 168].

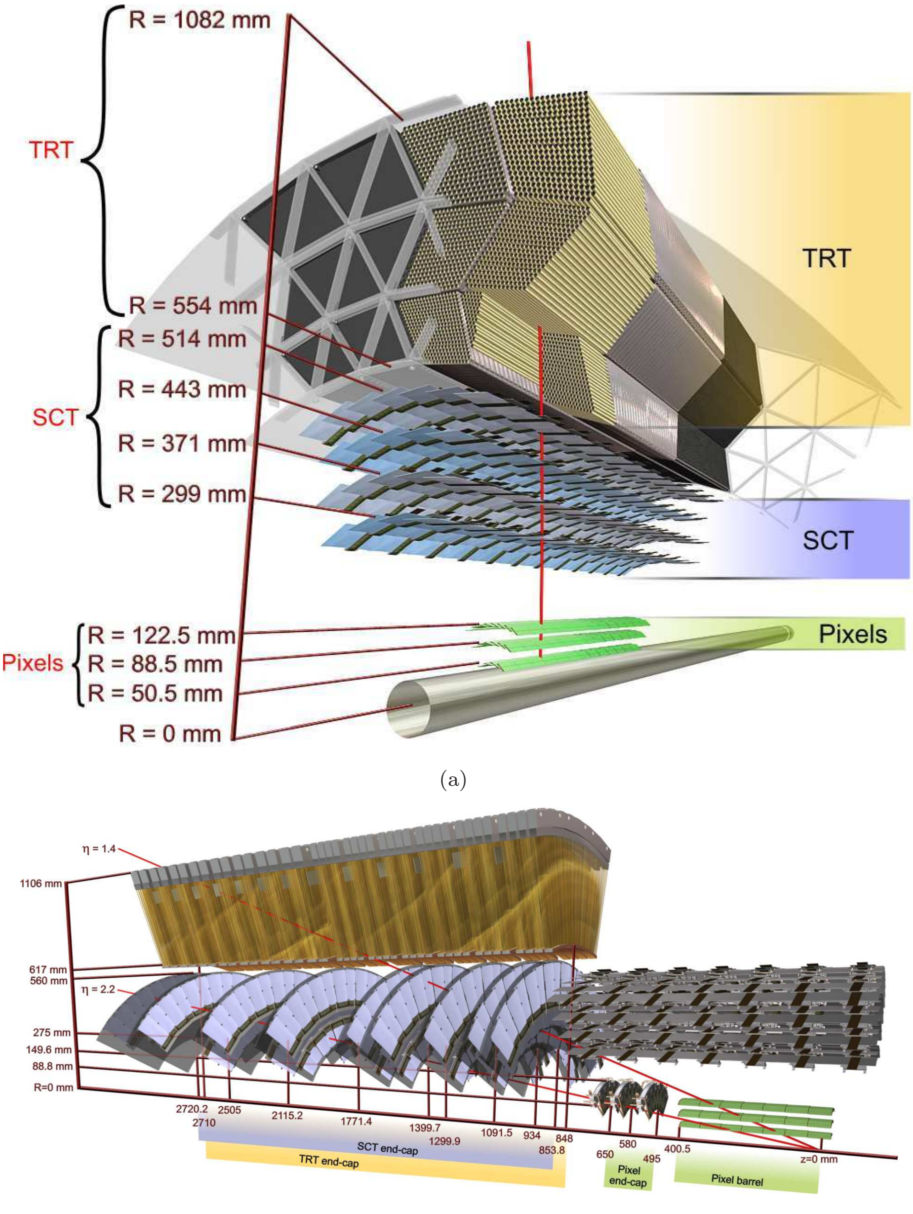

(a)

(b)

Figure 3.9: Illustration of inner detector sensors and structural elements in (a) barrel and (b) end-cap regions. The red lines show the trajectories of charged particle of 10 GeV transverse momentum with pseudorapidity $\eta = 0.3$ (a) and $\eta = 1.4$ / 2.2 (b). Figure from [132].

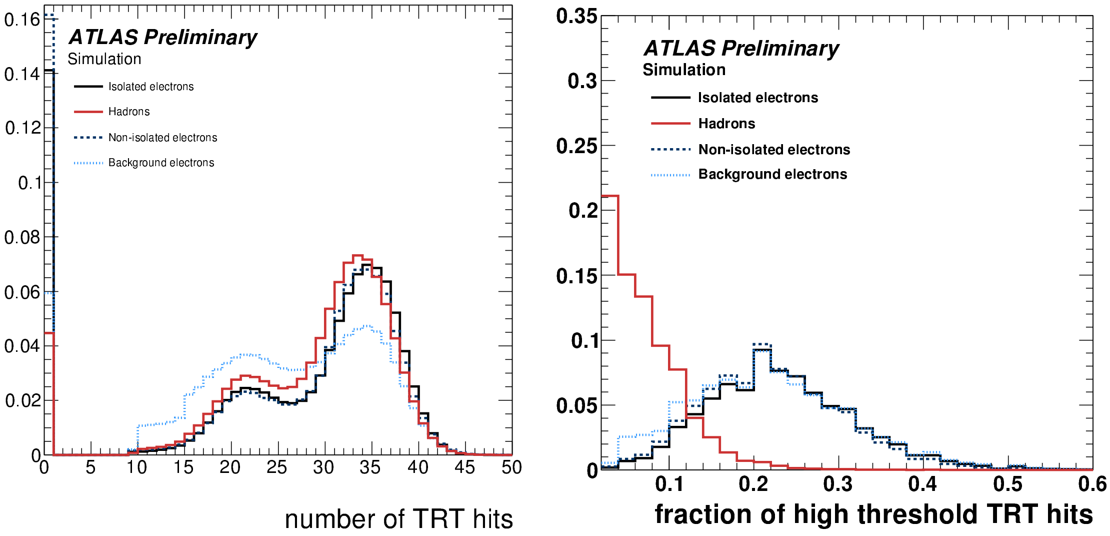

(a) (b)

Figure 3.10: Distribution of number of hits in TRT (a), and the fraction of hits in TRT fulfilling the high-threshold (HT) stetting to that fulfilling the low-threshold (LT) setting. The distribution are shown for electrons and hadrons. Figure (b) indicates a substantial discriminating power between charged hadrons and electrons in TRT. Figure from [169].

Silicon-based detectors are used in all modern general-purpose particle detectors for their excellent position resolution, which is typically on the order of microns. The sensors are thin pieces of high-purity doped silicon, which produce electron-hole pairs when traversed by an ionizing particle. An electric field is applied to the sensor to prevent the pairs from recombining, and the subsequent drift and capture of the free charge carriers produces a current pulse that is read out by analog electronics. In ATLAS, there are two silicon-based sub-detectors:

An important feature of TRT detector is its capability of identifying particle types through benefiting from the transition radiation mechanism, which results in higher-amplitude signals for particles at high $\beta = v/c$. In the front-end electronics of the TRT, the measured signals are discriminated against two thresholds, classifying the hits as low-threshold (LT) or high-threshold (HT) hits. This allows to discriminate between electrons and charged hadrons [163, 164] (see Fig. 3.10).

3.2.5 The ATLAS calorimeters

As any general-purpose detector, ATLAS has two types of calorimeters – *electromagnetic* (EM) and *hadronic*, sensitive to electromagnetic and strong interactions of charged particles with matter. The primary purpose of the calorimeter system is to stop all particles (except muons and neutrinos) emanating from the interaction point and thereby measure their energy and position. These calorimeters span the range $|\eta| < 4.9$ with full ϕ-symmetry and coverage around the beam axis.

Calorimeter	η-range
Electromagnetic calorimeters (EM)	
Barrel LAr EM calorimeter (EMB)	$\lvert\eta\rvert < 1.475$
End-cap LAr EM calorimeter (EMEC)	$1.375 < \lvert\eta\rvert < 3.2$
Hadronic calorimeters	
Tile hadronic calorimeter (TileCal)	$\lvert\eta\rvert < 1.7$
LAr end-cap hadronic calorimeter (HEC)	$1.5 < \lvert\eta\rvert < 3.2$
Forward hadronic calorimeter (FCal)	$3.1 < \lvert\eta\rvert < 4.9$

Table 3.1: List of ATLAS calorimeter sub-systems with the corresponding η-regions covered by these detectors.

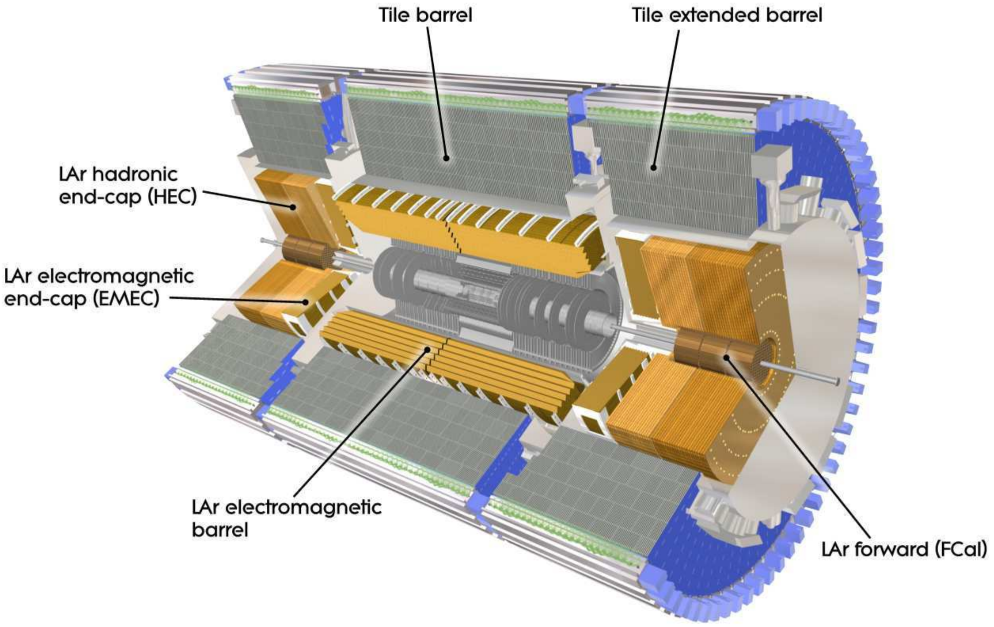

Figure 3.11: A cut-away illustration of the ATLAS calorimeter system. Figure from [132].

While hadronic calorimeters predominantly measure the energy of hadrons via the strong interaction with the heavy nuclei of the absorbing medium, the electromagnetic calorimeters measure the energy of electrons and photons and contribute to measuring the energy of hadrons in jets via the mechanisms of bremsstrahlung radiation of photons and production of electron-positron pairs (see f.ex. Ref. [170]). The overall sketch of ATLAS calorimetry is shown in Fig. 3.11 and the η-coverage of each sub-system is given in Table 3.1.

All calorimeters at ATLAS are of the sampling type, i.e. each calorimeter includes, first, dense absorber material (lead, iron, copper or tungsten) to fully absorb incident particles and, second, active material (liquid-argon or plastic scintillations) to produce an output signal proportional to the input energy. The absorbing medium is interleaved with detecting material ('sandwich' design), as shown in Fig. 3.12.

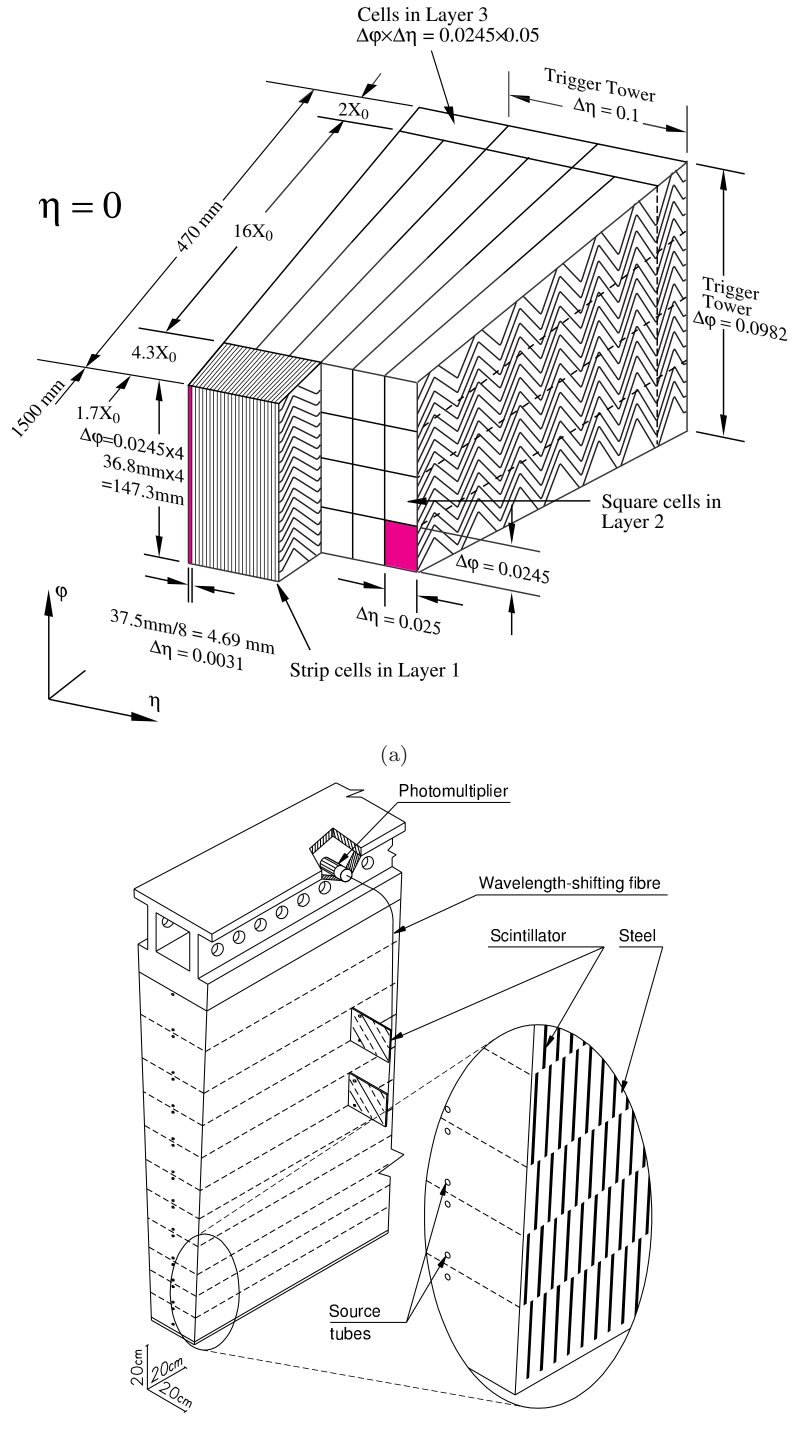

(a)

(b)

Figure 3.12: Sketch illustrating a fragment of (a) LAr electromagnetic calorimeter in the barrel region and (b) tile hadronic calorimeter. Absorbers and electrodes in (a) are of the accordion shape, with three layers clearly shown. The η–ϕ granularity decreases from first layer to the last one, i.e. first layer is the most fine-grained. Gaps between absorber and electrode "waves" are filled with liquid argon. For hadronic calorimeter (b), the various components are shown, including steel absorbers and optical read-out. The latter is composed of scintillating tiles, light-guiding fibres, and photomultipliers. Figure from [132].

Electromagnetic calorimeters

The EM calorimeter uses liquid argon as the active detector and lead as the absorber material. When a photon enters the detector, it interacts with the lead plates and produces electron-positron pair. The electron and positron continue to interact with the material in the calorimeter, producing bremsstrahlung photons, which in turn again produce electron-positron pairs, creating a "shower" of electromagnetic activity (see Fig. 3.13 – left). These electrons and positrons pass through the active material (liquid argon) and ionize the argon atoms, releasing ionization electrons which are collected as a current by applying an electric field. of about 10 kV/cm (see f.ex. Ref. [171]). The visible energy is scaled by the sampling fraction to obtain the true deposited energy in both the active material and the absorber. An electron entering the LAr calorimeter will undergo the same chain reaction as a photon.

The electromagnetic calorimeters share the same vacuum vessel with central solenoid and are divided into a barrel part and two end-cap components, each housed in their own cryostat, as described below

- **Barrel LAr EM calorimeter (EMB).** The barrel EM calorimeter consists of two identical half-barrels, separated by a small gap (4 mm) at z=0.
- **End-cap LAr EM calorimeter (EMEC).** Each end-cap EM calorimeter is mechanically divided into two coaxial wheels: an outer wheel covering the region 1.375< $|\eta|$ <2.5, and an inner wheel covering the region 2.5< $|\eta|$ <3.2.

The total thickness of EM calorimeter is more than 24 radiation lengths (X_0) in the barrel and above 26 X_0 in the endcaps. Over the region devoted to precision physics (η <2.5), the EM calorimeter is segmented in three sections in depth. For the end-cap inner wheel, the calorimeter is segmented in two sections in depth and has a coarser lateral granularity than for the rest of the acceptance. In the region of $|\eta|$ <1.8, a presampler detector is used to correct for the energy lost by electrons and photons upstream of the calorimeter. The presampler consists of an active LAr layer of thickness 1.1 cm (0.5 cm) in the barrel (endcap) region. The η–ϕ resolution of EM calorimeter varies depending on the η-region and calorimeter layer and is usually is of the order of 0.025×0.025 (in the second layer of barrel EM calorimeter).

Hadronic calorimeters

The mechanism of hadron interactions with matter differs from that of electrons and photons. Hadrons typically loose their energy through inelastic collisions with the nuclei of absorbing material (see Fig. 3.13 – right). However, the principle of operation of hadronic calorimeters is essentially the same as the electromagnetic one, i.e. charged particles are produced in the absorber medium and detected in the active material (plastic scintillator or liquid argon) [173]. The only difference is that the nuclear interaction

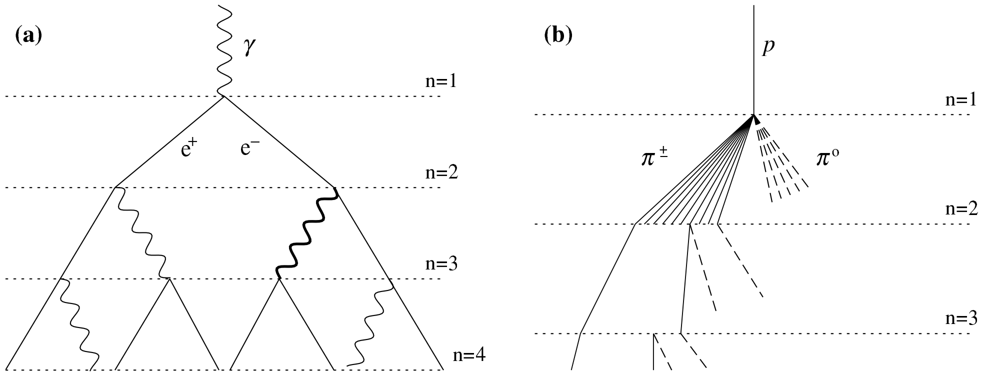

Figure 3.13: Simplified illustration of (left) electromagnetic and (right) hadronic shower evolution. Electromagnetic showers are governed by two mechanisms – electron-positron pair production and bremsstrahlung radiation of photons. In hadronic showers, initial hadron inelastically scatters on the nucleus of medium, producing mainly charged and neutral pions; charged pions scatter further on the nuclei of medium increasing the multiplicity of particles in the shower; neutral pions decay to photon pairs giving raise to electromagnetic contribution (not shown in this figure) in hadronic shower. Figure from [172].

length λ is larger than electromagnetic radiation length X_0 [4]. Hence the absorbing part of hadronic calorimeter needs to be denser (deeper). It should be noted also that a sizeable fraction of the energy deposited in a hadronic shower is electromagnetic – from production and decay of neutral pions ($\pi^0 \to \gamma\gamma$). The ATLAS hadronic calorimeter system comprises the following parts

- **Tile hadronic calorimeter (TileCal).** It uses steel as the absorber and scintillating tiles as the active material. The tile calorimeter is placed directly outside the EM calorimeter envelope. Its barrel covers the region $|\eta|$ <1.0, and its two extended barrels the range 0.8< $|\eta|$ <1.7. The total detector thickness at the outer edge of the tile-instrumented region is 9.7 λ at η=0.

- **LAr end-cap hadronic calorimeter (HEC)**. This uses copper as an absorber material. The copper plates are interleaved with LAr gaps, providing the active medium for this calorimeter. It consists of two independent wheels per end-cap, located directly behind the end-cap electromagnetic calorimeter and sharing the same LAr cryostats.

- **Forward LAr hadronic calorimeter (FCal)**. FCal consists of three modules in each end-cap: the first one uses copper as the absorber and is optimised for electromagnetic measurements, while the other two, made of tungsten, measure predominantly the energy of hadronic interactions. Each module consists of a metal matrix, with regularly spaced longitudinal channels filled with the electrode structure consisting of concentric rods and tubes parallel to the beam axis. The LAr in the gap between the rod and the tube is the sensitive medium. The depth of FCal

---

[4] Electromagnetic radiation length X_0 (nuclear interaction length λ) of the material defines the mean distance over which the the energy of electron (hadron) is reduced by a factor of 1/e as it pass through that material.

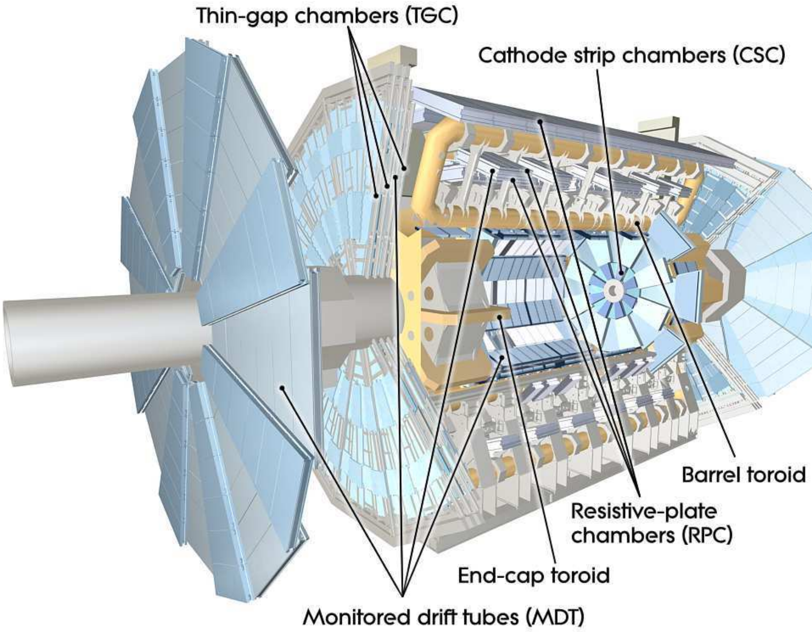

Figure 3.14: A cut-away view illustrating the layout of muon sub-detectors. Figure from [132].

is approximately 10 λ and, similarly to EMEC and HEC, it is integrated into the end-cap cryostats.

3.2.6 The ATLAS muon spectrometer

The outermost sub-detector of the ATLAS is the Muon Spectrometer (MS). It is designed to detect charged particles exiting the barrel and end-cap calorimeters and to measure their momentum in the pseudorapidity range $|\eta| < 2.7$. It is also designed to trigger on these particles in the region $|\eta| < 2.4$. The requirement to accurately measure the curvature of high-p_{T} tracks dictates the size of the MS and thereby defines the overall dimensions of the ATLAS detector.

The ATLAS muon system is designed to determine the momentum accurately for muons with 3 GeV $< p_{\mathrm{T}} <$ 1 TeV [165]. However, even at the high end of the accessible range, $p_{\mathrm{T}} \sim$3 TeV, MS still provides adequate momentum resolution and excellent charge identification. Muon system is composed of four types of detectors, two of them are for precision measurements – the Monitored Drift Tubes (MDT) and Cathode Strip Chambers (CSC), and two are for fast online selection of events (trigger chambers) – Resistive Plate Chambers (RPC) and Thin Gap Chambers (TGC). The η-coverage of each sub-detector is given in Table 3.2, and the general layout of muon systems is shown in Fig. 3.14.

The muon detectors are are immersed in the magnetic field from the toroid magnet discussed in Section 3.2.3. The momentum is measured through deflection of muon tracks in magnetic field. Over the range $\eta < 1.4$, magnetic bending is provided by the large barrel toroid. For $1.6 < |\eta| < 2.7$, muon tracks are bent by two smaller end-cap magnets inserted into both ends of the barrel toroid. Over $1.4 < |\eta| < 1.6$, usually referred to as the

Muon detector	η-range
Precision muon tracking	
Monitored Drift Tubes (MDT)	$\|\eta\| < 2.7$
Cathode Strip Chambers (CSC)	$2.0 < \|\eta\| < 2.7$
Triggering, second muon coordinate	
Resistive Plate Chambers (RPC)	$\|\eta\| < 1.05$
Thin Gap Chambers (TGC)	$1.05 < \|\eta\| < 2.7$ (2.4 for triggering)

Table 3.2: List of ATLAS muon sub-systems with the corresponding η-regions covered by these detectors.

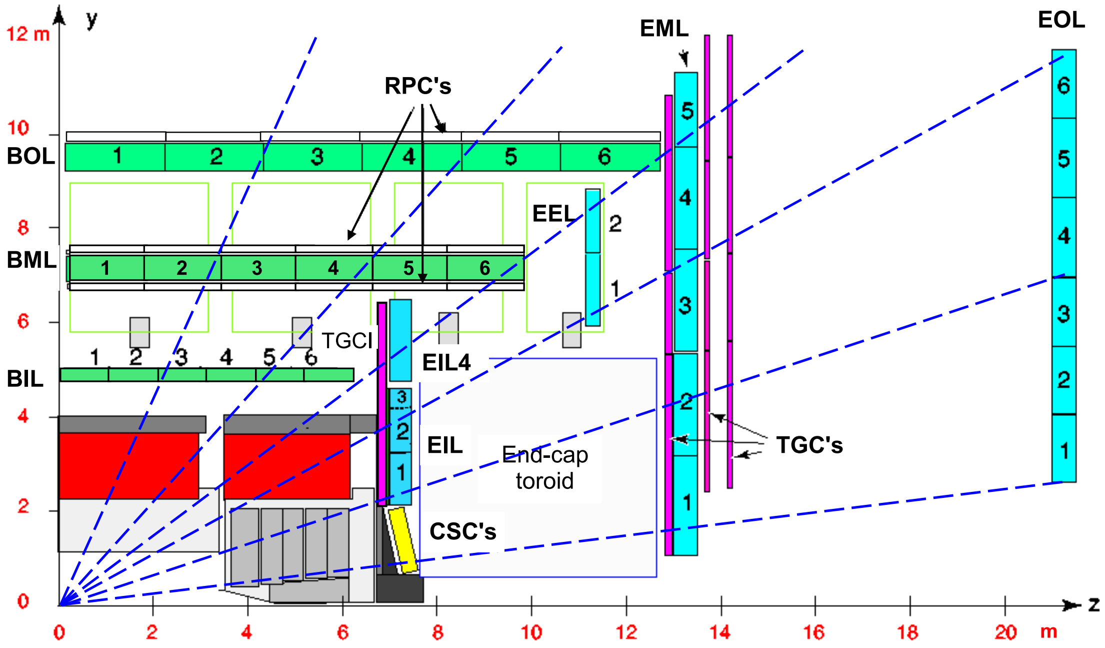

Figure 3.15: Cross-section of the muon system in a plane containing the beam axis (bending plane). Infinite-momentum muons would propagate along straight trajectories which are illustrated by the dashed lines and typically traverse three muon stations. Figure from [132].

transition region, deflection is provided by a combination of barrel and end-cap magnetic fields.

In the barrel region, tracks are measured in chambers arranged in three cylindrical layers around the beam axis; in the transition and end-cap regions, the chambers are installed in planes perpendicular to the beam, also in three layers, as shown in Fig. 3.15. The barrel chambers are located around the beam axis at radii of approximately r ≈ 5 m, 7.5 m, and 10 m, while the end-cap muon chambers form large wheels located at distances of z ≈ 7.4 m, 10.8 m, 14 m, and 21.5 m from the interaction point.

Precision muon detectors

The precision-tracking muon detectors are MDT and CSC chambers. MDT chambers consist of three to eight layers of drift tubes, operated at an absolute pressure of 3 bar, which achieve an average resolution of 80 μm per tube, or about 35 μm per chamber. The overall layout of the MDTs is projective: the layer dimensions and the chamber sizes increase in proportion of their distance from the interaction point. The CSC detectors are multiwire proportional chambers with cathode planes segmented into strips in orthogonal directions.

The purpose of the precision-tracking chambers is to determine the coordinate of the track in the bending plane (η). The CSC chambers provide also the ϕ coordinate, while there is no measurement of ϕ performed in MDT detectors. After matching of the MDT and trigger chamber hits in the bending plane, the trigger chambers coordinate in the non-bending plane is adopted as the second coordinate of the MDT measurement. This method assumes that in any MDT/trigger chamber pair a maximum of one track per event be present, since with two or more tracks the η and ϕ hits cannot be combined in an unambiguous way. Simulations have shown that the probability of a track in the muon spectrometer with $p_{\mathrm{T}} > 6$ GeV is about 6×10^{-3} per beam-crossing, corresponding to about 1.5×10^{-5} per chamber [132]. Assuming uncorrelated tracks, this leads to a negligible probability to find more than one track in any MDT/trigger chamber pair. When correlated close-by muon tracks do occur, caused for example by two-body-decays of low-mass particles, the ambiguity in η and ϕ-assignment will be resolved by matching the muon track candidates with tracks from the inner detector.

Trigger muon detectors

An essential design criterion of the muon system was the capability to trigger on muon tracks. The precision-tracking chambers have therefore been complemented by a system of fast trigger chambers capable of delivering track information within a few tens of nanoseconds after the passage of the particle. Both chamber types deliver signals with a spread of $15 - 25$ ns, thus providing the ability to tag the beam-crossing. The trigger chambers measure both coordinates of the track, one in the bending (η) plane and one in the non-bending (ϕ) plane.

The trigger system covers the pseudorapidity range $|\eta| < 2.4$. Resistive Plate Chambers (RPC) are used in the barrel and Thin Gap Chambers (TGC) in the end-cap regions. Apart from triggering, these detectors serve also for providing bunch-crossing identification, and for measuring the muon coordinate in the direction orthogonal to that determined by the precision-tracking chambers (ϕ-coordinate).

Alignment of muon detectors

The overall performance over the large areas involved, particularly at the highest momenta, depends on the alignment of the muon chambers with respect to each other and with respect to the overall detector. The accuracy of the stand-alone muon momentum measurement (without employing track information from inner detector) necessitates a precision of 30 μm on the relative alignment of chambers both within each projective tower and between consecutive layers in immediately adjacent towers. The accuracy required for the relative positioning of non-adjacent towers to obtain adequate mass resolution for multi-muon final states, lies in the few millimetre range [132].

The stringent requirements on the relative alignment of the muon chamber layers are met by the combination of precision mechanical-assembly techniques and optical alignment systems both within and between muon chambers, as reported in Refs. [174, 175].

3.2.7 The ATLAS trigger and data acquisition system

At nominal LHC running, bunches of protons collide inside ATLAS every 25 ns ($75-50$ ns in 2011 and 50 ns in 2012 data-taking periods). Neither the data acquisition system nor the resources for doing offline analysis are capable of handling such amounts of data. Therefore, a trigger system is required to select only the most interesting events to be written to disk and analyzed further offline. At ATLAS, a three-level trigger system [176] serves this purpose[5]. The level-1 (L1) trigger is implemented in hardware, operating synchronously with the collisions, and uses a subset of detector information to reduce the event rate from 20 MHz to a maximum level-1 output rate of 75 kHz. This is followed by two software-based trigger levels, level-2 (L2) and the event filter (EF), which together reduce the recorded event rate to designed value of $\sim 10^2$ Hz (approximately 300 Hz with an average event size of about 1.3 Mbyte in 2011 data-taking period).

The general scheme of ATLAS trigger system is shown in Fig. 3.16. Level-2 and event filter are usually referred to as high-level trigger (HLT). The L1 trigger is implemented using custom-made electronics, while HLT are almost entirely based on commercially available computers and networking hardware. The L1 uses information from calorimeter and muon trigger chambers only, while the HLT algorithms use the full granularity and precision of calorimeter and muon chamber data, as well as the data from the inner detector, to refine the trigger selections. Better information on energy deposition improves the threshold cuts, while track reconstruction in the Inner Detector significantly enhances the particle identification (for example distinguishing between electrons and photons). The event selection at both L1 and L2 primarily uses inclusive criteria, for example high-E_{T} electrons, muons and jets above defined thresholds.

---

[5] As discussed before, the rare processes of primary interest to ATLAS are in general characterized by large momentum transfer in the hard process, resulting in jets and/or leptons with large transverse momentum (p_{T}), and/or high missing transverse momentum ($E_{\mathrm{T}}^{\mathrm{miss}}$). The majority of p–p collisions exhibit low momentum transfer and, therefore, are discarded by the ATLAS trigger system, keeping only those events which are of high potential interest for further physics analysis. The decays of W/Z-bosons yielding high-p_{T} electrons (muons) and/or high $E_{\mathrm{T}}^{\mathrm{miss}}$are examples of 'interesting' events at ATLAS. The rate of W boson production is approximately 6 orders of magnitude lower than the total collision rate at LHC.

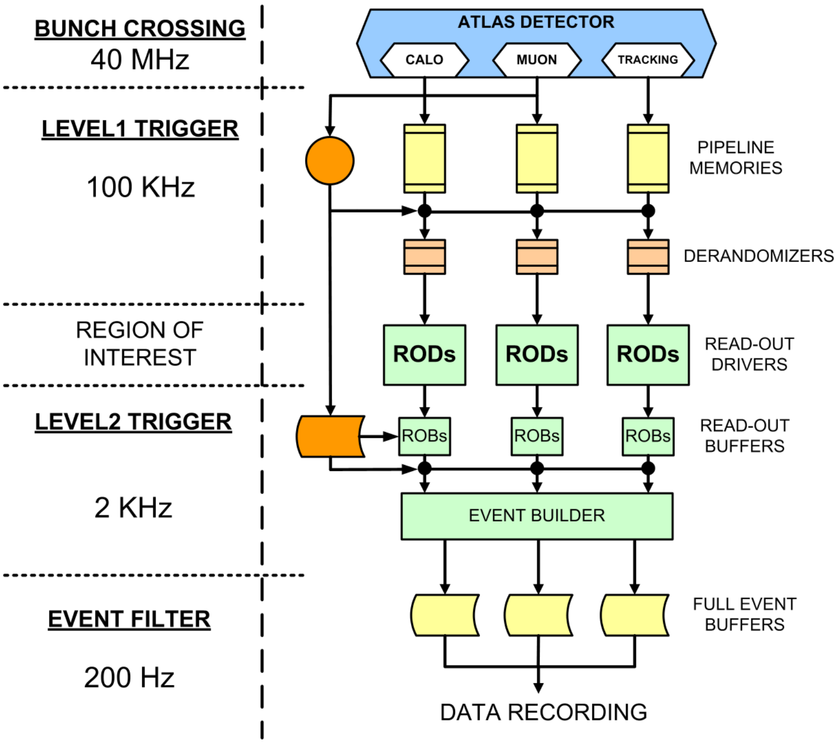

Figure 3.16: ATLAS trigger and data acquisition system.

Level 1 Trigger (L1)

The L1 trigger searches for high transverse-momentum muons, electrons, photons, jets, and τ-leptons decaying into hadrons, as well as large missing and total transverse momentum (see Fig. 3.17). Its selection is based on information from a calorimeter and muon detectors. High transverse-momentum muons are identified using trigger chambers in the barrel and end-cap regions of the spectrometer. Calorimeter selections are based on reduced-granularity information from all the calorimeters. Results from the L1 muon and calorimeter triggers are processed by the central trigger processor, which implements a trigger 'menu' made up of combinations of trigger selections.

In each event, the L1 trigger also defines one or more Regions-of-Interest (RoI), i.e. the geographical coordinates in η and ϕ, of those regions within the detector where its selection process has identified interesting features. The RoI data include information on the type of feature identified and the criteria passed, e.g. a threshold. This information is subsequently used by the high-level trigger.

High-level trigger (HLT)

The L2 selection is seeded by the RoI information provided by the L1 trigger over a dedicated data path. L2 selections use, at full granularity and precision, all the available detector data within the RoI's. The L2 menus are designed to reduce the trigger rate to approximately 3.5 kHz, with an event processing time of about 40 ms, averaged over all events. The final stage of the event selection is carried out by the event filter,

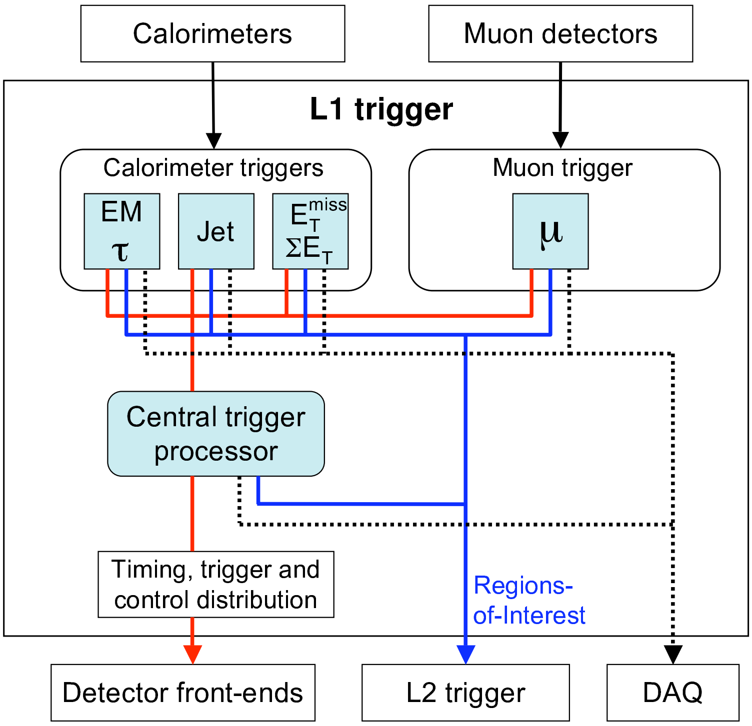

Figure 3.17: Block diagram of the L1 trigger. The overall L1 accept decision is made by the central trigger processor, taking input from calorimeter and muon trigger results. The paths to the detector front-ends, L2 trigger, and data acquisition system are shown from left to right in red, blue and black, respectively. Figure from [132].

which reduces the event rate to roughly $\sim 10^2$ Hz. Its selections are implemented using offline analysis procedures within an average event processing time of the order of few seconds [132].

Trigger menus and data streams

Data for events selected by the trigger system are written to inclusive data streams based on the trigger type. There are four primary physics streams, Egamma (electrons and photons), Muons, JetTauEtmiss (jets, b-jets, τ-leptons, and high missing transverse momentum), MinBias (strong interactions with small transverse momentum transfer), plus several additional calibration streams. Some overlap exists between streams, for example, the highest overlap is observed between Egamma and JetTauEtmiss streams – up to 15% [177]. The highest rates of recorded events are in the JetTauEtmiss, Egamma and Muons streams.

The trigger system is configured via a trigger menu which defines trigger chains – a set of selection criteria that start from a L1 trigger and specify a sequence of reconstruction and selection steps for the specific trigger signatures required in the trigger chain. A trigger chain is often referred to simply as a trigger. Some triggers are prescaled – that is, only some fraction of events fired by the trigger are eventually recorded to permanent data storages. For example, most of triggers in MinBias streams are prescaled. The trigger

Trigger	Name	p_{T} threshold [GeV] L1	 HLT	Rate [Hz]	Bandwidth [Hz]
Egamma					**55**
single electron	e20	14	20	20	
di-electron		7	12	0.5	
electron+muon		$5(e)$, $4(\mu)$	$10(e)$, $6(\mu)$	3.5	
single photon		14	80	1	
di-photon		14	20	1.5	
Muons					**45**
single muon	mu20	10	20	25	
di-muon		4	10	3	
JetTauEtmiss					**85**
jet+$E_{\mathrm{T}}^{\mathrm{miss}}$		50(jet), 20($E_{\mathrm{T}}^{\mathrm{miss}}$)	75(jet), 45($E_{\mathrm{T}}^{\mathrm{miss}}$)	15	
single jet		75	250	3	
single tau		30	100	4	
di-tau		11	29	4	
tau+electron		$6(\tau)$, $10(e)$	$16(\tau)$, $15(e)$	3	
tau+muon		$6(\tau)$, $4(\mu)$	$16(\tau)$, $15(\mu)$	5	
MinBias					**10**
Exotics					**10**
Calibration					**10**

Table 3.3: The approximate bandwidth allocation for different data streams in 2011 data-taking period [177]. Some of the most important unprescaled trigger menus are shown together with the corresponding mean rate of recorded events.

menus are given in Table 3.3. Single electron and muon triggers are the most relevant for the analysis presented in this thesis.

Readout drivers and data acquisition system

The data are recorded to permanent storages as follows. After an event is accepted by the L1 trigger, the data from the pipe-lines are transferred off the detector to the readout drivers (ROD's). Digitised signals are formatted as RAW data prior to being transferred to the data-acquisition (DAQ) system. The first stage of the DAQ, the readout system, receives and temporarily stores the data in local buffers. It is subsequently solicited by the L2 trigger for the event data associated to RoI's. Those events selected by the L2 trigger are then transferred to the event-building system and subsequently to the event filter for final selection. Events selected by the event filter are moved to permanent storage at the CERN computing center and another (so-called Tier-1) center in the worldwide computing GRID (WLCG). There are 10 Tier-1 centers total.

4

Data analysis

This chapter presents the details of the electron-jet data analysis. It is structured as follows: first, in Section 4.1, we discuss the simulation of signal and background precesses. Then, in Section 4.2, we describe the data set which was used for the analysis. The event selection procedure is described in Section 4.3. The determination of background contamination in the signal region is described in Section 4.4. Finally, the summary of all systematic uncertainties and methods for their determination are given in Section 4.5. The final results and conclusions are summed up in the two subsequent chapters.

4.1 Signal and background simulation

Simulated data samples are used to estimate the signal acceptance and efficiency, to optimize the signal selection criteria and to cross-check our understanding of the backgrounds. The final background estimate is determined from the data as described in Section 4.4.

The signal Monte Carlo (MC) samples of WH production with Higgs boson decaying to electron-jets are generated with MadGraph [178] to simulate the Higgs boson production and decay to the hidden sector, and BRIDGE [179] to simulate the hidden-sector cascades resulting in electron-jets. The output of these two programs is then interfaced to PYTHIA [180] for subsequent hadronization and modelling of the underlying event (UE). All leptonic decays modes of the W boson ($e\nu_e, \mu\nu_\mu, \tau\nu_\tau$) are included in the signal samples.

The most important sources of background are SM W/Z+jets and $t\bar{t}$ processes. A less important source of background comes from pair production of bosons, $WW/ZZ/WZ$, hereafter referred to as diboson production. These processes result in a lepton + jets event topology. In addition, multi-jet events in some instances can be misidentified as W-bosons.

Samples of simulated $W(\rightarrow \ell\nu)$+jets and $Z(\rightarrow \ell\ell)$+jets events ($\ell = e/\mu/\tau$) are generated using ALPGEN [181] with the MLM matching scheme [182] and interfaced to HERWIG [183] for parton shower and fragmentation processes and to JIMMY [184] for underlying event simulation. Simulated samples for $t\bar{t}$ processes are generated with MC@NLO [185] interfaced to HERWIG for parton showering. To study the possible dependence on the specific choice of MC generator, alternate W/Z+jets samples are also generated using SHERPA [186] with an UE modelling according to Ref. [187], and alternate top-quark production samples are generated with POWHEG [188] interfaced to PYTHIA for hadronization. The diboson processes are generated with HERWIG. Taus are decayed with TAUOLA [189] in both signal and background samples.

The event yields for $W \rightarrow \ell\nu$, $Z \rightarrow \ell\ell$ ($ell = e/\mu$) and $t\bar{t}$ processes, which give the largest contribution to background, are scaled using the measured production cross sections [190, 191]. The contributions from $W(\rightarrow \tau\nu)$ and $Z(\rightarrow \tau\tau)$, which are minor sources of background, are obtained using next-to-next-to-leading-order cross-section calculations [192]. The multi-jet background is obtained using normalized data templates [190], since the rate with which multi-jet events mimic the combined signature of a prompt charged lepton accompanied by missing transverse momentum is difficult to simulate accurately (see Section 4.4.1).

The GEANT4 toolkit [193] is used for a detailed simulation of the detector response [194]. The effect of multiple pp interactions per bunch crossing (pile-up) is modelled by overlaying simulated inelastic proton–proton collisions over the original hard-scattering event. The simulated events are then passed through the same reconstruction and analysis chain as the data. All simulated processes used in the analysis are summarized in Tables 4.2 and 4.1.

4.1.1 Simulation of signal process

The kinematic distributions for simulated signal processes are given in Figs.4.1 and 4.2. As seen in Fig. 4.1, the sought signal features a high multiplicity ($\gtrsim$4) of electrons in electron-jet (a), and soft p_{T} of electrons (c). Moreover, electron pairs in the electron-jets are highly collimated (see Fig. 4.2). As seen in Fig. 4.1 (a and b) the number of electrons, reconstructed by the standard algorithms [195] in the ATLAS detector, is only half as large as the number of truth electrons in signal process[1]. Furthermore, from Fig.4.2(c) it is seen that there are no reconstructed electron pairs, having cone separation between electrons as small as $\Delta R \lesssim 0.02$. The standard electron reconstruction procedure is based on clusters reconstructed in the electromagnetic calorimeter, which then are associated to tracks of charged particles reconstructed in the Inner Detector [195]. A typical resolution of electromagnetic calorimeter in the middle layer is 0.025×0.025 in the η–ϕ plane [195]. Therefore, it is impossible to reconstruct two highly-collimated electrons using the standard ATLAS algorithms. However, as can be seen from Fig. 4.3,

---

[1] See Section 4.3.1 for the description of the standard ATLAS electron reconstruction algorithm.

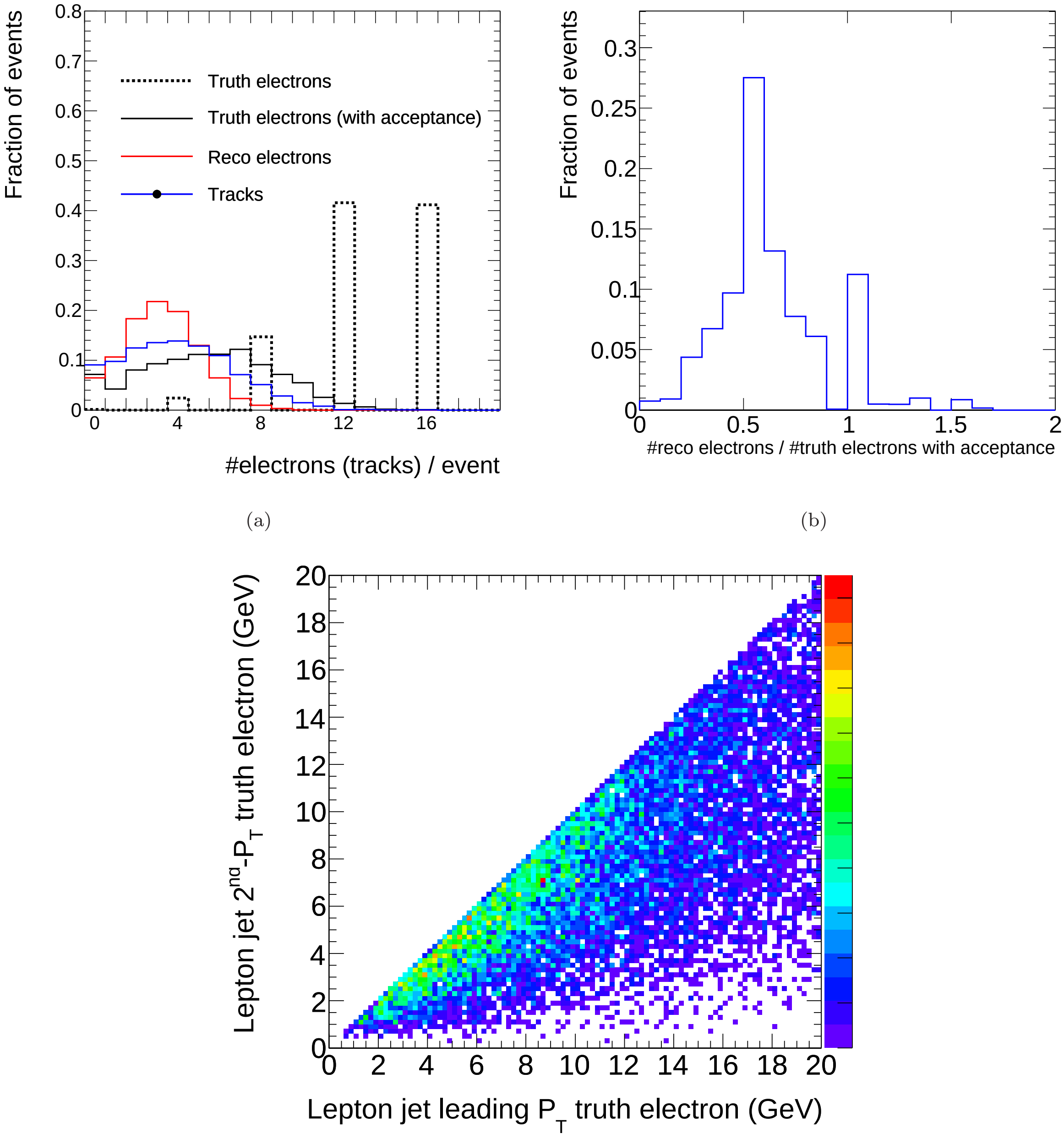

(a)

(b)

(c)

Figure 4.1: Number of electrons (tracks) per event in simulated signal process (a); fraction of truth electrons reconstructed by standard electron algorithm (b); transverse momenta of two leading-p_T truth electrons in the electron-jet (c). “Truth” stands for electrons coming from a hidden sector cascade (i.e. $W \to e\nu$ electrons are not taken into account), while “reco” – denotes electrons reconstructed using standard algorithm [195]. Electrons, corresponding to each point in (c) are checked on a truth level to have originated from one electron-jet (from the same $h_{d,1}$ particle). Reco electrons, tracks and “truth electrons with acceptance” are required to pass kinematic acceptance cuts of $|\eta| < 2.0$, $p_T > 5$ GeV, and distance from $W \to l\nu$ lepton $\Delta R > 0.6$. Plots are for 3-step $m_{\gamma_d} = 100$ Mev signal model.

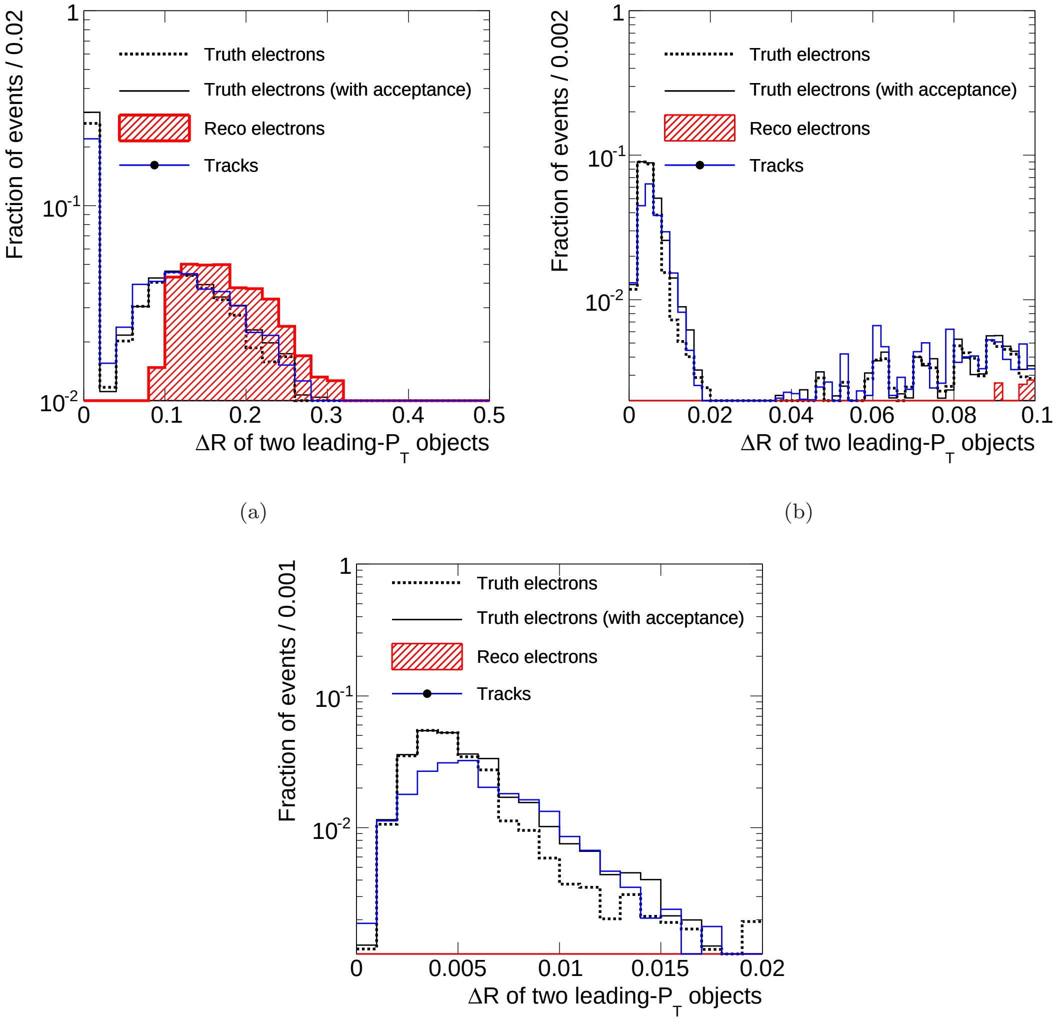

(a) (b)

(c)

Figure 4.2: Cone separation between two leading-p_T electrons in event in simulated signal process. “Truth” stands for electrons coming from a hidden sector cascade (i.e. $W \to e\nu$ electrons are not taken into account), while “reco” – denotes electrons reconstructed using standard algorithm [195]. Reco electrons, tracks and “truth electrons with acceptance” are required to pass kinematic acceptance cuts of $|\eta| < 2.0$, $p_T > 5$ GeV, and distance from $W \to l\nu$ lepton $\Delta R > 0.6$. Plots are for 3-step $m_{\gamma_d} = 100$ Mev signal model. Zoom is shown into three regions of interest: (a) $\Delta R = 0.0 - 0.5$, (b) $\Delta R = 0.0 - 0.1$, (c) $\Delta R = 0.0 - 0.02$.

Process	MC generator	Int. lumi. (fb^{-1})	$\sigma \times BR$ (pb)
$W \to e\nu$ + jets	ALPGEN + JIMMY ($\mathrm{N_{jet}} = 0, 1, ..., 5$)	0.4, 1.6, 8.5, 8.5, 8.5, 8.3	10207
	SHERPA	0.1	10207
$W \to \mu\nu$ + jets	ALPGEN + JIMMY ($\mathrm{N_{jet}} = 0, 1, ..., 5$)	0.4, 1.6, 8.5, 8.3, 8.4, 8,5	10207
	SHERPA	0.1	10207
$W \to \tau\nu$ + jets	ALPGEN + JIMMY ($\mathrm{N_{jet}} = 0, 1, ..., 5$)	0.4, 1.4, 8.3, 8.3, 8.1, 7.5	10460
$Z \to ee$ + jets	ALPGEN + JIMMY ($\mathrm{N_{jet}} = 0, 1, ..., 5$)	9.0, 9.0, 8.8, 8.9, 9.4, 9.8	945
	SHEPRA	1.1	945
$Z \to \mu\mu$ + jets	ALPGEN + JIMMY ($\mathrm{N_{jet}} = 0, 1, ..., 5$)	9.0, 9.0, 8.9, 8.9, 9.4, 10.1	945
$Z \to \tau\tau$ + jets	ALPGEN + JIMMY ($\mathrm{N_{jet}} = 0, 1, ..., 5$)	8.7, 8.9, 9.0 8.9, 9.7, 12.0	945
$W + b\bar{b}$ + jets	ALPGEN + JIMMY ($\mathrm{N_{jet}} = 0, 1, 2, 3$)	10.0, 5.2, 10.1, 10.6	107
$Z \to ee + b\bar{b}$ + jets	ALPGEN + JIMMY ($\mathrm{N_{jet}} = 0, 1, 2, 3$)	22.8, 32.2, 44.0, 25.5	10.3
$Z \to \mu\mu + b\bar{b}$ + jets	ALPGEN + JIMMY ($\mathrm{N_{jet}} = 0, 1, 2, 3$)	22.8, 40.2, 45.1	10.3
$W + \gamma$ + jets	ALPGEN + JIMMY ($\mathrm{N_{jet}} = 0, 1, ..., 5$)	6.8, 10.1, 10.2 49.0, 50.1, 59.0	289
$Z \to \mu\mu + \gamma$ + jets	SHERPA	25.9	15.4
$Z \to ee + \gamma$ + jets		25.9	15.4
$t\bar{t}$	MC@NLO + JIMMY	117.3	97.2
	POWHEG + PYTHIA	30.8	97.2
WW	HERWIG	49.9	45
WZ		13.5	18.5
ZZ		41.6	6.0

Table 4.1: Simulated background processes.

one can make use of electron-tracks for identifying electrons (even highly collimated) with high probability, as discussed in Section 4.3.2.

Comparison of kinematic distributions in 3-step and 2-step signal models (see Section 2.3) is shown in Fig. 4.5. As seen in the figure, since there are no invisible decays in hidden sector in 2-step model, there are always 2 electron-jets (b), and the number of electrons always equals eight in this model (a). Characteristic cone separation of particles in electron-jet can be seen in Fig. 4.5(c).

According to the analysis in Ref. [70] the sought signal should not produce too much missing transverse momentum, i.e $\mathrm{E_T}^{\mathrm{miss}} \lesssim 50$ GeV. This scenario is less constrained, taking into account the results of OPAL searches for a Higgs boson decaying to invisible

Process	MC generator	Int. lumi. (fb^{-1})	$\sigma \times BR$ (pb)
3-step signal processes, $m_{\gamma_d} = 100 MeV$			
WH, m_H=100 GeV	MadGraph + BRIDGE	25.6	0.390
WH, m_H=125 GeV	+ PYTHIA	53.6	0.187
WH, m_H=140 GeV		77.3	0.129
3-step signal processes, $m_{\gamma_d} = 200 MeV$			
WH, m_H=100 GeV	MadGraph + BRIDGE	25.6	0.390
WH, m_H=125 GeV	+ PYTHIA	53.6	0.187
WH, m_H=140 GeV		77.3	0.129
2-step signal processes, $m_{\gamma_d} = 100 MeV$			
WH, m_H=100 GeV	MadGraph + BRIDGE	25.6	0.390
WH, m_H=125 GeV	+ PYTHIA	53.6	0.187
WH, m_H=140 GeV		77.3	0.129
2-step signal processes, $m_{\gamma_d} = 200 MeV$			
WH, m_H=100 GeV	MadGraph + BRIDGE	25.6	0.390
WH, m_H=125 GeV	+ PYTHIA	53.6	0.187
WH, m_H=140 GeV		77.3	0.129

Table 4.2: Simulated signal processes.

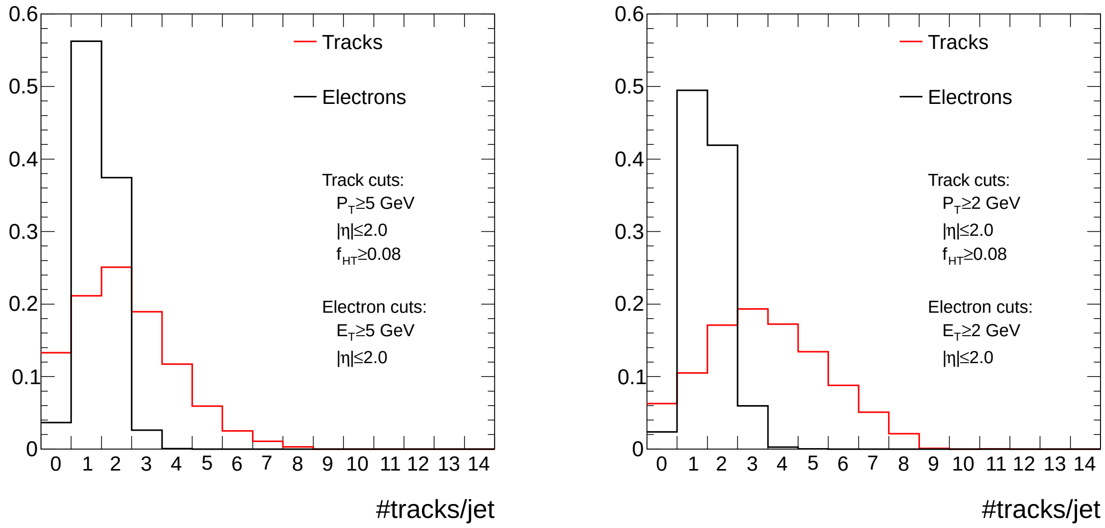

(a) (b)

Figure 4.3: Number of tracks and reconstructed electrons in jets in simulated signal MC samples. Jets and tracks are required to fulfil selection criteria described in Section 4.3.2 (left). In the figure (right) tracks (electrons) p_{T} cut is relaxed to 2 GeV. Electrons are reconstructed using standard cluster-based algorithm [195], and are required to fulfil the same kinematic cuts as the tracks.

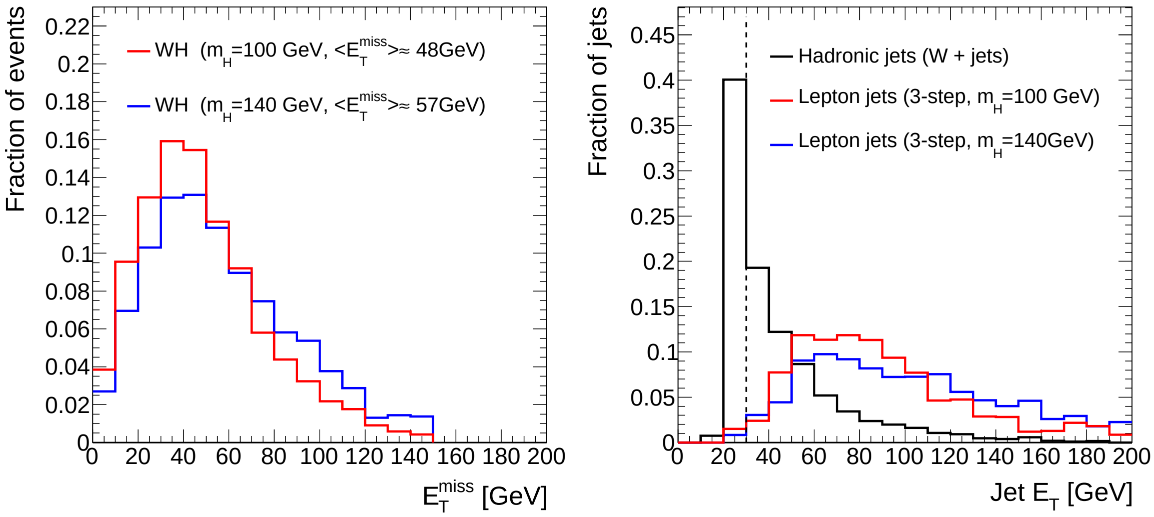

Figure 4.4: Reconstructed missing transverse momentum in simulated signal samples (left); transverse momentum of reconstructed jets in simulated signal and background (W+jets) samples (right); dashed line indicates the the cut on jet transverse momentum, used in Section 4.3.2

energy [196]. In the 3-step signal model, the amount of decays to invisible particles in the hidden sector is chosen to fulfil the aforementioned $\mathrm{E_T}^{\mathrm{miss}}$ requirement. Namely, the branching fraction of $h_{\mathrm{d},2}$ decays to stable (invisible) scalars n is set to 20%, while remaining 80% correspond to branching fraction of $h_{\mathrm{d},2}$ decaying to dark-photon γ_d pairs. This produces the required amount of missing transverse momentum (see Fig. 4.4). At the same time in the 2-step model there is no missing transverse momentum produced in the hidden sector, i.e. the branching fraction of $h_{\mathrm{d},2}$ decaying to invisible scalars n is zero. We should emphasize that the presence of missing transverse momentum in the hidden sector only marginally affects the sensitivity of the analysis to the hypothetical signal, which can be seen by comparing signal efficiencies for 2-step and 3-step models as the $W \to \ell\nu$ selection is applied. The efficiencies are given in Tables 4.4 and 4.5.

4.1.2 Electron and muon energy (momentum) calibration

To calibrate the electron energy and to match the resolution of the electron energy and muon momentum observed in data, corrections are applied to electrons in data and electrons and muons in simulated MC samples according to the prescriptions of Refs. [195, 197].

Corrections were obtained by comparing the predicted shapes of $Z \to ee$ ($Z \to \mu\mu$) dielectron (dimuon) invariant mass distributions with those observed in the data, and were derived using 40 fb^{-1}of data collected by ATLAS detector in 2010 [195, 197]. There are two types of corrections:

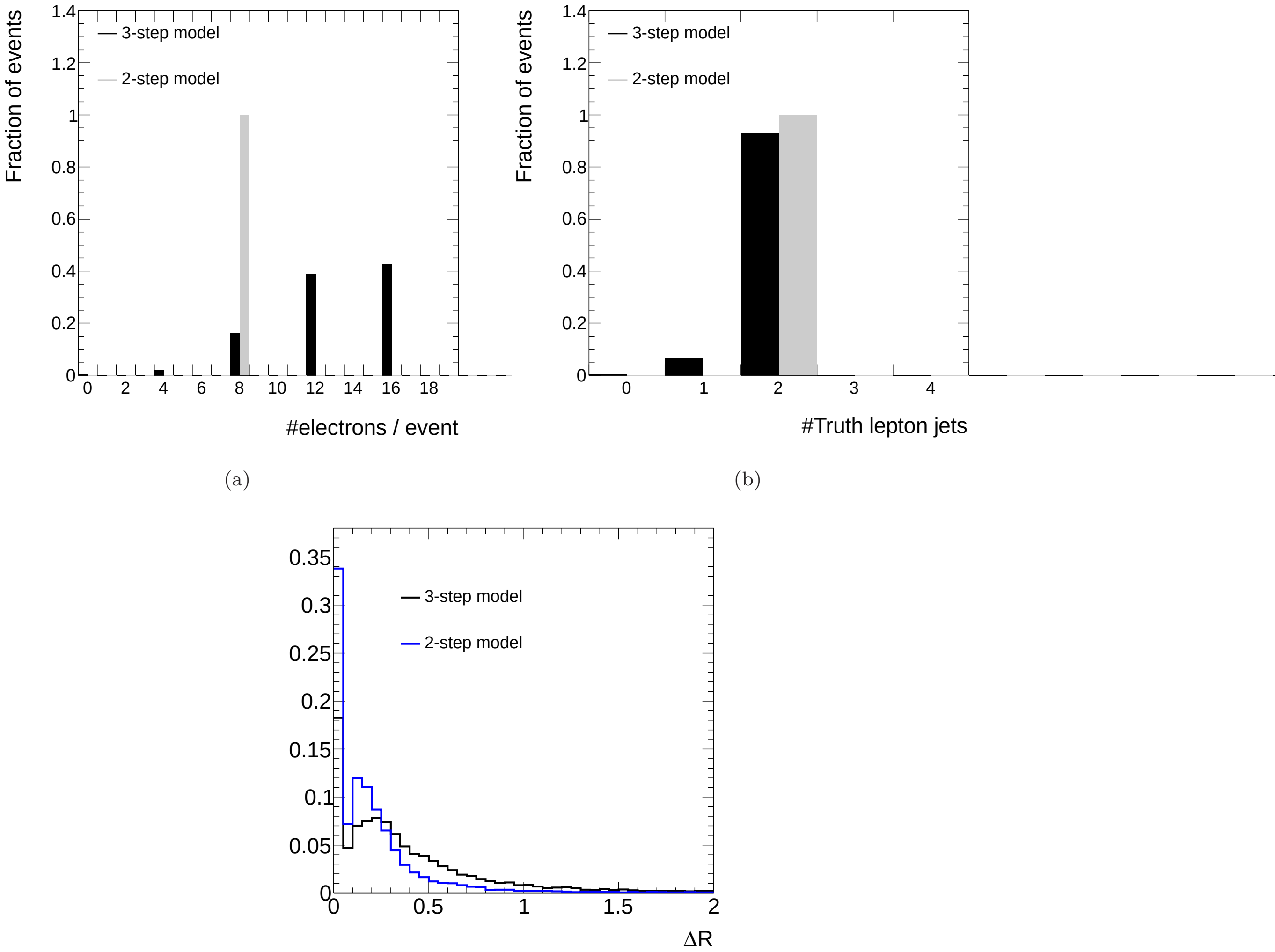

(a) (b)

(c)

Figure 4.5: Comparison of 3-step and 2-step models of the signal processes: number of truth electrons that originate from a Higgs decay (a); number of truth lepton jets in event (b); cone separation between leading-p_T electron and all other electrons in a truth lepton jet. In case of 3-step model we call "truth lepton jet" a set of electrons originating from one $h_{d,1}$ particle, while in case of 2-step model electrons in electron-jet are required to having originated from one $h_{d,2}$ particle. The plots are for $m_{\gamma_d} = 100$ MeV.

- **Energy (momentum) scale corrections**. The truth and measured electron energy are expressed through each other via the energy correction factor α_i

  $$E^{\text{meas}} = E^{\text{truth}}(1 + \alpha_i) \tag{4.1}$$

  where i denotes the electron η and $\mathrm{E_T}$ region considered for the energy calibration. The α correction factors were determined by fitting the $Z \to ee$ mass peak, more precisely by minimizing the negative unbinned log-likelihood [165]:

  $$-\ln L_{\text{tot}} = \sum_{i,j} \sum_{k=1}^{N_{i,j}^{\text{events}}} -\ln L_{i,j}\left(\frac{m_k}{1+\frac{\alpha_i+\alpha_j}{2}}\right) \tag{4.2}$$

  where one of the electrons from $Z \to ee$ decay is in region i and other is in region j, $N_{i,j}^{\text{events}}$ is the total number of selected $Z \to ee$ decays in the data with electrons in regions i and j, m_k is the measured dielectron mass in the given decay, and $L_{i,j}(m)$ is the probability density function (pdf) quantifying the compatibility of event with the Z lineshape. This pdf was obtained using PYTHIA MC simulation of $Z \to ee$ processes and was smoothed to get continuous distribution. The electron-energy correction factors were derived with this procedure for different values of electron pseudorapidity η, and were found to be within 2% [195]. Following the usual scheme, we use these correction factors to scale the reconstructed electron energy in the data.

  For muons, the accuracy of momentum scale was probed by measuring the average deviation of the measured dimuon invariant mass from the Z mass world average ($\mathrm{M}(Z) = 91.1876$ GeV [68]). A good agreement of measured mass with the world average is indicative of a plausible modelling of muon momentum scale, and therefore no corrections need to be applied to muon momentum [197].

- **Energy (momentum) resolution corrections**. The electron energy resolution can be parametrized as

  $$\frac{\sigma(E)}{E} = \frac{a}{\sqrt{E}} \oplus \frac{b}{E} \oplus c \tag{4.3}$$

  Here a, b and c are η-dependent parameters: a is the sampling term, b is the noise term and c is the constant term [165].

  The muon momentum is determined using information form both the MS and ID subdetectors. The relative resolution on the momentum measurement, $\sigma(p)/p$, is dictated by different effects related to the amount of material that the muon traverses, the spatial resolution of the individual track points and the degree of internal alignment of the two subsystems [165]. The corresponding momentum resolution can be parametrized as

  $$\begin{aligned} \frac{\sigma^{\text{MS}}(p)}{p} &= \frac{p_0^{\text{MS}}}{p_{\text{T}}} \oplus p_1^{\text{MS}} \oplus p_2^{\text{MS}} \cdot p_{\text{T}} \\ \frac{\sigma^{\text{ID}}(p)}{p} &= p_1^{\text{ID}} \oplus p_2^{\text{ID}} \cdot p_{\text{T}} \end{aligned} \tag{4.4}$$

where p_0^{MS}, p_1^{MS} and p_2^{MS} are coefficients related to the energy loss in the calorimeters material, multiple scattering and intrinsic resolution terms, respectively; p_1^{ID} and p_2^{ID} are the multiple scattering and intrinsic resolution terms, respectively.

The examined quantity, sensitive to energy (momentum) resolution, is the width of Z mass peak (also J/Ψ resonance is used to calibrate the energy(momentum) resolution for low-p_{T} leptons). For electrons, the resolutions are derived from fits to the invariant $Z \to ee$ mass distributions using a Breit-Wigner convolved with a Crystal Ball function in the mass range 80 - 100 GeV (75 - 105 GeV – depending on pseudorapidity region). The Breit-Wigner width is fixed to the measured Z width [198], and the experimental resolution is described by the Crystal Ball function. Studies in Ref. [195] have shown that the measured Gaussian components of the experimental resolution are always slightly worse than those predicted by MC. For muons, the $Z \to \mu\mu$ invariant mass distributions were obtained separately for momentum, measured in ID and MS, and were then fitted using a convolution of the Z lineshape and two Gaussian functions modelling the resolution effects in these two sub-detectors [197]. An overall discrepancy between simulated and measured resolution was observed in all detector regions. It is partly understood as a result of the limited accuracy with which the calibration and alignment constants were known prior to the first pass reconstruction. For the MS also the material distribution and magnetic field description can, if inaccurate, contribute to a coarser resolution at low momenta.

The actual resolution parameters were measured and the correction parameters were provided for the simulated electron $\mathrm{E_T}$ and muon p_{T} to reproduce the data [195, 197]. In our analysis, electron energy (muon momentum) in simulated signal and background samples were smeared using these correction parameters.

4.1.3 Details of pile-up simulation

In order to correctly reproduce the effect of multiple pp interactions (pile-up) the events in Monte Carlo are re-weighted such the number of primary vertices in Monte Carlo agrees with the data (see Fig. 4.6). This is done according to official ATLAS pile-up re-weighting procedure, using official ATLAS algorithms [199]. The two possible options for pile-up re-weighting are offered in [199]. The difference between these two are in the way one gets the "μ distribution" for the data (μ is a measure of how many proton-proton collisions are expected on average per event). Let's outline these options here:

- First method uses the $\mu|_{LB,BCID}$ value averaged across all bunch crossing IDs (BCIDs) in the luminosity block (LB).
- Second method uses the distribution of the per BCID, $\mu|_{LB}$(BCID) (averaged across the LB).

In our analysis we use the first option. The pile-up systematic uncertainty was estimated by comparing the event yields obtained with two aforementioned methods of pile-up re-weighting and was found negligible.

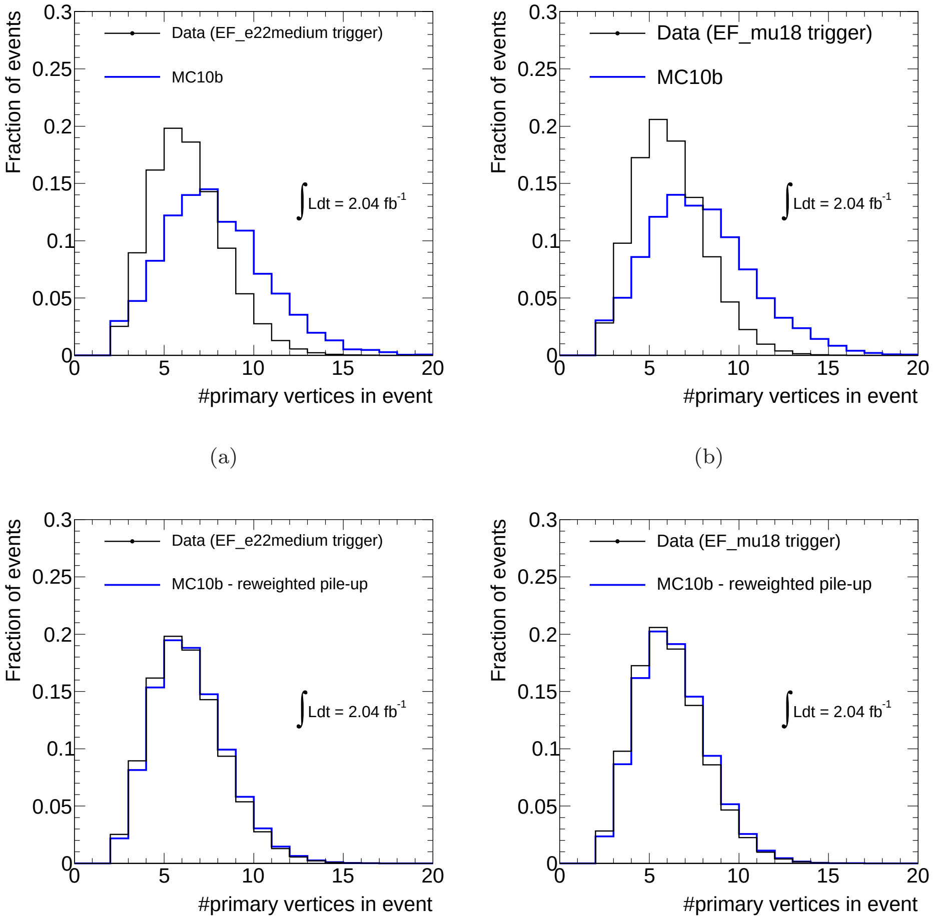

(a)

(b)

(c)

(d)

Figure 4.6: Number of primary vertices in data (black histograms) and simulated MC samples (blue histograms). Simulated samples in the the bottom figures are taken after pile-up re-weighting.

4.2 Data samples and trigger selection

The data sample for this analysis was collected by the ATLAS detector in proton–proton collisions at a centre-of-mass energy of 7 TeV in early 2011. The data sample used was required to be recorded during LHC stable-beam conditions when the ATLAS detector components relevant to this analysis were operating within nominal parameters. The total integrated luminosity of the selected data sample is 2.04 fb^{-1} with a 3.7% uncertainty [200, 201].

For the $W \to e\nu$ channel, at least one reconstructed electron trigger object with transverse energy above 22 GeV in the region of $|\eta| \leq 2.5$ is required. For the $W \to \mu\nu$ channel, a muon candidate trigger object in the region of $|\eta| \leq 2.4$ having transverse momentum above 18 GeV, reconstructed in both the inner detector and muon spectrometer, is required. The muon trigger object must be consistent with having originated from the interaction region.

4.3 Event Selection

Signal events are required to have exactly one reconstructed W boson candidate in the $e\nu$ or $\mu\nu$ decay channel and at least two jets identified as electron-jets.

4.3.1 W boson selection

A W-decay electron candidate is required to pass the tight electron selection criteria [190, 195] with $p_{\mathrm{T}} > 25$ GeV and $|\eta| \leq 2.47$. Electrons in the transition region between the barrel and endcap calorimeters ($1.37 < |\eta| < 1.52$) are rejected. A W-decay muon candidate is required to be identified in both the ID and the MS subsystems and to have $p_{\mathrm{T}} > 20$ GeV and $|\eta| < 2.4$.

To reduce background from multi-jet events, electron and muon candidates are required to satisfy an isolation criterion: the sum of the p_{T} of all tracks in a cone of $\Delta R = 0.4$ around the electron (muon) divided by the electron (muon) p_{T} is required to be less than 0.3 (0.2).

W boson candidates are required to have missing transverse momentum $E_{\mathrm{T}}^{\mathrm{miss}} \geq 25$ GeV and exactly one isolated electron or muon. Events with two or more isolated same-flavour leptons are rejected, substantially reducing the background from Drell–Yan production.

The lepton candidate from the W boson decay is required to match the object that satisfies the trigger selection criteria: the distance between the trigger object and the reconstructed $W \to \ell\nu$ ($\ell = e/\mu$) lepton (transverse impact parameter) is required to be $\Delta R < 0.1$.

To reduce the background from cosmic rays, heavy-flavour production and photon conversions, the W candidate is required to originate from the primary vertex. In events with multiple vertices along the beam axis, the vertex with the largest $\sum p_{\mathrm{T}}^2$, where the sum is over all tracks associated with the vertex, is taken to be the primary vertex of the event. The longitudinal and transverse impact parameters of the charged-lepton track with respect to the primary vertex must be less than 10 mm and 0.1 mm, respectively.

Finally, if an event meets the requirements both for the $W \to e\nu$ and the $W \to \mu\nu$ channels simultaneously, the event is considered to belong to the $W \to \mu\nu$ channel, due to lower potential backgrounds.

Good agreement is observed in W-related distributions between data and MC simulation, as can be seen from Fig. 4.7. Here the distribution of $W \to \ell\nu$ candidate transverse is shown, where transverse mass is defined as follows[2]

$$m_{\mathrm{T}}^2 = 2E_{\mathrm{T}}^l E_{\mathrm{T}}^\nu - 2\boldsymbol{p}_{\mathrm{T}}^l \boldsymbol{p}_{\mathrm{T}}^\nu \tag{4.5}$$

The discrepancy at low m_{T} in $W \to e\nu$ channel is due to the large uncertainty on the shape of m_{T} distribution in the multi-jet data template, and also due to fact that the

---

[2] Transverse mass equals normal mass in case if W-decay products have zero longitudinal momenta

template was scaled to data in the range $m_{\mathrm{T}} > 40$ GeV where its contribution is largest (see Section 4.4.1). The uncertainties in Fig 4.7 include the variation due to choice of MC generator, luminosity and cross-section uncertainties, the variation due to choice of multi-jet background template, and the uncertainties due to electron (muon) energy scale and resolution corrections (for details, see Section 4.5). In this chapter, the same set of uncertainties is assumed also in other figures, in which data is compared to MC simulation, unless otherwise stated.

Details of electron selection

In the electron channel, events were selected online using the trigger EF_e22_medium that required the presence of at least one reconstructed electron with transverse energy above 22 GeV in the region of $\eta \leq 2.5$. In the offline analysis, the electrons are reconstructed using the standard ATLAS electron reconstruction procedure [169]. It is based on clusters reconstructed in the electromagnetic calorimeter, which then are associated to tracks of charged particles reconstructed in the Inner Detector.

Electron reconstruction begins with the creation of a preliminary set of seed clusters. Seed clusters with energies above 2.5 GeV are formed by a sliding window algorithm, where the seed clusters are 3×5 in η/ϕ middle layer cell units (0.25×0.25). After an energy comparison, duplicate clusters are removed from nearby seed clusters. In the η-region relevant to the studies in the thesis ($|\eta| < 2.5$), an electron is defined by the existence of one or more reconstructed tracks matched to a seed cluster. Reconstructed tracks are matched to seed clusters by extrapolating them from their last measurement point to the second (middle) layer of the calorimeter. If the ΔR-difference between track and cluster is below a certain threshold then the track is considered matched to the cluster. Special care is taken in order to account for Bremsstrahlung losses. Namely, the sign-corrected threshold on the $\Delta\phi$ difference between track and cluster is larger on the side where the extrapolated track bends as it traverses the tracker magnetic field.

Next, there is an inherent ambiguity between a prompt electron (like those from W-decay) and a photon converted to an electron-positron pair (conversion photon), since both objects are characterized by the existence of tracks pointing to an electromagnetic cluster. Conversions arise from the interaction of photons with the material of the detector. At photon energies above 1 GeV, the interaction of photons with the tracker and supporting material is completely dominated by e^+e^- pair production, while all other processes, such as Compton or Rayleigh scattering, are negligible. At the electron-reconstruction stage, almost all converted photons will be treated as electrons, which results in a significant contamination of the electron sample by converted photons. Photon conversions are removed at the next step of electron identification, as described below.

Electrons were required to have $E_T > 25$ GeV and $\eta \leq 2.47$; electrons in the transition region between the barrel and end-cap calorimeter ($1.37 < \eta < 1.52$) were rejected. Next, electrons were required to pass the standard ATLAS "tight" electron selection criteria [169]. This implies a set of cuts on the ratio of electron $\mathrm{E_T}$ in the hadronic calorimeter to $\mathrm{E_T}$ of the EM cluster (hadronic leakage), ratio of the energy in 3×5 cells over the energy in 7×7 cells centred at the electron cluster position, lateral EM shower

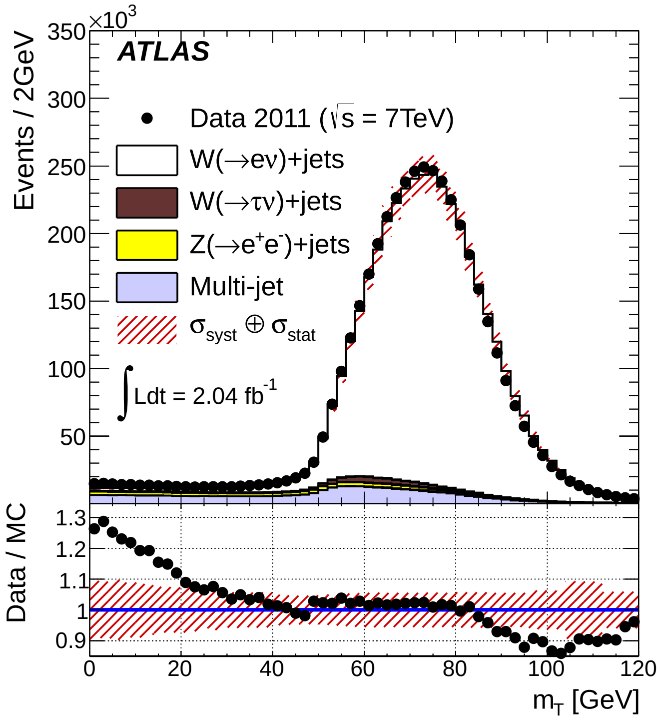

(a)

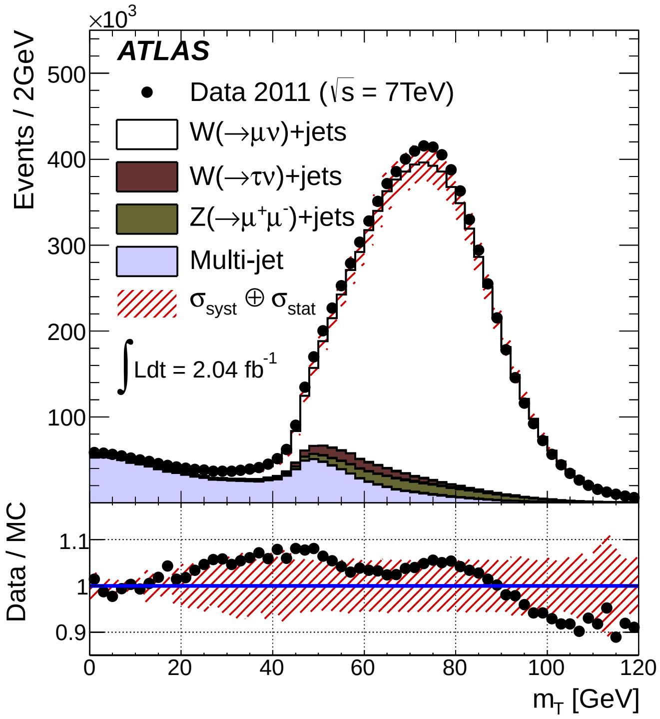

(b)

Figure 4.7: Transverse mass of W boson candidates in $W \to e\nu$ (top) and $W \to \mu\nu$ (bottom) decay channels. Data are shown by dots with error bars and are compared to the expectation from SM processes, given by stacked histograms of different colors. The hatched bands represent the quadratic sum of statistical and systematic uncertainties of the SM background prediction described in Section 4.5.

width, number of hits in Pixel and SCT detectors, cone separation ΔR between track and EM cluster, total number of TRT hits and fraction of high-threshold TRT hits to the total number of hits in TRT; to avoid conversion photons, electrons are required to have at least on hit in the innermost layer of Pixel detector (b-layer), also electrons that are explicitly matched to the conversion photons are rejected [202].

To reject background multi-jet events, faking W-decay signature, the electron isolation criteria with respect to inner detector tracks is applied. The sum of transverse momenta of tracks in the cone of $R = 0.4$ around electron track divided by the total electron transverse energy is required to be

$$\sum_{\Delta R \leq 0.4} \frac{p_{\mathrm{T}}^{\mathrm{ID}}}{\mathrm{E_T}^{e}} \leq 0.3. \tag{4.6}$$

Tracks, used to calculate the isolation, are required to have $p_T > 1$ GeV. There are no quality cuts applied to these tracks, in particular, tracks from photon conversions are not rejected. Photon conversions are discarded in the standard ATLAS evaluation of electron isolation. The electron isolation obtained in this way would result in the high probability of misidentifying electron-jet as a W boson. To avoid this, a custom-made electron isolation is used in the analysis.

Details of muon selection

In the muon channel, events were selected online using the trigger EF_mu18 or EF_mu18_medium – depending on the data collection periods, that required the presence of a muon candidate reconstructed in the muon spectrometer consistent with having originated from the interaction region. The STACO algorithm [203] has been used for muon reconstruction, requiring muons to be identified in both ID and MS subsystems. This algorithm exploits the statistical combination of two independent measurements of muon momenta (in ID and MS) by means of their covariance matrices. Namely, if P_1 and P_2 are parameter vectors of muon track in ID and MS, respectively, then the parameter vector of combined track, P, is obtained by minimizing the following chi-squared distribution

$$\chi^2 = (P - P_1)^T C_1^{-1} (P - P_1) + (P - P_2)^T C_2^{-1} (P - P_2) \tag{4.7}$$

where C_1 and C_2 are the covariance matrices of track parameters in ID and MS, respectively. These matrices characterize the degree of correlation between different track parameters [204]. Initially, the track combination is tried only for pairs of tracks that show a reasonable matching in the η/ϕ plane. The track combination is accepted only if the global χ^2 is below a maximal value. Finally, the pair giving the best combined χ^2 is retained, and the corresponding tracks are removed from the initial samples of tracks to be combined.

In the offline analysis, the muons were required to have $p_T > 20$ GeV and $\eta < 2.4$. To reduce the number of events from non-isolated muons such as those from decays of heavy-flavour quarks (multi-jet background), the muon isolation criterion with respect to inner detector tracks has been applied in a similar way as for electrons:

$$\sum_{\Delta R \leq 0.4} \frac{p_T^{ID}}{p_T^{\mu}} \leq 0.2 \tag{4.8}$$

For the numerator, i.e. sum of tracks transverse momenta in the cone, we employ standard ptcone40 variable [205].

To increase the robustness against track reconstruction mismatches, the difference between the ID and MS p_{T} measurements is required to be less than 15 GeV [190]. In addition to the requirements listed, quality criteria are applied to the ID tracks associated to muon candidates in order to ensure optimal muon reconstruction. These are recommended by the ATLAS Muon Combined Performance group (MCP) [205] and are listed below:

- if hits in the b-layer are geometrically expected, then the muon track must have at least one b-layer hit;
- $N_{PIX} + N_{DEAD-PIX} > 1$, where N_{PIX} is the number of pixel hits and $N_{DEAD-PIX}$ is the number of crossed dead pixel sensors; here and further 'dead' means the module is out of operation.
- $N_{SCT} + N_{DEAD-SCT} \geq 6$, where N_{SCT} is the number of SCT hits and $N_{DEAD-SCT}$ is the number of crossed dead SCT sensors;
- $N_{PIX\_HOLES} + N_{SCT\_HOLES} < 2$, where N_{PIX_HOLES} and N_{SCT_HOLES} are the numbers of holes along the muon track in the pixel and SCT sensors, respectively. The 'hole' denotes the absence of detector module along the muon track;
- A successful TRT extension is required in the eta acceptance of the TRT. If $N_{TRT-HITS}$ denote the number of TRT hits on the muon track, $N_{TRT-OUTLIERS}$ the number of TRT outliers[3] on the muon track, and $N_{TRT} = N_{TRT-HITS} + N_{TRT-OUTLIERS}$, then
  - in the interval $|\eta| < 1.9$: $N_{TRT} > 5$ and $N_{TRT-OUTLIERS}/N_{TRT} < 0.9$ is required;
  - in the interval $|\eta| \geq 1.9$: if $N_{TRT} > 5$ then $N_{TRT-OUTLIERS}/N_{TRT} < 0.9$ is required

Corrections for electron and muon selection efficiency

To account for data/MC disagreement in electron (muon) selection efficiency, scale factors are applied to the simulated MC samples according to prescriptions of Refs. [195, 197]. Namely, if simulated event meets the requirement of $W \to e\nu$ ($W \to \mu\nu$) selection,

---

[3] TRT outliers appear in two forms in the track reconstruction, as a straw tube with a signal but not crossed by the nearby track, or as a set of TRT measurements in the prolongation of a track which, however, failed to form a smooth trajectory together with the pixel and SCT measurements [206].

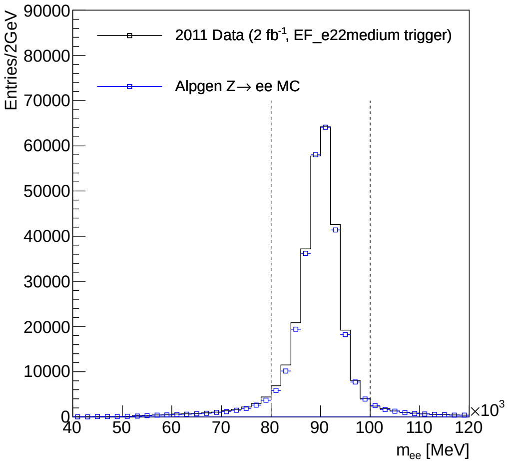

Figure 4.8: Invariant mass of tag-and-probe electron pairs. Data are shown by black histogram and is compared to MC simulation of $Z \to ee$ process, given by the blue dots. MC simulation is normalized to the data. Vertical dashed lines indicate the region where tag-and-probe events were selected for the evaluation of electron scale factors.

then MC weight of this event is multiplied by the corresponding electron (muon) scale factor. Scale factors are provided as a function of electron (muon) p_{T} and η, and were derived using full 2010 dataset [207] for muons and partial 2011 dataset for electrons. The efficiency correction varies depending on electron (muon) transverse momentum, and is conservatively within 5%.

Furthermore, as described in Section 4.3.1, we employ a custom-made (non-standard) electron isolation in our analysis. To account for possible miss-modelling of this quantity, the corresponding scale factors are evaluated with respect to electron-isolation cut, and are applied to simulated physics processes using a procedure, similar to the one described above. The same applies also to the electron (muon) impact-parameter selection criterion. Scale factors are derived using data-driven tag-and-probe method [207] from a sample of electrons (muons) that originate from $Z \to ee$ ($Z \to \mu\mu$) decay. For electrons, the tight selection criterion, the isolation criterion, and impact-parameter criterion are applied to tag electron of the Z candidate, while for probe electron the tight criterion is applied only. After selecting tag-and-probe pair, the probe electron is checked to pass the combined isolation and transverse impact parameter cut. The corresponding efficiencies are evaluated both for data and simulated Monte Carlo samples, and the scale factors are obtained as a ratio of two efficiencies, i.e. $\epsilon_{\mathrm{data}}/\epsilon_{\mathrm{MC}}$. They are obtained as a function of η for different values of electron $\mathrm{E_T}$. η and $\mathrm{E_T}$ regions are chosen similar to that in Ref. [195]. The distribution of invariant mass of tag-and-probe electron pairs is shown in Fig. 4.8, and is compared to that obtained form MC simulation. The resulting scale factors are shown in Fig. 4.9. As seen in the figure, the variations due to these scale factors are within 10%. The highest values are observed at η ∼1.5 – transition region between barrel and end-cap EM calorimeters. Systematic uncertainties are assigned to these scale factors. They are calculated as the difference between scale factors obtained at high and low pile-up, where former corresponds to subset of tag-and-probe events with

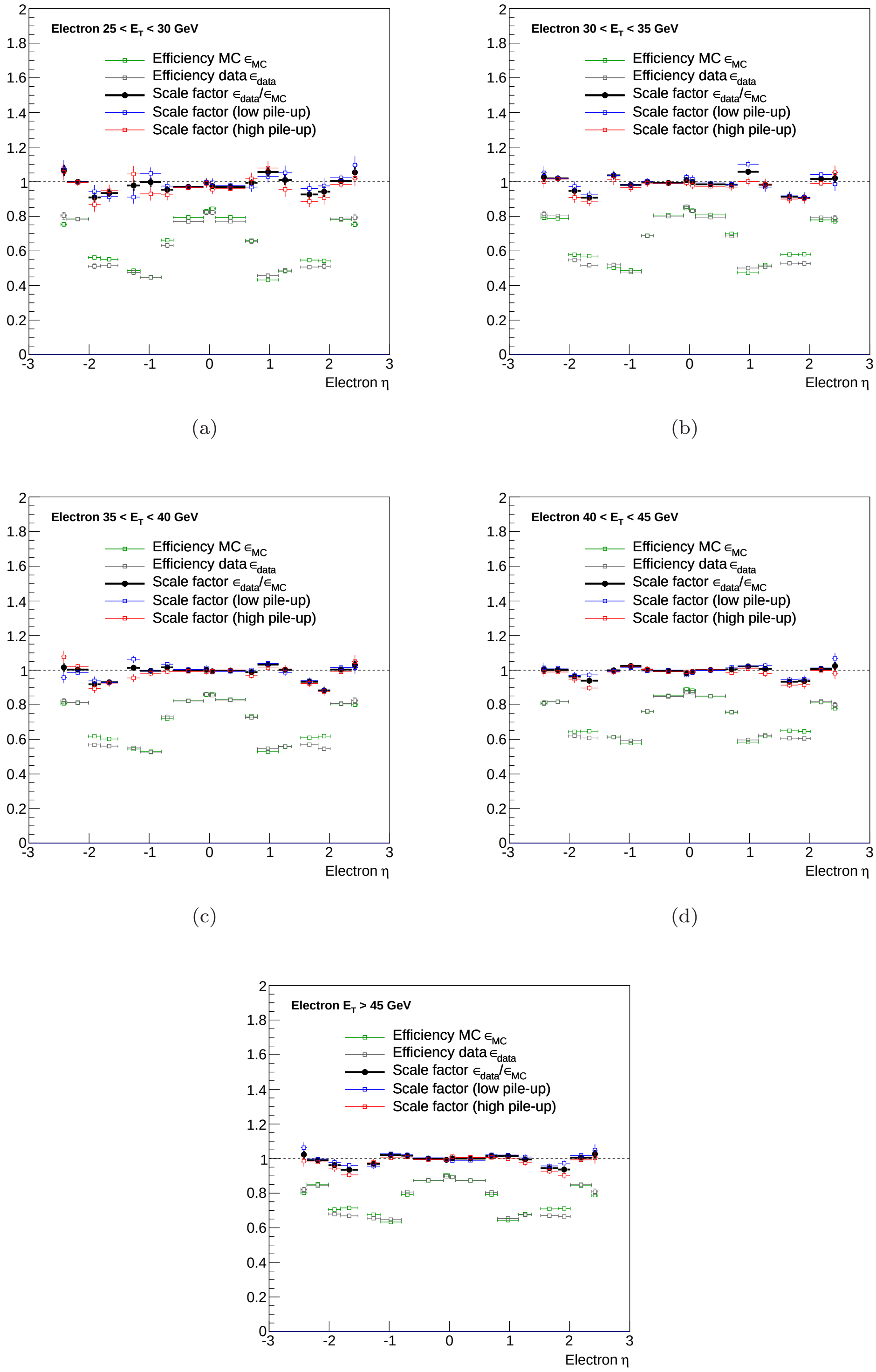

(a) (b)

(c) (d)

(e)

Figure 4.9: Efficiencies and scale factors for combined electron-isolation and impact-parameter selection criteria, given as a functions of electron pseudorapidity η in different electron-$\mathrm{E_T}$ regions. All numbers are obtained with the tag-and-probe method as described in Section 4.3.1.

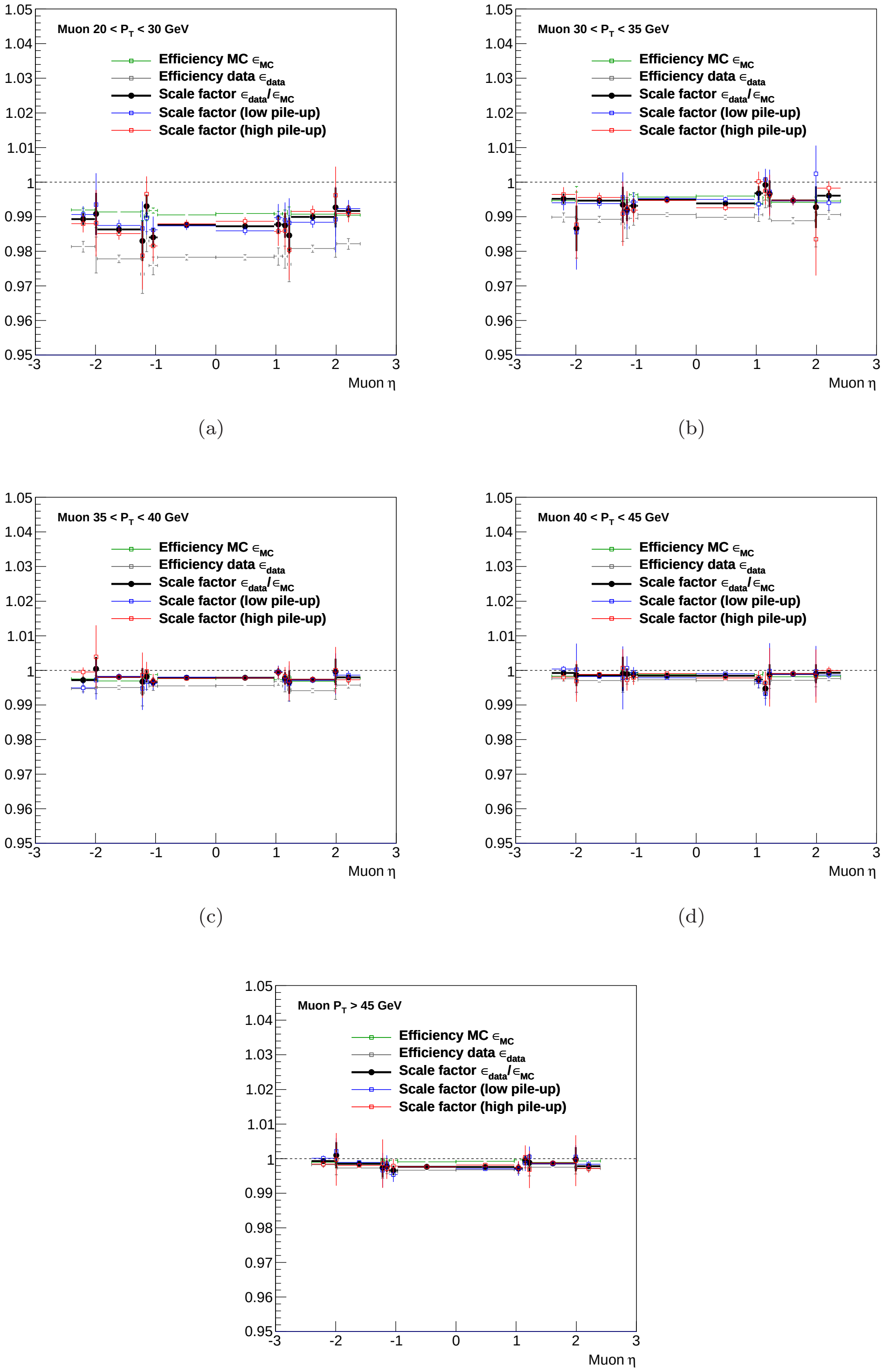

(a) (b) (c) (d) (e)

Figure 4.10: Efficiencies and scale factors for combined muon isolation and impact-parameter selection criteria, given as a functions of muon pseudorapidity η in different muon-p_{T} regions. All numbers are obtained with the tag-and-probe method as described in Section 4.3.1.

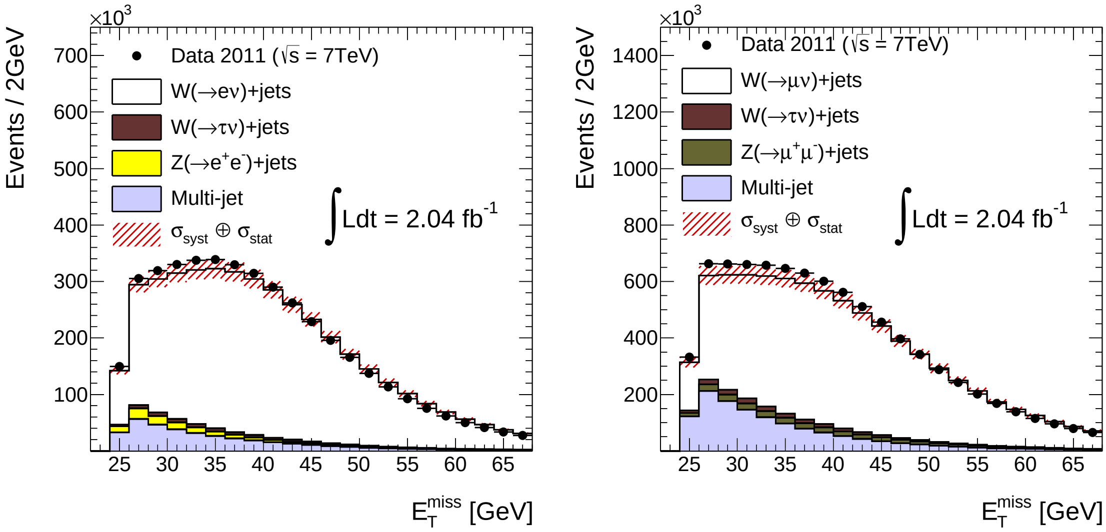

Figure 4.11: Missing transverse momentum of W-candidate events in $W \to e\nu$ (left) and $W \to \mu\nu$ (right) channels.

$\leq$5 reconstructed primary vertices per event, and later – to events with >5 primary vertices, respectively. Similar scale factors are obtained for muons. Here, the muon-quality criteria, isolation criterion and impact-parameter criterion are applied to tag a muon of $Z \to \mu\mu$ decay, while for probe muon the quality criteria are applied only. The resulting efficiencies and scale factors with respect to combined muon impact-parameter and isolation criteria are shown in Fig. 4.10. As can be seen from figure, the corrections due to these scale factors are far below 2%, which is expected, since we use standard (fine-tuned) muon isolation.

Missing transverse momentum

In ATLAS reconstruction, the missing transverse momentum includes two terms. The first one is calculated from the contributions of transverse energy deposits in calorimeters, and second term comes from muons reconstructed in the Muon Spectrometer. The total missing transverse momentum is [208]

$$E_{\mathrm{T}}^{\mathrm{miss}} = E_{\mathrm{T}}^{\mathrm{miss,\ calo}} + E_{\mathrm{T}}^{\mathrm{miss,\ muons}} \tag{4.9}$$

The calorimeter term is calculated as follows: first, calorimeter cells are associated with a parent reconstructed and identified high-p_{T} object, in a chosen order: electrons, photons, hadronically decaying tau-leptons, jets and muons. Refined calibration of the object is then used in $E_{\mathrm{T}}^{\mathrm{miss}}$ to replace the initial global calibration of cells. The calibration of these objects is known to higher accuracy, enabling to improve the $E_{\mathrm{T}}^{\mathrm{miss}}$ reconstruction. The calorimeter cells are associated with the reconstructed objects through the use of an association map. This map is filled starting from the reconstructed/identified objects in the chosen order written above, navigating back to their component clusters and back again to their cells. If a cell belongs to several kinds of reconstructed objects, only the first association is included in the map, i.e. the overlap removal is done at cell level. This avoids double counting of cells in the $E_{\mathrm{T}}^{\mathrm{miss}}$ calculation. If a cell belongs to more than one object of the same kind, all associations are included in the map and the geometrical weight of the cells, accounting for the sharing of energy of cells owned by to two different topological clusters, are also included to avoid double counting.

The muon term is calculated from the momenta of muon tracks reconstructed with $|\eta| < 2.7$. In order to deal properly with the energy deposited by the muon in calorimeters, the muon term is calculated differently for isolated and non-isolated muons. For isolated muons with matched inner detector track, muon p_{T} is determined from the combined measurement in inner detector and muon spectrometer. In this case the energy lost by muon in calorimeter is not added to calorimeter term in order to avoid double counting. In case of non-isolated muons, the muon energy lost in the calorimeter cannot be distinguished from the nearby jet energy. Therefore, the muon momentum in muon spectrometer (after energy loss) is used, unless there is a significant mismatch between combined and MS measurement. In the latter case the combined measurement minus the parametrized energy deposit in the calorimeter is used. Aside from the loss of muons outside the acceptance of muon spectrometer ($|\eta| > 2.7$), muons can be lost due to limited coverage of muon spectrometer (around $\eta = 0$ and $|\eta|$ 1.2). In these cases muon inner detector and calorimeter energy deposits are used to recover their contribution to $E_{\mathrm{T}}^{\mathrm{miss}}$. Although the core of $E_{\mathrm{T}}^{\mathrm{miss}}$ is not affected much by the muon term, badly reconstructed or fake muons can be a source of considerably large fake $E_{\mathrm{T}}^{\mathrm{miss}}$.

Finally, $E_{\mathrm{T}}^{\mathrm{miss}}$ is calibrated using so-called RefFinal recipe [208]. Distributions of W-candidate events with respect to missing transverse momentum are shown in Fig. 4.11. As can be seen from figure, data are in a good agreement with the MC simulation, within the given uncertainties. The slight excess of number of events observed in the data with respect to number of predicted events, in the $W \to \mu\nu$ channel is due to high normalization uncertainty of multi-jet background in this channel.

4.3.2 Electron-jet pair selection

In this search, the ultimate signature of the Higgs boson decay is two or more electron-jets, i.e. highly collimated (clustered) sets of electrons. Electron-jet candidates are selected from jets in the calorimeters, reconstructed by the standard ATLAS algorithm, which uses the anti-k_t jet clustering approach [209] with a radius parameter $R = 0.4$.

The electrons in an electron-jet are too closely collimated to be identified efficiently with the standard ATLAS algorithm, used e.g. to identify electrons from W boson decays. Instead, electron-jets are identified with three discriminating observables, which are described in detail below: the jet electromagnetic fraction (f_{EM}), the jet charged particle fraction (f_{CH}) and the fraction of high-threshold hits originating from transition radiation in the TRT (f_{HT}).

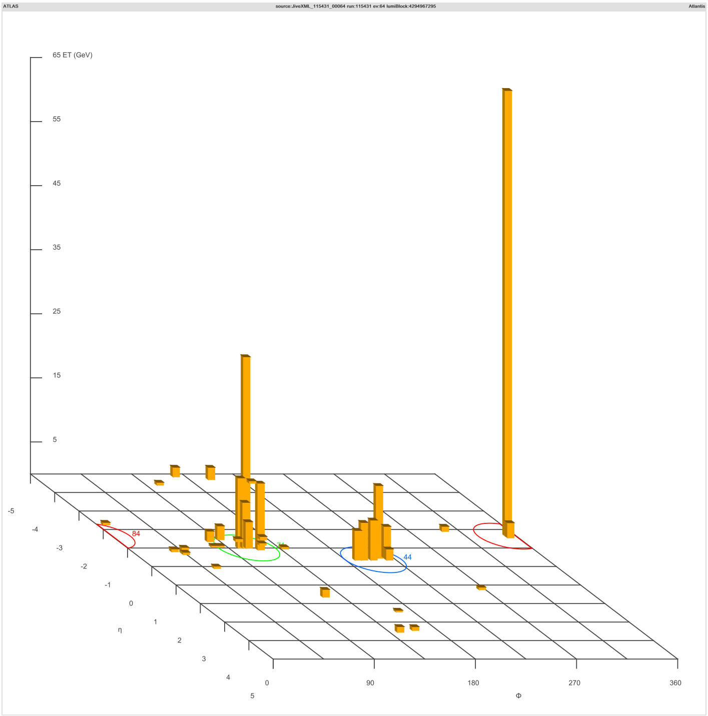

Figure 4.12: Display of simulated event of associate WH production with W boson decaying to electron and neutrino and Higgs boson decaying to a pair of electron-jets. The calibrated energy deposits in the calorimeter are shown with respect to η and ϕ. Each 'tower' corresponds to the energy measured in the $\eta \times \phi = 0.1 \times 0.1$ region in the calorimeter. The red, green and blue circles represent the electron from W boson decay and two electron-jets, respectively.

Reconstruction of jets

The jets are reconstructed following the standard ATLAS scheme [204]. First, energy deposits in the calorimeter are projected in the η/ϕ plane with the granularity of 0.1×0.1, forming the "towers" in the calorimeter (see Fig. 4.12). Various calorimeter compartments have different degrees of non-compensation and different amount of dead material (supporting constructions, envelopes, etc.) in front of the calorimeter. As a result, the observed energy differs from the truth particle energy. Furthermore, this energy response is usually nonlinear. The energy calibration procedure is applied to account for these effects [204]. The calorimeter towers are required to have calibrated $\mathrm{E_T}$ higher than 2 GeV (more precisely, the cut value varies in the range $2-3$ GeV depending on the η region and energy calibration procedure used). Next, calorimeter towers are passed to the anti-k_t clustering algorithm, which combines these towers into jets. The clustering algorithms usually comprise the following stages [209]:

- The "distances" are defined for N input objects to be combined

$$D_{ij} = \min\left(E_{\mathrm{T}i}^{2p}, E_{\mathrm{T}j}^{2p}\right)\frac{\Delta R_{ij}^2}{R^2}, \;\; D_i = E_{\mathrm{T}i}^{2p} \tag{4.10}$$

- The minimal distance is computed

$$d = \min \left.\right|_{i,j=1\ldots N} (D_{ij}, D_i) \tag{4.11}$$

  - If $d = D_{ij}$ – then i and j objects are combined;
  - If $d = D_i$ – then object i is defined as a final jet and is removed from the sample of objects to be combined;

- Reiterate first two steps until the input sample is empty.

Here R is the radius parameter. For $p = 0$ one recovers a simple cone algorithm, which confines any objects if their relative distance is lower than R. The two other cases, $p = 1$ and $p = -1$, correspond to k_t and anti-k_t algorithms, respectively. The two latter algorithms are essentially similar to the cone algorithm, with the only difference that, in case of k_t algorithm, the objects are combined into jets starting from the lowest $\mathrm{E_T}$ object to highest, and vice-versa in case of anti-k_t algorithm. As jets are reconstructed, they are further identified using the three discriminating observables, described below.

Identification of electron jets

In electron-jets, the electrons typically deposit all of their energy in the electromagnetic calorimeter, so that the fraction of the jet energy deposited in the electromagnetic calorimeter divided by the total jet energy deposited in both the electromagnetic and hadronic calorimeters, f_{EM}, is typically close to unity (see Fig. 4.13a). The slight degradation of f_{EM} towards lower values is due to the occasional leakage of electromagnetic showers into the hadronic calorimeter, calorimeter noise and electron-jets overlapping with ordinary jets. Hadronic jets reaching the calorimeters mainly consist of $\pi^{\pm}$ and photons from π^0 decays. Most $\pi^{\pm}$ deposit a sizable fraction of their energy in the hadronic calorimeter, while photons deposit almost all their energy in the electromagnetic calorimeter. The distribution of f_{EM} is further broadened by fluctuations of the electromagnetic and hadronic showers in the detector. The pedestal corrections for noise in the hadronic calorimeter can sometimes lead to reconstructed energies in the hadronic calorimeter that are less than zero, resulting in a value of f_{EM} slightly higher than unity. The simulation models this situation accurately. The distribution of f_{EM} for hadronic jets peaks around 0.85, with a few percent of these jets having $f_{\mathrm{EM}} \geq 0.99$.

Since f_{EM} only provides a limited background rejection, additional variables are exploited. The quantity f_{CH} is defined as the fraction of the jet energy deposited in calorimeter cells that are associated with tracks within the jet:

$$f_{\mathrm{CH}} = \frac{\displaystyle\sum_{\text{“track−cells”}} E^{\mathrm{cell}}}{E^{\mathrm{jet}}}. \tag{4.12}$$

A track is associated with a jet if it is within a distance of $\Delta R = 0.4$ from the jet axis and has $p_{\mathrm{T}} \geq 400$ MeV. The “track-cells”, i.e. calorimeter cells associated with tracks within the jet, consist of the cells within a cone of $\Delta R = 0.2$ around each of the tracks

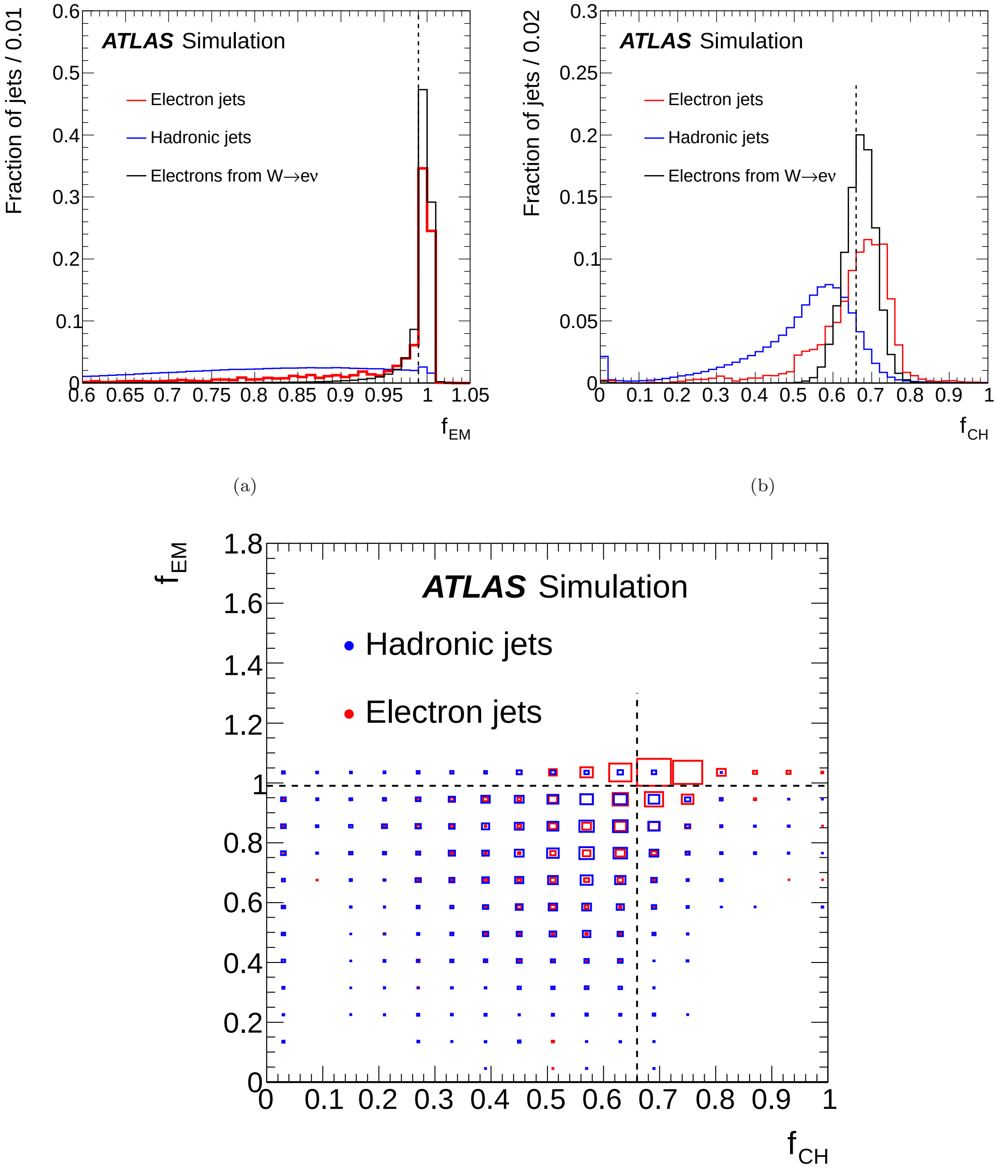

(a)

(b)

(c)

Figure 4.13: Distribution of the jet electromagnetic, f_{EM}(a), jet charged particles fraction, f_{CH} (b), and 2-dimensional distribution of jets in combined f_{EM}–f_{CH} plane (c). Electron-jets in simulated signal process (red histogram), hadronic jets in simulated W+jets background process (dark-blue histogram) and jets matched to electron that originate from $W \to e\nu$-decay (black histogram) are shown. All jets are required to fulfil $\mathrm{E_T}$ and η selection criteria of Section 4.3.2. The simulated MC sample for three-step model, $m_{\gamma_{\mathrm{d}}} = 100$ MeV is taken to present the electron-jets signal. Dashed lines indicate the electron-jets selection criteria.

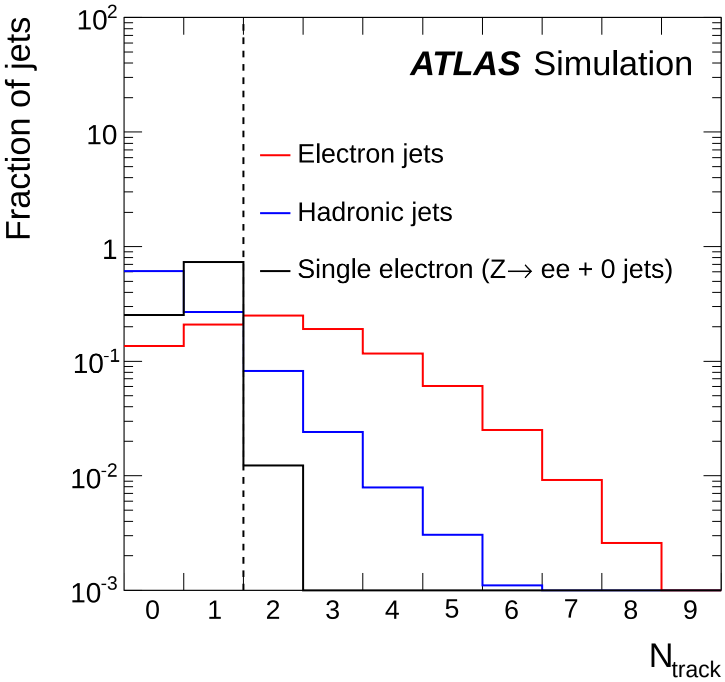

Figure 4.14: Distribution of number of tracks that have $f_{\mathrm{HT}} \geq 0.08$ in electron-jets (blue histogram), hadronic jets (red histogram), and jets matched to electron that originate from $Z \to ee$-decay (black histogram). Simulated MC sample for three-step model, $m_{\gamma_{\mathrm{d}}} = 100$ MeV, is taken for electron-jets. Two other types of jets are taken in simulated $W \to e\nu$ and $Z \to ee$ MC samples respectively. Dashed line indicates the region where electron-jets are sought.

associated with the jet, giving the sum of energy deposits of charged particles within the jet in both the electromagnetic and hadronic calorimeters.

Signal electron-jets consist exclusively of electrons and should have large f_{EM} and f_{CH}. Hadronic jets with large f_{EM} are expected to contain mostly neutral pions decaying to photons and, therefore, fewer charged tracks and low f_{CH}. Photons that convert to electron–positron pairs in the material they traverse before entering the calorimeter increase the value of f_{CH}. Normalized f_{EM} and f_{CH} distributions of electron-jets in simulated signal process and hadronic jets in simulated background process are shown in Fig. 4.13. Two-dimensional distribution of jets in combined f_{EM}–f_{CH} plane is shown as well.

Additional rejection of hadronic jets is achieved by exploiting the identification of electrons using transition radiation. The discriminating quantity is the fraction of TRT hits on a track, f_{HT}, that exceed the high discriminator threshold in the read-out electronics of the TRT straws. Detailed studies of this quantity are reported in Refs. [163,195]. This high-threshold setting corresponds to the size of the large energy deposit from transition radiation in the straw-tube gas. The distribution of f_{HT} for tracks from electrons has a maximum at $f_{\mathrm{HT}} \sim 0.2$, while it peaks at zero and then decreases monotonically for charged hadron tracks. A requirement that $f_{\mathrm{HT}} \geq 0.08$ has an efficiency of over 95% for electrons in the momentum range relevant to this analysis and at the same time effectively rejects charged hadrons. Normalized distribution of electron-jets, hadronic jets, and jets

		Data	Expected background	Expected signal, m_H=125 GeV	Eff.
				$W \to e\nu$ channel	
$W \to e\nu$ selection		4351732	4330000 ± 250000	$46.7 \pm 1.8^{(\text{stat})}$	13%
$\geq$2 jets	$p_T \geq$30 GeV, $\lvert\eta\rvert \leq 2.0$	173551	183000 ± 16000	$25.6 \pm 1.4^{(\text{stat})}$	7.1%
	$f_{\text{EM}} \geq$0.99	837	1070 ± 200	$10.8 \pm 0.9^{(\text{stat})}$	3.0%
	$f_{\text{CH}} \geq$0.66	39	35 ± 8	$6.3 \pm 0.7^{(\text{stat})}$	1.7%
	$N_{\text{track}} \geq 2$	0	$0.10\,^{+\,0.11}_{-\,0.10}$	$5.3 \pm 0.6^{(\text{stat})} \pm 0.4^{(\text{syst})}$	1.5%
				$W \to \mu\nu$ channel	
$W \to \mu\nu$ selection		8870713	8620000 ± 350000	$60.3 \pm 2.3^{(\text{stat})}$	17%
$\geq$2 jets	$p_T \geq$30 GeV, $\lvert\eta\rvert \leq 2.0$	326956	353000 ± 33000	$31.5 \pm 1.7^{(\text{stat})}$	8.8%
	$f_{\text{EM}} \geq$0.99	1008	1240 ± 180	$13.9 \pm 1.2^{(\text{stat})}$	3.9%
	$f_{\text{CH}} \geq$0.66	45	41 ± 16	$7.5 \pm 0.9^{(\text{stat})}$	2.1%
	$N_{\text{track}} \geq 2$	1	$0.11\,^{+\,0.13}_{-\,0.11}$	$6.0 \pm 0.8^{(\text{stat})} \pm 0.4^{(\text{syst})}$	1.7%

Table 4.3: The expected number of background and signal events in 2.04 fb^{-1} of data, as well as the number of events observed in the data, after applying the various signal selection criteria for the $W \to e\nu$ and $W \to \mu\nu$ channels. The "$\geq$2 jets" in the first column denotes the requirement of two or more jets per event, satisfying the corresponding selection criteria. The signal predictions correspond to the three-step model with m_H = 125 GeV and m_{γ_d}=100 MeV. The signal efficiencies are the fraction of signal events satisfying all the selection criteria up to and including that particular criterion. They are given with respect to the signal sample including all three decay modes of the W boson ($e\nu_e$, $\mu\nu_\mu$, $\tau\nu_\tau$). The background expectations include statistical and systematic uncertainties, and are determined using the MC method (see Section 4.4.1). The statistical uncertainty shown for the signal is due to Monte Carlo statistics; the systematic uncertainty is only given for the final event selection and its detailed composition is given in Table 4.9.

matched to electron that originate from $Z \to ee$ decay, with respect to number of tracks having $f_{\text{HT}} \geq 0.08$, in simulated signal and background MC samples, is shown in Fig. 4.14. As seen in figure, in addition to substantial reduction of background from hadronic jets (by factor of ten), this requirement also reduces the background from single electrons, like those from $Z \to ee$ decay, by two orders of magnitude. The remaining irreducible background from single electrons is due to hard bremsstrahlung photons emitted by such electrons and that are converted to electrons in the material of detector.

Exploiting the selection criteria described above, a jet is classified as an electron-jet if it satisfies the following requirements:

- jet pseudorapidity $|\eta| \leq 2.0$,
- jet transverse momentum $p_T \geq 30$ GeV,
- jet electromagnetic fraction $f_{\text{EM}} \geq 0.99$,

- jet charged particle fraction $f_{\text{CH}} \geq 0.66$ and
- number of tracks associated with the jet $N_{\text{track}} \geq 2$, where the tracks must satisfy the following criteria:
    - track pseudorapidity $|\eta| \leq 2.0$,
    - track transverse momentum $p_{\text{T}} \geq 5$ GeV,
    - number of hits in the pixel detector $N_{\text{PIX}} \geq 2$,
    - total number of pixel and SCT hits $N_{\text{PIX}} + N_{\text{SCT}} \geq 7$,
    - fraction of high-threshold TRT hits $f_{\text{HT}} \geq 0.08$.

Good agreement is observed between data and MC simulation in the f_{EM}, f_{CH} and track-related distributions at the different stages of selection, as can be seen in Figs. 4.15 and 4.16. The number of events observed in the data and the yields expected for the background and the signal as the selection criteria are applied are shown in Table 4.3. The background yield given here is determined by MC, and signal yield is determined for 3-step model with $m_H = 125$ GeV and $m_{\gamma_{\text{d}}} = 100$ MeV.

The expected signal yields for all signal models are given in Tables 4.4 and 4.5. From the tables it is seen that the number of events after applying trigger selection in $W \to e\nu$ channel is higher than that of the $W \to \mu\nu$ channel. The reason is because, in addition to electrons from W-decay, electron-jets can also pass the trigger selection criterion. However, it has been checked that, due to electron-isolation requirement (Section 4.3.1), the probability of electron-jet to fulfil $W \to e\nu$ selection criteria is almost negligible (below 1%). Or, equivalently, electrons from W-decay are distinguished from electron-jets with ≥99% probability. Thus, by using the electron-isolation requirement in $W \to e\nu$ selection, we avoid the possible situation when electron-jet would be falsely considered as electron from W-decay, and, because of this, the considered event wouldn't pass the final selection.

The efficiencies of electron-jet selection are shown in Figs. 4.17 and 4.18. As can be seen, efficiency drops sharply at $|\eta|$ ∼1.5, the transition region between the barrel and end-cap EM calorimeters.

4.4 Background estimation

The dominant background in this search is the associated production of a W boson with hadronic jets which mimic the electron-jet signature. Detailed MC studies of the background contamination from hadronic jets faking electron-jets have shown that the high electron content in those jets originates either from final-state photon radiation or from π^0 decays with subsequent photon conversions in the material of the detector. A background prediction from MC simulation would depend on the modelling of final-state photon radiation and parton showering and hadronization, which would introduce large uncertainties in the background rate. Instead, the background contamination in the

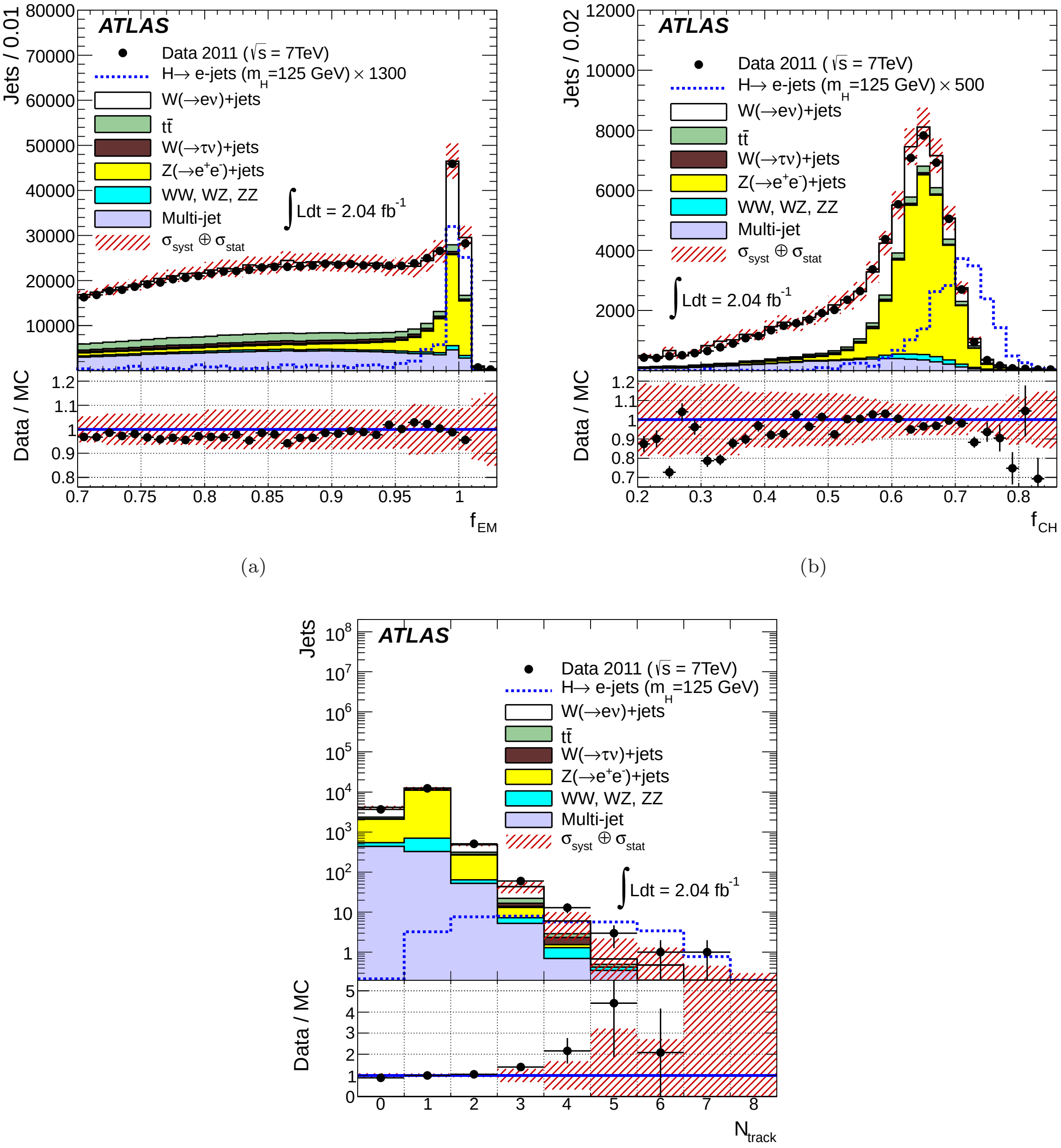

(a)

(b)

(c)

Figure 4.15: Distribution of the jet electromagnetic fraction, $f_{\rm EM}$, after the $W \to e\nu$ selection (a), the jet charged particle fraction, $f_{\rm CH}$, after the $f_{\rm EM}$ selection (b) and the number of associated tracks, $N_{\rm track}$, fulfilling the criteria of Section 4.3.2 after the $f_{\rm EM}$ and $f_{\rm CH}$ selection (c). Data are shown as dots with error bars and are compared to the expectation from Standard Model processes, given by stacked histograms of different colors. The signal distributions in the three-step model of a hidden sector with dark photon mass $m_{\gamma_d} = 100$ MeV are presented as dashed histograms with arbitrary scale (a and b) and with the nominal scale (c), where nominal scale implies the SM value for WH production cross section and 100% branching ratio of a Higgs boson decaying to electron-jets. The hatched bands represent the quadratic sum of statistical and systematic uncertainties of the Standard Model background prediction described in Section 4.5.

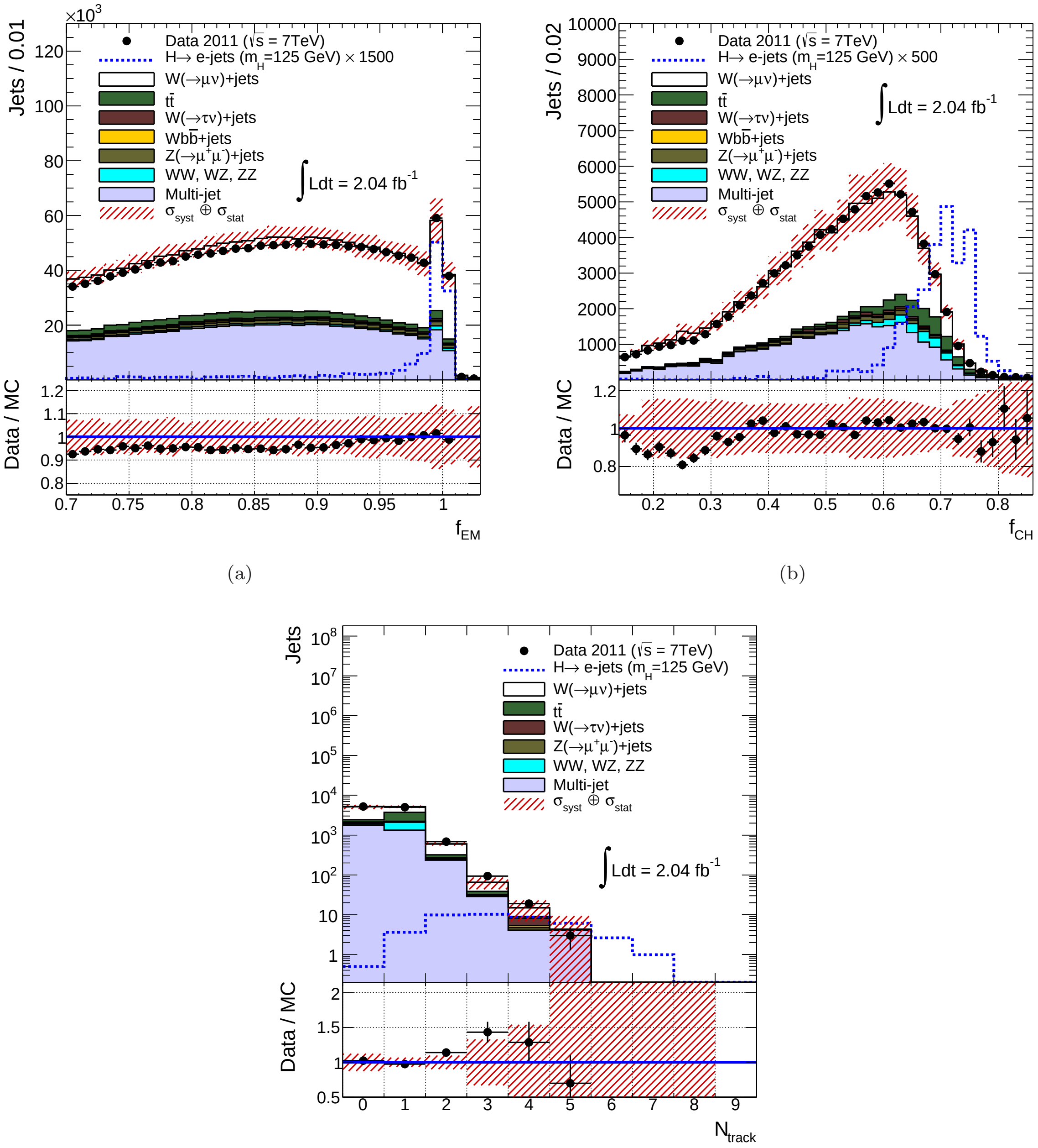

(a)

(b)

(c)

Figure 4.16: Distribution of the jet electromagnetic fraction, f_{EM}, after the $W \to \mu\nu$ selection (a), the jet charged particle fraction, f_{CH}, after the f_{EM} selection (b) and the number of associated tracks, N_{track}, fulfilling the criteria of Section 4.3.2 after the f_{EM} and f_{CH} selection (c). Data are shown as dots with error bars and are compared to the expectation from Standard Model processes, given by stacked histograms of different colors. The signal distributions in the three-step model of a hidden sector with dark photon mass $m_{\gamma_d} = 100$ MeV are presented as dashed histograms with arbitrary scale (a and b) and with the nominal scale (c), where nominal scale implies the SM value for WH production cross section and 100% branching ratio of a Higgs boson decaying to electron-jets. The hatched bands represent the quadratic sum of statistical and systematic uncertainties of the Standard Model background prediction described in Section 4.5.

		3-step model (Eff.)		2-step model (Eff.)	
		$m_{\gamma_d} = 100MeV$	$m_{\gamma_d} = 200MeV$	$m_{\gamma_d} = 100MeV$	$m_{\gamma_d} = 200MeV$
		Higgs mass 100 GeV			
Before all cuts		755.9	755.9	755.9	755.9
Electron trigger		374.4 ± 5.6	311.1 ± 5.5	553.2 ± 4.9	470.3 ± 5.4
$W \to e\nu$		82.6 ± 3.5	87.8 ± 3.7	98.7 ± 3.8	108.1 ± 3.9
≥2J	p_T ≥30 GeV, $\|\eta\| \leq 2.0$	37.9 ± 2.4	41.5 ± 2.6	55.6 ± 3.0	61.2 ± 3.0
	$N_{\text{track}} \geq 2$	18.2 ± 1.7	20.1 ± 1.8	28.0 ± 2.2	30.3 ± 2.2
	f_{CH} ≥0.66	8.4 ± 1.2	9.2 ± 1.2	14.0 ± 1.6	18.1 ± 1.7
	f_{EM} ≥0.99	5.3 ± 1.0	6.2 ± 1.0	9.2 ± 1.2	12.4 ± 1.4
		Higgs mass 125 GeV			
Before all cuts		361.8	361.8	361.8	361.8
Electron trigger		199.6 ± 2.7	158.5 ± 2.6	271.7 ± 2.3	238.8 ± 2.5
$W \to e\nu$		46.7 ± 1.8	46.0 ± 1.8	54.8 ± 2.0	51.8 ± 1.9
≥2J	p_T ≥30 GeV, $\|\eta\| \leq 2.0$	25.6 ± 1.4	23.4 ± 1.3	33.4 ± 1.6	32.6 ± 1.5
	$N_{\text{track}} \geq 2$	14.4 ± 1.0	12.8 ± 1.0	17.9 ± 1.2	20.1 ± 1.2
	f_{CH} ≥0.66	8.7 ± 0.8	7.5 ± 0.8	11.2 ± 0.9	11.2 ± 0.9
	f_{EM} ≥0.99	5.3 ± 0.6	5.4 ± 0.7	7.1 ± 0.7	7.3 ± 0.8
		Higgs mass 140 GeV			
Before all cuts		250.7	250.7	250.7	250.7
Electron trigger		143.7 ± 1.8	121.1 ± 1.8	190.2 ± 1.6	169.1 ± 1.7
$W \to e\nu$		37.0 ± 1.3	35.3 ± 1.3	35.5 ± 1.3	37.2 ± 1.3
≥2J	p_T ≥30 GeV $\|\eta\| \leq 2.0$	21.6 ± 1.1	20.2 ± 1.0	23.5 ± 1.1	23.3 ± 1.1
	$N_{\text{track}} \geq 2$	12.3 ± 0.8	11.8 ± 0.8	12.8 ± 0.8	14.3 ± 0.9
	f_{CH} ≥0.66	7.2 ± 0.6	6.7 ± 0.6	9.4 ± 0.7	8.9 ± 0.7
	f_{EM} ≥0.99	5.3 ± 0.5	4.4 ± 0.5	6.1 ± 0.6	6.2 ± 0.6

Table 4.4: The expected number of signal events in $W \to e\nu$ channel after applying various selection criteria. The "≥2J" in the first column denotes the requirement of two or more jets per event, satisfying the corresponding jet selection criteria. The uncertainties are statistical only.

		3-step model (Eff.)		2-step model (Eff.)	
		$m_{\gamma_d} = 100 MeV$	$m_{\gamma_d} = 200 MeV$	$m_{\gamma_d} = 100 MeV$	$m_{\gamma_d} = 200 MeV$
		Higgs mass 100 GeV			
Before all cuts		749.9	749.9	749.9	749.9
Muon trigger		188.2 ± 5.5	190.5 ± 5.5	181.3 ± 5.5	179.3 ± 5.4
$W \to m\nu$		129.4 ± 4.8	130.5 ± 4.9	122.3 ± 4.7	121.4 ± 4.7
≥2J	$p_T \geq$30 GeV	56.7 ± 3.4	53.7 ± 3.3	70.4 ± 3.7	68.6 ± 3.7
	$\lvert\eta\rvert \leq 2.0$				
	$N_{\text{track}} \geq 2$	24.6 ± 2.2	25.2 ± 2.4	37.6 ± 2.8	35.6 ± 2.7
	$f_{CH} \geq$0.66	14.1 ± 1.7	9.3 ± 1.5	17.5 ± 1.9	17.5 ± 1.9
	$f_{EM} \geq$0.99	9.0 ± 1.4 ± 0.7	6.2 ± 1.2	13.4 ± 1.7	11.1 ± 1.5
		Higgs mass 125 GeV			
Before all cuts		358.9	358.9	358.9	358.9
Muon trigger		86.3 ± 2.6	90.6 ± 2.6	86.7 ± 2.6	92.0 ± 2.7
$W \to m\nu$		60.3 ± 2.3	62.7 ± 2.3	59.9 ± 2.3	63.5 ± 2.3
≥2J	$p_T \geq$30 GeV	31.5 ± 1.7	32.9 ± 1.8	37.7 ± 1.9	41.6 ± 2.0
	$\lvert\eta\rvert \leq 2.0$				
	$N_{\text{track}} \geq 2$	17.2 ± 1.3	17.7 ± 1.3	19.7 ± 1.4	24.7 ± 1.6
	$f_{CH} \geq$0.66	9.6 ± 1.0	9.6 ± 1.0	13.0 ± 1.2	15.3 ± 1.3
	$f_{EM} \geq$0.99	6.0 ± 0.8 ± 0.4	5.3 ± 0.8	9.1 ± 1.0	10.8 ± 1.1
		Higgs mass 140 GeV			
Before all cuts		248.7	248.7	248.7	248.7
Muon trigger		58.9 ± 1.8	59.9 ± 1.8	60.3 ± 1.8	59.9 ± 1.8
$W \to m\nu$		40.0 ± 1.6	41.7 ± 1.6	42.9 ± 1.6	43.3 ± 1.6
≥2J	$p_T \geq$30 GeV	22.1 ± 1.2	23.2 ± 1.2	29.4 ± 1.4	29.2 ± 1.4
	$\lvert\eta\rvert \leq 2.0$				
	$N_{\text{track}} \geq 2$	12.5 ± 0.9	13.9 ± 1.0	17.2 ± 1.1	18.9 ± 1.1
	$f_{CH} \geq$0.66	6.9 ± 0.7	7.9 ± 0.7	11.0 ± 0.9	11.7 ± 0.9
	$f_{EM} \geq$0.99	4.3 ± 0.6 ± 0.3	4.6 ± 0.6	7.6 ± 0.7	7.7 ± 0.7

Table 4.5: The expected number of signal events in $W \to \mu\nu$ channel after applying various selection criteria. The "≥2J" in the first column denotes the requirement of two or more jets per event, satisfying the corresponding jet selection criteria. The uncertainties are statistical only.

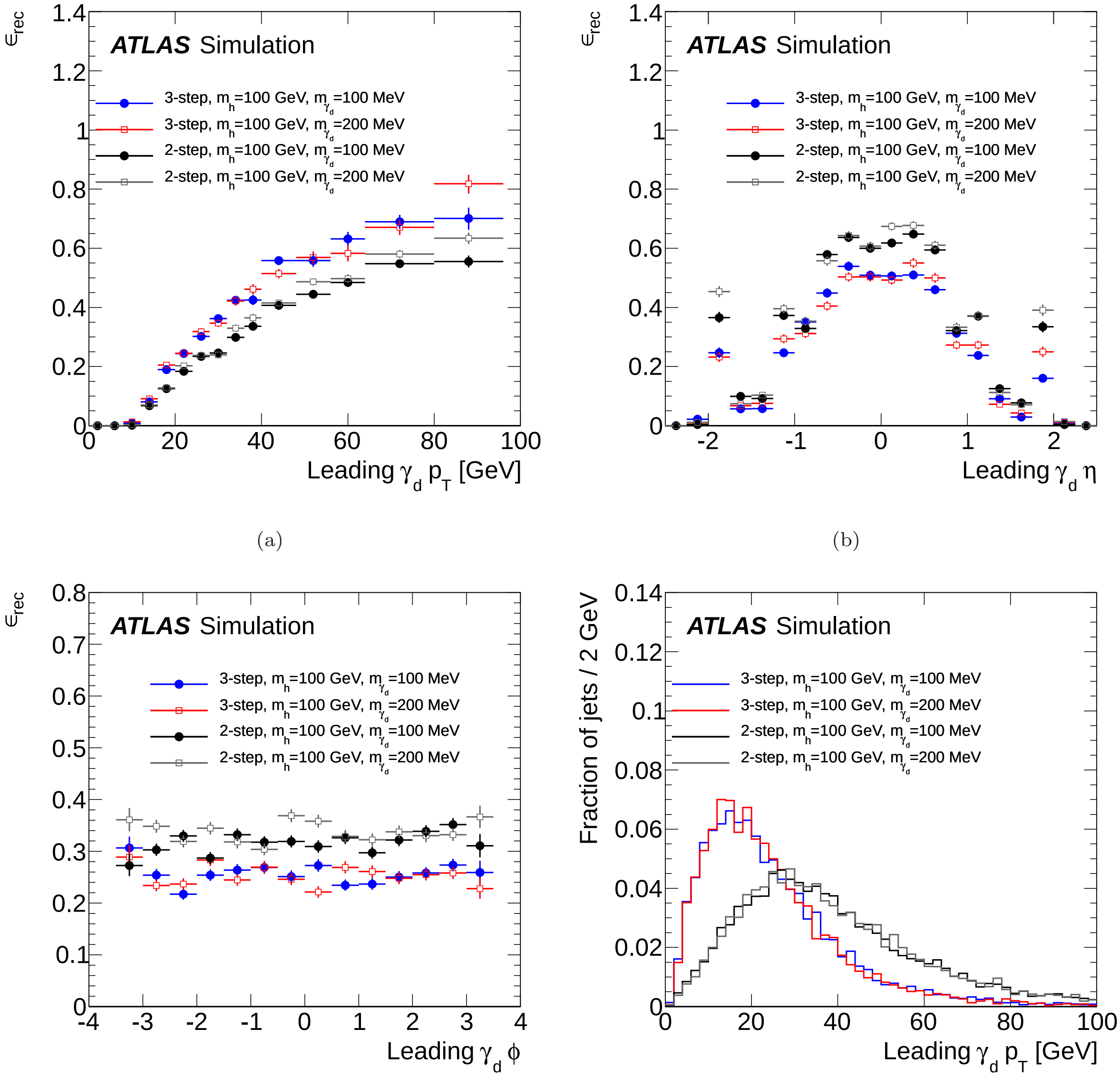

(a)

(b)

(c)

(d)

Figure 4.17: Electron-jet reconstruction efficiency as a function of various parameters of leading-p_T dark photon in the electron-jet: transverse momentum ,p_T (a), pseudorapidity, η (b), and azimuthal angle, ϕ (c). For convenience, distributions of leading dark-photon p_T in electron-jet is shown in (d) for all considered signal models. All distributions are for $m_H = 100$ GeV. Errors are statistical only.

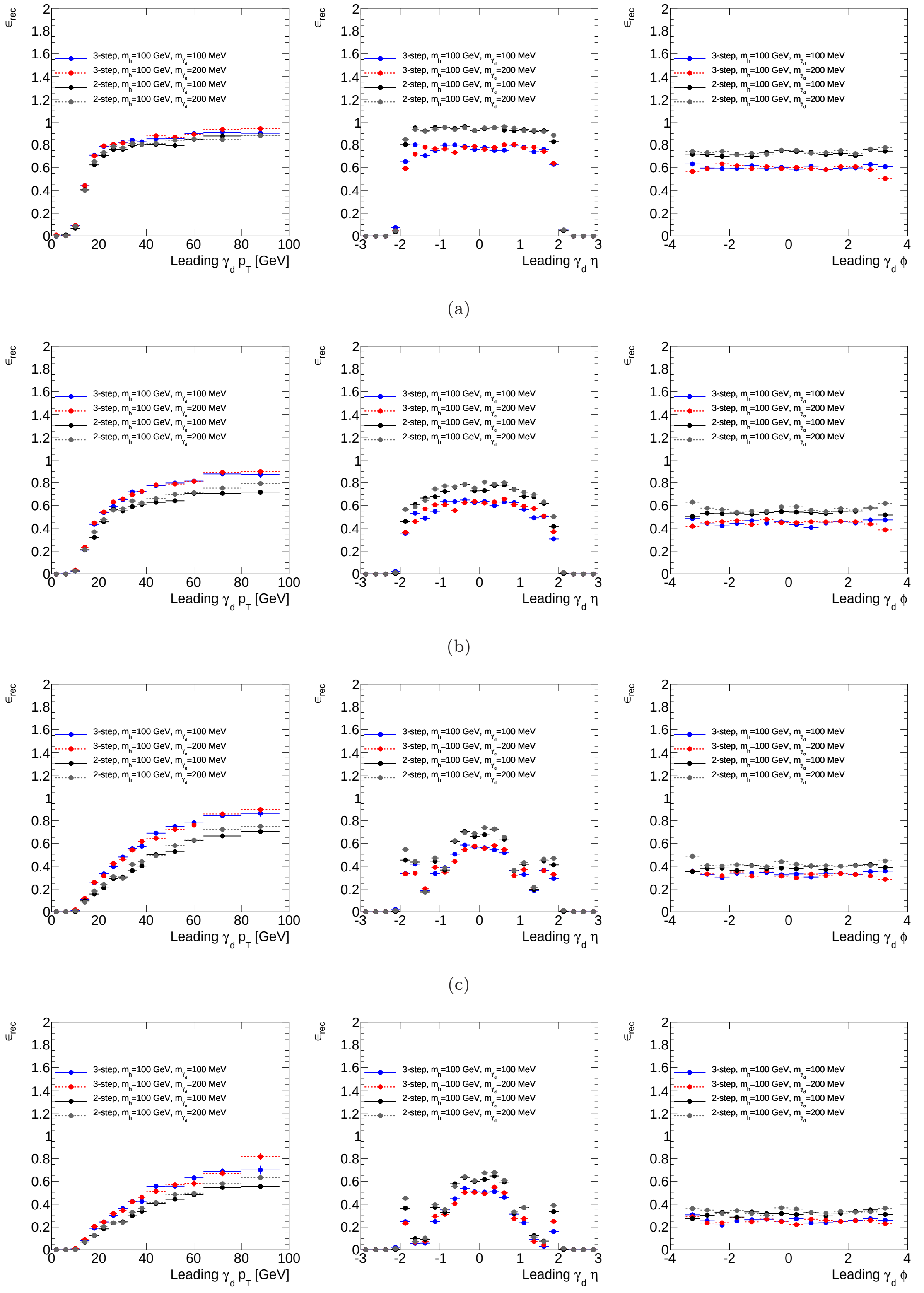

(a)

(b)

(c)

(d)

Figure 4.18: Efficiency of electron-jet selection criteria up to and including particular criterion: transverse momentum and pseudorapidity (a), number of associated tracks, N_{track} (b), jets charged particles fraction, f_{CH} (c), and jet electromagnetic fraction, f_{EM} (d). Distributions (d) are the same as in Fig. 4.17. Errors are statistical only.

signal region is estimated from the data using a simplified matrix method [210] which is completely data-driven. Two alternative background estimates were tried and found to be consistent with the matrix method result. One of these estimates – referred to as the ABCD method below – is based on data; the second estimate is based on Monte Carlo simulation. The methods are described in a reverse order in this section, starting from the Monte Carlo based method. This is useful in order to estimate the relative yield of different physics processes that are expected to contribute to the background contamination.

4.4.1 Background sources and its estimation using Monte Carlo simulation

In this method, the background prediction is obtained by using data templates and simulated samples with the appropriate cross sections scaled by the measured integrated luminosity, as described in Section 4.1. All potential backgrounds are summarize below

- **$W \to l\nu$ + jets** ($l = e/\mu$). This is the dominant source of background with the production of W and hadronic jets faking electron-jet signature.
- **$W \to \tau\nu$ + jets**. This process is expected to contribute via leptonic τ decays, $\tau \to l\nu\nu$, to both electron and muon final states in W selection.
- **$Z \to \mu\mu$ + jets**. $Z \to \mu\mu$ decays with one muon outside of the muon-spectrometer acceptance generate apparent missing transverse momentum and constitute a fake signature of $W \to \mu\nu$ decay. Similar to $W \to \mu\nu$ process, accompanying hadronic jets can mimic electron-jet signature.
- **$Z \to ee$ + jets**. Effects of energy miscalibration in electromagnetic and hadronic calorimeters and electrons traversing the transition regions in EM calorimeter, in some fraction of $Z \to ee$ decays, generate fake missing transverse momentum. Then, potentially, one of the electrons that originate from $Z \to ee$ fulfils the $W \to e\nu$-selection requirement, while the other fails. Then, the 'failed' electron, due to emission of hard bremsstrahlung photon and its subsequent conversion into electron-positron pair, fulfils the electron-jet selection criteria. The remaining hadronic jets can also mimic electron-jets. As it is shown in this section, this process contributes to background as considerably as $W \to e\nu$ process does.
- **$Z \to \tau\tau$ + jets**. Contribution to background is smaller than from $W \to \tau\nu$+jets process.
- **$t\bar{t}$**. The production of top pairs contributes to both $W \to e\nu$ and $W \to \mu\nu$ search channels due to the high multiplicity of jets and presence of W bosons, that originate from decays of top quarks.
- **$Wb\bar{b}$ + jets**. In addition to hadronic jets, decays of b quarks can produce electrons, which can mimic electron-jets.

- **Diboson (WW, WZ and ZZ)**. All sources of multilepton final states, accompanied by missing transverse momentum, are potential backgrounds in the electron-jet search. For example, fully leptonic WZ decay with W decaying to electron (muon) plus neutrino and Z decaying to e^+e^-. The contribution of diboson process to background is lower than that of W/Z+jets and $t\bar{t}$, due to a small diboson production cross section.

- **Multi-jet (QCD background)**. Hadronic jets in some cases can mimic a signature of isolated electron. This, for example, can be due to the high content of π^0 in the jet and their subsequent decay to photons, giving a high energy deposition in the electromagnetic calorimeter, similar to that of an isolated electron. In other cases, hadronic jets that penetrate to muon spectrometer can be mis-reconstructed as muons. Furthermore, single isolated leptons can also be produced in the decays of heavy-flavour quarks. All this, accompanied by fake missing transverse momentum, large enough to pass W selection criterion, can result in the signature of $W \to e\nu$ or $W \to \mu\nu$ decay. Despite the low probability of such events, appreciating the high cross section of multi-jet production, the contribution of this background is approximately half as large as that of W+jets.

The Monte Carlo programs, used to simulate background processes, are listed in Table 4.1 of Section 4.1.

For the multi-jet physics process, the contribution to background in both $W \to e\nu$ and $W \to \mu\nu$ channels is obtained directly from the data by using normalized data templates. The multi-jet data template is a sample of events obtained from the real data, with kinematic characteristics similar to that of the signal region, and selected such that, the contribution of processes other than multi-jet ones, in particular electroweak processes, is expected to be negligible in the sample. The same technique is used, for example, for background determination in the measurement of W production cross section, performed in Ref. [190]. In $W \to e\nu$ channel, the multi-jet template is derived by relaxing the tight electron-selection criteria to medium one. More precisely, the requirements on the ratio of cluster energy to track momentum, on the number of hits in the TRT, and on the ratio of high-threshold TRT hits are omitted [195]. Events with tight electrons are vetoed, ensuring the low electroweak contamination in the multi-jet data template. The normalization of multi-jet background is obtained by fitting the transverse mass distribution in the range 40 GeV$< m_{\mathrm{T}} <$60 GeV to that in the data, with subtracted contribution from simulated processes (see Fig. 8.3(a)). In $W \to \mu\nu$ channel, the multi-jet template is obtained by relaxing the muon isolation criterion. Events with isolated muons are vetoed. The normalization is derived by fitting transverse mass distribution to that in the data, in the range $m_T < 40$ GeV (see Fig. 8.3(b)).

Although the number of simulated MC events that are used in this analysis reaches in some cases up to fifty million, this statistics is still not enough to get an adequate number of events that survive the electron-jet pair selection (Section 4.3.2). Thus, to estimate the background yield that originate from a given physics process X after the final selection,

$W \to e\nu$ channel		$W \to \mu\nu$ channel	
Source	Events with 2 LJs	Source	Events with 2 LJs
$W \to e\nu$+jets	0.021	$W \to \mu\nu$+jets	0.030
$Z \to ee$+jets	0.020	$Z \to \mu\mu$+jets	0.001
$W \to \tau\nu$+jets	0.002	$W \to \tau\nu$+jets	0.005
$Z \to \tau\tau$+jets	< 0.001	$Z \to \tau\tau$+jets	0.003
$W + b\bar{b}$+jets	< 0.001	$W + b\bar{b}$+jets	0.003
$Z + b\bar{b}$+jets	0.001	$Z + b\bar{b}$+jets	< 0.001
$W + \gamma$+jets	0.001	$W + \gamma$+jets	0.001
$t\bar{t}$	0.037	$t\bar{t}$	0.046
WW/WZ/ZZ	0.009	WW/WZ/ZZ	0.003
QCD	0.005	QCD	0.021
TOTAL	0.096	TOTAL	0.113

Table 4.6: Expected background yields for each contributing SM process, obtained using Eqs. 4.13 and 4.14.

the following probabilistic formulae are exploited

$$N_{\mathrm{B}}^{X} = \epsilon_{\mathrm{hadr}}^{2} \times \sum_{n=2}^{n_{\mathrm{max}}} N_{n}^{X} \frac{n!}{2!(n-2)!} \tag{4.13}$$

or, in case of $Z \to ee$ process

$$N_{\mathrm{B}}^{Z\to ee} = \epsilon_{\mathrm{hadr}} \cdot \epsilon_{\mathrm{e}} \times \sum_{n=2}^{n_{\mathrm{max}}} N_{n}^{Z\to ee}(n-1), \tag{4.14}$$

where ϵ_{hadr} (ϵ_{e}) is the probability to misreconstruct hadronic jet (single electron) as an electron-jet, and N_n^X is the number of events in simulated MC sample (multi-jet data template), featuring exactly n hadronic jets per event. Candidate jets (electrons) are required to fulfil the $\mathrm{E_T}$ and η selection criteria (Section 4.3.2).

$$\begin{aligned} \epsilon_{\mathrm{hadr}} &= 4.5 \pm 0.5 \;\; \times 10^{-4} \\ \epsilon_{\mathrm{e}} &= 3.0 \pm 1.0 \;\; \times 10^{-3} \end{aligned}$$

ϵ_{hadr} and ϵ_{e} are obtained using W+jets and $Z \to ee$ MC samples respectively. Uncertainties include statistical and systematic components and are conservatively rounded up. Few different MC generators were used and the corresponding variation of ϵ was taken as a systematic uncertainty of determination of ϵ.

The expected background yields for all contributing SM processes, obtained using Eqs. 4.13 and 4.14, are listed in Table 4.6. Closure tests are performed to estimate the systematic uncertainty of background determination with the Monte Carlo approach. Namely, f_{CH}, f_{EM} and track p_{T} selection criteria were relaxed, and observed yields after the final selection were compared to yields, obtained using Eqs. 4.13, 4.14, in all considered MC

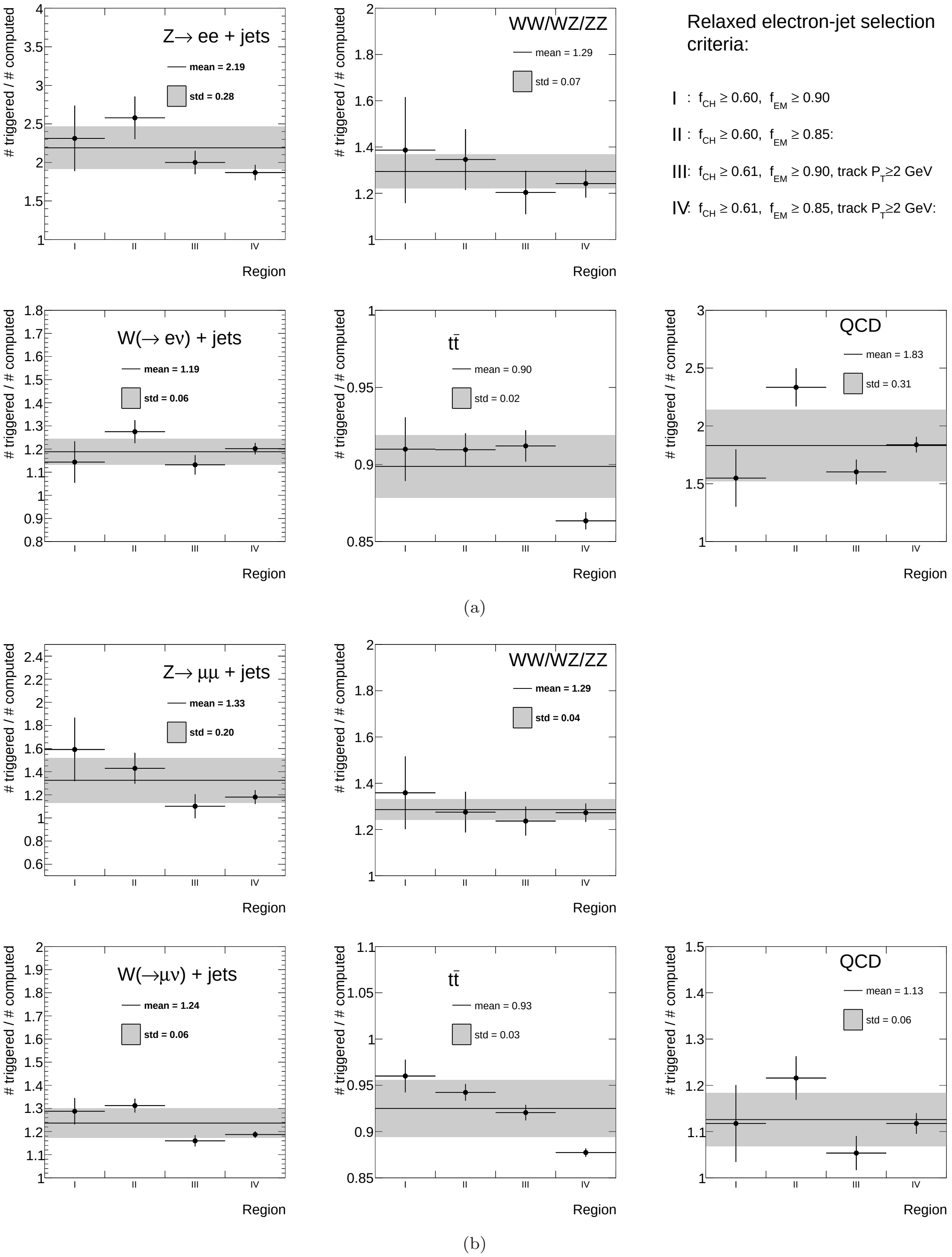

(a)

(b)

Figure 4.19: The ratio of number of events observed in $W \rightarrow e\nu$ (a) and $W \rightarrow \mu\nu$ (b) selection channels and satisfying the the relaxed electron-jet pair selection criteria, to the number of events, obtained using Eqs. 4.13 and 4.14. Electron-jet selection criteria are relaxed according to one of four configurations, given in the legend. Each plot corresponds to one of simulated MC processes (multi-jet data templates).

samples and multi-jet data templates. The selection criteria were relaxed according to one of four configurations

- **I**: $f_{CH} \geq 60$, $f_{EM} \geq 090$;
- **II**: $f_{CH} \geq 60$, $f_{EM} \geq 085$;
- **III**: $f_{CH} \geq 61$, $f_{EM} \geq 090$, tracks $p_{\mathrm{T}} \geq 2$ GeV;
- **IV**: $f_{CH} \geq 61$, $f_{EM} \geq 085$, tracks $p_{\mathrm{T}} \geq 2$ GeV;

The highest deviation of about 100% is observed in $Z \to ee$ MC sample, as can be seen in Fig. 4.19. The second-leading source of systematic uncertainty in this method is due to mismodelling of f_{HT} parameter (see Section 4.5). Finally, combining $W \to e\nu$ and $W \to \mu\nu$ selection channels, the expected background yield is

$$n_{\mathrm{bckg}} = 0.21 \pm 0.21 \text{ (method) } \pm 0.10 \text{ (}f_{HT}\text{ miss-modelling)} \pm 0.05 \text{ (stat)}$$

4.4.2 Background determination with the ABCD method

The ABCD technique is based on counting events in control and signal regions. In this method, two signal selection criteria, (1) and (2), are considered, and events are classified into four regions depending on whether or not events meet either criterion: signal region A – events fulfils both criteria, control region B – event fulfils the first criterion and fails to pass the second criterion, control region C – event fails to pass the first criterion and fulfils the second criterion, and control region D – events fails to pass both criteria. The kinematic distribution of events with respect to parameter (1) is required to be similar in both regions where events pass and do not pass the selection criterion (2), and vice-versa. In other words, in the perfect case, the two selection parameters must be uncorrelated. The background in the signal region is extracted from the yield in the control regions. In this analysis, events are assigned to one of four regions according to whether or not the jets meet the f_{EM} and the track-quality conditions of the electron-jet classification (see Fig. 4.20). These two conditions are chosen because they are less correlated than other selection variables that could have been used. The background yield in the signal region is thus given by

$$n_{\mathrm{bkgd}} = N_A^{\mathrm{predicted}} = \frac{N_B \cdot N_C}{N_D} \cdot \mathrm{c_{MC}} \ , \tag{4.15}$$

where $\mathrm{c_{MC}} = 0.36$ is the correction factor determined from MC simulation that corrects for the effect of the correlations between the two selection criteria. N_i is the number of events observed in region i.

The regions are defined as:

(A) Signal region: Two jets with $f_{\mathrm{EM}} \geq 0.99$ are required; for both jets $N_{\mathrm{track}} \geq 2$, i.e. the number of tracks associated with the candidate jets and fulfilling the requirements of the electron-jet selection must be greater than two (see Section 4.3.2).

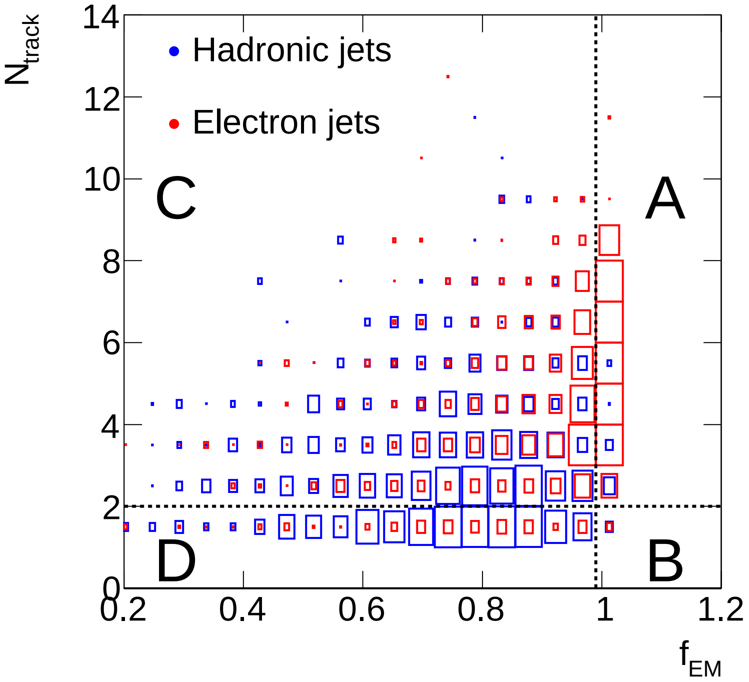

Figure 4.20: Distribution of jets in the combined plane of the f_{EM} and N_{track} parameters. Jets are required to have at least one track, fulfilling the quality criteria of Section 4.3.2, plus at least one additional track with the relaxed f_{HT} selection criterion associated with a jet. Track p_{T} requirement is loosened to 2 GeV. Electron-jets in simulated signal process (red histogram) and hadronic jets in simulated W+jets background process (dark-blue histogram) are shown. Simulated MC sample for three-step model, $m_{\gamma_{\mathrm{d}}} = 100$ MeV, is taken for electron-jets. Dashed lines indicate the electron-jet selection criteria. In the ABCD method of background determination, events in the data are assigned to one of four regions depending on whether or not jets in event meet the f_{EM} and N_{track} selection criteria, as described in Section 4.4.2.

(B) Anti-track quality region: At least one jet must fail the associated track requirements of the electron-jet selection. Each of the two candidate jets must have two associated tracks separated by $\Delta R < 0.1$, both tracks satisfying looser requirements $p_{\mathrm{T}} \geq 2$ GeV and $f_{\mathrm{HT}} > 0$. At least one of these tracks must fail the requirement $f_{\mathrm{HT}} > 0.08$.

(C) Anti-f_{EM} region: At least one jet must fail the condition $f_{\mathrm{EM}} \geq 0.99$.

(D) Anti-track quality and anti-f_{EM} region: Both conditions “B” and “C” are fulfilled.

4.4.2.1 Monte Carlo correction factor, c_{MC}

In ABCD method it is important that the two considered selection criteria are uncorrelated. In some cases, however, it is impossible to find completely uncorrelated variables, as is the case in our analysis. Here, the two selection criteria are f_{EM} and the track-quality conditions. These two were checked to have the minimal correlation than other pairs of variables that could have been used, for example, f_{EM} and f_{CH} pair. The residual correlation is taken into account using modified ABCD formula

$$\frac{N_A^{\mathrm{data}}/N_A^{\mathrm{MC}}}{N_C^{\mathrm{data}}/N_C^{\mathrm{MC}}} = \frac{N_B^{\mathrm{data}}/N_B^{\mathrm{MC}}}{N_D^{\mathrm{data}}/N_D^{\mathrm{MC}}} \tag{4.16}$$

or

$$N_A^{\mathrm{predicted}} \equiv N_A^{\mathrm{data}} = \frac{N_B^{\mathrm{data}} N_C^{\mathrm{data}}}{N_D^{\mathrm{data}}} \times \frac{N_A^{\mathrm{MC}}}{N_C^{\mathrm{MC}}} \frac{N_D^{\mathrm{MC}}}{N_B^{\mathrm{MC}}} \tag{4.17}$$

Hence, the essence of correction factor in Eq. 4.15, c_{MC}, can be seen

$$c_{\mathrm{MC}} \equiv \frac{N_A^{\mathrm{MC}}}{N_C^{\mathrm{MC}}} \frac{N_D^{\mathrm{MC}}}{N_B^{\mathrm{MC}}} \tag{4.18}$$

Equivalently, one can determine the correction factor by re-weighting f_{EM} distributions of jets fulfilling anti-track quality requirement in the data. The weights are obtained from Monte Carlo simulation as a relative difference between f_{EM} distributions of jets in the region with nominal track-quality selection and those in the anti-track quality one. As can be seen in Fig. 4.21, as re-weighting is applied, the shapes of f_{EM} distributions in the data, with nominal and anti-track quality selections, agree well within statistical uncertainties. In other words, the f_{EM} distributions become "decorrelated". The correction factor is determined as follows

$$c_{\mathrm{MC}} = \frac{f_{A,C}^{\mathrm{leading}}}{f_{B,D}^{\mathrm{leading}}} \frac{f_{A,C}^{\mathrm{second}}}{f_{B,D}^{\mathrm{second}}} \tag{4.19}$$

where f denotes the relative fraction of jets fulfilling f_{EM} selection requirement. For convenience, leading-p_{T} and second-leading jets are treated separately, and are taken after W selection, f_{CH} selection, and either track-quality selection (A, C) or anti-track quality selection (B, D). The numbers are obtained using simulated samples (multi-jet data templates), taken with the appropriate normalization.

4.4.2.2 Alternate ABCD splitting

To estimate the possible dependence on the specific choice of regions in this method, alternate splitting of regions is performed with omitted requirement of cone separation between tracks in anti-track quality selection. As can be seen in Fig. 4.22, in that case, the difference between shapes of f_{EM} distributions with track-quality and anti-track quality selections is higher than that of the baseline anti-track quality definition. In other words, the correlation between f_{EM} and track-quality jet selection criteria is much higher in this case, and the correction factor is $c_{\mathrm{MC}} = 0.08$. The event yields in all regions are given in Table 4.7 for two considered types of ABCD selection. The predicted background yields in the signal region are shown in Fig. 4.23 with the corresponding statistical uncertainties originating from small number of events in region 'B'. Finally, the background prediction

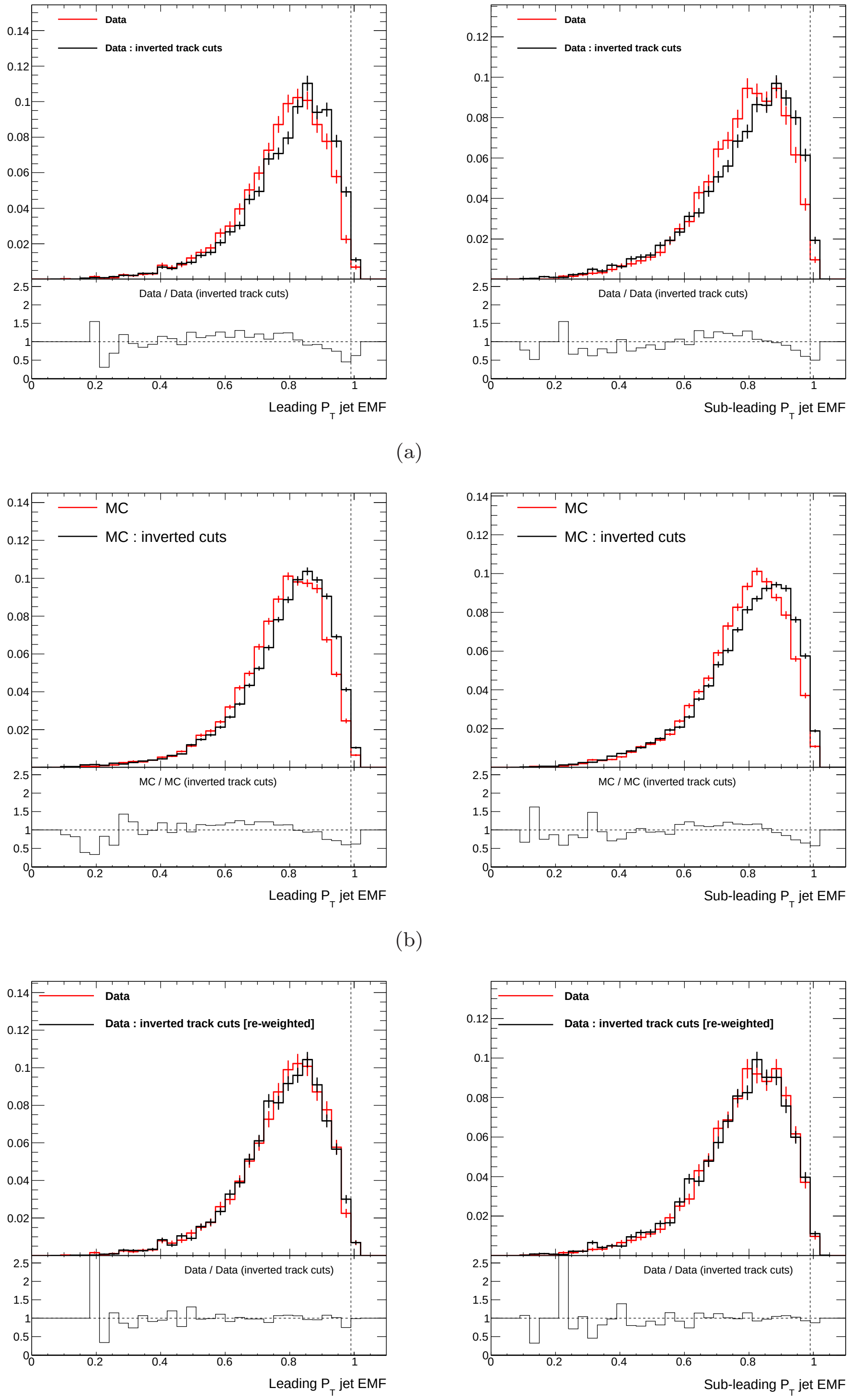

(a)

(b)

(c)

Figure 4.21: Distribution of jet electromagnetic fraction, f_{EM}, for leading-p_{T} (left) and second-leading-p_{T} (right) jets, after the W selection. Red histograms correspond to events where jets fulfil nominal track-quality selection criteria, while black histograms correspond to events falling into anti-track quality region. Jets are required to fulfil $\mathrm{E_T}$ and η requirements. The distributions are shown for (a) data, (b) for combination of properly normalized simulated MC samples and multi-jet data templates, and (c) for data after re-weighting f_{EM} jet distributions in anti-track geniality region, as described in Section 4.4.2.1.

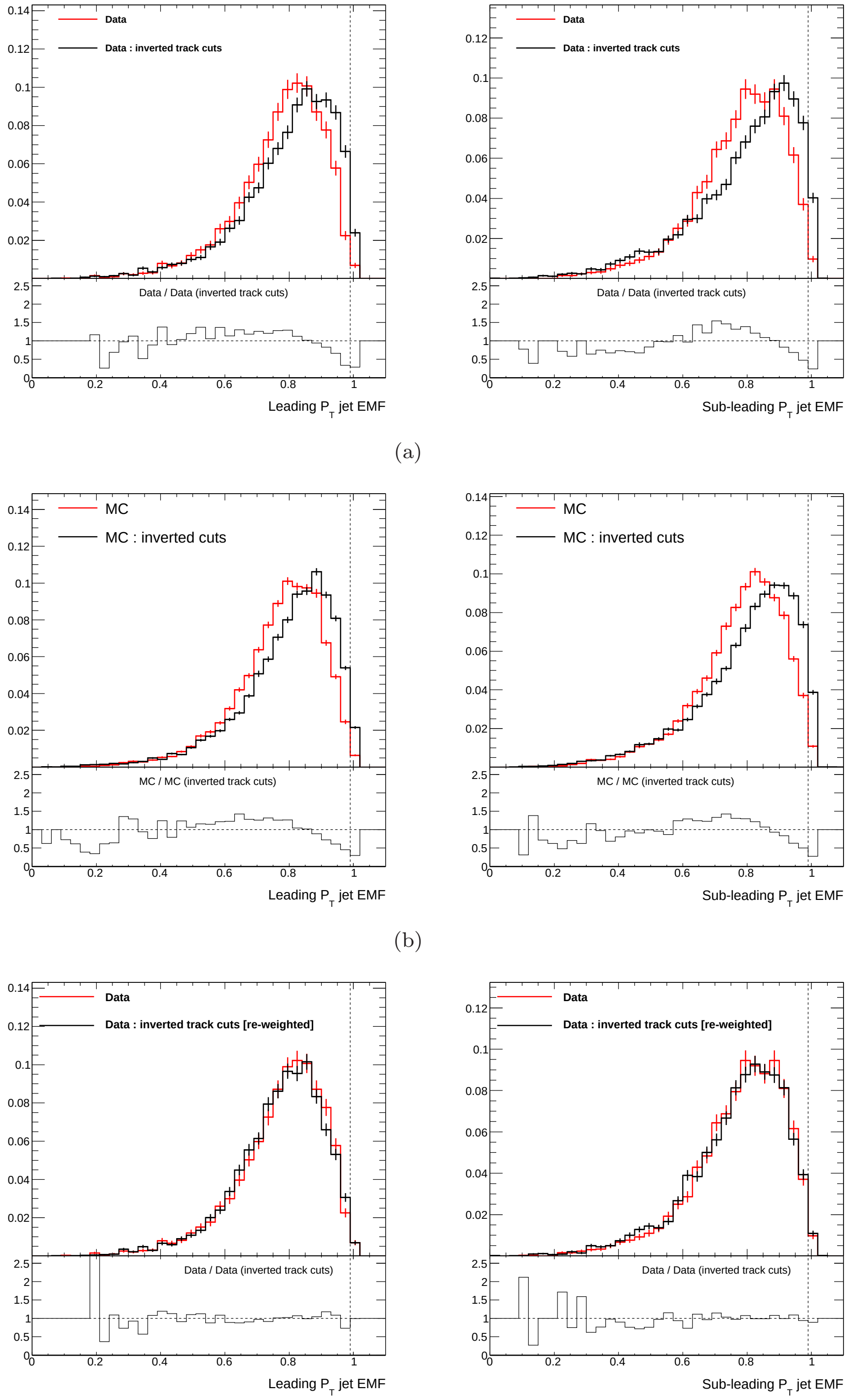

(a)

(b)

(c)

Figure 4.22: Distribution of jet electromagnetic fraction, f_{EM}, for leading-p_{T} (left) and second-leading-p_{T} (right) jets, after the W selection. Red histograms correspond to events where jets fulfil nominal track-quality selection criteria, while black histograms correspond to events falling into anti-track quality region. Jets are required to fulfil $\mathrm{E_T}$ and η requirements. The distributions are shown for (a) data, (b) for combination of properly normalized simulated samples and multi-jet data templates, and (c) for data after re-weighting f_{EM} jet distributions in anti-track geniality region (c), as described in Section 4.4.2.1. Anti-track quality region with omitted ΔR-requirement (Section 4.4.2.2) is used here.

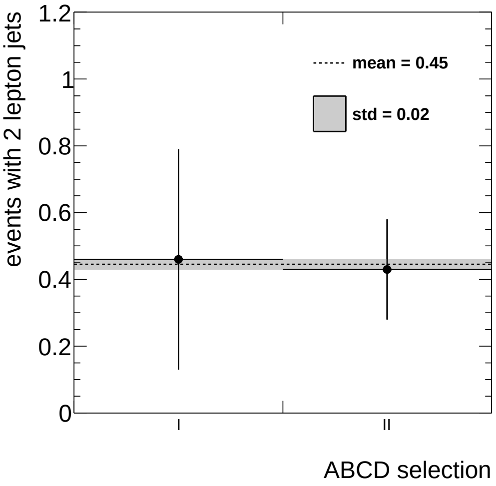

Figure 4.23: The predicted background yield as obtained with ABCD method, given with respect to two different selection of ABCD regions, considered in the analysis. The first selection is taken as a baseline, since the MC correction factor is minimal in this case. The difference between two yields is treated as a systematic uncertainty of the method.

	Data	Expected background	Expected signal, $m_H = 100$ GeV
		Baseline ABCD selection (I)	
A	Signal region	0.17 ± 0.07	14.3 ± 1.7
B	2	1.44 ± 0.44	0.4 ± 0.3
C	3913	4287 ± 450	8.6 ± 1.3
D	6071	7885 ± 981	1.0 ± 0.4
		Cross-check ABCD selection (II)	
A	Signal region	0.17 ± 0.07	14.3 ± 1.7
B	8	7.06 ± 1.07	-
C	3913	4287 ± 450	8.6 ± 1.3
D	5993	7686 ± 1143	0.2 ± 0.2

Table 4.7: The expected number of background and signal events in 2.04fb^{-1}of data, as well as the number of events observed in the data, in each region of ABCD selection. Two types of ABCD selection are shown. Baseline and cross-check selections are described in Sections 4.4.2 and 4.4.2.2 respectively. The signal predictions correspond to the three-step model with m_H=100 GeV and $m_{\gamma_{\rm d}}$=100 MeV. The background expectations include statistical and systematic uncertainties. The uncertainties shown for signal are statistical only.

with this method is

$$n_{\mathrm{bckg}} = 0.46 \pm 0.32\ (\mathrm{stat})\ \pm 0.09\ (\text{signal contamination})\ \pm 0.02\ (\text{ABCD selection})$$

4.4.3 Background determination with the matrix method

In the matrix method, one defines a "loose" electron-jet selection criterion by relaxing the minimum track p_{T} requirement from 5 GeV to 2 GeV. The fraction f is the ratio of the number of background jets passing the nominal signal selection N_T to that passing the loose selection N_L:

$$f = \frac{N_T}{N_L}. \tag{4.20}$$

The following equations, usually referred to in the matrix method [211, 212], take place

$$\begin{pmatrix} n_{TT} \\ n_{TL} \\ n_{LT} \\ n_{LL} \end{pmatrix} = \begin{pmatrix} r^2 & rf & fr & f^2 \\ r(1-r) & r(1-f) & f(1-r) & f(1-f) \\ (1-r)r & (1-r)f & (1-f)r & (1-f)r \\ (1-r)^2 & (1-r)(1-f) & (1-f)(1-r) & (1-f)^2 \end{pmatrix} \begin{pmatrix} n_{RR} \\ n_{RF} \\ n_{FR} \\ n_{FF} \end{pmatrix} \tag{4.21}$$

Here, r is the ratio of the number of electron-jets in a signal sample passing the nominal signal selection to that passing the loose selection. n_{TT}, n_{TL}, and n_{LL} denote respectively the number of events in the data with two jets fulfilling the tight requirement, with one jet fulfilling tight requirement and other one fulfilling loose and failing tight requirement, and with two jets, both fulfilling loose and failing tight requirement. n_{RR}, n_{FR} and n_{FF} denote the number of events with two jets that satisfy loose criteria, with both jets being electron-jets, with one electron-jet and one background jet, and with both background jets respectively. Next, the relative fraction of events featuring one electron-jet and one background jet that pass the loose selection criterion is zero in our signal

$$n_{RF} = n_{FR} = 0 \tag{4.22}$$

Hence, equation 4.21 is simplified

$$\begin{cases} n_{TT} = r^2 n_{RR} + f^2 n_{FF} \\ n_{TL} + n_{LT} = 2r(1-r)n_{RR} + 2f(1-f)n_{FF} \\ n_{LL} = (1-r)^2 n_{RR} + (1-f)^2 n_{FF} \end{cases} \tag{4.23}$$

The number of fake electron-jet background events passing the nominal selection criteria for two electron-jet candidates and entering the signal region is therefore:

$$n_{\mathrm{bkgd}} = f^2 n_{\mathrm{fake}}, \tag{4.24}$$

where $n_{\mathrm{fake}} \equiv n_{FF}$ is the number of background events passing the loose criterion for both electron-jet candidates. On the other hand, neglecting the signal term $(1-r)^2 n_{RR}$ in the third line of Eq 4.23, the number of fake electron-jet events in which neither electron-jet

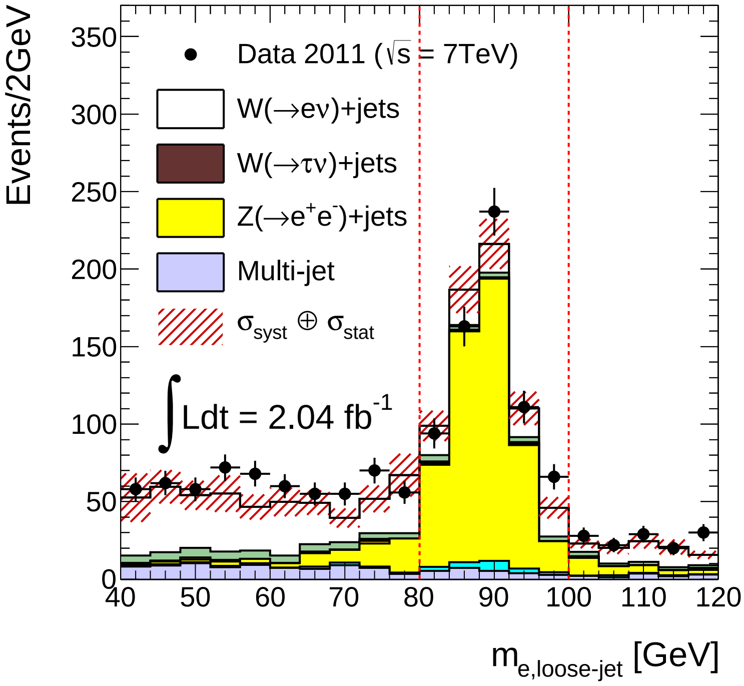

Figure 4.24: Invariant mass of electron matched to $W \to e\nu$ decay and jet that is required fulfil loose electron-jet selection criterion of Section 4.4.3, after $W \to e\nu$ selection. Dashed lines indicate the mass window where jets are selected for evaluation of $\bar{f}_e$ parameter. Data are compared to the expectation from SM processes, given by stacked histograms of different colors.

candidate passes the nominal selection criterion is

$$n_{\text{loose}} = (1-f)^2 n_{\text{fake}}. \tag{4.25}$$

where $n_{\text{loose}} \equiv n_{LL}$. Combining Eqs. (4.24) and (4.25) yields

$$n_{\text{bkgd}} = \frac{f^2}{(1-f)^2} n_{\text{loose}} = \bar{f}^2 n_{\text{loose}}, \tag{4.26}$$

where $\bar{f}$ is referred to below as the fake factor. In this way the number of background events is derived directly from the data events failing to pass the nominal criteria for both electron-jet candidates (n_{loose}), where the signal contamination has been checked to be small.

The fake factor $\bar{f}$ is measured from background-enriched data samples where the signal contamination is checked to be completely negligible. The first sample is obtained by reversing the W-candidate electron or muon selection criteria to select a sample of multi-jet background with kinematic characteristics similar to those of the signal sample. A fake factor is obtained from the jets in this sample. In the second sample, the fake factor is determined from a sample of jets that originate from electrons in $Z \to e^+e^-$ decays. The tight selection criteria and the lepton isolation criteria are applied to one leg of the Z boson candidate, and the invariant mass of this electron and the candidate jet, $m_{e,\text{jet}}$,

Method of background estimation		Estimated background yield
Matrix	(baseline)	0.41 ± 0.29 (stat) $\pm$ 0.12 (syst)
ABCD	(cross-check)	0.46 ± 0.32 (stat) $\pm$ 0.10 (syst)
MC	(cross-check)	0.21 ± 0.05 (stat) $^{+\,0.23}_{-\,0.21}$ (syst)

Table 4.8: Estimated number of background events after the final selection, including statistical and systematic uncertainties, from three different methods. The matrix method is used for the background estimate while the ABCD and MC methods provide a cross-check of the matrix method.

is required to fall in the range 80 GeV $< m_{e,\mathrm{jet}} <$ 100 GeV.

$$\begin{aligned}
\bar{f}_{\mathrm{hadronic}} &= \frac{172}{426} = 0.40 \pm 0.03 \quad \text{from multi-jet data template in } W \to e\nu \text{ channel} \\
\bar{f}_{\mathrm{hadronic}} &= \frac{716}{1594} = 0.45 \pm 0.02 \quad \text{from multi-jet data template in } W \to \mu\nu \text{ channel} \\
\bar{f}_{e} &= \frac{214}{457} = 0.47 \pm 0.03 \quad \text{from data template as shown in Fig. 4.24}
\end{aligned}$$

The two fake factors (hadronic and single-electron) are found to be consistent within statistical uncertainties: 0.44 ± 0.02 (stat) and 0.47 ± 0.03 (stat), respectively. The first value is used in the analysis and the difference between these two estimates is taken as a systematic uncertainty in the fake factor. The resulting value is $\bar{f} = 0.44 \pm 0.04$, where the uncertainty is the sum of the statistical and systematic uncertainties added in quadrature.

Finally, taking $n_{\mathrm{loose}} = 2$ obtained form the data, the predicted background yield with this method is

$$n_{\mathrm{bckg}} = 0.41 \pm 0.29(\mathrm{stat}) \pm 0.09(\text{fake factor}) \pm 0.08(\text{signal contamination})$$

The resulting background yields, together with the evaluated statistical and systematic uncertainties, are given in Table 4.8. The estimates from the different background evaluation methods agree well within the uncertainties.

4.5 Systematic uncertainties

The systematic uncertainties considered for the signal are given in Table 4.9 and described in detail below:

1. **Monte Carlo statistics:** The uncertainty due to the limited number of Monte Carlo signal events is 13%.
2. **Luminosity**: The uncertainty in the integrated luminosity is determined to be 3.7% [200, 201].

3. **Signal cross sections:** The uncertainty of the SM WH production cross section at Higgs mass $m_H = 125$ GeV is $^{+3.7\%}_{-4.3\%}$ [213]. For 100 GeV and 140 GeV Higgs mass the corresponding uncertainties are ±4% [213].

4. **Electron and muon efficiency:** The combined uncertainty on the efficiency of the lepton trigger, identification and isolation as well as transverse impact parameter requirements is found to be 5% for electrons and 3% for muons. The uncertainties were derived using data-driven methods [195, 197].

5. **Jet electromagnetic and charged particle fractions (f_{EM} and f_{CH}):** The uncertainty due to possible mismodelling of these parameters, which impacts the signal acceptance, are studied by comparing the measured f_{EM} and f_{CH} line shape for jets, which are matched to electron from W-decay, to the one predicted by the simulation. They are found to be 3% and 0.1% for f_{EM} and f_{CH}, respectively.

6. **Fraction of high-threshold hits in the TRT (f_{HT}):** Mismodelling of the f_{HT} distribution in the simulation has been previously studied [163, 195]. The impact of this mismodelling on the signal efficiency was checked using the data samples, enriched with highly collimated pairs of electron tracks, as described in Section 4.5.3, and is found to be less than 1%.

7. **Electron and muon energy/momentum scale and resolution:** These uncertainties are evaluated by varying the corresponding correction factors, described in Sections 4.1 and 4.3.1, within their systematic uncertainties. This results in the corresponding uncertainties of 0.2%, 0.5% and 0.5% for electron/muon energy resolution and electron energy scale respectively.

8. **Pile-up impact:** The effect of additional inelastic collisions overlapping with the primary hard scatter (pile-up) on the signal efficiency has been evaluated using simulated signal samples and found to be negligible.

The systematic uncertainties on the background determinations are given in Table 4.10 and are estimated in the following ways:

- **Matrix method:** The uncertainty is assessed by varying the fake factor within its uncertainty and is summed in quadrature with the statistical uncertainty on the number of events observed in the loose region. An uncertainty due to possible signal contamination is also taken into account. These result in an 80% uncertainty in the background yield.

- **ABCD method:** The uncertainty is assessed by employing different region selections in the ABCD method and the difference between yields is treated as a systematic uncertainty. The uncertainty due to limited statistics in region B is also considered. The resulting uncertainty in the background yield is 75% with this method.

- **MC method**: The largest contributions to the uncertainty on the background yield are the systematic uncertainty on the MC-based prediction on the probability

Systematic Source	Systematic Uncertainty
(1) Monte Carlo statistics	13%
(2) Luminosity	3.7%
(3) $\sigma \times$ BR	$^{+3.7}_{-4.3}\%$
(4) Electron efficiency	5%
(4) Muon efficiency	3%
(5) f_{EM} modelling	3%
(5) f_{CH} modelling	0.1%
(6) f_{HT} modelling	1%
(7) Electron energy scale	0.5%
(7) Electron energy resolution	0.2%
(7) Muon momentum resolution	0.5%
(8) Pile-up	<0.1%
Total	15%

Table 4.9: Systematic uncertainties for the signal. The numbers in parentheses refer to the descriptions in the numbered list in the text. All uncertainties are applied to the combination of $W \to e\nu$ and $W \to \mu\nu$ channels; the only exceptions are the specific electron and muon uncertainties in items (4) and (7), and are applied separately. The total uncertainty is conservatively rounded and is given for the combination of channels.

of two or more jets to be incorrectly identified as electron-jets (100%), modelling of f_{HT} (50%), f_{CH} (10%), f_{EM} (10%). The choice of MC generators and multi-jet data templates contributes about 10% each, as described in Section 4.5.1. The assigned theoretical uncertainties on the cross sections are 4% ($W \to \ell\nu$, $Z \to \ell\ell$), 5% ($W \to \tau\nu$, $Z \to \tau\tau$, WZ/ZZ) and 7% ($t\bar{t}$, WW), respectively [190, 191]. Limited MC sample sizes contributes a 5% uncertainty. The total uncertainty of background estimation with MC method is 110%.

4.5.1 Choice of MC generator and multi-jet data template

A considerable fraction of background comes from the QCD multi-jet production. The systematic uncertainty related to the choice of multi-jet data template is estimated from the comparison of two data templates, corresponding to different ways of relaxing the muon (electron) isolation criteria (see Figs. 4.25c and 4.25d).

To take into account the possible variation of the background on the parton shower, underlying event and fragmentation models, further MC samples were checked in addition to that generated with the baseline MC generators. Namely, SHERPA [186] is compared with ALPGEN [181], which is used as a primary MC generator for W+jets (Z+jets) processes, and POWHEG [188] was compeered with M@NLO [185], which is the primary ATLAS choice for $t\bar{t}$ processes (see Figs. 4.25a and 4.25b).

The relative difference from two MC generators (two different multi-jet data templates) is taken as the systematic uncertainty. These uncertainties are used in all figures where

Systematic Source	Systematic Uncertainty
Matrix method (baseline)	
Statistics of events in loose region	71%
Possible signal contamination in loose region	20%
Fake factor	22%
Total	80%
ABCD method (cross-check)	
Statistics in region B	71%
Possible signal contamination in region B	20%
Selection of ABCD regions	5%
Total	75%
MC method (cross-check)	
Uncertainty of probabilistic approach	100%
f_{HT} modelling	50%
f_{EM} modelling	10%
f_{CH} modelling	10%
$\sigma \times BR$	4% ($W \to \ell\nu / Z \to \ell\ell$)
	5% ($W \to \tau\nu / Z \to \tau\tau$)
	7% ($t\bar{t}$)
	7% (WW)
	5% (WZ/ZZ)
Luminosity	3.7%
Electron reconstruction efficiency	2%
Electron energy resolution	0.2%
Electron energy scale	0.5%
Electron isolation + impact parameter	4%
Muon isolation + impact parameter	2%
Muon reconstruction efficiency	1.8%
Muon momentum resolution	0.2%
Choice of multi-jet data template	10%
Choice of W/Z+jets MC generator	10%
Choice of $t\bar{t}$ MC generator	5%
Monte-Carlo statistics	5%
Total	115%

Table 4.10: Systematic uncertainties for the background using three methods of background determination. All uncertainties are applied to the combination of $W \to e\nu$ and $W \to \mu\nu$ channels; the only exceptions are the specific electron and muon uncertainties in the MC method, and are applied separately. The total uncertainty is conservatively rounded and is given for the combination of channels.

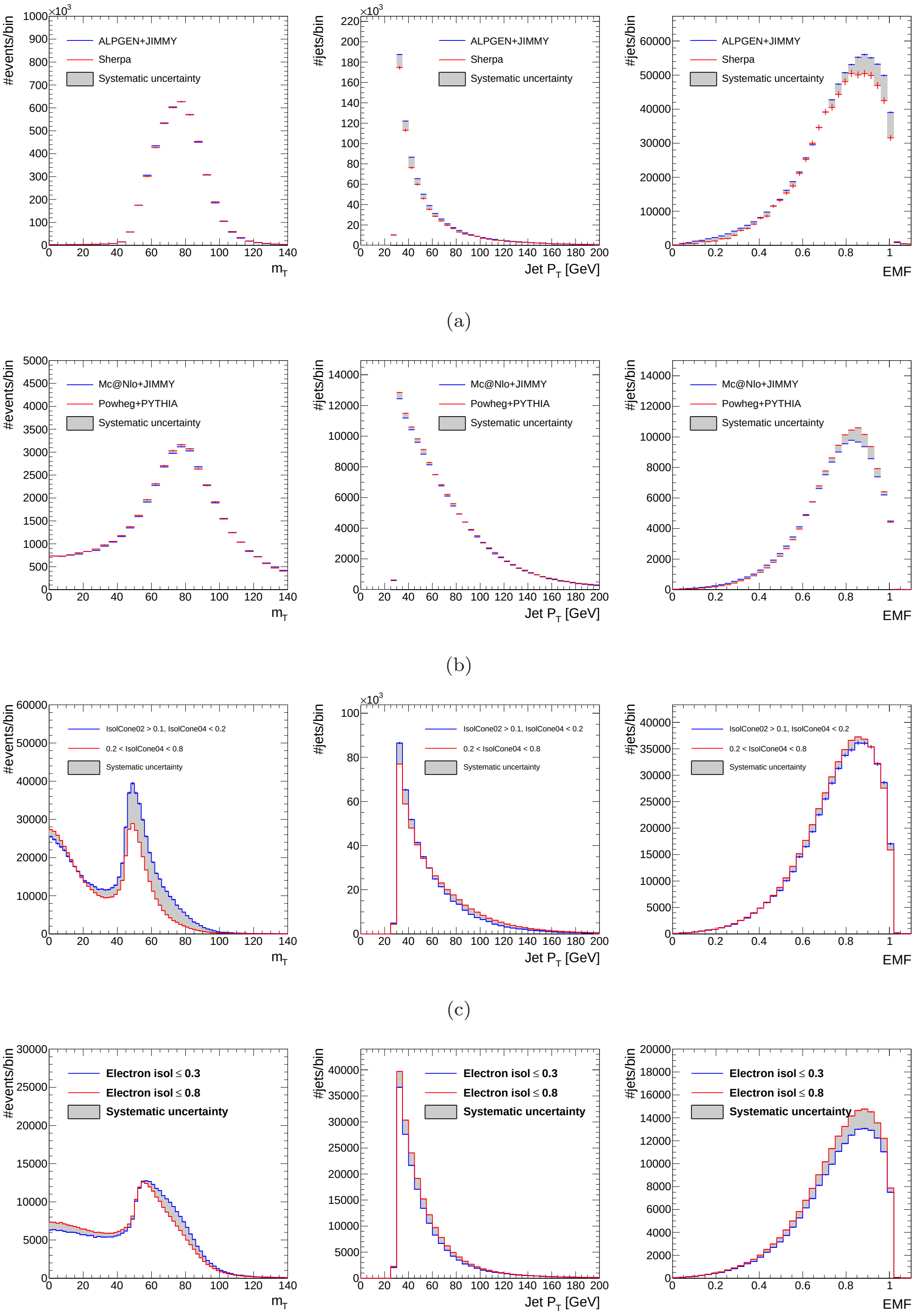

(a)

(b)

(c)

(d)

Figure 4.25: Distribution of the transverse mass of W candidates, m_{T} (left), transverse momentum of jests after W selection, p_{T} (middle), and jet electromagnetic fraction after W selection, f_{EM} (right). Distributions are shown for W+jets simulated samples (a), $t\bar{t}$ simulated samples (b), multi-jet data templates used in $W \to \mu\nu$ channel (c), and multi-jet data templates of $W \to e\nu$ channel (d). Different MC generators are compared with each other and the relative difference (dark shaded area) is taken as a systematic variation due to the choice of particular MC generator (multi-jet data template).

data are compared with Monte Carlo predictions, and also in the background estimation with the MC method.

4.5.2 Modelling of f_{EM} and f_{CH} parameters

The impact of possible mismatches in the modelling the jet f_{EM} and f_{CH} parameters on the efficiency of signal selection is studied in this section. We make use of the fact that the distribution of jet f_{EM} and f_{CH} parameters for electron-jets are similar to that of single high-p_{T} electrons, and, in particular, to that of the jets that are matched to electrons from W-decay, as shown in Fig. 4.26. To estimate the systematic uncertainty, the toy Monte Carlo signal samples are generated as shown in Fig. 4.27. They are produced using either regular f_{EM} (f_{CH}) distribution or the one, corrected for data/MC difference, which is taken from Fig. 4.26. The distribution of jet f_{EM} and f_{CH} in toy MC samples are shown in Fig. 4.26(a). About 100 toy Monte Carlo signal samples are generated for each parameter using regular and corrected distributions (400 samples total). The relative difference between two yields, obtained before and after the correction, is taken as a corresponding systematic uncertainty, and is found to be about 0.1% and 3% for f_{CH} and f_{EM} parameters respectively.

4.5.3 Modelling of f_{HT} parameter

The observed probability of high-threshold (HT) hits in TRT is not modelled perfectly in the MC simulation. The HT probability in data is measured to be significantly higher than in MC, resulting in a better than expected electron identification performance [163, 195]. This effect is most evident at $|\eta| > 0.6$. In our analysis we employ the fraction of HT hits in TRT, f_{HT}, for identifying tracks from electrons in electron-jets. Since the hypothetical signal comprises pairs of highly collimated electrons, it is of high importance to check whether f_{HT} parameter is properly modelled in case of close-by electron-tracks, and to study the impact of possible mismodelling on the efficiency of signal selection. The data template, enriched with $Z \to ee$ events, is used for this purpose. Selected events are required to have transverse momentum $E_{\mathrm{T}}^{\mathrm{miss}} \leq 25$ GeV, at least one tight isolated electron per event, as that of Section 4.3.1, and at least one jet, where jets must satisfy the electron-jet selection criteria (see Section 4.3.2) with the omitted N_{track} requirement. The invariant mass of selected electron and jet, $m_{e,\mathrm{jet}}$, is required to fall into the range 80 GeV$< m_{e,\mathrm{jet}} <$100 GeV. As seen in Fig. 4.28, the sample is dominated by $Z \to ee$ events, while the contribution of other processes is negligible. The distribution of jets in this sample with respect to f_{HT} of leading-p_{T} track in the jet is shown in Fig. 4.29, for different η regions. The mismodelling of f_{HT} is clearly seen.

Next, to get a data sample, enriched with highly-collimated electron pairs, the further selection is applied to the jets in the sample considered above, requiring at least one companion track with $p_{\mathrm{T}} \geq$5 GeV in addition to leading-p_{T} track in the jet. The cone separation between leading and second-leading tracks is required to be $\Delta R < 0.02$, similar to what is expected for sought signal. The additional tracks in the selected sample originate from bremsstrahlung photons that are radiated by hard electrons and that

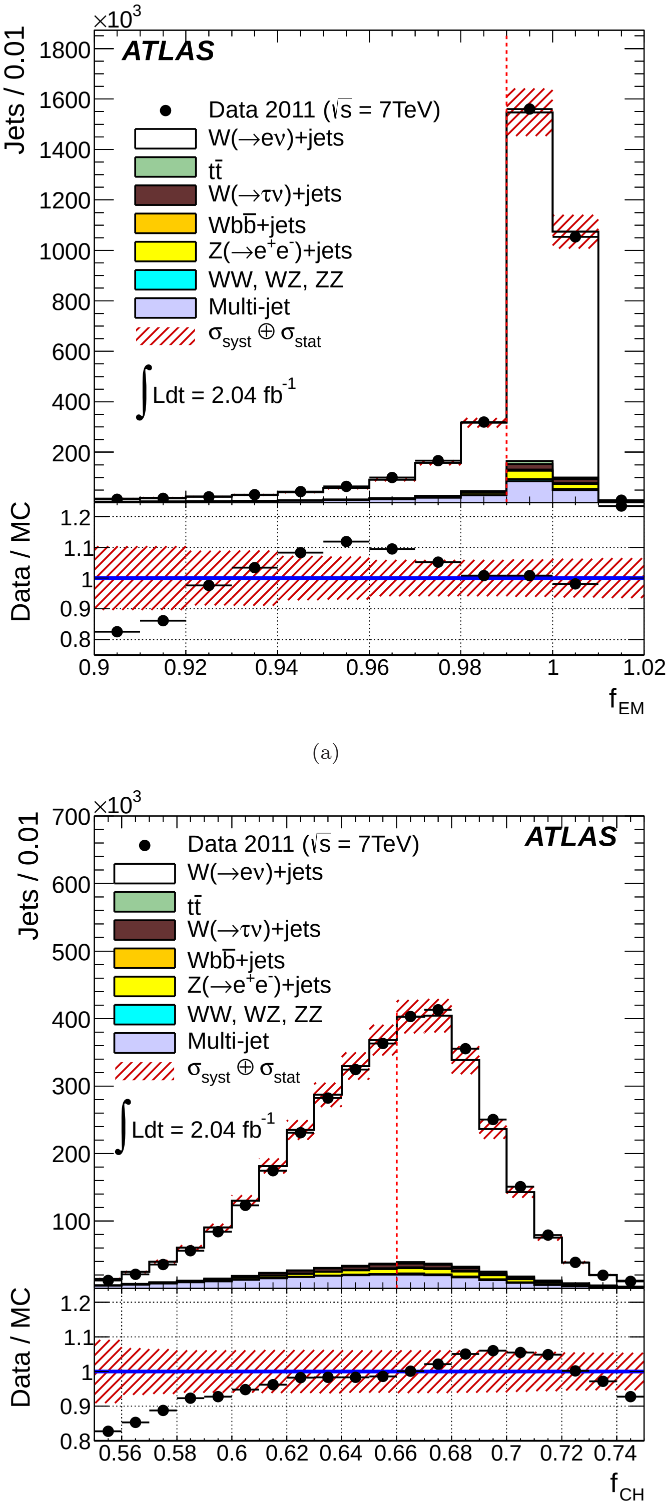

(a)

(b)

Figure 4.26: Distribution of the jet f_{EM} (top) and f_{CH} (bottom) parameters for jets that are matched to electrons of W candidate. Jets are required to fulfil $\mathrm{E_T}$ and η selection criteria of Section 4.3.2. Dashed lines indicate the values of f_{EM} and f_{CH} electron-jet selection criteria.

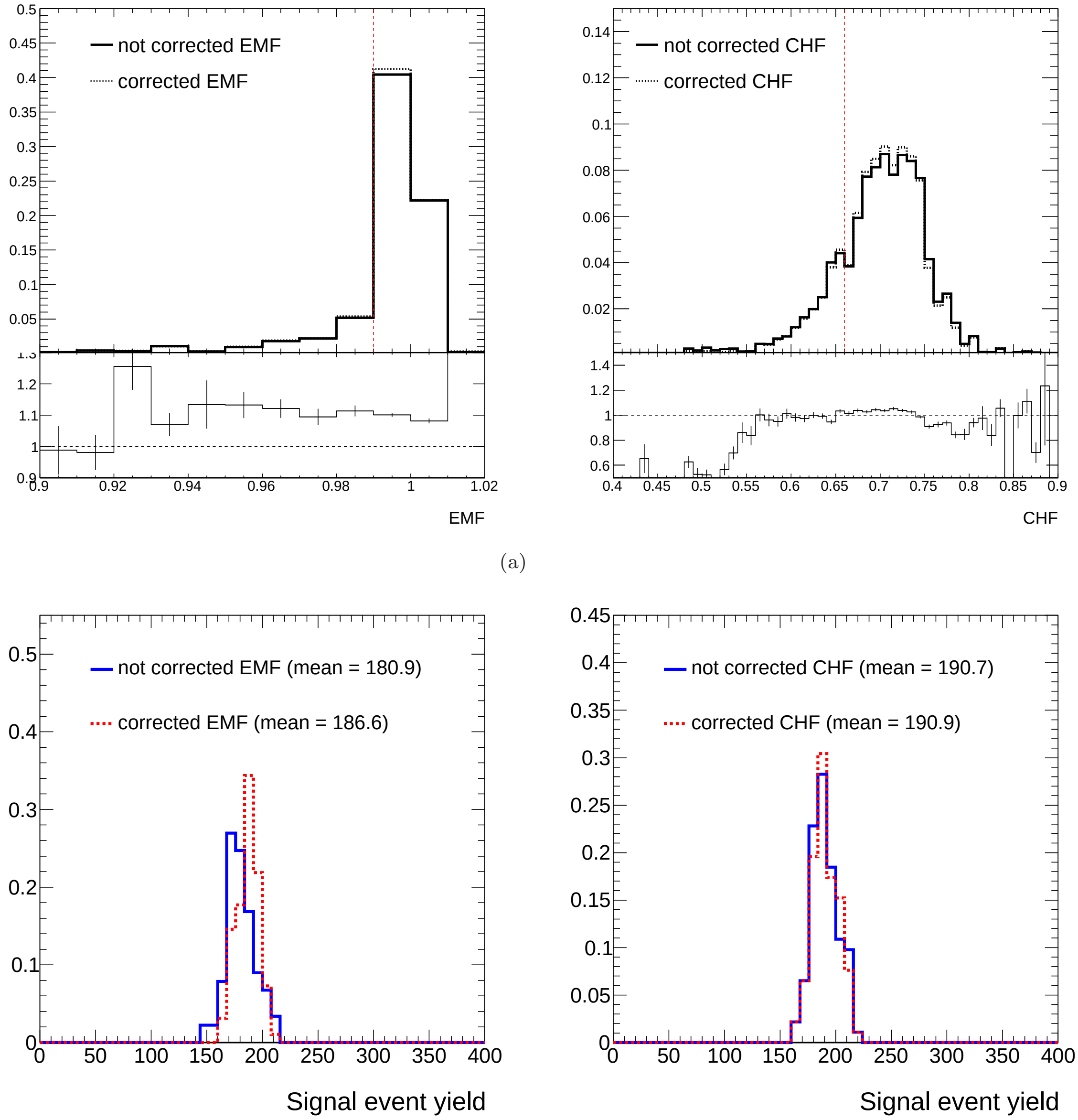

(a)

(b)

Figure 4.27: (a) distribution of the jet electromagnetic fraction, f_{EM}, and jet charged particles fraction, f_{CH} (right) in the toy Monte Carlo signal samples. (b) the distribution of toy Monte Carlo signal samples with respect to the number of events observed in the signal region, after the final selection of Section 4.3.2. Solid lines correspond to toy Monte Carlo samples generated using regular f_{EM} (left) and f_{CH} (right) distributions, and dashed lines are for that generated with corrected f_{EM} (left) and f_{CH} (right) distributions.

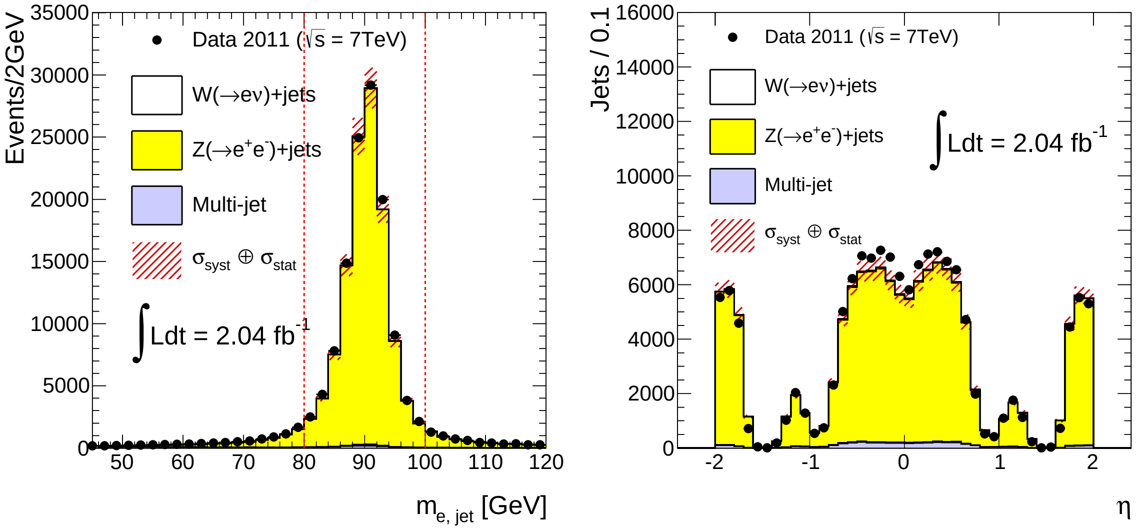

Figure 4.28: Invariant mass of tight isolated electron and jet, after f_{EM} and f_{CH} selection, and $E_{\mathrm{T}}^{\mathrm{miss}} \leq 25$ GeV requirement (left), and pseudorapidity of jet, η, after invariant mass requirement (right). Dashed lines indicate the mass window where events are selected for studies of f_{HT} parameter, as described in Section 4.5.3.

convert to electron-positron pairs in the material of the detector. The data to MC ratios of f_{HT} distributions are shown in Fig. 4.30 for leading-p_{T} and sub-leading-p_{T} tracks in the jets in the considered sample. Different η regions are considered, similar to that in Fig 4.29. As can be seen from the figure, the same mismodelling as for single-electron tracks also takes place for highly-collimated pairs of electron-tracks.

To estimate the systematic uncertainty of signal efficiency due to f_{HT} missmodelling, toy signal MC samples are generated, using either regular f_{HT} distributions, or those, corrected for data/MC discrepancy, as shown in Fig. 4.31. The relative difference between signal yields obtained with and without correction is taken as a systematic uncertainty of f_{HT} modelling, and is found to be 0.1%. In spite of the fact that mismodelling of f_{HT} is high, the uncertainty of signal selection efficiency due to this effect is small. This is because the requirement of $f_{\mathrm{HT}} \geq 0.08$ has a high efficiency for electrons, retaining most of the signal. This is not the case for the background. Namely, the f_{HT} selection criteria rejects hadrons with about 90% efficiency, keeping only those, which are in the tail of f_{HT} distribution. Therefore, the uncertainty of background determination with MC method due to this effect is as large as 50% (see Table 4.10).

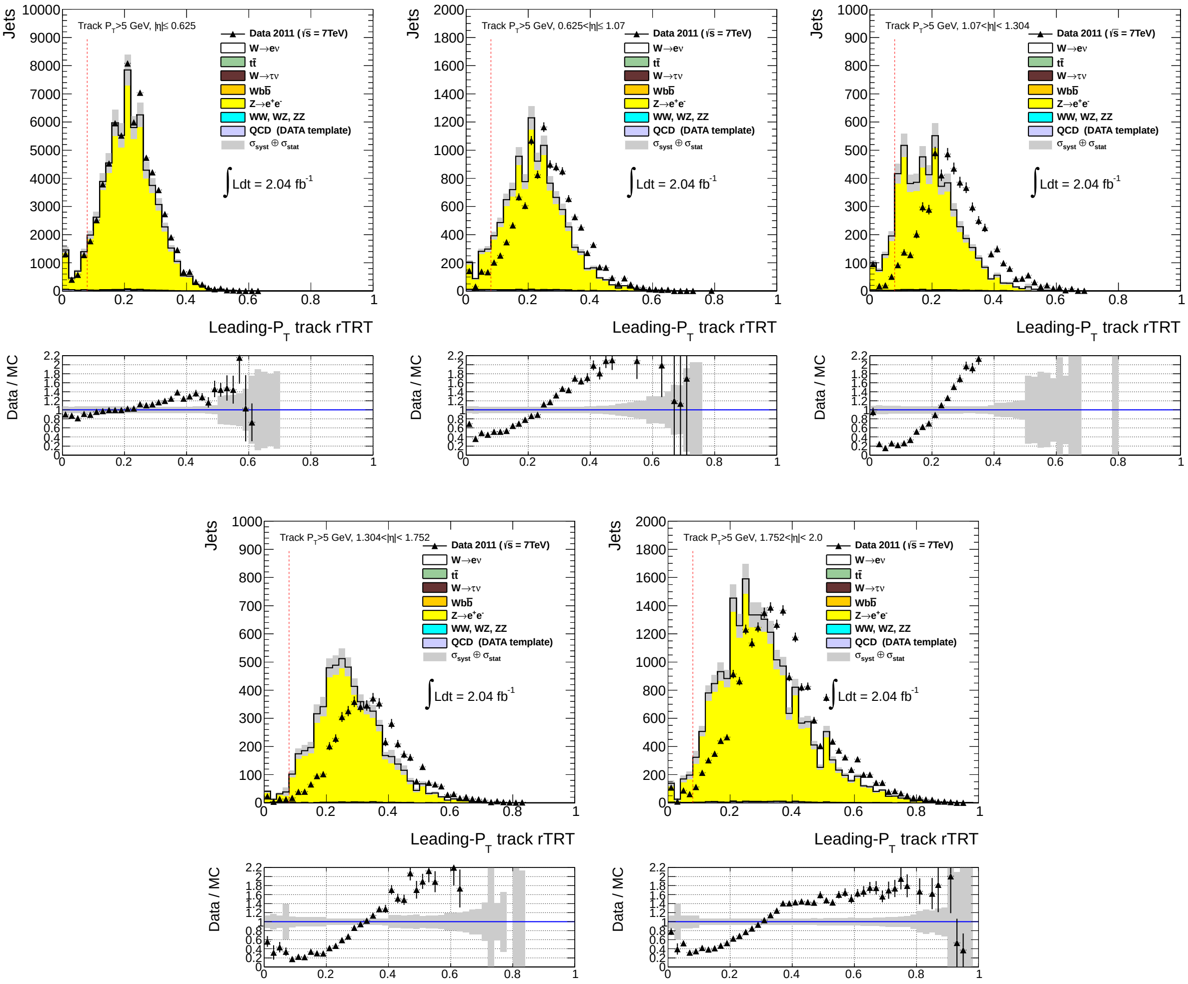

Figure 4.29: The distribution of fraction of high-threshold TRT hits, f_{HT}, for leading-p_{T} track in the jets, after the f_{EM}, f_{CH} and invariant mass selection, as described in Section 4.5.3. Five η regions are considered, $|\eta| < 0.625$ (top-left), $0.625 < |\eta| < 1.07$ (top-middle), $1.07 < |\eta| < 1.304$ (top-right), $1.304 < |\eta| < 1.752$ (bottom-left), and $1.752 < |\eta| < 2.0$ (bottom-right). The η regions are chosen similar to that in Ref. [195].

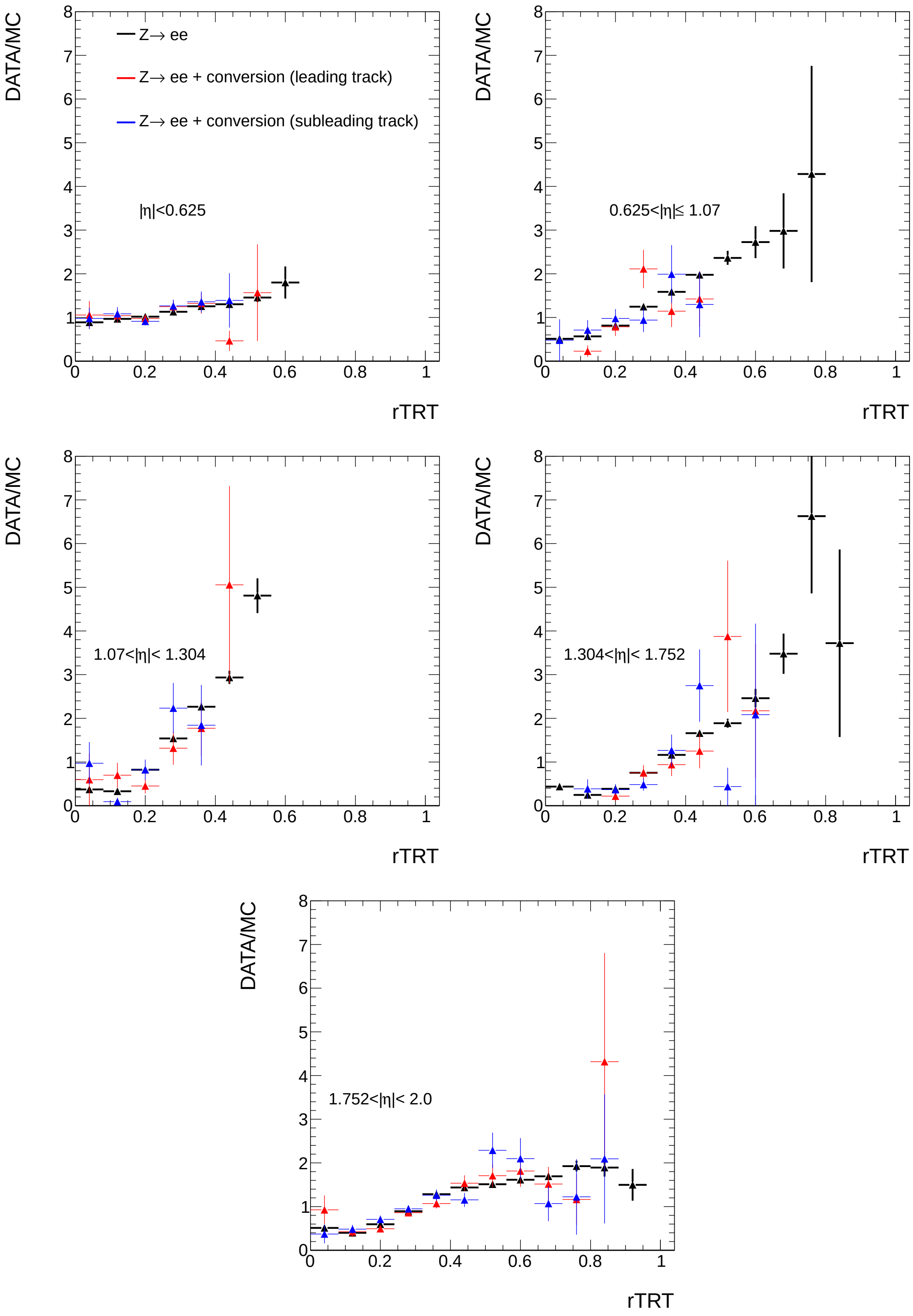

Figure 4.30: Data versus MC ratio for f_{HT} distributions of tracks in the jets in the $Z \to ee$-enriched data sample. Each figure correspond to one of η regions, similar to those in Fig. 4.29. Black dots correspond to leading-p_{T} tracks in the jets, which are shown as well in Fig. 4.29, while red (blue) dots correspond to leading-p_{T} (sub-leading-p_{T}) tracks in the jets, where jets are required to have at least one companion track in addition to the leading track, as described in Section 4.5.3.

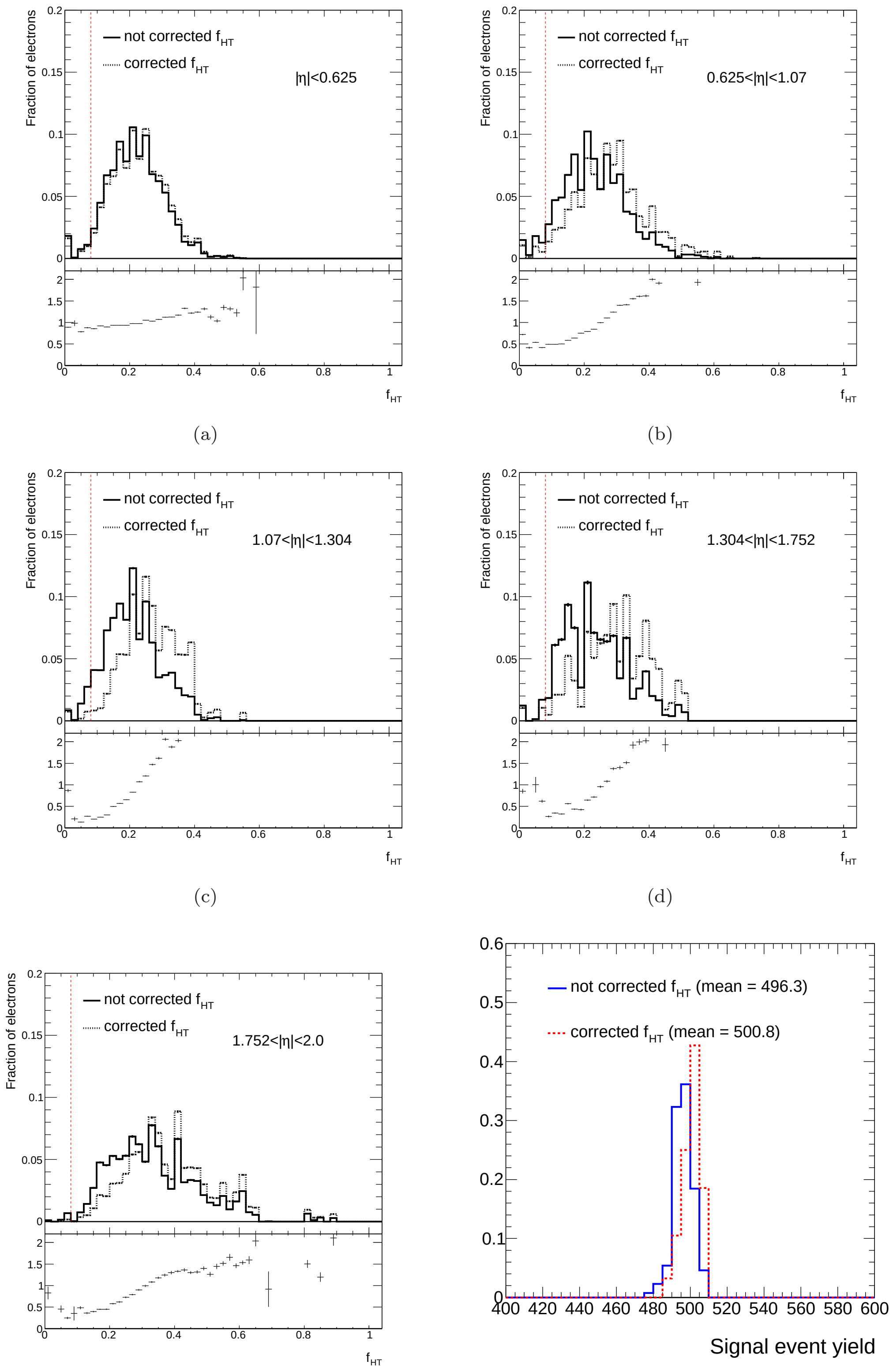

(a) (b) (c) (d) (e) (f)

Figure 4.31: Distribution of the f_{HT} of electron-tracks in the toy MC signal samples, for five η regions (a – e), and the distribution of toy MC samples with respect to the event yield, observed in the signal region (d). Toy MC samples are generated using either default (solid line) or corrected (dashed line) f_{HT} distributions, as described in Section 4.5.3.

5

Results

5.1 Final yields

The observed and predicted event yields after the final selection are shown in Table 5.1 and Fig. 5.1. The event yield in the signal region is consistent with the background-only hypothesis, with one data event passing the final selection in the $W \to \mu\nu$ channel and no data events passing the final selection in the $W \to e\nu$ channel. The display of candidate data event is shown in Appendix 7.2.

Consequently one estimates a 95% confidence limit on the signal strength, $\sigma(WH) \times \mathrm{BR}(H \to e\text{-jets})/\sigma_{\mathrm{SM}}(WH)$, where $\sigma(WH)$ denotes the WH production cross section times the sum of the branching ratios for the W boson decaying to leptons ($e\nu_e$, $\mu\nu_\mu$, $\tau\nu_\tau$)

Signal	three-step model		two-step model	
m_H (GeV)	$m_{\gamma_d} = 100$ MeV	$m_{\gamma_d} = 200$ MeV	$m_{\gamma_d} = 100$ MeV	$m_{\gamma_d} = 200$ MeV
100	$14.3 \pm 1.7 \pm 0.8$	$12.4 \pm 1.6 \pm 0.7$	$22.6 \pm 2.1 \pm 1.2$	$23.5 \pm 2.1 \pm 1.2$
125	$11.3 \pm 1.0 \pm 0.6$	$10.7 \pm 1.1 \pm 0.6$	$16.2 \pm 1.2 \pm 0.9$	$18.1 \pm 1.4 \pm 1.0$
140	$9.6 \pm 0.8 \pm 0.5$	$9.0 \pm 0.8 \pm 0.4$	$13.7 \pm 0.9 \pm 0.8$	$13.9 \pm 0.9 \pm 0.8$
Background	$0.41 \pm 0.29 \pm 0.12$			
Data	1			

Table 5.1: Numbers of expected and observed events after final selection. Expected signal yields are provided for both the three-step and two-step models with dark photon masses of 100 and 200 MeV. Statistical (first) and systematic (second) uncertainties are presented separately. The results are given for the combination of the $W \to e\nu$ and $W \to \mu\nu$ channels. One candidate event is observed in the data in the $W \to \mu\nu$ channel.

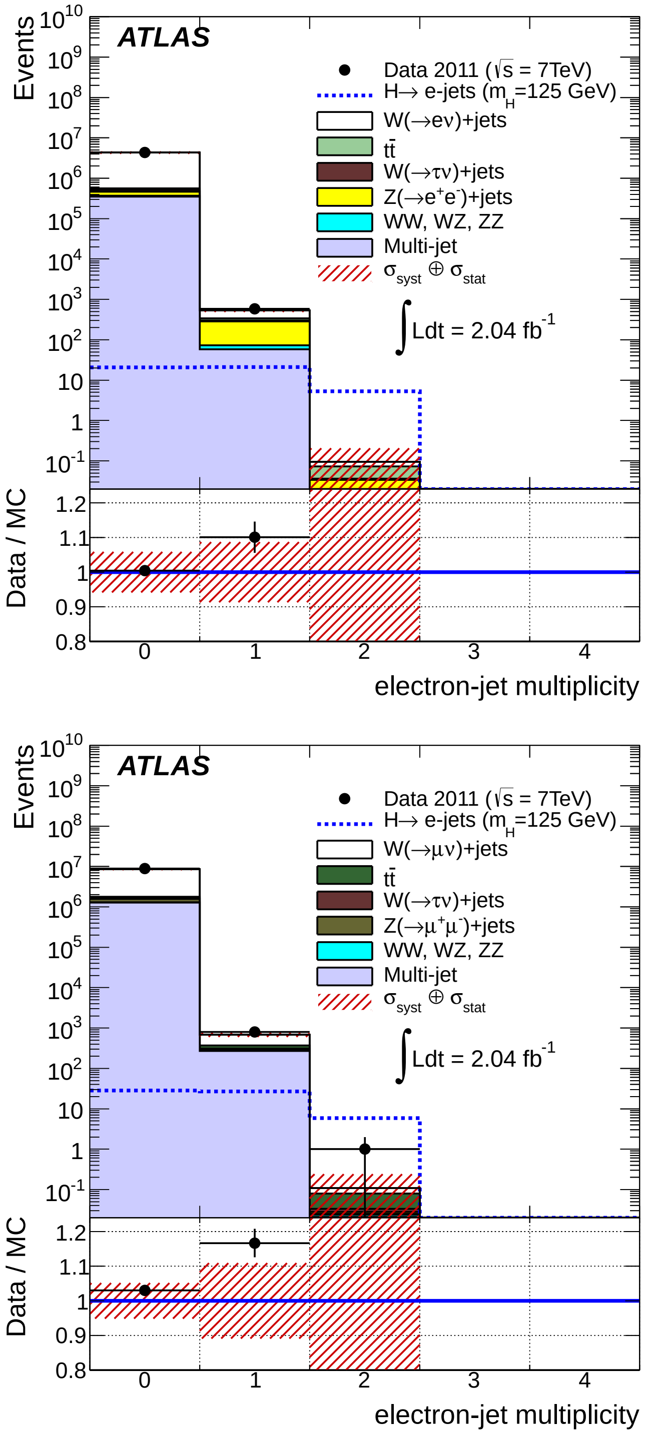

Figure 5.1: Distribution of events after (top) $W \rightarrow e\nu$ and (bottom) $W \rightarrow \mu\nu$ selection with respect to the number of tagged electron-jets per event. Data are shown by dots with error bars and are compared to the expectation from Standard Model processes, given by stacked histograms of different colors. The signal distribution in the three-step model of a hidden sector with dark photon mass $m_{\gamma_{\rm d}} = 100$ MeV is presented as a dashed histogram with a nominal scale, i.e., assuming SM value for WH production cross section and 100% branching ratio of a Higgs boson decaying to electron-jets.

Signal	three-step model		two-step model	
m_H (GeV)	$m_{\gamma_d} = 100$ MeV	$m_{\gamma_d} = 200$ MeV	$m_{\gamma_d} = 100$ MeV	$m_{\gamma_d} = 200$ MeV
100	$15.5 \pm 1.7 \pm 0.8$	$12.6 \pm 1.6 \pm 0.7$	$15.7 \pm 1.7 \pm 0.9$	$18.6 \pm 1.8 \pm 1.0$
125	$11.2 \pm 1.0 \pm 0.6$	$10.0 \pm 1.0 \pm 0.6$	$11.9 \pm 1.0 \pm 0.6$	$13.3 \pm 1.1 \pm 0.7$
140	$9.4 \pm 0.8 \pm 0.5$	$9.2 \pm 0.8 \pm 0.5$	$10.5 \pm 0.8 \pm 0.6$	$10.0 \pm 0.8 \pm 0.5$
Background	$0.28 \pm 0.20 \pm 0.06$			
Data	0			

Table 5.2: Numbers of expected and observed events after final selection using alternate electron-jet identification, described in Appendix 7.1. Expected signal yields are provided for both the three-step and two-step models with dark photon masses of 100 and 200 MeV. Statistical (first) and systematic (second) uncertainties are presented separately. Background yield is determined with the matrix method. No candidate events are observed in the data.

and $\sigma_{\mathrm{SM}}(WH)$ is the corresponding SM expectation [213] for this quantity ($\sigma_{\mathrm{SM}}(WH) = 223^{+8}_{-10}$ fb for the Higgs boson mass of 125 GeV). BR($H \to e$-jets) denotes the branching ratio for Higgs boson decays to electron-jets. Limits are derived using the CLs technique [214], as described below.

5.1.1 Final yields using the alternate electron-jet identification

In addition to the baseline analysis, the alternate analysis using complementary electron-jet identification was performed, as described in Appendix 7.1, requiring three tracks per electron-jet instead of two of baseline analysis, with lower p_{T} cut of tracks. This analysis was performed in order not to miss the potential signal, featuring very high multiplicity of electrons in the electron-jet (about ten electrons per electron-jet and higher).

The event yields for alternate analysis are shown in Table 5.2, with no events passing the final selection, consistent with the background-only hypothesis. The results of the alternate analysis are not taken into account for the limit setting, and are aimed to complement the baseline results only.

5.2 Limits

5.2.1 Description of CLs method

There are a few different ways of interpreting results in high-energy physics experiments. These are usually tied to either Bayesian or frequentist approaches (for a useful discussion see Ref. [215]). It has been argued in [214] that the CLs method, which is the frequentist approach by construction, is the appropriate method if the absence of sought signal is clear and one is interested in setting limit on a particular signal model. The CLs method is usually employed for this purpose in the ATLAS experiment. For brevity, let us introduce the following notations

$$\begin{aligned} \mathrm{CL_{s+b}} &\equiv P(n_{s+b} \leq n_0) \\ \mathrm{CL_b} &\equiv P(n_b \leq n_0) \\ \mathrm{CL_s} &\equiv P(n_{s+b} \leq n_0 | n_b \leq n_0) = \frac{P(n_{s+b} \leq n_0)}{P(n_b \leq n_0)} \end{aligned} \tag{5.1}$$

where n_0 is the number of events observed in the data, $\mathrm{CL_{s+b}}$ is the probability of observing $n_{s+b} \leq n_0$ events under signal+background hypothesis, $\mathrm{CL_b}$ is the probability of observing $n_b \leq n_0$ under the background-only hypothesis, and $\mathrm{CL_s}$ is the probability of observing $n_{s+b} \leq n_0$ events given there are already $n_b \leq n_0$ background events under signal+background hypothesis.

At this point, one can usually hear of "the signal strength $\mu = x$ is excluded at a 95% confidence level", where x is some particular number. That is, $\mathrm{CL_s} < 5\%$ – for any signal strength $\mu \geq x$, where $\mu = 1$ corresponds to the nominal signal hypothesis[1]. In the idealized case when signal and background hypothesis do not comprise systematic uncertainties, the signal and background yields are described by the Poison statistics. The systematic uncertainties are introduced as a nuisance parameters

$$\begin{aligned} P(n|s) &= \int \frac{(\Lambda_s \cdot \alpha)^n e^{-(\Lambda_s \cdot \alpha)}}{n!} f_s(\alpha) d\alpha, \\ P(n|b) &= \int \frac{(\Lambda_b \cdot \beta)^n e^{-(\Lambda_b \cdot \beta)}}{n!} f_s(\beta) d\beta, \\ \int \alpha f_s(\alpha) d\alpha &= \int \beta f_b(\beta) d\beta = 1 \end{aligned} \tag{5.2}$$

where $P(n|s)$ ($P(n|b)$) is the probability of obtaining n signal (background) events, Λ_s (Λ_b) is the expected signal (background) yield, and α (β) is the signal (background) nuisance parameter, which represents the corresponding signal (background) systematic uncertainty[2] with the corresponding probability density function $f_s(\alpha)$ ($f_b(\beta)$). The probability of obtaining n events in the combined signal plus background hypothesis is therefore

$$P(n|s+b) = \sum_{n_s=0}^{n} P(n_s|s) P(n - n_s|b) \tag{5.3}$$

Then, $\mathrm{CL_s}$ is expressed through $P(n|s+b)$ and $P(n|b)$ as follows

$$\mathrm{CL_s} = \frac{\sum_{n=0}^{n_0} P(n|s+b)}{\sum_{n=0}^{n_0} P(n|b)} \tag{5.4}$$

---

[1] In case of our analysis, the signal strength is

$$\mu \equiv \sigma(WH) \times \mathrm{BR}(H \to \mathrm{e-jets}) / \sigma_{\mathrm{SM}}(WH)$$

where nominal signal hypothesis refers to the SM value for WH production cross section and 100% branching ratio of a Higgs boson decaying to electron-jets.

[2] For clarity, it is assumed that there is only one source of systematic uncertainty.

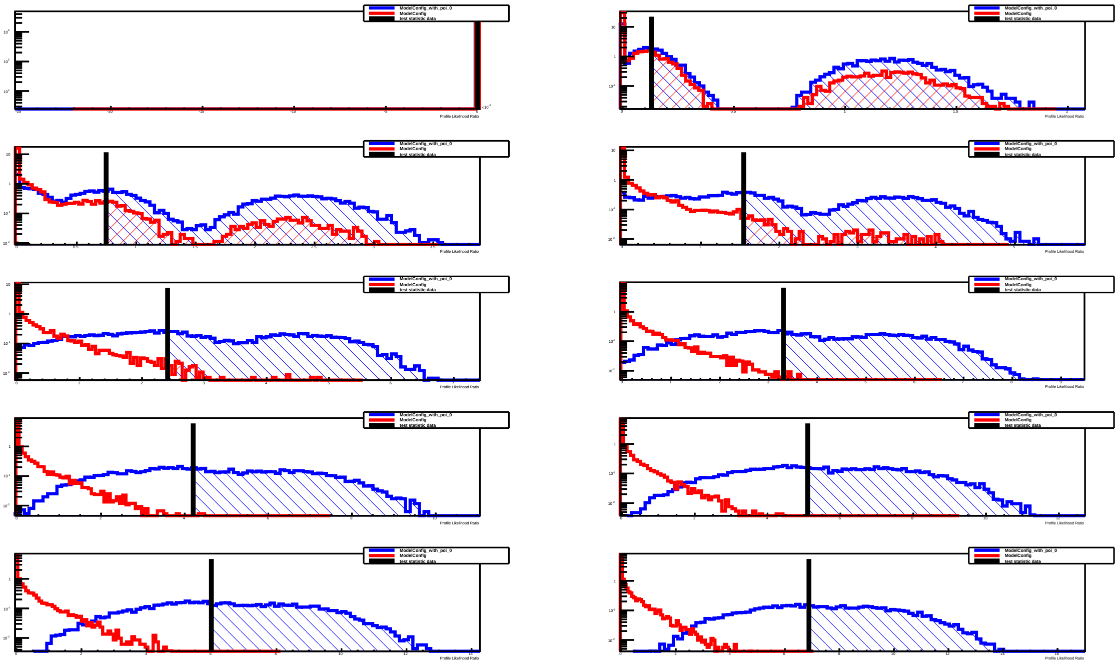

Figure 5.2: An illustration of limit setting procedure. Red and blue histograms depict the probability densities of log-likelihood ratio, obtained from pseudo-experiments using signal + background and background-only hypotheses, respectively. The black vertical line indicates the value of log-likelihood ratio observed in the experiment. The background yield is determined as described in Section 4.4 and signal corresponds to the three-step model with $m_{\mathrm{H}} = 100$ GeV and $m_{\gamma_{\mathrm{d}}} = 100$ MeV. Each plot corresponds to one of ten values of signal strength, with signal strength ranging from zero (top-left) to unity (bottom-right).

In practice, for limit setting purpose it is more convenient to deal with the so-called likelihood ratio, $Q = P(n|s+b)/P(n|b)$, or log-likelihood ratio, $-2\ln(Q)$, instead of n_0. This is due to the fact that usually the result of experiment can not be expressed in terms of one single observable (number of events in the single-count experiment). In a more general case, the likelihood ratio, $Q(\vec{X})$ is the ratio of the probability densities for a given experimental result $\vec{X}$ for two alternate hypothesis. In searches for new physics an appropriate likelihood ratio is $Q = L(\vec{X}, s+b)/L(\vec{X}, b)$, that is the ratio of probability density for the signal+background hypothesis to the signal-free or background-only hypothesis [215]. This enables one to map the experimental result $\vec{X}$ onto one single variable, $Q(\vec{X})$. Given the particular value of likelihood ratio, Q_0, obtained in the experiment, the $\mathrm{CL_s}$ is therefore

$$\mathrm{CL_s} = \frac{\int_{Q_0}^{\infty} P_{s+b}(Q)dQ}{\int_{Q_0}^{\infty} P_b(Q)dQ} \tag{5.5}$$

where $P_{s+b}(Q)$ and $P_b(Q)$ are the probability densities of likelihood ratio, obtained from the pseudo-experiments generated using signal plus background and background-only hypotheses, respectively. An illustrative example is shown in Fig. 5.2, where the probability densities are depicted as a functions of $-2\ln(Q)$ together with the values of log-likelihood ratio, $-2\ln(Q_0)$, observed in the experiment. Literally, the $\mathrm{CL_s}$ for each plot in the figure is the ratio of the dashed red area to the dashed blue area. The meaning of log-likelihood

Model	m_{γ_d} (MeV)	**Observed**	Expected	-1σ	+1σ	-2σ	+2σ
three-step	100	**0.39**	0.37	0.30	0.53	0.28	0.73
three-step	200	**0.45**	0.44	0.36	0.63	0.34	0.81
two-step	100	**0.29**	0.28	0.24	0.35	0.19	0.55
two-step	200	**0.24**	0.24	0.25	0.36	0.23	0.55

Table 5.3: The 95% CL upper limits on the signal strength, $\sigma(WH) \times \mathrm{BR}(H \to e\text{-jets})/\sigma_{\mathrm{SM}}(WH)$, for a Higgs boson mass of 125 GeV for different choices of the hidden-sector model parameters. Here, $\sigma(WH)$ is the WH production cross section times the sum of the branching ratios for the W boson decaying to leptons ($e\nu_e$, $\mu\nu_\mu$, $\tau\nu_\tau$), $\sigma_{\mathrm{SM}}(WH)$ is the corresponding SM expectation and $\mathrm{BR}(H \to e\text{-jets})$ is the branching ratio for Higgs boson decays to electron-jets.

ratio becomes intuitively clear if one think of it as follows: the "signal-like" outcome of experiment tends to have low value of $-2\ln(Q)$, while that of background-only is more likely to occur at the higher end of the log-likelihood ratio range.

For the nuisance parameter, either truncated Gauss, Gamma or LogNormal probability density functions are usually employed [216]. When the uncertainty of predicted event yield is dominated by the statistical uncertainty of counting events in a control region, like in the matrix method (Section 4.4.3), it is a most accurate to describe the systematic uncertainty with a Poisson distribution. It is shown in [216] that Poisson probability density together with a uniform prior leads to a Gamma posterior, thus, this type of nuisance-parameter constrain is often called a "gamma". This type of constrain is incorporated for the systematic uncertainties in the present analysis.

5.2.2 Limit setting results

The limits on a signal strength are presented in Fig. 5.3 and Table 5.3 for both the three-step and two-step models. As can be seen from Fig. 5.4, the results are compatible within the statistical uncertainty of the signal for both dark photon masses $m_{\gamma_d} = 100$ MeV and 200 MeV. The likelihoods are given by the Poisson distribution for the total number of events in the signal region and are calculated using the number of expected and observed events, whereby the results of the electron and muon channels are summed and enter the likelihood function together. The corresponding signal and background systematic uncertainties are incorporated into the likelihoods as nuisance parameters with Gamma probability density functions [216]. Assuming that the WH cross section has the SM value, for the specific set of hidden-sector parameters chosen here, the analysis excludes Higgs boson branching ratios to electron-jets between 24% and 45% for $m_H = 125$ GeV at 95% confidence level.

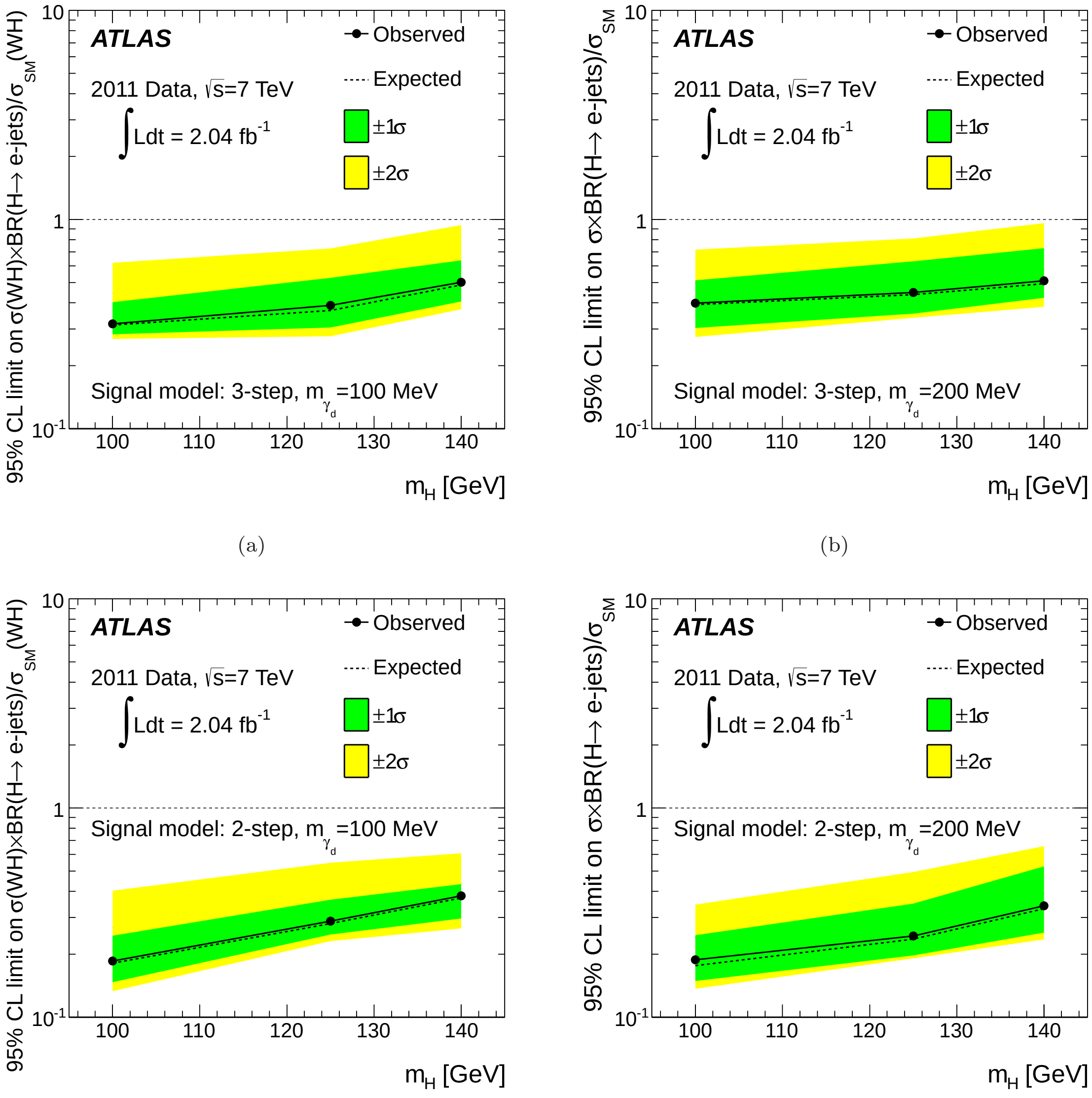

(a) (b)

(c) (d)

Figure 5.3: Observed and expected 95% CL upper limits on the signal strength, $\sigma(WH) \times \mathrm{BR}(H \to e\text{-jets})/\sigma_{\mathrm{SM}}(WH)$, as a function of the Higgs boson mass for the (a) three-step and (c) two-step models of a hidden sector with a dark photon mass $m_{\gamma_d} = 100$ MeV, and for the (b) three-step and (d) two-step models of a hidden sector with a dark photon mass $m_{\gamma_d} = 200$ MeV. The dark (light) shaded band contains 68% (95%) of the outcomes of pseudo-experiments generated under the background-only hypothesis.

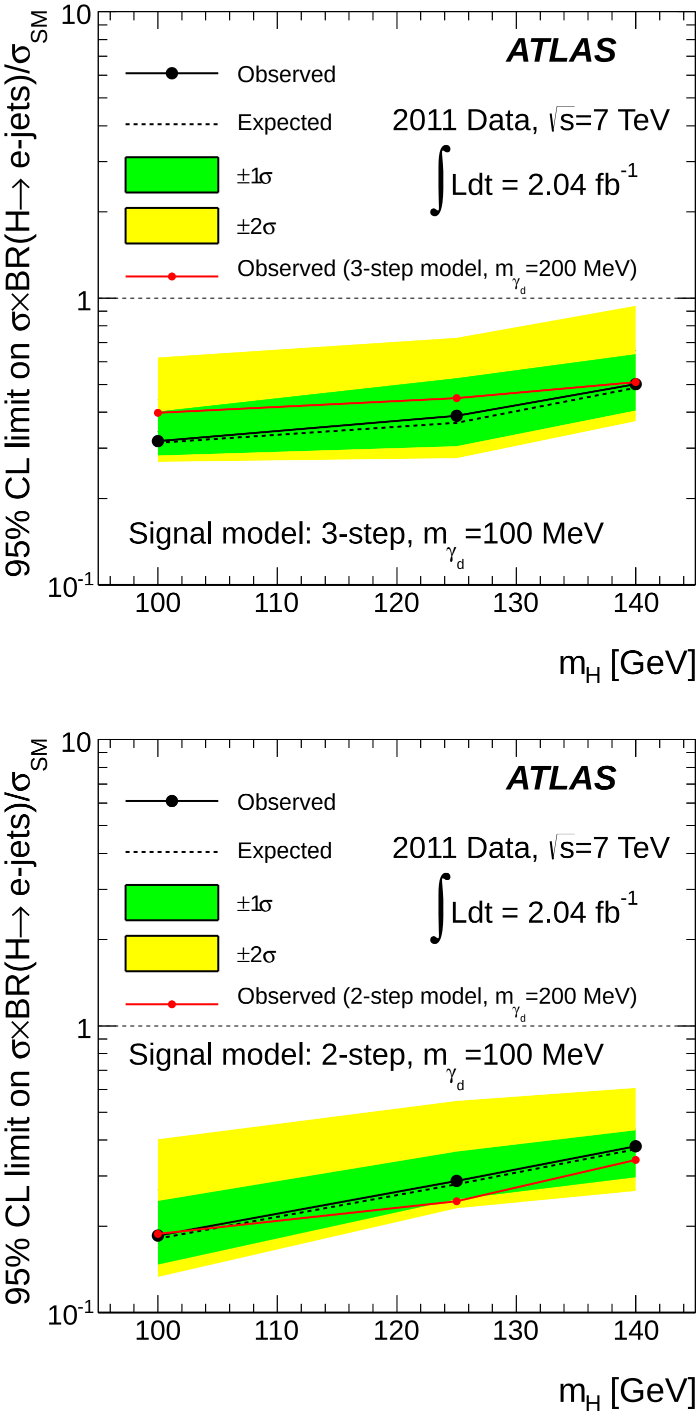

Figure 5.4: Observed and expected 95% CL upper limits on the signal strength, $\sigma(WH) \times \mathrm{BR}(H \rightarrow e\text{-jets})/\sigma_{\mathrm{SM}}(WH)$, as a function of the Higgs boson mass for the (left) three-step and (right) two-step models of a hidden sector with a dark photon mass $m_{\gamma_d} = 100$ MeV. The dark (light) shaded band contains 68% (95%) of the outcomes of pseudo-experiments generated under the background-only hypothesis. For convenience, the observed limits for the same signal models with a dark photon mass $m_{\gamma_d} = 200$ MeVare shown as well (red line).

6

Conclusions

A search is presented for a light Higgs boson decaying to a light hidden sector and subsequently into highly collimated jets of electrons, which are expected to be seen in the detector as distinct objects called “electron-jets”. The analysis has been performed using 2.04 fb^{-1} of proton–proton collision data at $\sqrt{s}$=7 TeV, collected with the ATLAS detector at the LHC in 2011.

The search is performed in the WH production mode with the choice of hidden-sector parameter space resulting in Higgs boson decaying into prompt electron-jets. The electron-jet identification method presented here provides good discrimination against background sources and avoids sensitivity to the detailed topology of the electrons within the electron-jet.

The observed data are consistent with the Standard Model background hypothesis. Consequently, 95% confidence level limits are set on the WH production cross section times the branching ratio into electron-jets, assuming the two benchmark models of a hidden sector and the condition of a dark photon mass below 210 MeV.

So far, no direct evidence of a Higgs boson decaying to lepton-jets has been seen. This fact is yet another confirmation that the Higgs boson, recently observed by ATLAS and CMS collaborations, is more likely to be the Standard Model Higgs boson. However, at the moment this dissertation was finished, the ATLAS experiment has completed collecting a data set of proton–proton collision at $\sqrt{s}$=8 TeV, which comprises ten times more statistics than that, upon which the presented analysis is done. The analysis of this data would allow to probe a lower branching fractions of a Higgs boson decaying to electron-jets, and, hence, to seek for a more subtle hidden-sector effects. Moreover, the order-of-magnitude higher statistics also encourages to look for electron-jets in ZH production channel, in addition to WH. While it has about ten times lower cross-section than WH, the background is substantially lower in this case. Also, due to the fact that the leptonic decays of Z boson have no invisible decay products, one can reconstruct the invariant mass of the Higgs decay products. As a result, this mode provides much cleaner environment for lepton-jet analysis.

In addition to electron-jets, it is of high importance to look also for muon-jets. There seem to be no clear preference on either electron or muon decay modes in hidden-sector models, although some authors even claim the models with muons fit the the data somewhat better [217].

Finally, an important ingredient of lepton-jet investigation is the search for the direct Higgs production with a Higgs boson decaying to lepton-jets. This channel has orders of magnitude higher cross-section, though with a substantially higher relative background. It also represents a challenge to experimentalists, since triggering on lepton-jets that are produced in the Higgs decays is a highly non-trivial task.

In conclusion, we should note that the lepton-jet search programme has just made its first – although very important steps. A small part of data collected by the ATLAS detector have been analysed so far, and a broad activity is now underway at ATLAS, targeted at the analysis of the full data set. The models featuring hidden sector remain among the most natural candidates for the dark matter, capable of simultaneous elegant explanation of various astrophysical observations. Hence, it is important to keep track of possible manifestation of hidden sectors at colliders – of lepton jets.

7

Appendices

7.1 Data analysis with alternate electron-jet identification

In the 3-step model the multiplicity in the electron jets may vary up to about ten electrons per lepton jet [70, 71]. The average transverse momentum of electrons is in this case much lower than in case of the 2-step model. To ensure we do not miss this peculiar signal, an analysis with alternate electron-jet identification was performed in addition to baseline analysis. It is completely identical to the baseline analysis with the only exception for track selection criteria. In the alternate analysis the track p_{T} requirement is relaxed to 2 GeV (instead of 5 GeV) and at-least 3 tracks are required per electron-jet (instead of 2).

The background in this case is estimated using ABCD method only. Events are assigned to one of four regions according to whether or not the jets meet the f_{EM} and the track-quality conditions of the electron-jet classification. The regions B and D are defined similar to that of Section 4.4.2, A is the signal region, and C is the region where one or both jets fail f_{EM} selection requirement. Similar to baseline analysis, the residual correlation between two considered selection criteria is removed by re-weighting f_{EM} distributions of jets fulfilling anti-track quality requirement in the data. The weights are obtained from Monte Carlo simulation as a relative difference between f_{EM} distributions of jets in the region with nominal track-quality selection, and those in the anti-track quality one. As the re-weighting is applied, the shapes of f_{EM} distributions in the nominal and anti-track quality regions agree well within statistical uncertainties (Fig. 7.1). The event yields in different ABCD regions are given in Table 7.1. The background prediction with this method is

$$n_{\mathrm{bckg}} = 0.28 \pm 0.20 \text{ (stat) } \pm 0.06 \text{ (signal contamination) } \pm 0.01 \text{ (ABCD selection)}$$

	Data	Expected background	Expected signal, $m_H = 100$ GeV
A	Signal region	0.23 ± 0.09	15.5 ± 1.8
B	2	1.44 ± 0.44	0.4 ± 0.3
C	4447	4630 ± 592	8.5 ± 1.3
D	6071	7885 ± 981	1.0 ± 0.4

Table 7.1: The expected number of background and signal events in 2.04fb^{-1}of data, as well as the number of events observed in the data, in each region of ABCD selection. The alternate electron-jet selection is used (Section 7.1). The signal predictions correspond to the three-step model with m_H=100 GeV and $m_{\gamma_{\mathrm{d}}}$=100 MeV. The background expectations include statistical and systematic uncertainties. The uncertainties shown for signal are statistical only.

The expected signal and background yields as the final selection is applied are given in Section 5 for comparison.

7.2 Event displays

The event display of candidate $W \to \mu\nu$+2 electron-jets event is shown in Fig.7.2. The illustration of simulated signal event is shown in Fig. 7.3.

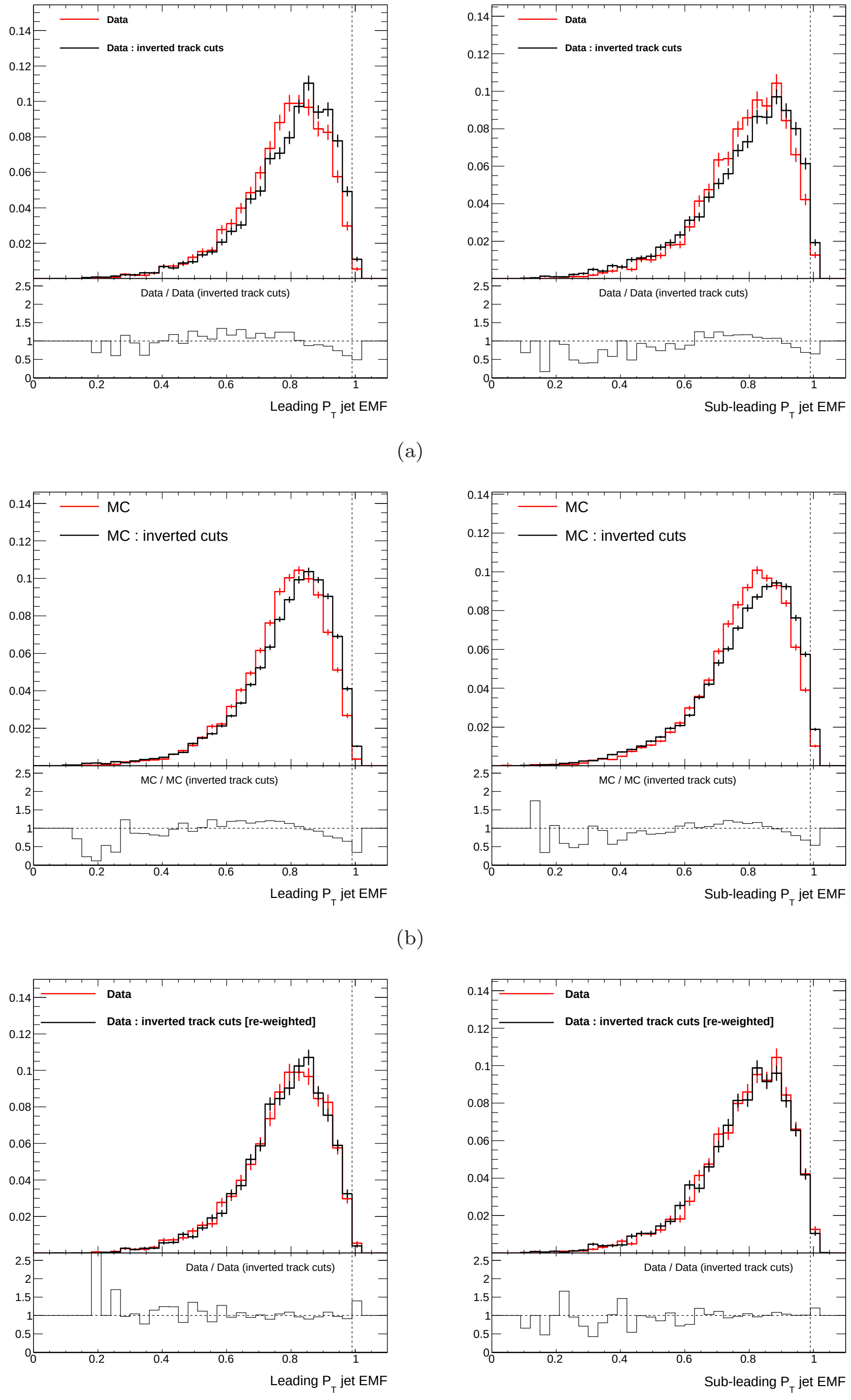

(a)

(b)

(c)

Figure 7.1: Distribution of jet electromagnetic fraction, f_{EM}, for leading-p_{T} (left) and second-leading-p_{T} (right) jets, after the W selection. Red histograms correspond to events where jets fulfil alternate-nominal track-quality selection criteria (Section 7.1), while black histograms correspond to events falling into anti-track quality region. Jets are required to fulfil $\mathrm{E_T}$ and η requirements. The distributions are shown for (a) data, (b) for combination of properly normalized simulated MC samples and multi-jet data templates, and (c) for data after re-weighting f_{EM} jet distributions in anti-track geniality region. The re-weighting procedure is described in Section 4.4.2.1.

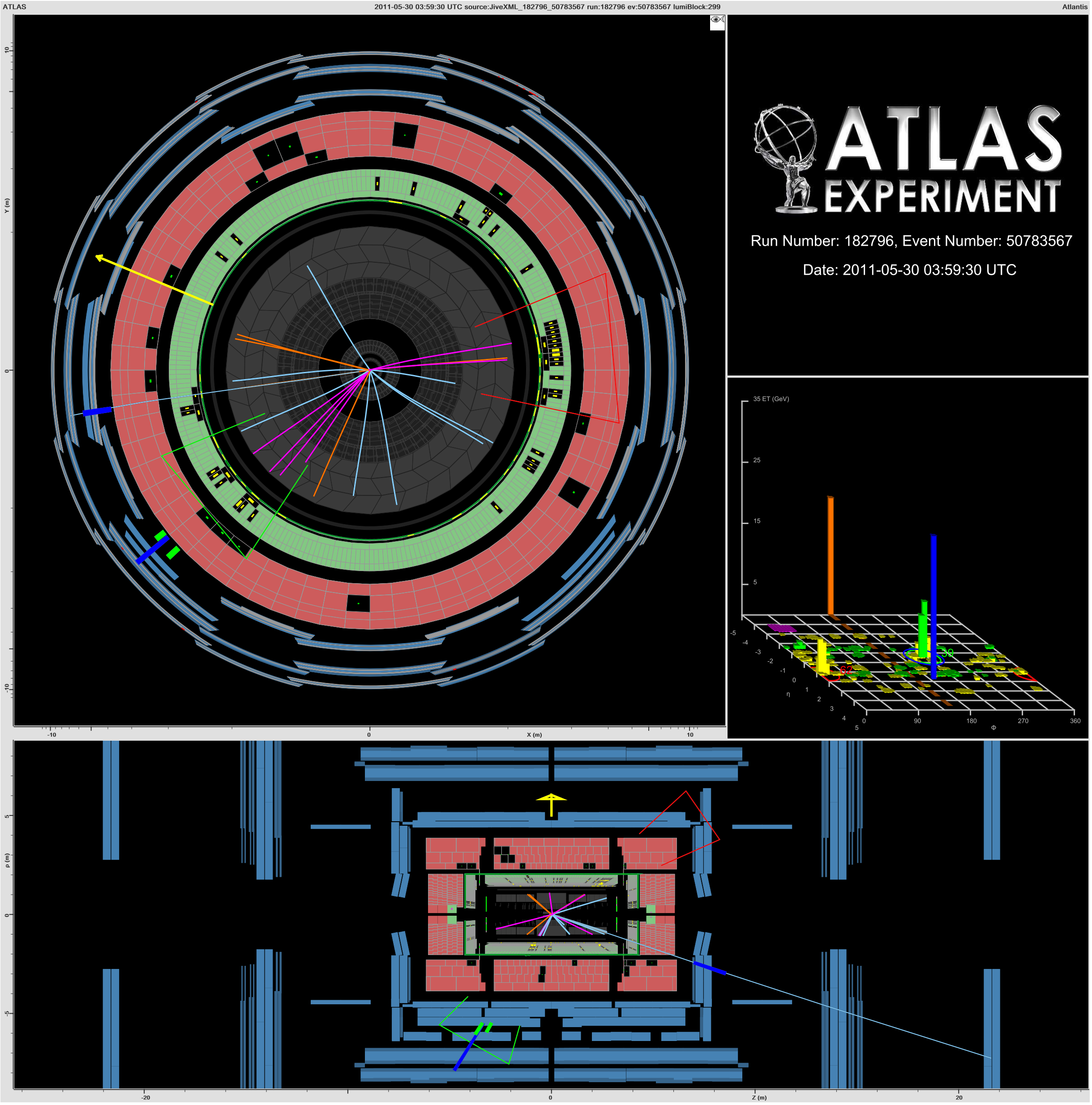

Figure 7.2: ATLAS event display of the candidate $W \rightarrow \mu\nu$+2 electron-jets event observed in the data. Tracks with $p_{\mathrm{T}} \geq 2$ GeV are shown. The electron-jet candidates are displayed with red and green wedges and the muon candidate is shown with a blue line crossing the muon spectrometer. Missing transverse momentum is shown with the yellow arrow in the left and bottom sub-plots and with the orange tower in the lego-plot. The blue tower in the lego-plot marks the muon and the green ones are the EM clusters. The calorimeter cells are tagged as follows: yellow – LAr cells, green – tile calorimeter cells, magenta – forward calorimeter.

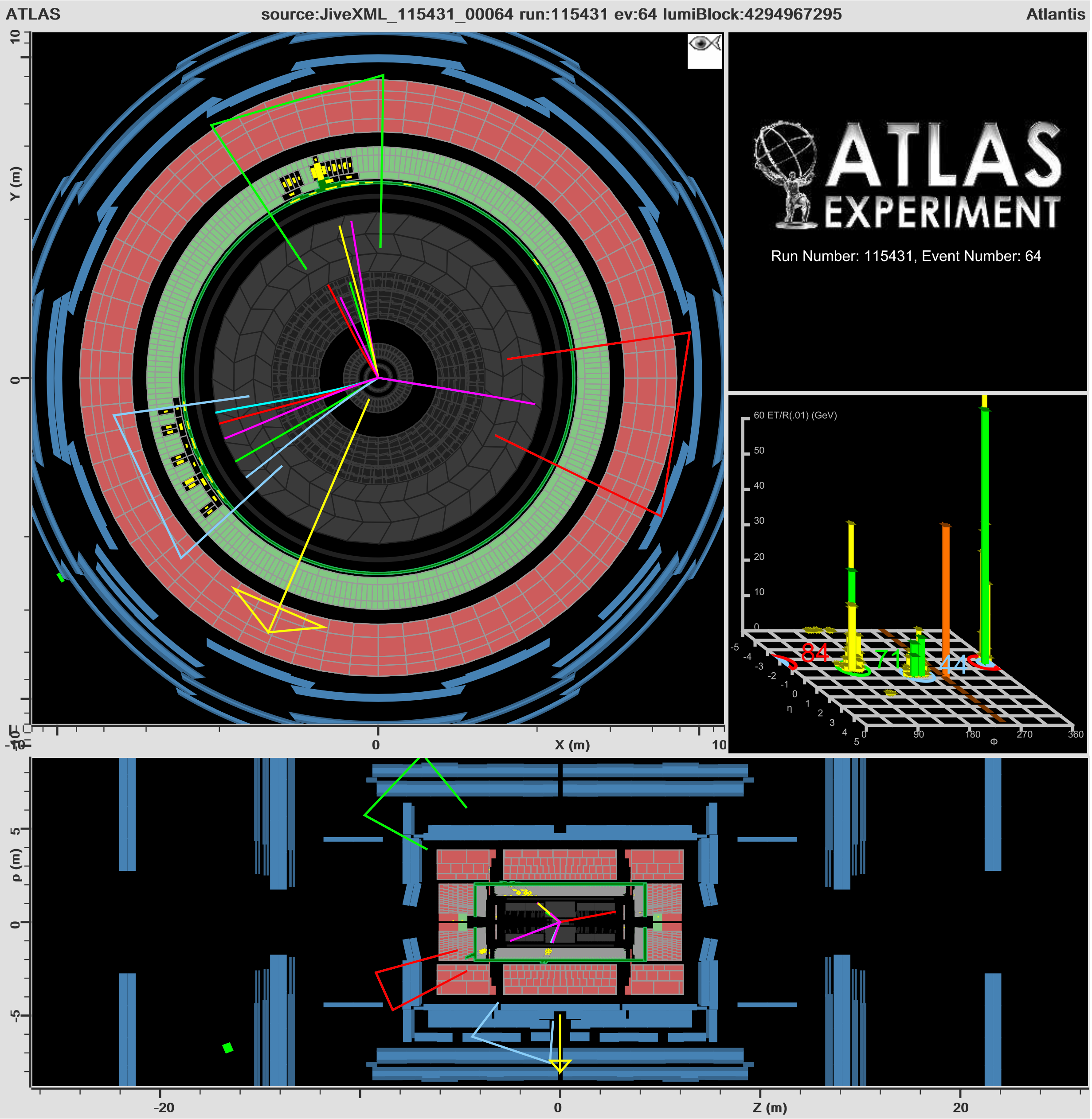

Figure 7.3: ATLAS event display of simulated event of $W \to e\nu$ + Higgs decaying to electron-jets. The three-step model with dark photon mass 100 MeV is used to produce the event. Tracks with $p_{\mathrm{T}} \geq 2$ GeV are shown. The electron-jets are displayed with green and blue wedges and the red wedge corresponds to electron from W-decay. Missing transverse momentum is shown with the yellow arrow in the left and bottom sub-plots and with the orange tower in the lego-plot. The EM clusters are shown with the green towers in the lego-plot. The calorimeter cells are tagged as follows: yellow – LAr cells, green – tile calorimeter cells, magenta – forward calorimeter.

8

Povzetek doktorskega dela

8.1 Uvod

Nova doba v fiziki se je začela, ko so v Velikem hadronskem trkalniku (Large Hadron Collider, LHC, CERN, Ženeva) začeli krožiti prvi stabilni žarki protonov. Trenutno je Standardni model (SM) zelo uspešna teorija narave na energijskih skalah do okoli 100 GeV in vzdrži različne eksperimentalne teste z izjemno natančnostjo. V lanskem letu so fiziki na eksperimentih ATLAS [1] in CMS [2] na LHC objavili odkritje Higgsovega bozona – to je prvi osnovni delec s spinom, drugačnim do sedaj znanih umeritvenih bozonov s spinom 1 in fermionov s spinom 1/2 - zadnji manjkajoči košček v Standardnem modelu. Navkljub uspehu pa obstajajo vidiki, ki jih v SM ne moremo obravnavati. Kot prvo je Standardni model kombinirana teorija elektrošibke in močne interakcije in tako ne vključuje opisa gravitacije. Naslednja pomanjkljivost je, da ne razloži rezultatov astrofizikalnih eksperimentov. Iz opazovanj gibanja oddaljenih galaksij in iz rezultatov gravitacijskega lečenja sklepamo, da snov, ki jo lahko vidimo, predstavlja samo približno 20% mase v vesolju [6,7], pri čemer izvor preostalih 80% ostaja neznan. Ta neznana snov se imenuje temna snov (TS) in ni opisana v SM. Zaznamo jo samo preko gravitacijskih vplivov na gibanje galaksij in svetlobe, ki prehaja skozi. Temna in vidna snov skupaj predstavljata približno 25% energije v vesolju, medtem ko drugih 75% prinaša temna energija, ki je odgovorna za to, da se naše vesolje širi s pozitivnim pospeškom [7,9]. Izvor temne snovi in temne energije ostaja skrivnost.

Najbolj privlačni kandidati za temno snov so slabo interagirajoči masivni delci (Weakly Interacting Massive Particle – WIMP), ki se najbolj naravno pojavljajo v supersimetričnih modelih. Za te delce se domneva, da imajo maso do 10 TeV in sodelujejo samo v šibkih interakcijah. Sipalni presek anihilacije temne snovi na elektrošibki skali avtomatično ustvarja pravo količino temne snovi v današnjem vesolju. To dejstvo je znano kot WIMP čudež [64]. Vendar pa je vrsta eksperimentov s kozmičnimi žarki in z iskanjem temne snovi v zadnjem desetletju prinesla nove rezultate, ki jih je težko razložiti v običajnih WIMP modelih. Iz med teh so najpomembnejše meritve toka elektronov in pozitronov, pa tudi meritve relativnega deleža pozitronov glede na elektrone v kozmičnih žarkih [10–14]. Običajni WIMP modeli ne morejo razložiti elektronske (pozitronske) anomalije iz dveh glavnih razlogov: kot prvo, sipalni presek anihilacije temne snovi mora biti dva reda velikosti večji kot sipalni presek ki ustvari pravo količino temne snovi v današnem vesolju; kot drugo, temna snov se mora anihilirati samo v leptone, ne pa tudi v hadrone.

Arkani-Hamed [19] je predlagal privlačno rešitev, da bi uskladili nesoglasja med astrofizikalnimi anomalijami, ki so jih nedavno opazili, in običajnimi modeli temne snovi. Predlagan je bil obstoj novega sektorja delcev, skriti sektor. Polja skritega sektorja ne sodelujejo v interakcijah, ki obstajajo v Standardnem modelu. Vendar pa delci skritega sektorja interagirajo s fotonom, Z bozonom, in Higgsovim bozonom Standardnega modela preko tako imenovanih portalov. Najbolj pomemben portal je tako imenovano kinetično mešanje [20], ki povezuje hipernaboj Standardnega modela z umeritvenim bozonom, ki ustreza Abelovi grupi skritega sektorja. Ta bozon se imenuje temni foton. Pomembna predpostavka je, da temna snov sodeluje v interakcijah skritega sektorja. Dalje, če je temni foton masiven in njegova masa približno 100 MeV – 1 GeV, potem: (1) zaradi interakcije s skritim sektorjem se temna snov anihilira ali razpade samo v leptone (elektrone ali mione), ne pa tudi v hadrone; (2) zaradi prisotnosti masivnega temnega fotona se sipalni presek anihilacije poveča preko Sommerfeldovega mehanizma [21] in tako lahko opiše visok tok elektronov in pozitronov ki ga eksperimentalno opazimo.

Pomemben atribut modelov skritega sektorja so tako imenovani leptonski pljuski. To so kolimirani snopi elektronov ali mionov, ki nastanejo v razpadih temne snovi ali delcev Standardnega modela preko interakcij s skritim sektorjem. Potencialno odkritje leptonskih pljuskov na LHC bi lahko namigovalo na izvor temne snovi ter pokazalo signal nove fizike.

Iskanje leptonskih pljuskov je zelo pomembno tudi z vidika nedavnega odkritja Higgsovega bozona [1,2]. Odkritje je skladno z opazovanjem Higgsovega bozona Standardnega modela [22–24]. Okrepitev ali zavrnitev hipoteze Higgsovega bozona Standardnega modela je trenutno izjemno pomebna in s tem iskanje razpadov Higgsovega bozona, ki v Standardnem modelu ne obstajajo, zlasti razpadov v leptonske pljuske. Poleg Higgsovega bozona pa lahko obstaja tudi druga vrsta skalarnih polj, ki se pojavljajo v Higgsovem sektorju v številnih razširitvah Standardnega modela, in leptonski pljuski lahko predstavljajo pomeben kanal za odkritje nove fizike.

V doktorskem delu je predstavljeno iskanje razpadov Higgsovega bozona v elektronskih pljuskih v WH kanalu produkcije Higgsovega bozona. To je prvo iskanje tovrstnih signatur. Doktorsko delo vsebuje podrobno študijo, na kateri temelji članek [25].

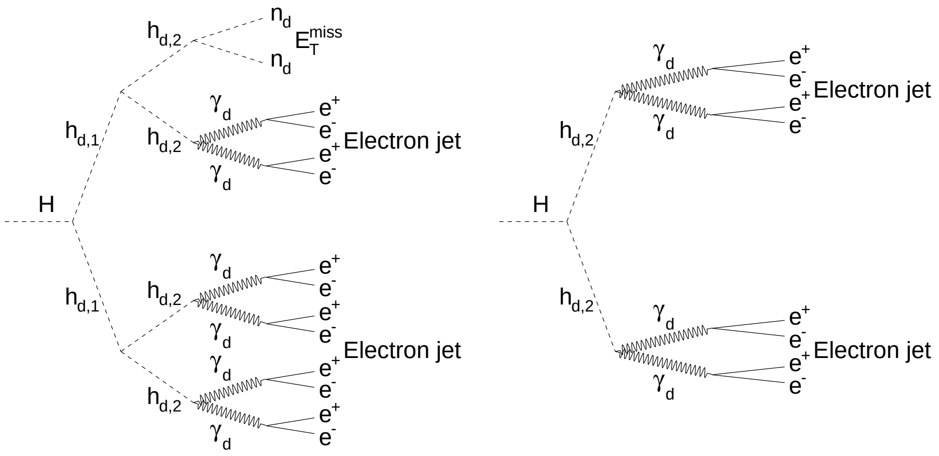

Slika 8.1: Diagrami, ki ponazarjajo razpad Higgsovega bozona na delce skritega sektorja preko tristopenjske kaskade (levo) in dvostopenjske kaskade (desno). Vsak delec $h_{\mathrm{d},2}$ lahko razpade na dva temna fotona γ_{d} ali na dva stabilna skalarja n_{d}, z razvejitvenimi razmerji, ki so prikazani v tabeli 8.1.

8.2 Teoretični model

V tem delu upoštevam dva modela, obravnavana v viru [71]. Modela se razlikujeta v načinu, kako Higgsov bozon razpade; preko tristopenjske kaskade (slika 8.1 levo) ali dvostopenjske kaskade (slika 8.1 desno) v skritem sektorju. V obeh modelih so obravnavane mase delcev skritega sektorja znatno nižje od mase Higgsovega bozona, s čimer ima topologija razpada Higgsovega bozona dva pljuska. Ti modeli vsebujejo temni foton γ_{d}, ki se kinetično meša s fotonom Standrdnega modela [79, 80], nevtralni šibko-interagirajoči skalar, n_{d}, in dva skalarja skritega sektorja, $h_{\mathrm{d},1}$ in $h_{\mathrm{d},2}$. Če je vrednost kinetičnega mešanja več od 10^{-5}, imajo temni fotoni zelo kratek življenjski čas. Zato izbrana vrednost kinetičnega mešanja 10^{-4}, priporočena v viru [71], zagotavlja, da so razpadi razpadnih produktiov Higgsovega bozona takojšnji. Masa temnega fotona v teh modelih mora biti manj kot 2 GeV, da bi lahko uspešno opisali rezultate eksperimentov s kozmičnimi žarki in z iskanjem temne snovi [11–14], ki opazijo nepričakovan presežek elektronov in pozitronov v kozmičnih žarkih, medtem ko ne opazijo nobenega presežka protonov. Če ima γ_{d} maso pod 210 MeV, razpade izključno v e^+e^- pare. V tem delu obravnavam temne fotone z maso 100 oziroma 200 MeV.

Signal ima posebno topologijo, ki vsebuje dva elektornska pljuska, kjer ima vsak pljusk približno 4 elektrone, ki so zelo kolimirani. Parametri skritega sektorja so navedeni v tabeli 8.1. Izbrane mase Higgsovega bozona so 100, 125 in 140 GeV. Pričakujemo, da bodo rezultati analize neodvisni od izbire mase skalarjev $h_{\mathrm{d},1}$ in $h_{\mathrm{d},2}$, dokler so te mase bistveno manjše od mase Higgsovega bozona, torej mase $h_{\mathrm{d},1}$ in $h_{\mathrm{d},2}$ manj kot 10 GeV. Zlasti če so mase $h_{\mathrm{d},1}$ in $h_{\mathrm{d},2}$ veliko manjše od mase Higgsovega bozona, so $h_{\mathrm{d},1}$ in $h_{\mathrm{d},2}$ "potisnjeni" in njihovi razpadni produkti zelo kolimirani, kar se kaže v dveh leptonskih pljuskih. Tudi v tristopenjskem modelu se pričakuje, da bodo rezultati analize neodvisni od izbire vrednosti razvejitvenega razmerja razpada delca $h_{\mathrm{d},2}$ v šibko interagirajoče

Parameter	
$m_{h_{\mathrm{d},1}}$	10 GeV
$m_{h_{\mathrm{d},2}}$	4 GeV
m_{n_d}	90 MeV
m_{γ_d}	$100, 200$ MeV
ϵ	10^{-4}
tristopenjski model	
$\mathrm{BR}(h_{\mathrm{d},1} \to h_{\mathrm{d},2} h_{\mathrm{d},2})$	1
$\mathrm{BR}(h_{\mathrm{d},2} \to \gamma_\mathrm{d} \gamma_\mathrm{d})$	0.8
$\mathrm{BR}(h_{\mathrm{d},2} \to n_\mathrm{d} n_\mathrm{d})$	0.2
dvostopenjski model	
$\mathrm{BR}(h_{\mathrm{d},2} \to \gamma_\mathrm{d} \gamma_\mathrm{d})$	1
$\mathrm{BR}(h_{\mathrm{d},2} \to n_\mathrm{d} n_\mathrm{d})$	0

Tabela 8.1: Parametri modelov skritega sektorja: mase delcev skritega sektorja; kinetično mešanje in razvejitvena razmerja v tristopenjskem in dvostopenjskem modelu skritega sektorja.

nevtralne delce, n_d, dokler je razvejitveno razmerje manj kot 20%. Za to vrednost razvejitvenega razmerja delci $h_{\mathrm{d},1}$ razpadejo v vidne produkte z več kot 90% verjetnostjo. Za večje razvejitveno razmerje bomo imeli precejšen del dogodkov, v katerih samo en (ali noben) delec $h_{\mathrm{d},1}$ razpade v vidne delce.

8.3 Opis eksperimenta: eksperiment ATLAS na Velikem hadronskem trkalniku

Veliki hadronski trkalnik je najmočnejši in najsodobnejši pospeševalnik za raziskave v fiziki visokih energij [127, 128]. To je sinhrotron, ki je med rednim obratovanjem v letih 2010 – 2012 pospeševal in trkal žarke protonov z izjemno visoko težiščno energijo do 8 TeV. ATLAS in CMS sta glavna eksperimenta na LHC. ATLAS [132] je večnamenski detektor osnovnih delcev z naprej-nazaj simetrično cilindrično geometrijo in sestoji iz več detektorskih komponent, ki so opisane v nadaljevanju. Notranji detektor ATLASu (Inner detector – ID) omogoča natančno rekonstrukcijo sledi nabitih delcev. Sestavljen je iz treh silicijevih pixel detektorjev blizu trkalne cevi, štirih silicijevih mikrostrip detektorskih modulov v cilindrični regiji s pari enostranski senzorjev (Semiconductor Tracker – SCT), ki zagotavljajo približno 8 zadetkov na poti delca, in detektorjev prehodnega sevanja (Transition Radiation Tracker – TRT) na zunanjem radiju, ki zagotavljajo okoli 35 zadetkov na poti delca. TRT ponuja veliko diskriminatorne moči med elektroni in hadroni v širokem razponu gibalnih količin (med 0.5 in 100 GeV) z detektiranjem rentgenskih žarkov, ki jih proizvaja prehodno sevanje. Notranji detektor je obdan s tankim superprevodnim magnetom, ki proizvaja aksialno magnetno polje v velikosti 2T. Naslednji del ATLASa sta elektromagnetni (EM) in hadronski (Had) kalorimeter, ki merita energijo in položaj elektromagnetnih in hadronskih kaskad. Skupna debelina EM kalorimetra je

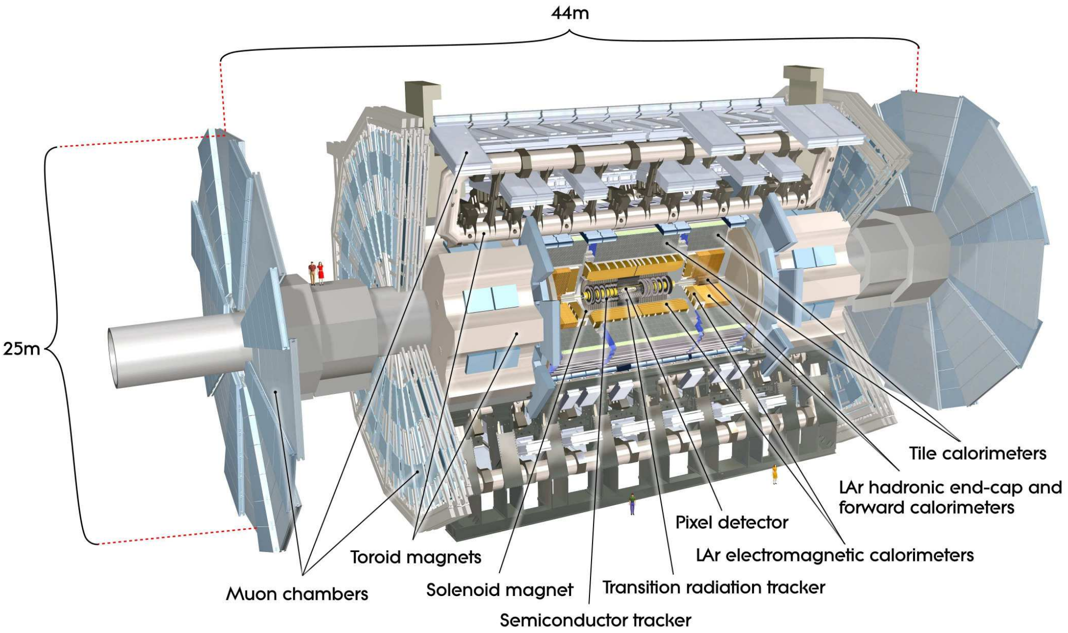

Slika 8.2: Ilustracija detektorja ATLAS. Dimenzije detektorja so 25 m v višino in 44 m v širino. Skupna teža detektorja je približno 7000 ton. Slika iz [132].

več kot 24 sevalnih dolžin X_0. Zadnji del detektorja ATLAS je mionski spektrometer (MS), ki meri gibalno količino in naboj mionov. Shema detektorja ATLAS je prikazana na sliki 8.2.

ATLAS ima tristopenjski prožilni sistem, ki izbere dogodke, primerne za analizo [176]. Prva stopnja sprožilca (Level-1) se izvaja v strojni opremi, ki deluje sinhrono s trki in uporablja del informacij detektorja za zmanjšanje frekvence dogodkov z 20 MHz na približno 75 kHz. Temu sledita dve programski stopnji proženja: druga stopnja sprožilca in filter dogodkov, ki skupaj zmanjšata frekvenco dogodkov na približno 300 Hz.

8.4 Analiza podatkov

V tej analizi iščemo dogodke, ki morajo imeti natančno enega rekonstruiranega kandidata za bozon W v elektronskem ali mionskem kanalu razpada in najmanj dva pljuska, opredeljena kot elektronska pljuska. Obravnava kanala produkcije WH Higgsovega bozona omogoča, da dosežemo visoko učinkovitost za izbiro dogodkov in visoko diskriminacijo signala od ozadja.

Vzorec podatkov za to analizo je bil pridobljen z detektorjem ATLAS pri trkih protonov s težiščno energijo 7 TeV v začetku leta 2011. Skupna integrirana luminoznost izbranega vzorca podatkov je 2.04 fb^{-1} s 3.7% negotovostjo [200, 201]. Prožilni sistem se sproži zaradi prisotnosti elektrona ali miona s transverzalno gibalno količino, večjo od 22 GeV oziroma 18 GeV.

Za oceno sprejemljivosti in učinkovitosti signala, optimizacijo rezov za izbiro signala in oceno razumevanja ozadja smo uporabili simulirane vzorce podatkov (Monte Carlo). Oceno končnega ozadja smo določili iz podatkov, kot je opisano v poglavju 8.4.3.

8.4.1 Izbira bozonov W

Kandidat za elektron mora prestati tesno ('tight') selekcijo [190, 195] s $p_T > 25$ GeV in $|\eta| < 2.47$. Elektroni v prehodnem območju med cilindričnimi in pokrovnimi kalorimetri ($1.37 < |\eta| < 1.52$) so zavrnjeni. Mionski kandidat mora biti identificiran tako v ID kot v MS in mora imeti $p_T > 20$ GeV ter $|\eta| < 2.4$. Razlika med meritvama pT v ID in MS mora biti manjša od 15 GeV, da bi povečali odpornost proti napačni rekonstrukciji mionov [190]. Da bi zmanjšali ozadje zaradi hadronskih pljuskov, od elektronskih in mionskih kandidatov zahtevamo, da izpolnjujejo tudi merila izolacije: vsota p_T vseh sledi v stožcu $R = 0.4$ okoli elektrona (miona), deljena z elektronsko (mionsko) p_T, mora biti manj kot 0.3 (0.2).

Od kandidatov za bozon W zahtevamo manjkajočo transverzalno gibalno količino, večjo kot 25 GeV, poleg tega zahtevamo natanko en izoliran elektron ali mion. Dogodki z dvema ali več izoliranami leptoni istega okusa so zavrnjeni, da bi znatno zmanjšali ozadje iz dogodkov Drell-Yan. Za leptonski kandidat iz razpada bozona W zahtevamo, da ima razdaljo od prožitvenega objekta manj kot 0.1.

Da bi zmanjšali ozadje iz kozmičnih žarkov, hadronskih pljuskov, ki izvirajo iz kvarkov težkega okusa, in fotonskih pretvorb, mora kandidat za bozon W izvirati iz interakcijske točke (primarno vozlišče). Pri dogodkih z več kot eno interakcijsko točko vzdolž osi protonskega curka za primarno vozlišče štejemo vozlišče, v katerem je vsota vseh tansverzalnih gibalnih količin sledi, ki izhajajo iz tega vozlišča, največja. Vzdolžni in prečni vpadni parameter sledi nabitega leptona glede na primarno vozlišče morata biti manj kot 10 oziroma 0.1 mm.

Primerjava porazdelitev kandidatov W, izmerjenih z detektorjem ATLAS z napovedmi generatorjev trkov Monte Carlo, je prikazana na sliki 8.3. Kot je razvidno iz slike, med podatki in simulacijami MC opazimo dobro ujemanje.

8.4.2 Rekonstrukcija leptonskih pljuskov

Kandidati za elektronske pljuske so sestavljeni iz pljuskov, rekonstruiranih v kalorimetrih, z uporabo algoritma "anti-k_t" za pljuske [209] s parametrom $R = 0.4$.

Elektroni v elektronskem pljusku so preveč tesno kolimirani za učinkovito identifikacijo z algoritmom, ki se uporablja za identifikacijo elektronov iz razpadov bozonov W. Namesto tega so leptonski pljuski opredeljeni s tremi parametri identifikacije: elektromagnetni delež (f_{EM}), delež nabitih delcev v pljusku (f_{CH}), in delež zadetkov na poti delca z visokim pragom prehodnega sevanja v TRT (f_{HT}). Pljusk je identificiran kot elektronski pljusk, če izpolnjuje naslednje pogoje:

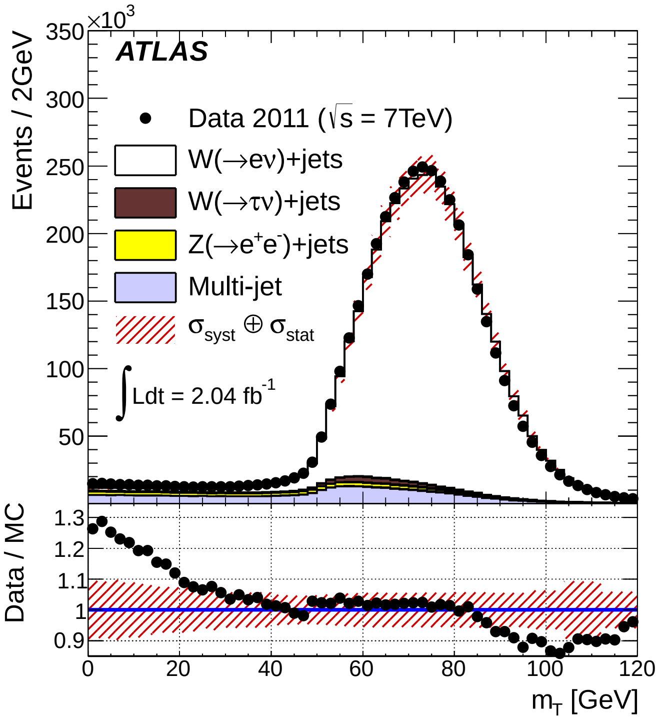

(a)

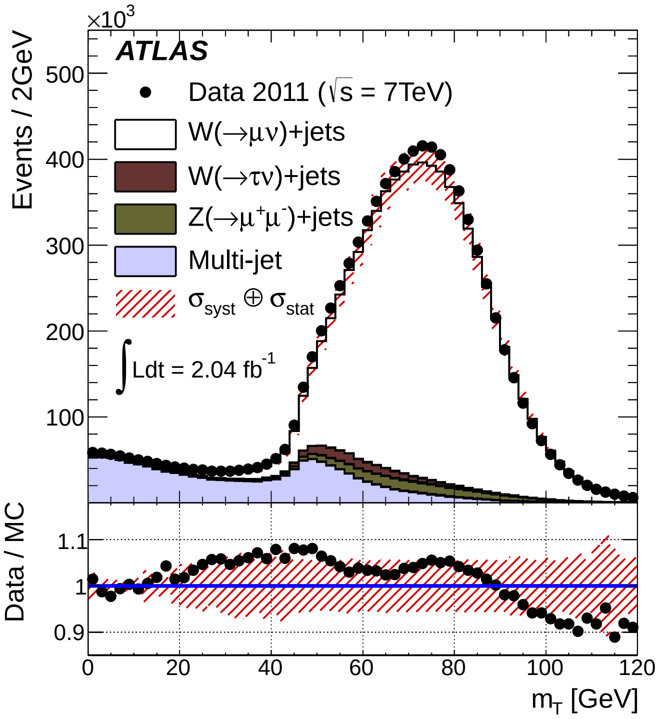

(b)

Slika 8.3: Transverzalna masa kandidatov za bozon W v razpadnih kanalih $W \rightarrow e\nu$ (zgoraj) in $W \rightarrow \mu\nu$ (spodaj). Podatki so prikazani s pikami in so prikazani v primerjavi s pričakovanji procesov Standardnega modela, ki so prikazani z zloženimi histogrami različnih barv. S poševnimi črtami je prikazan kvadratni seštevek statistične in sistematične negotovosti, kot je opisano v podpoglavju 8.4.3.

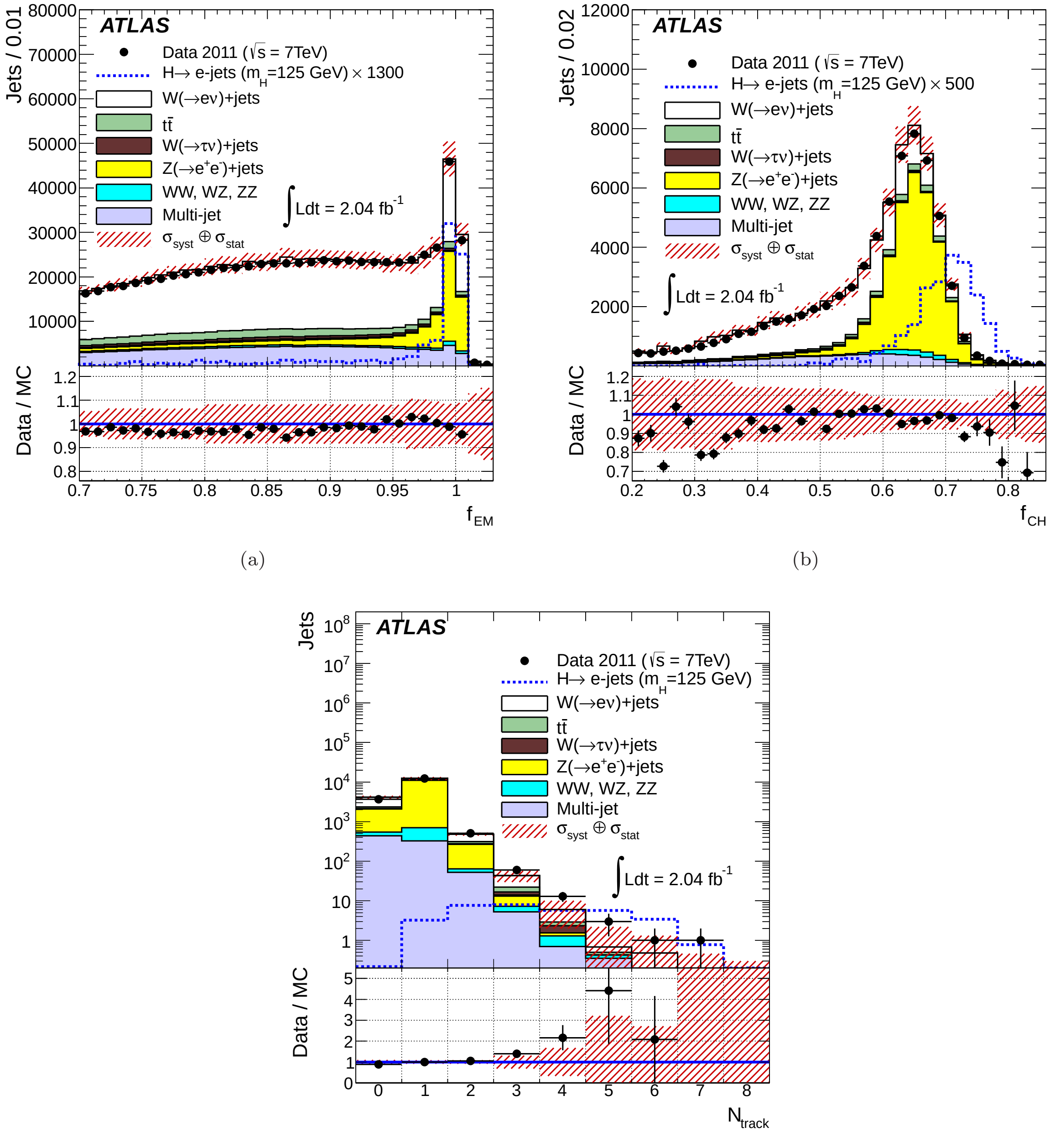

(a)

(b)

(c)

Slika 8.4: Porazdelitev elektromagnetnega deleža pljuskov, f_{EM}, po $W \to e\nu$ izboru (a), deležu nabitih delcev, f_{CH}, po izbiri f_{EM} (b) in števila sledi, povezanih z pljuskom, N_{track}, po f_{EM} in f_{CH} izboru (c). Podatki so prikazani s pikami in so prikazani v primerjavi s pričakovanji SM procesov, ki so prikazani z zloženi histogrami različnih barv. Signalna porazdelitev ustreza za tristopenjskemu modelu skritega sektorja z maso temnega fotona $m_{\gamma_{\mathrm{d}}} = 100$ MeV. S poševnimi črtami je prikazan kvadratni seštevek statistične in sistematične negotovosti.

- $p_T > 30$ GeV
- $|\eta| < 2.0$
- $f_{\mathrm{EM}} \geq 0.99$
- $f_{\mathrm{CH}} \geq 0.66$
- število sledi, povezanih s pljuskom, mora biti $N_{\mathrm{track}} \geq 2$, kjer posamezna sled izpolnjuje naslednje pogoje:
  - $|\eta| < 2.0$
  - $p_T \geq 5$ GeV
  - število zadetkov v pixel detektorju, $N_{\mathrm{pix}} \geq 2$
  - skupno število zadetkov v pixel in SCT detektorjih, $N_{\mathrm{pix}} + N_{\mathrm{SCT}} \geq 7$
  - delež zadetkov z visokim pragom prehodnega sevanja v TRT, $f_{\mathrm{HT}} \geq 0.08$

Med podatki in simulacijami MC opazimo dobro ujemanje v f_{EM}, f_{CH} in številu sledi, povezanih s pljuskom, kot je razvidno iz slike 8.4.

8.4.3 Določitev ozadja in sistematske negotovosti

Prevladujoče ozadje v iskanju tega signala izhaja iz produkcije bozona W skupaj s hadronskimi pljuski, ki v detektorju posnemajo signaturo elektronskih pljuskov. Podrobna simulacija MC tega ozadja je pokazala, da visoka vsebnost elektronov v teh pljuskih izvira iz sevanja končnega stanja oziroma razpadov nevtralnih pionov in kasnejše pretvorbe fotonov v pare elektrona in pozitrona. Napoved ozadja iz simulacije MC bi bila odvisna od modeliranja sevanja končnega stanja in hadronizacije partona, ki bi pripeljala do velike negotovosti. Namesto tega je prispevek ozadja v področju signala ocenjen iz podatkov, ki uporabljajo tako imenovano matrično metodo [210], ki temelji izključno na podatkih (nobena simulacija ni uporabljena). Rezultate matrične metode smo preverili še z dvema drugima metodama določitve ozadja in ugotovili, da se rezultati ujemajo. Ena od teh ocen ozadja – ABCD metoda – temelji na podatkih, druga ocena pa na simulaciji MC. Rezultati ocene ozadja, skupaj z ocenjenima statističnio in sistematično negotovostjo, so podani v tabeli 8.2. Ocene iz različnih metod se ob upoštevanju negotovosti dobro ujemajo med sabo. Sistematične negotovosti za signal so navedene v tabeli 8.3.

8.5 Rezultati

Opazovani in napovedani donosi dogodkov po končnem izboru so prikazani v tabeli 8.4 in na sliki 8.5. Število dogodkov v signalni regiji je v skladu s predpostavko, da k dogodkom prispevajo samo procesi SM, z enim dogodkom, opaženim v končnem izboru v $W \to \mu\nu$ kanalu, in brez opaženih dogodkov v končnem izboru v $W \to e\nu$ kanalu.

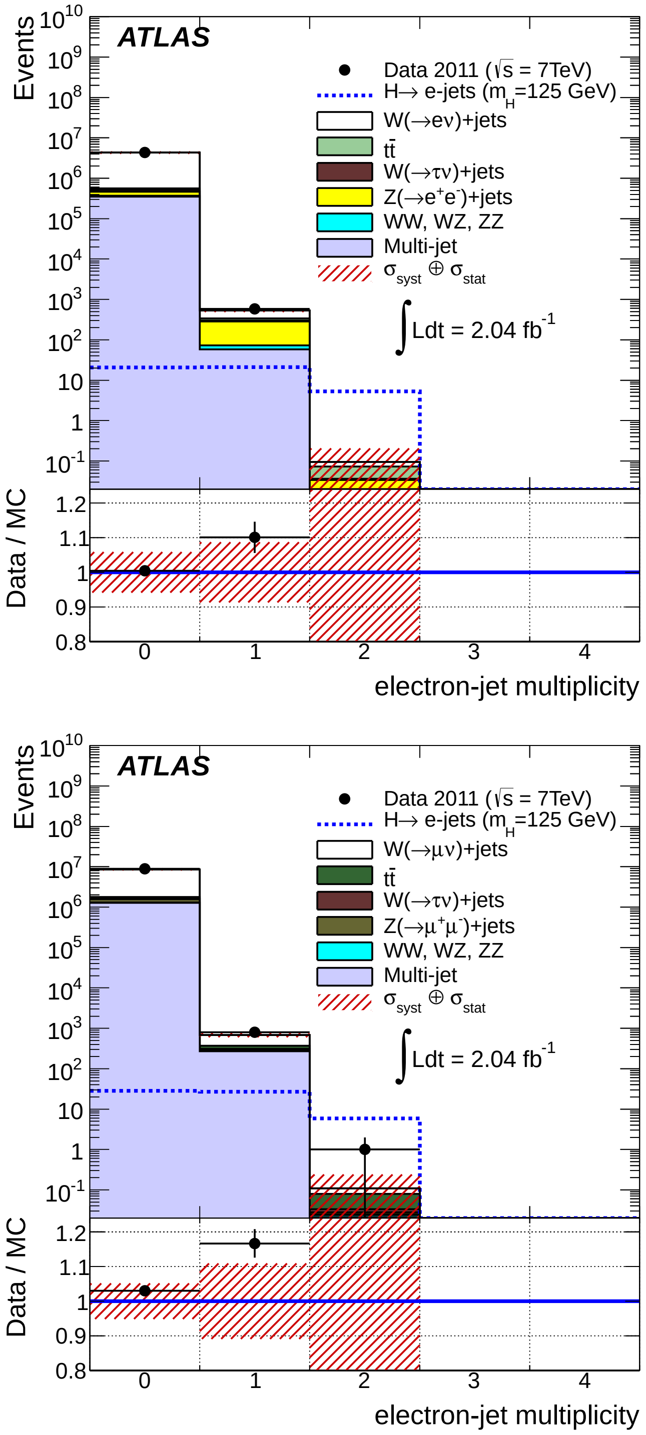

Slika 8.5: Porazdelitev dogodkov v kanalih $W \to e\nu$(zgoraj) in $W \to \mu\nu$ (spodaj) glede na število leptonskih pljuskov na dogodek. Podatki so prikazani s pikami s črtami in so primerjani s pričakovanji procesov Standardnega modela, ki so prikazani z zloženimi histogrami različnih barv. Signalna porazdelitev je prikazana kot črtkan histogram in ustreza tristopenjskemu modelu skritega sektorja z maso temnega fotona $m_{\gamma_\mathrm{d}} = 100$ MeV. Pri tem predpostavljamo, da sipalni presek signala ustreza vrednosti SM za produkcijo WH in 100% razvejitveno razmerje razpadov Higgsovega bozona v elektronske pljuske.

Na podlagi tega ocenimo 95% mejo intervala zaupanja za velikost signala, $\sigma(WH) \times \text{BR}(H \to e\text{-jets})/\sigma_{\text{SM}}(WH)$, kjer $\sigma(WH)$ označuje produkt sipalnega preseka produkcije WH in razvejitvenega razmerja za razpad bozona W v leptone (elektron, mion, tau) in $\sigma_{\text{SM}}(WH)$ ustreza pričakovanju SM [213] za te količine. BR($H \to e$-jets) označuje razvejitveno razmerje za razpad Higgsovega bozona v elektronske pljuske. Rezultati so predstavljeni na sliki 8.6 in v tabeli 8.5 za tristopenjski in dvostopenjski model skritega sektorja. Rezultati se znotraj statistične negotovosti signala ujemajo za obe masi temnih fotonov $m_{\gamma_d} = 100$ in 200 MeV. Meje so določene z uporabo tehnik CLs [214]. Verjetnosti so podane s Poissonovo porazdelitvijo za skupno število dogodkov v signalni regiji in so izračunane z uporabo števila pričakovanih in opaženih dogodkov, pri čemer rezultati elektronskih in mionskih kanalov v verjetnostni funkciji nastopajo hkrati. Sistematične negotovosti signala in ozadja so vključene v verjetnostno funkcijo kot moteči parametri z uporabo funkcije gama verjetnostne gostote [216]. Ob predpostavki, da ima sipalni presek produkcije WH vrednost SM, za posamezen sklop parametrov skritega sektorja, ki smo ga tukaj izbrali, analiza izključuje razvejitveno razmerje Higgsovega bozona v elektronske pljuske med 24 in 45% za $m_H = 125$ GeV v 95% mejah zaupanja.

Metoda določitve ozadja	Predvideno število dogodkov ozadja
Matrična (osnovna)	0.41 ± 0.29 (stat) ± 0.12 (syst)
ABCD (navzkrižno preverjanje)	0.46 ± 0.32 (stat) ± 0.10 (syst)
MC (navzkrižno preverjanje)	0.21 ± 0.05 (stat) $^{+\,0.23}_{-\,0.21}$ (syst)

Tabela 8.2: Predvideno število dogodkov ozadja po končnem izboru, vključno s statističnimi in sistematičnimi negotovostmi, pridobljeno s tremi različnimi metodami. Matrična metoda je osnovno orodje za določanje ozadja. Dve drugi metodi smo uporabili kot navzkrižno preverjanje.

Vir sistematične negotovosti	Prispevek (%)
Majhna statistika simuliranega signala	13%
Luminoznost pospeševalnika	3.7%
Sipalni presek signala, $\sigma \times$ BR	$^{+3.7}_{-4.3}$%
Učinkovitost izbora elektronov	5%
Učinkovitost izbora mionov	3%
Modeliranje parametra f_{EM}	3%
Modeliranje parametra f_{CH}	0.1%
Modeliranje parametra f_{HT}	1%
Skala energije elektrona	0.5%
Resolucija energije elektrona	0.2%
Resolucija gibalne količine miona	0.5%
Večkratne protonske interakcije na trk curkov (pile-up)	<0.1%
Skupaj	15%

Tabela 8.3: Sistematične negotovosti za signal.

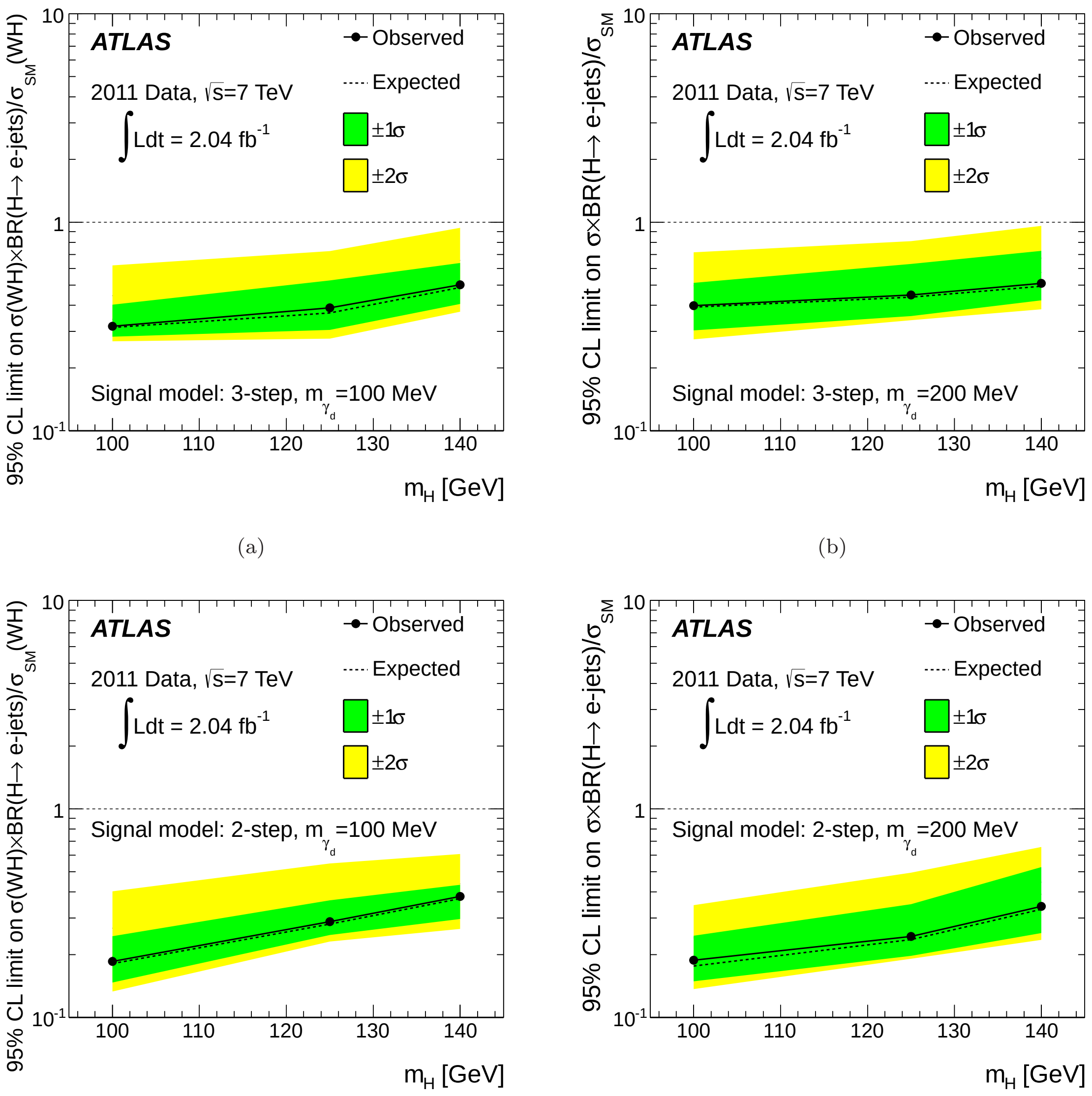

(a) (b)

(c) (d)

Slika 8.6: Opažena in pričakovana 95% meja intervala zaupanja za velikost signala, $\sigma(WH) \times \mathrm{BR}(H \to e\text{-jets})/\sigma_{\mathrm{SM}}(WH)$, je prikazana kot funkcija mase Higgsovega bozona za tristopenjski (a) in dvostopenjski (c) model skritega sektorja z maso temnega fotona $m_{\gamma_d} = 100$ MeV, tristopenjski (b) in dvostopenjski (d) model skritega sektorja z maso temnega fotona $m_{\gamma_d} = 200$ MeV. Temni (svetli) pas vsebuje 68% (95%) rezultatov psevdoeksperimentov, ustvarjenih v okviru predpostavke, da k dogodkom prispevajo samo procesi SM.

8.6 Sklepi in razprava

Predstavljeno je iskanje razpadov Higgsovega bozona v skriti sektor in nadalje v zelo kolimirane snope elektronov, za katere pričakujemo, da bodo v detektorju videti kot samostojni objekti, imenovani elektronski pljuski. Analiza je bila izvedena na vzorcu podatkov z integrirano luminoznostjo 2.04 fb^{-1}, zbranih v protonskih trkih pri težiščni energiji 7 TeV z detektorjem ATLAS na LHC v letu 2011.

Iskanje je bilo izvedeno v kanalu WH produkcije Higgsovega bozona z izbiro parametrov skritega sektorja, kjer Higgsov bozon razpada v takojšnje elektronske pljuske. Za namen tega dela smo razvili metode identifikacije elektronskih pljuskov, ki zagotavljajo dobro diskriminacijo signala od ozadja in hkrati preprečujejo občutljivost na podrobne topologije elektronov v elektronskih pljuskih.

Opaženi podatki so skladni s predpostavko, da k dogodkom prispevajo samo procesi SM. Zato smo ocenili 95% mejo intervala zaupanja za velikost produkta sipalnega preseka produkcije WH in razvejitvenega razmerja za razpad Higgsovega bozona v elektronske

Signal	tristopenjski model		dvostopenjski model	
m_H (GeV)	$m_{\gamma_d} = 100$ MeV	$m_{\gamma_d} = 200$ MeV	$m_{\gamma_d} = 100$ MeV	$m_{\gamma_d} = 200$ MeV
100	$14.3 \pm 1.7 \pm 0.8$	$12.4 \pm 1.6 \pm 0.7$	$22.6 \pm 2.1 \pm 1.2$	$23.5 \pm 2.1 \pm 1.2$
125	$11.3 \pm 1.0 \pm 0.6$	$10.7 \pm 1.1 \pm 0.6$	$16.2 \pm 1.2 \pm 0.9$	$18.1 \pm 1.4 \pm 1.0$
140	$9.6 \pm 0.8 \pm 0.5$	$9.0 \pm 0.8 \pm 0.4$	$13.7 \pm 0.9 \pm 0.8$	$13.9 \pm 0.9 \pm 0.8$
Ozadje	$0.41 \pm 0.29 \pm 0.12$			
Podatki	1			

Tabela 8.4: Število pričakovanih in opaženih dogodkov po končnem izboru. Pričakovani donosi signalov so prikazani tako za tristopenjski kot za dvostopenjski model skritega sektorja z masama temnega fotona 100 in 200 MeV. Statistična (prva) in sistematična (druga) negotovost sta predstavljeni ločeno. Rezultati so podani za kombinacijo kanalov $W \to e\nu$ in $W \to \mu\nu$. En kandidat za signalni dogodek je opažen v podatkih v kanalu $W \to \mu\nu$.

Model	m_{γ_d} (MeV)	**Opazovana**	Pričakovana	-1σ	+1σ	-2σ	+2σ
tristopenjski	100	**0.39**	0.37	0.30	0.53	0.28	0.73
tristopenjski	200	**0.45**	0.44	0.36	0.63	0.34	0.81
dvostopenjski	100	**0.29**	0.28	0.24	0.35	0.19	0.55
dvostopenjski	200	**0.24**	0.24	0.25	0.36	0.23	0.55

Tabela 8.5: 95% meja intervala zaupanja za velikost signala, $\sigma(WH) \times \text{BR}(H \to e\text{-jets})/\sigma_{\text{SM}}(WH)$, za maso Higgsovega bozona 125 GeV za različne izbire parametrov modela skritega sektorja. Tukaj $\sigma(WH)$ označuje produkt sipalnega preseka produkcje WH in razvejitvenega razmerja za razpad bozona W v leptone (elektron, mion, tau). $\sigma_{\text{SM}}(WH)$ ustreza pričakovanju SM te količine in $\text{BR}(H \to e\text{-jets})$ ustreza razvejitvenemu razmerju razpadov Higgsovega bozona v elektronske pljuske.

pljuske ob predpostavki za tristopenjski oziroma dvostopenjski model skritega sektorja in maso temnega fotona pod 210 MeV.

Doslej nismo opazili nobenega neposrednega dokaza o razpadu Higgsovega bozona v leptonske pljuske. To dejstvo je še ena potrditev, da je Higgsov bozon, ki so ga opazili fiziki na eksperimentih ATLAS in CMS, bolj verjetno Higgsov bozon Standardnega modela. Vendar pa se je ob zaključku pisanja te disertacije na ATLAS-u končalo zbiranje podatkov v trkih protonov s težiščno energijo 8 TeV in novi vzorec zbranih podatkov vsebuje desetkrat več statistike kot vzorec, na katerem je izvedena predstavljena analiza. Analiza teh podatkov bi omogočila raziskovanje nižjega razvejitvenega razmerja razpada Higgsovega bozona v elektronske pljuske in s tem testiranje bolj subtilnih učinkov skritega sektorja. Poleg tega velikostni red večja statistika nudi priložnost za preučevanje elektronskih pljuskov v kanalu produkcije ZH, poleg WH. Navkljub temu, da ima ta kanal približno desetkrat manjši sipalni presek kot WH, je tu ozadje je bistveno manjše. Ker leptonski razpadi bozona Z nimajo nevidnih razpadnih produktov, je mogoče rekonstruirati invarianto maso Higgsovega bozona, kar omogoča precej čistejše okolje za analizo leptonskih pljuskov.

Poleg elektronskih pljuskov je zelo pomembna tudi analiza z mionskimi pljuski. Zdi se, da sta v modelih skritega sektorja elektronski ali mionski način razpada enako verjetna, čeprav nekateri avtorji trdijo, da modeli z mioni razložijo podatke nekoliko bolje [217].

Končno, pomemben vidik analize leptonskih pljuskov je njihovo iskanje v kanalu direktne produkcije Higgsovega bozona. Ta kanal ima dva velikostna razreda višji sipalni presek, čeprav z bistveno višjim relativnim ozadjem. Prav tako tudi predstavlja izziv za eksperimentalne fizike, saj proženje na leptonskih pljuskih, ki nastanejo v razpadih Higgsovega bozona, ni enostavna naloga.

Na koncu moramo omeniti, da je program za iskanje leptonskih pljuskov pravkar napravil svoje prve – čeprav zelo pomembne korake. Doslej je bil analiziran samo majhen del podatkov, zbranih z detektorjem ATLAS, in v tem trenutku je na ATLAS-u v teku široka dejavnost, namenjena analizi celotnega nabora podatkov. Modeli ki vsebujejo skriti sektor, ostajajo med najbolj naravnimi kandidati za temni snov, saj lahko sočasno elegantno razložijo različna astrofizikalna opazovanja. Zato je pomembno, da iščemo morebitne manifestacije skritih sektorjev na trkalnikih – leptonske pljuske.

Bibliography

[1] ATLAS Collaboration. Observation of a new particle in the search for the Standard Model Higgs boson with the ATLAS detector at the LHC. *Phys. Lett. B*, 716:1–29, 2012, arXiv:1207.7214 [hep-ex].

[2] CMS Collaboration. Observation of a new boson at a mass of 125 GeV with the CMS experiment at the LHC. *Phys. Lett. B*, 716:30–61, 2012, arXiv:1207.7235 [hep-ex].

[3] Study of the spin of the new boson with up to 25 fb^{-1} of atlas data. Technical Report ATLAS-CONF-2013-040, CERN, Geneva, Apr 2013, cds.cern.ch/record/1542341/files/ATLAS-CONF-2013-040.pdf.

[4] Hajime Aoki and Satoshi Iso. Revisiting the Naturalness Problem – Who is afraid of quadratic divergences? *Phys.Rev.*, D86:013001, 2012, 1201.0857.

[5] Stephen P. Martin. A Supersymmetry primer. 1997, hep-ph/9709356.

[6] V. A. Ryabov, V. A. Tsarev, and A. M. Tskhovrebov. The search for dark matter particles. *Physics-Uspekhi*, 51(11):1091–1121, 2008.

[7] Neta A. Bahcall, Jeremiah P. Ostriker, Saul Perlmutter, and Paul J. Steinhardt. The Cosmic triangle: Assessing the state of the universe. *Science*, 284:1481–1488, 1999, astro-ph/9906463.

[8] R. Bernabei, Pierluigi Belli, F. Cappella, R. Cerulli, F. Montecchia, et al.. Dark matter search. *Riv.Nuovo Cim.*, 26N1:1–73, 2003, astro-ph/0307403.

[9] A. D. Chernin. Dark energy and universal antigravitation. *Physics-Uspekhi*, 51(3):253–282, 2008.

[10] M. Aguilar, AMS collaboration, et al.. First Result from the Alpha Magnetic Spectrometer on the International Space Station: Precision Measurement of the Positron Fraction in Primary Cosmic Rays of 0.5350 GeV. *Phys.Rev.Lett.*, 110(14), 2013.

[11] HEAT Collaboration, S. W. Barwick, et al.. Measurements of the Cosmic-Ray Positron Fraction from 1 to 50 GeV. *The Astrophysical Journal Letters*, 482(2):L191, 1997, arXiv:9703192 [astro-ph].

[12] Fermi LAT Collaboration, A. A. Abdo, et al.. Measurement of the Cosmic Ray $e^+ + e^-$ Spectrum from 20 GeV to 1 TeV with the Fermi Large Area Telescope. *Phys. Rev. Lett.*, 102:181101, 2009, arXiv:0905.0025 [astro-ph].

[13] PAMELA Collaboration, O. Adriani, et al.. An anomalous positron abundance in cosmic rays with energies 1.5-100 GeV. *Nature*, 458:607–609, 2009, arXiv:0810.4995 [astro-ph].

[14] J. Chang, J.H. Adams, H.S. Ahn, G.L. Bashindzhagyan, M. Christl, et al.. An excess of cosmic ray electrons at energies of 300-800 GeV. *Nature*, 456:362–365, 2008.

[15] R. Bernabei et al.. New results from DAMA/LIBRA. *Eur. Phys. J. C*, 67:39–49, 2010, arXiv:1002.1028 [astro-ph.GA].

[16] C.E. Aalseth, P.S. Barbeau, J. Colaresi, J.I. Collar, J. Diaz Leon, et al.. Search for an Annual Modulation in a P-type Point Contact Germanium Dark Matter Detector. *Phys.Rev.Lett.*, 107:141301, 2011, 1106.0650.

[17] C.E. Aalseth et al.. Results from a Search for Light-Mass Dark Matter with a P-type Point Contact Germanium Detector. *Phys.Rev.Lett.*, 106:131301, 2011, 1002.4703.

[18] P. Adamson, MINOS Collaboration, et al.. Comparisons of annual modulations in minos with the event rate modulation in cogent. *Phys. Rev. D*, 87:032005, Feb 2013.

[19] N. Arkani-Hamed, D. P. Finkbeiner, T. R. Slatyer, and N. Weiner. A theory of dark matter. *Phys. Rev. D*, 79:015014, 2009, arXiv:0810.0713 [hep-ph].

[20] Clifford Cheung, Joshua T. Ruderman, Lian-Tao Wang, and Itay Yavin. Kinetic Mixing as the Origin of Light Dark Scales. *Phys.Rev.*, D80:035008, 2009, 0902.3246.

[21] A. Sommerfeld. *Ann. Phys. (Leipzig)*, 403:257, 1931.

[22] P. W. Higgs. Broken symmetries, massless particles and gauge fields. *Phys. Lett.*, 12:132–133, 1964.

[23] F. Englert and R. Brout. Broken Symmetry and the Mass of Gauge Vector Mesons. *Phys. Rev. Lett.*, 13:321–323, 1964.

[24] G.S. Guralnik, C.R. Hagen, and T.W.B. Kibble. Global Conservation Laws and Massless Particles. *Phys. Rev. Lett.*, 13:585–587, 1964.

[25] ATLAS collaboration. Search for WH production with a light Higgs boson decaying to prompt electron-jets in proton-proton collisions at sqrt(s)=7 TeV with the ATLAS detector. *New J.Phys.*, 15:043009, 2013, 1302.4403.

[26] N. Prakash. *Dark Matter, Neutrino, and Our Solar System.* World Scientific Publishing Company Incorporated, 2012, ISBN:9789814304535.

[27] J. H. Oort. The force exerted by the stellar system in the direction perpendicular to the galactic plane and some related problems. *Bulletin of the Astronomical Institutes of the Netherlands*, 6:249, 1932.

[28] John N. Bahcall, Chris Flynn, and Andrew Gould. Local dark matter from a carefully selected sample. *Astrophys.J.*, 389:234–250, 1992.

[29] K. Kuijken and G. Gilmore. The galactic disk surface mass density and the Galactic force K(z) at Z = 1.1 kiloparsecs. *Astrophys.J.*, 367:L9–L13, 1991.

[30] Adam G. Riess et al.. Observational evidence from supernovae for an accelerating universe and a cosmological constant. *Astron.J.*, 116:1009–1038, 1998, astro-ph/9805201.

[31] S. Perlmutter, The Supernova Cosmology Project, et al.. Measurements of and from 42 high-redshift supernovae. *The Astrophysical Journal*, 517(2):565, 1999.

[32] Albert Einstein. Cosmological Considerations in the General Theory of Relativity. *Sitzungsber.Preuss.Akad.Wiss.Berlin (Math.Phys.)*, 1917:142–152, 1917.

[33] A Friedmann. Uber die krummung des raumes. *Z. Phys.*, 10:377–386, 1922.

[34] Lev A. Kofman, Nickolay Y. Gnedin, and Neta A. Bahcall. Cosmological constant, COBE cosmic microwave background anisotropy, and large scale clustering. *Astrophys.J.*, 413:1–9, 1993.

[35] J.P. Ostriker and Paul J. Steinhardt. The Observational case for a low density universe with a nonzero cosmological constant. *Nature*, 377:600–602, 1995.

[36] LawrenceM. Krauss and MichaelS. Turner. The cosmological constant is back. *General Relativity and Gravitation*, 27:1137–1144, 1995.

[37] T. Totani, Y. Yoshii, and K. Sato. Evolution of the luminosity density in the universe: Implications for the nonzero cosmological constant. *The Astrophysical Journal Letters*, 483(2):L75, 1997.

[38] Edvige Corbelli and Paolo Salucci. The extended rotation curve and the dark matter halo of m33. 1999, astro-ph/9909252.

[39] A. Bosma. 21-cm line studies of spiral galaxies. 2. The distribution and kinematics of neutral hydrogen in spiral galaxies of various morphological types. *Astron.J.*, 86:1825, 1981.

[40] V. C. Rubin, W. K. J. Ford, and N. . Thonnard. Rotational properties of 21 SC galaxies with a large range of luminosities and radii, from NGC 4605 /R = 4kpc/ to UGC 2885 /R = 122 kpc/. *Astrophys.J.*, 238:471–487, 1980.

[41] C. Carignan and K. C. Freeman. Basic parameters of dark halos in late-type spirals. *Astrophys.J.*, 294:494–501, 1985.

[42] Y Sofue and V C Rubin. Rotation curves of spiral galaxies. Technical Report astro-ph/0010594. ASTRO-2000-09, Oct 2000.

[43] M. Milgrom and E. Braun. The rotation curve of DDO 154 - A particularly acute test of the modified dynamics. *Astrophys.J.*, 334:130–133, 1988.

[44] Matthias Bartelmann. Gravitational Lensing. *Class.Quant.Grav.*, 27:233001, 2010, 1010.3829.

[45] Frank Lenzen, Sabine Schindler, and Otmar Scherzer. Automatic detection of arcs and arclets formed by gravitational lensing. *Astron.Astrophys.*, 416:391–401, 2004, astro-ph/0311554.

[46] Matthias Bartelmann and Peter Schneider. Weak gravitational lensing. *Phys.Rept.*, 340:291–472, 2001, astro-ph/9912508.

[47] Ramesh Narayan and Matthias Bartelmann. Lectures on gravitational lensing. 1996, astro-ph/9606001.

[48] M. Meneghetti, M. Bartelmann, H. Dahle, and M Limousin. Arc Statistics. 2013, 1303.3363.

[49] J. Merten, D. Coe, R. Dupke, R. Massey, A. Zitrin, et al.. Creation of cosmic structure in the complex galaxy cluster merger Abell 2744. *Mon.Not.Roy.Astron.Soc.*, 417:333–347, 2011, 1103.2772.

[50] M. Bartelmann, L. J. King, and P. Schneider. Weak-lensing halo numbers and dark-matter profiles. *Astron. Astrophys.*, 378:361–369, 2001, arXiv:astro-ph/0103465.

[51] Henk Hoekstra, Matthias Bartelmann, Haakon Dahle, Holger Israel, Marceau Limousin, et al.. Masses of galaxy clusters from gravitational lensing. 2013, 1303.3274.

[52] A.D. Dolgov. Neutrinos in cosmology. *Phys.Rept.*, 370:333–535, 2002, hep-ph/0202122.

[53] Scott Dodelson and Lawrence M. Widrow. Sterile-neutrinos as dark matter. *Phys.Rev.Lett.*, 72:17–20, 1994, hep-ph/9303287.

[54] Z.G. Berezhiani and M.I. Vysotsky. NEUTRINO DECAY IN MATTER. *Phys.Lett.*, B199:281, 1987.

[55] Gerard Jungman, Marc Kamionkowski, and Kim Griest. Supersymmetric dark matter. *Phys.Rept.*, 267:195–373, 1996, hep-ph/9506380.

[56] Hsin-Chia Cheng, Jonathan L. Feng, and Konstantin T. Matchev. Kaluza-Klein dark matter. *Phys.Rev.Lett.*, 89:211301, 2002, hep-ph/0207125.

[57] ATLAS collaboration. Search for magnetic monopoles in $\sqrt{s} = 7$ TeV pp collisions with the ATLAS detector. *Phys.Rev.Lett.*, 109:261803, 2012, 1207.6411.

[58] L.J. Rosenberg and K.A. van Bibber. Searches for invisible axions. *Phys.Rept.*, 325:1–39, 2000.

[59] Karim Benakli, John R. Ellis, and Dimitri V. Nanopoulos. Natural candidates for superheavy dark matter in string and M theory. *Phys.Rev.*, D59:047301, 1999, hep-ph/9803333.

[60] Roshan Foadi, Mads T. Frandsen, and Francesco Sannino. Technicolor Dark Matter. *Phys.Rev.*, D80:037702, 2009, 0812.3406.

[61] L.B. Okun. Mirror particles and mirror matter: 50 years of speculations and search. *Phys.Usp.*, 50:380–389, 2007, hep-ph/0606202.

[62] Gianfranco Bertone, Dan Hooper, and Joseph Silk. Particle dark matter: Evidence, candidates and constraints. *Phys.Rept.*, 405:279–390, 2005, hep-ph/0404175.

[63] E. Komatsu et al.. Seven-Year Wilkinson Microwave Anisotropy Probe (WMAP) Observations: Cosmological Interpretation. *Astrophys.J.Suppl.*, 192:18, 2011, 1001.4538.

[64] K. Freese, M. Lisanti, and C. Savage. Annual Modulation of Dark Matter: A Review. 2012, 1209.3339.

[65] Pierre Fayet. Spontaneously Broken Supersymmetric Theories of Weak, Electromagnetic and Strong Interactions. *Phys.Lett.*, B69:489, 1977.

[66] Lars Bergstrom. Nonbaryonic dark matter: Observational evidence and detection methods. *Rept.Prog.Phys.*, 63:793, 2000, hep-ph/0002126.

[67] T.P. Cheng and L.F. Li. GAUGE THEORY OF ELEMENTARY PARTICLE PHYSICS. 1984.

[68] K Nakamura and Particle Data Group. Review of particle physics. *Journal of Physics G: Nuclear and Particle Physics*, 37(7A):075021, 2010.

[69] ATLAS collaboration. Combined measurements of the mass and signal strength of the higgs-like boson with the atlas detector using up to 25 fb^{-1} of proton-proton collision data. Technical report, CERN, Geneva, Mar 2013, cds.cern.ch/record/1523727/files/ATLAS-CONF-2013-014.pdf.

[70] A. Falkowski, J. T. Ruderman, T. Volansky, and J. Zupan. Hidden Higgs Decaying to Lepton Jets. *JHEP*, 1005:077, 2010, arXiv:1002.2952 [hep-ph].

[71] A. Falkowski, J. T. Ruderman, T. Volansky, and J. Zupan. Discovering higgs boson decays to lepton jets at hadron colliders. *Phys. Rev. Lett.*, 105(24):241801, 2010, arXiv:1007.3496 [hep-ph].

[72] M. J. Strassler and K. M. Zurek. Echoes of a hidden valley at hadron colliders. *Phys. Lett. B*, 651(5-6):374 – 379, 2007, arXiv:0604261 [hep-ph].

[73] N. Arkani-Hamed and N. Weiner. LHC Signals for a SuperUnified Theory of Dark Matter. *JHEP*, 12:104. mult. p, 2008, arXiv:0810.0714 [hep-ph].

[74] M. Baumgart, C. Cheung, J. T. Ruderman, L.-T. Wang, and I. Yavin. Non-abelian dark sectors and their collider signatures. *JHEP*, 0904(04):014, 2009, arXiv:0901.0283 [hep-ph].

[75] B. Patt and F. Wilczek. Higgs-field portal into hidden sectors. 2006, arXiv:0605188 [hep-ph].

[76] H. Davoudiasl, R. Kitano, Tianjun Li, and H. Murayama. The new minimal standard model. *Phys. Lett. B*, 609(1-2):117 – 123, 2005, arXiv:0405097v2 [hep-ph].

[77] D. J. Gross, J. A. Harvey, E. Martinec, and R. Rohm. Heterotic string theory (I). The free heterotic string. *Nucl. Phys. B*, 256:253 – 284, 1985.

[78] H. Georgi. Unparticle physics. *Phys. Rev. Lett.*, 98(22):221601, 2007, arXiv:0703260 [hep-ph].

[79] B. Holdom. Searching for epsilon charges and a new U(1). *Phys. Lett. B*, 178(1):65 – 70, 1986.

[80] K. R. Dienes, C. F. Kolda, and J. March-Russell. Kinetic mixing and the supersymmetric gauge hierarchy. *Nucl. Phys. B*, 492:104–118, 1997, arXiv:9610479v2 [hep-ph].

[81] Yi-Zhong Fan, Bing Zhang, and Jin Chang. $e^{\pm}$ Excesses in the Cosmic Ray Spectrum and Possible Interpretations. *Int.J.Mod.Phys.*, D19:2011–2058, 2010, 1008.4646.

[82] G.B. Pisani, L. Izzo, R. Ruffini, C.L. Bianco, M. Muccino, et al.. Novel distance indicator for gamma-ray bursts associated with supernovae. *A&A 552,*, L5, 2013, 1304.1764.

[83] Andrew W. Strong, Igor V. Moskalenko, and Olaf Reimer. Diffuse galactic continuum gamma rays. A Model compatible with EGRET data and cosmic-ray measurements. *Astrophys.J.*, 613:962–976, 2004, astro-ph/0406254.

[84] A.W. Strong and I.V. Moskalenko. Models for galactic cosmic ray propagation. *Adv.Space Res.*, 27:717–726, 2001, astro-ph/0101068.

[85] I.V. Moskalenko and A.W. Strong. Production and propagation of cosmic ray positrons and electrons. *Astrophys.J.*, 493:694–707, 1998, astro-ph/9710124.

[86] M. Simon, A. Molnar, and S. Roesler. A new calculation of the interstellar secondary cosmic-ray antiprotons. *The Astrophysical Journal*, 499(1):250, 1998.

[87] F. Donato et al.. Antiprotons from spallations of cosmic rays on interstellar matter. *The Astrophysical Journal*, 563(1):172, 2001.

[88] V.S. Ptuskin et al.. Dissipation of magnetohydrodynamic waves on energetic particles: impact on interstellar turbulence and cosmic ray transport. *Astrophys.J.*, 642:902–916, 2006, astro-ph/0510335.

[89] O. Adriani, G.C. Barbarino, G.A. Bazilevskaya, R. Bellotti, M. Boezio, et al.. A new measurement of the antiproton-to-proton flux ratio up to 100 GeV in the cosmic radiation. *Phys.Rev.Lett.*, 102:051101, 2009, 0810.4994.

[90] E.A. Baltz, B. Berenji, G. Bertone, L. Bergstrom, E. Bloom, et al.. Pre-launch estimates for GLAST sensitivity to Dark Matter annihilation signals. *JCAP*, 0807:013, 2008, 0806.2911.

[91] Borut Bajc, Tsedenbaljir Enkhbat, Dilip Kumar Ghosh, Goran Senjanovic, and Yue Zhang. MSSM in view of PAMELA and Fermi-LAT. *JHEP*, 1005:048, 2010, 1002.3631.

[92] ATLAS collaboration. Search for new phenomena in monojet plus missing transverse momentum final states using 10fb-1 of pp collisions at sqrts=8 tev with the atlas detector at the lhc. (ATLAS-CONF-2012-147), 2012, cds.cern.ch/record/1493486/files/ATLAS-CONF-2012-147.pdf.

[93] Wilfried Buchmuller. Gravitino Dark Matter. *AIP Conf.Proc.*, 1200:155–164, 2010, 0910.1870.

[94] Lars Bergstrom, Gianfranco Bertone, Torsten Bringmann, Joakim Edsjo, and Marco Taoso. Gamma-ray and Radio Constraints of High Positron Rate Dark Matter Models Annihilating into New Light Particles. *Phys.Rev.*, D79:081303, 2009, 0812.3895.

[95] Maxim Pospelov, Adam Ritz, and Mikhail B. Voloshin. Secluded WIMP Dark Matter. *Phys.Lett.*, B662:53–61, 2008, 0711.4866.

[96] R. Bernabei et al.. First results from dama/libra and the combined results with dama/nai. arXiv:0804.2741 [astro-ph].

[97] R. Bernabei et al.. Dark matter particles in the galactic halo: results and implications from dama/nai. arXiv:0501412 [astro-ph].

[98] Z. Ahmed et al.. Search for annual modulation in low-energy CDMS-II data. 2012, 1203.1309.

[99] R. Agnese et al.. Dark Matter Search Results Using the Silicon Detectors of CDMS II. *Phys.Rev.Lett.*, 2013, 1304.4279.

[100] E. Aprile et al.. Dark Matter Results from 225 Live Days of XENON100 Data. *Phys.Rev.Lett.*, 109:181301, 2012, 1207.5988.

[101] D. Yu. Akimov, H.M. Araujo, E.J. Barnes, V.A. Belov, A. Bewick, et al.. WIMP-nucleon cross-section results from the second science run of ZEPLIN-III. *Phys.Lett.*, B709:14–20, 2012, 1110.4769.

[102] S.C. Kim, H. Bhang, J.H. Choi, W.G. Kang, B.H. Kim, et al.. New Limits on Interactions between Weakly Interacting Massive Particles and Nucleons Obtained with CsI(Tl) Crystal Detectors. *Phys.Rev.Lett.*, 108:181301, 2012, 1204.2646.

[103] L. Baudis, J. Hellmig, G. Heusser, H.V. Klapdor-Kleingrothaus, S. Kolb, et al.. New limits on dark matter WIMPs from the Heidelberg - Moscow experiment. *Phys.Rev.*, D59:022001, 1999, hep-ex/9811045.

[104] David Tucker-Smith and Neal Weiner. Inelastic dark matter. *Phys.Rev.*, D64:043502, 2001, hep-ph/0101138.

[105] Spencer Chang, Graham D. Kribs, David Tucker-Smith, and Neal Weiner. Inelastic Dark Matter in Light of DAMA/LIBRA. *Phys.Rev.*, D79:043513, 2009, 0807.2250.

[106] Ilias Cholis, Lisa Goodenough, and Neal Weiner. High Energy Positrons and the WMAP Haze from Exciting Dark Matter. *Phys.Rev.*, D79:123505, 2009, 0802.2922.

[107] J. Knodlseder, P. Jean, V. Lonjou, G. Weidenspointner, N. Guessoum, et al.. The All-sky distribution of 511 keV electron-positron annihilation emission. *Astron.Astrophys.*, 441:513–532, 2005, astro-ph/0506026.

[108] A. Vecchio, A.C. Vincent, J. Miralda-Escude, and C. Pena-Garay. The positron density in the intergalactic medium and the galactic 511 keV line. 2013, 1304.0324.

[109] Douglas P. Finkbeiner and Neal Weiner. Exciting Dark Matter and the INTEGRAL/SPI 511 keV signal. *Phys.Rev.*, D76:083519, 2007, astro-ph/0702587.

[110] Claude Amsler et al.. Review of Particle Physics. *Phys.Lett.*, B667:1–1340, 2008.

[111] James D. Bjorken, Rouven Essig, Philip Schuster, and Natalia Toro. New Fixed-Target Experiments to Search for Dark Gauge Forces. *Phys.Rev.*, D80:075018, 2009, 0906.0580.

[112] Anson Hook, Eder Izaguirre, and Jay G. Wacker. Model Independent Bounds on Kinetic Mixing. *Adv.High Energy Phys.*, 2011:859762, 2011, 1006.0973.

[113] Joshua T. Ruderman and Tomer Volansky. Decaying into the Hidden Sector. *JHEP*, 1002:024, 2010, 0908.1570.

[114] Clifford Cheung, Joshua T. Ruderman, Lian-Tao Wang, and Itay Yavin. Lepton Jets in (Supersymmetric) Electroweak Processes. *JHEP*, 1004:116, 2010, 0909.0290.

[115] M. J. Strassler and K. M. Zurek. Discovering the higgs through highly-displaced vertices. *Phys. Lett. B*, 661(4):263 – 267, 2008, arXiv:0605193 [hep-ph].

[116] M. J. Strassler. Possible Effects of a Hidden Valley on Supersymmetric Phenomenology. 2006, arXiv:0607160 [hep-ph].

[117] M. J. Strassler. Why Unparticle Models with Mass Gaps are Examples of Hidden Valleys. 2008, arXiv:0801.0629 [hep-ph].

[118] R. Essig, P. Schuster, and N. Toro. Probing dark forces and light hidden sectors at low-energy e+e- colliders. *Phys. Rev. D*, 80.

[119] Adam Falkowski, Joshua T. Ruderman, and Tomer Volansky. Asymmetric Dark Matter from Leptogenesis. *JHEP*, 1105:106, 2011, 1101.4936.

[120] ATLAS collaboration. A search for prompt lepton-jets in pp collisions at $\sqrt{s} = 7$ TeV with the ATLAS detector. *Phys.Lett.*, B719:299–317, 2013, 1212.5409.

[121] CMS Collaboration. Search for light resonances decaying into pairs of muons as a signal of new physics. *JHEP*, 07:098. 30 p, 2011, arXiv:1106.2375 [hep-ex].

[122] ATLAS Collaboration. Search for displaced muonic lepton jets from light Higgs boson decay in proton-proton collisions at $\sqrt{s} = 7$ TeV with the ATLAS detector. *Phys.Lett.*, B721:32–50, 2013, 1210.0435.

[123] CDF Collaboration, T. Aaltonen, et al.. Search for anomalous production of multiple leptons in association with W and Z bosons at CDF. *Phys. Rev. D*, 85:092001, 2012, arXiv:1202.1260v2 [hep-ex].

[124] D0 Collaboration, V. M. Abazov, et al.. Search for events with leptonic jets and missing transverse energy in ppbar collisions at sqrts=1.96 tev. *Phys. Rev. Lett.*, 105:211802, 2010, arXiv:1008.3356 [hep-ex].

[125] Brian Batell, Maxim Pospelov, and Adam Ritz. Exploring Portals to a Hidden Sector Through Fixed Targets. *Phys.Rev.*, D80:095024, 2009, 0906.5614.

[126] Radovan Dermisek and John F. Gunion. Escaping the large fine tuning and little hierarchy problems in the next to minimal supersymmetric model and $h \to aa$ decays. *Phys.Rev.Lett.*, 95:041801, 2005, hep-ph/0502105.

[127] L. Evans and P. Bryant. LHC Machine. *JINST*, 3:S08001, 2008.

[128] O. Bruning, H. Burkhardt, and S. Myers. The large hadron collider. *Progress in Particle and Nuclear Physics*, 67(3):705 – 734, 2012.

[129] J. Abraham et al.. Measurement of the energy spectrum of cosmic rays above 1018 ev using the pierre auger observatory. *Physics Letters B*, 685(45):239 – 246, 2010.

[130] E. Eichten, I. Hinchliffe, K. Lane, and C. Quigg. Supercollider physics. *Rev. Mod. Phys.*, 56:579–707, Oct 1984.

[131] Jason Nielsen. Fundamentals of LHC Experiments. 2011, 1106.2516.

[132] G. Aad et al.. The ATLAS Experiment at the CERN Large Hadron Collider. *JINST*, 3:S08003, 2008.

[133] S. Chatrchyan et al.. The CMS experiment at the CERN LHC. *JINST*, 3:S08004, 2008.

[134] K. Aamodt et al.. The ALICE experiment at the CERN LHC. *JINST*, 3:S08002, 2008.

[135] Jr. Alves, A. Augusto et al.. The LHCb Detector at the LHC. *JINST*, 3:S08005, 2008.

[136] O. Adriani et al.. The LHCf detector at the CERN Large Hadron Collider. *JINST*, 3:S08006, 2008.

[137] TOTEM Collaboration, G. Anelli, et al.. The TOTEM experiment at the CERN Large Hadron Collider. *JINST*, 3:S08007, 2008.

[138] MoEDAL collaboration, James Pinfold, et al.. Technical design report of the moedal experiment. Technical Report CERN-LHCC-2009-006. MoEDAL-TDR-001, CERN, Geneva, 2009.

[139] ATLAS Collaboration. ATLAS high-level trigger, data acquisition and controls: Technical design report. 2003, CERN-LHCC-2003-022, ATLAS-TRD-016.

[140] David d'Enterria. Physics at the LHC: A Short overview. *J.Phys.Conf.Ser.*, 270:012001, 2011, 1010.1491.

[141] Alessia Tricomi. Results from LHCf Experiment. *EPJ Web Conf.*, 28:02003, 2012, 1202.2083.

[142] James L. Pinfold. Searching for the magnetic monopole and other highly ionizing particles at accelerators using nuclear track detectors. *Radiat.Meas.*, 44:834–839, 2009.

[143] James L. Pinfold. Dirac's dream: The search for the magnetic monopole. *AIP Conf.Proc.*, 1304:234–239, 2010.

[144] G. Antchev, P. Aspell, I. Atanassov, V. Avati, V. Berardi, et al.. The TOTEM detector at LHC. *Nucl.Instrum.Meth.*, A617:62–66, 2010.

[145] D. Brandt and D. Brandt. Intermediate accelerator physics. Proceedings, CERN Accelerator School, Zeuthen, Germany, September 15-26, 2003. 2006, cds.cern.ch/record/603056/files/CERN-2006-002.pdf.

[146] P. Schmser. Superconductivity in high energy particle accelerators. *Progress in Particle and Nuclear Physics*, 49(1):155 – 244, 2002.

[147] L Rossi. Experience with lhc magnets from prototyping to large scale industrial production and integration. (LHC-Project-Report-730. CERN-LHC-Project-Report-730):Streaming video ; 6 transparencies, 2004, accelconf.web.cern.ch/AccelConf/e04/PAPERS/WEXCH01.PDF.

[148] R. Assmann, M. Lamont, and S. Myers. A brief history of the LEP collider. *Nucl.Phys.Proc.Suppl.*, 109B:17–31, 2002.

[149] R Bailey and Paul Collier. Standard filling schemes for various lhc operation modes. Technical Report LHC-PROJECT-NOTE-323, CERN, Geneva, Sep 2003, http://cds.cern.ch/record/691782/files/project-note-323.pdf.

[150] T. Bohl, O. Brunner, F. Dubouchet, D.C. Glenat, J. Lollierou, et al.. The LHC RF System - Experience with Beam Operation. *Conf.Proc.*, C110904:202–204, 2011, accelconf.web.cern.ch/AccelConf/IPAC2011/papers/MOPC054.PDF.

[151] Luca Arnaudon, Philippe Baudrenghien, Olivier Brunner, and Andrew Butterworth. Operation Experience with the LHC RF System. *Conf.Proc.*, C100523:TUPEB056, 2010, accel-conf.web.cern.ch/AccelConf/IPAC10/papers/tupeb056.pdf.

[152] Oswald Grobner. Bunch induced multipactoring. Technical Report CERN-ISR-VA-77-38, CERN, Geneva, Jun 1977.

[153] Frank Zimmermann. A simulation study of electron-cloud instability and beam-induced multipacting in the lhc. Technical Report LHC-Project-Report-95. CERN-LHC-Project-Report-95. SLAC-PUB-7425, CERN, Geneva, Feb 1997.

[154] P. Chiggiato, V. Baglin, P. Cruikshank, J.M. Jimenez, G. Bregliozzi, et al.. Observations of Electron Cloud Effects with the LHC Vacuum System. *Conf.Proc.*, C110904:1560–1562, 2011, accel-conf.web.cern.ch/accelconf/ipac2011/papers/tups018.pdf.

[155] ATLAS collaboration. A particle consistent with the Higgs Boson observed with the ATLAS Detector at the Large Hadron Collider. *Science*, 338:1576–1582, 2012.

[156] J. Pequenao and P. Schaffner. A computer generated image representing how atlas detects particles. Jan 2013, cds.cern.ch/record/1505342.

[157] ATLAS collaboration. Search for stable hadronising squarks and gluinos with the ATLAS experiment at the LHC. *Phys.Lett.*, B701:1–19, 2011, 1103.1984.

[158] ATLAS collaboration. Search for Massive Long-lived Highly Ionising Particles with the ATLAS Detector at the LHC. *Phys.Lett.*, B698:353–370, 2011, 1102.0459.

[159] S Haywood, L Rossi, R Nickerson, and A Romaniouk. ATLAS inner detector: Technical Design Report, 2. 1997, atlas.web.cern.ch/Atlas/GROUPS/INNER_DETECTOR/TDR/tdr.html.

[160] ATLAS Collaboration. ATLAS liquid-argon calorimeter: Technical Design Report. 1996.

[161] ATLAS Collaboration. ATLAS tile calorimeter: Technical design report. 1996, atlas.web.cern.ch/Atlas/SUB_DETECTORS/TILE/TDR/TDR.html.

[162] ATLAS Collaboration. ATLAS muon spectrometer: Technical Design Report. 1997, atlas.web.cern.ch/Atlas/GROUPS/MUON/TDR/Web/TDR.html.

[163] ATLAS Collaboration. Performance of Particle Identification with the ATLAS Transition Radiation Tracker. 2011, arXiv:1109.5925 [physics.ins-det].

[164] J Adelman, M Donega, S Fratina, S Heisterkamp, E Hines, E Klinkby, T Koffas, T Peterson, K Tackmann, and E Thomson. Study of high-threshold probability in the atlas transition radiation tracker. (ATL-COM-INDET-2011-009), 2011.

[165] G. Aad et al.. Expected Performance of the ATLAS Experiment - Detector, Trigger and Physics. 2009, 0901.0512.

[166] G Aad et al.. Atlas pixel detector electronics and sensors. *Journal of Instrumentation*, 3(07):P07007, 2008.

[167] A. Ahmad et al.. The silicon microstrip sensors of the {ATLAS} semiconductor tracker. *Nuclear Instruments and Methods in Physics Research Section A: Accelerators, Spectrometers, Detectors and Associated Equipment*, 578(1):98 – 118, 2007.

[168] The ATLAS TRT collaboration, E Abat, et al.. The atlas transition radiation tracker (trt) proportional drift tube: design and performance. *Journal of Instrumentation*, 3(02):P02013, 2008.

[169] ATLAS Collaboration. Expected electron performance in the ATLAS experiment. 2011, ATL-PHYS-PUB-2011-006.

[170] D. Green. The physics of particle detectors. *Camb.Monogr.Part.Phys.Nucl.Phys.Cosmol.*, 12:1–361, 2000.

[171] E. Abat, J.M. Abdallah, T.N. Addy, P. Adragna, M. Aharrouche, et al.. Response and shower topology of 2 to 180 GeV pions measured with the ATLAS barrel calorimeter at the CERN test-beam and comparison to Monte Carlo simulations. 2010, cds.cern.ch/record/1263861/files/ATL-CAL-PUB-2010-001.pdf.

[172] J. Matthews. A Heitler model of extensive air showers. *Astroparticle Physics*, 22:387–397, January 2005.

[173] P. Amaral et al.. Hadronic shower development in iron scintillator tile calorimetry. *Nucl.Instrum.Meth.*, A443:51–70, 2000, hep-ex/9904032.

[174] J.C. Barriere et al.. The alignment system of the ATLAS barrel muon spectrometer. 2008, cds.cern.ch/record/1081769/files/muon-pub-2008-007.pdf.

[175] S Aefsky et al.. The optical alignment system of the atlas muon spectrometer endcaps. *Journal of Instrumentation*, 3(11):P11005, 2008.

[176] ATLAS Collaboration. Performance of the atlas trigger system in 2010. *Eur. Phys. J. C*, 72:1849, 2012, arXiv:1110.1530 [hep-ex].

[177] ATLAS collaboration. Performance of the ATLAS Trigger System in 2010. *Eur.Phys.J.*, C72:1849, 2012, 1110.1530.

[178] J. Alwall, P. Demin, S. de Visscher, R. Frederix, M. Herquet, et al.. MadGraph/-MadEvent v4: The New Web Generation. *JHEP*, 0709:028, 2007, arXiv:0706.2334 [hep-ph].

[179] P. Meade and M. Reece. BRIDGE: Branching Ratio Inquiry/Decay Generated Events. 2007, arXiv:0703031 [hep-ph].

[180] T. Sjostrand, S. Mrenna, and P. Z. Skands. PYTHIA 6.4 Physics and Manual. *JHEP*, 0605:026, 2006, arXiv:0603175 [hep-ph].

[181] M. L. Mangano, M. Moretti, F. Piccinini, R. Pittau, and A. D. Polosa. ALPGEN, a generator for hard multiparton processes in hadronic collisions. *JHEP*, 0307:001, 2003, arXiv:0206293 [hep-ph].

[182] J. Alwall, S. Hoche, F. Krauss, N. Lavesson, L. Lonnblad, et al.. Comparative study of various algorithms for the merging of parton showers and matrix elements in hadronic collisions. *Eur. Phys. J. C*, 53:473–500, 2008, arXiv:0706.2569 [hep-ph].

[183] G. Corcella et al.. HERWIG 6.5: an Event Generator for Hadron Emission Reactions With Interfering Gluons (Including Supersymmetric Processes). *JHEP*, 0101:010, 2001, arXiv:0011363 [hep-ph].

[184] J M Butterworth et al.. Multiparton Interactions in Photoproduction at HERA. *Z. Phys. C.*, 72(4):21, 1996, arXiv:9601371 [hep-ph].

[185] S. Frixione and B. R. Webber. Matching NLO QCD computations and parton shower simulations. *JHEP*, 0206:029, 2002, arXiv:0204244 [hep-ph].

[186] T. Gleisberg et al.. Event generation with SHERPA 1.1. *JHEP*, 02:007, 2009, arXiv:0811.4622 [hep-ph].

[187] T. Sjöstrand and M. van Zijl. A multiple-interaction model for the event structure in hadron collisions. *Phys. Rev. D*, 36:2019–2041, 1987.

[188] S. Frixione, P. Nason, and C. Oleari. Matching NLO QCD computations with Parton Shower simulations: the POWHEG method. *JHEP*, 0711:070, 2007, arXiv:0709.2092 [hep-ph].

[189] N. Davidson, G. Nanava, T. Przedzinski, E. Richter-Was, and Z. Was. Universal Interface of TAUOLA Technical and Physics Documentation. 2010, arXiv:1002.0543 [hep-ph].

[190] ATLAS Collaboration. Measurement of the inclusive $\mathrm{W}^{\pm}$ and Z/γ cross sections in the electron and muon decay channels in pp collisions at $\sqrt{s} = 7$ TeV with the ATLAS detector. *Phys. Rev. D*, 85:072004, 2012, arXiv:1109.5141 [hep-ex].

[191] ATLAS Collaboration. Measurement of the top quark pair production cross-section with ATLAS in the single lepton channel. *Phys. Lett. B*, 711:244–263, 2012, arXiv:1201.1889 [hep-ex].

[192] K. Melnikov and F. Petriello. Electroweak gauge boson production at hadron colliders through $O(\alpha_s^2)$. *Phys. Rev. D*, 74:114017, 2006, arXiv:0609070 [hep-ph].

[193] J. Allison, K. Amako, J. Apostolakis, H. Araujo, P.A. Dubois, et al.. Geant4 developments and applications. *IEEE Trans.Nucl.Sci.*, 53:270, 2006.

[194] ATLAS Collaboration. The ATLAS Simulation Infrastructure. *Eur. Phys. J. C*, 70:823–874. 53 p, 2010, arXiv:1005.4568 [physics.ins-det].

[195] ATLAS Collaboration. Electron performance measurements with the ATLAS detector using the 2010 LHC proton-proton collision data. *Eur. Phys. J. C*, 72:1909, 2012, arXiv:1110.3174 [hep-ex].

[196] G. Abbiendi et al.. Search for invisibly decaying Higgs bosons in $e^+e^- \to Z^0h^0$ production at $\sqrt{s}$=183 - 209 GeV. *Phys. Lett. B*, 682:381–390, 2010, arXiv:0707.0373 [hep-ex].

[197] ATLAS Collaboration. Muon Momentum Resolution in First Pass Reconstruction of pp Collision Data Recorded by ATLAS in 2010. 2011, cds.cern.ch/record/1338575/files/ATLAS-CONF-2011-046.pdf.

[198] S. Schael et al.. Precision electroweak measurements on the Z resonance. *Phys.Rept.*, 427:257–454, 2006, hep-ex/0509008.

[199] twiki.cern.ch/twiki/bin/viewauth/AtlasProtected/PileupReweighting.

[200] ATLAS Collaboration. Luminosity Determination in pp Collisions at $\sqrt{s}$=7 TeV Using the ATLAS Detector at the LHC. *Eur. Phys. J. C*, 71:1630, 2011, arXiv:1101.2185 [hep-ex].

[201] ATLAS Collaboration. Luminosity Determination in pp Collisions at $\sqrt{s} = 7$ TeV using the ATLAS Detector in 2011. 2011, cds.cern.ch/record/1376384/files/ATLAS-CONF-2011-116.pdf.

[202] ATLAS Collaboration. Expected photon performance in the ATLAS experiment. 2011, ATL-PHYS-PUB-2011-007, ATL-COM-PHYS-2010-1051.

[203] S. Hassani, L. Chevalier, E. Lancon, J.F. Laporte, R. Nicolaidou, et al.. A muon identification and combined reconstruction procedure for the ATLAS detector at the LHC using the (MUONBOY, STACO, MuTag) reconstruction packages. *Nucl.Instrum.Meth.*, A572:77–79, 2007.

[204] *ATLAS detector and physics performance: Technical Design Report, 1.* Technical Design Report ATLAS. CERN, Geneva, 1999, http://cds.cern.ch/record/391176/files/cer-0317330.pdf.

[205] twiki.cern.ch/twiki/bin/viewauth/AtlasProtected/MCPAnalysisGuidelinesPLHC2011.

[206] ATLAS collaboration. Search for supersymmetry in final states with jets, missing transverse momentum and one isolated lepton in sqrts = 7 TeV pp collisions using 1 fb^{-1} of ATLAS data. *Phys.Rev.*, D85:012006, 2012, 1109.6606.

[207] ATLAS Collaboration. Muon reconstruction efficiency in reprocessed 2010 LHC proton-proton collision data recorded with the ATLAS detector. 2011, cds.cern.ch/record/1345743/files/ATLAS-CONF-2011-063.pdf.

[208] ATLAS Collaboration. Reconstruction and Calibration of Missing Transverse Energy and Performance in Z and W events in ATLAS Proton-Proton Collisions at 7 TeV. 2011, cds.cern.ch/record/1355703/files/ATLAS-CONF-2011-080.pdf.

[209] M. Cacciari, G. P. Salam, and G. Soyez. The anti-k_t jet clustering algorithm. *JHEP*, 04:063, 2008, arXiv:0802.1189 [hep-ph].

[210] ATLAS Collaboration. Measurement of the top quark-pair production cross section with ATLAS in pp collisions at sqrts=7 TeV. *Eur. Phys. J. C*, 71:1577, 2011, arXiv:1012.1792 [hep-ex].

[211] ATLAS Collaboration. Background studies for top-pair production in lepton plus jets final states in $\sqrt{s} = 7TeV$ ATLAS data. 2010, cds.cern.ch/record/1298967/files/ATLAS-CONF-2010-087.pdf.

[212] J-F Arguin, K Hamano, A Hawkins, B Heinemann, M Hurwitz, E Lytken, D Olivito, N Rodd, L Skinnari, and E Thomson. Search for anomalous production of prompt like-sign lepton pairs and constraints on physics beyond the standard model. Technical Report ATL-COM-PHYS-2012-529, CERN, Geneva, May 2012.

[213] LHC Higgs Cross Section Working Group, S. Dittmaier, C. Mariotti, G. Passarino, and R. Tanaka (Eds.). Handbook of LHC Higgs Cross Sections: 2. Differential Distributions. *CERN-2012-002*, CERN, Geneva, 2012, arXiv:1201.3084 [hep-ph].

[214] A. L. Read. Presentation of search results: The CL(s) technique. *J. Phys. G*, 28:2693–2704, 2002.

[215] F. James, Y. Perrin, and L. Lyons. Workshop on confidence limits, CERN, Geneva, Switzerland, 17-18 Jan 2000: Proceedings. 2000.

[216] K. Cranmer, G. Lewis, L. Moneta, A. Shibata, and W. Verkerke. Histfactory: A tool for creating statistical models for use with roofit and roostats. Technical Report CERN-OPEN-2012-016, New York U., New York, 2012.

[217] Lars Bergstrom, Joakim Edsjo, and Gabrijela Zaharijas. Dark matter interpretation of recent electron and positron data. *Phys.Rev.Lett.*, 103:031103, 2009, 0905.0333.

Spodaj podpisani Andrii Tykhonov izjavljam, da je disertacija rezultat mojega samostojnega raziskovalnega dela.

Andrii Tykhonov

Ljubljana, 2013